



PhD-FSTM-2024-068

The Faculty of Science, Technology and Medicine

DISSERTATION

Presented on 23/09/2023 in Esch-sur-Alzette, Luxembourg

to obtain the degree of

DOCTEUR DE L'UNIVERSITÉ DU LUXEMBOURG

EN CHIMIE

by

Daniil NOSOV

Born on 25th July 1996 in Moscow, (Russia)

NOVEL POLYMER ELECTROLYTES DERIVED FROM COACERVATION OF COMPLEMENTARY POLY(IONIC LIQUIDS) AND/OR CHARGED SILICA NANOPARTICLES

Dissertation defence committee

Prof., Dr. Alexander Shaplov, dissertation supervisor

Luxembourg Institute of Science and Technology, Luxembourg

Prof., Dr. Alex Redinger, chairman

University of Luxembourg, Luxembourg

Prof., Dr. Patrik Johansson, vice-chairman, external referee

Chalmers University of Technology, Sweden

Prof., Dr. Heikki Tenhu, external referee

University of Helsinki, Finland

Prof., Dr. Cedric Plesse, external referee

Cergy Paris University, France

“Dreams. Each man longs to pursue his dream. Each man is tortured by this dream, but the dream gives meaning to his life. Even if the dream ruins his life, man cannot allow himself to leave it behind. In this world, is man ever able to possess anything more solid, than a dream?”
— **Kentaro Miura**

Contents

Contents	3
List of Acronyms, Abbreviations and Symbols	6
I. Thesis goal and objectives	9
II. Literature review	13
1. Poly(ionic liquid)s (PIL)s	14
1.1 Design of poly(ionic liquid)s	18
1.1.1 The type of organic cation.	19
1.1.2 Polymer backbone.	20
1.1.3 The type of anion.....	22
1.1.4 Block copolymers.....	23
2. Ion gels.....	25
3. Polyelectrolyte complexes.....	26
4. Conclusions	28
III. Results and discussions.....	30
1. Design and synthesis of ionic liquid like monomers (ILM)s	30
1.1 Methacrylic ionic monomers	30
1.1.1 Design and selection.....	30
1.1.2 Synthesis and characterization	32
1.1.3 Selected properties of ILMs	38
1.2 Dipropargyl ionic monomers	40
1.2.1 Design and selection.....	40
1.2.2 Synthesis and characterisation	41
1.2.3 Thermal properties	42
1.2.4 Spectroscopic analysis of dipropargyl ionic monomers	42
2. Synthesis of poly(ionic liquid)s (PIL)s	46
2.1 Triazole/triazolium PILs (PIL1-PIL9).....	47
2.1.1 Polyaddition of ionic monomers	47
2.1.2 Transformation of triazole polymers into triazolium PILs with charge density increase	48
2.1.3 Spectroscopic analysis	49
2.1.4 Thermal properties	52
2.1.5 Electrochemical properties	54
2.1.6 Rheological properties	59
2.2 Methacrylate based polyelectrolytes (PIL10-PIL29) prepared by Reversible Addition Fragmentation chain Transfer (RAFT) polymerization	60
2.2.1 Synthesis and characterization	60

2.2.2 Spectroscopic analysis	66
2.2.3 Thermal properties	69
2.2.4 Morphological properties.....	76
2.2.5 Electrochemical properties	78
2.2.6 Electrochemical stability	85
2.2.7 Rheological properties	86
2.3 Epichlorohydrin-derived PILs prepared by chemical modification of a neutral polymer (PIL30-PIL37).....	90
2.3.1 Synthesis and characterization	91
2.3.2 Spectroscopic analysis	95
2.3.1 Thermal properties	99
2.3.2 Electrochemical properties	102
2.3.3 Rheological properties	104
3. Development of dynamic ion gels (DIG)s	106
3.1 Model Dynamic Ion Gel DIG1 (proof-of-concept).....	107
3.1.1 Synthesis and characterization	107
3.1.2 Proof of dynamic ion exchange.....	109
3.1.3 Thermal properties	111
3.1.4 Ionic conductivity.....	112
3.1.5 Rheological properties	113
3.2 Approaches for further improvement of DIGs properties	115
3.3 1 st approach for the improvement of DIGs - introduction of one localized charge (DIG2-DIG5).....	116
3.3.1 Synthesis and characterization	116
3.3.2 Thermal properties	117
3.3.3 Ionic conductivity.....	119
3.3.4 Rheological properties	121
3.4 2 nd approach for the improvement of DIGs - introduction of block copolymers (DIG6-DIG13).....	123
3.4.1 Synthesis and characterization	123
3.4.2 Thermal properties	126
3.4.3 Morphological properties.....	127
3.4.4 Ionic conductivity.....	129
3.4.5 Rheological properties	132
3.5 Optimization of DIG structure.....	133
3.5.1 Thermal properties of DIG14.....	136
3.5.2 Ionic conductivity of DIG14.....	136

3.5.3 Rheological properties of DIG14	137
4. Application of PILs and DIGs in all-solid-state supercapacitors.....	138
4.1 Preparation of electrodes and supercapacitor assembly	138
4.2 Supercapacitors testing.....	139
IV. Experimental part	143
1. Methods.....	143
1.1 NMR spectroscopy.....	143
1.2 IR spectroscopy	143
1.3 Kinematic and dynamic viscosities	143
1.4 Differential scanning calorimetry (DSC)	143
1.5 Thermal mechanical analysis (TMA).....	144
1.6 Thermogravimetric analysis (TGA).....	144
1.7 Electrochemical impedance spectroscopy (EIS).....	144
1.8 Broadband dielectric spectroscopy (BDS)	145
1.9 Cyclic voltammetry (CV)	146
1.10 Size exclusion chromatography (SEC).....	146
1.11 Rheological measurements	146
1.12 Atomic force microscopy (AFM)	147
2. Synthesis	148
2.1 Ionic liquid like monomers (ILMs).....	148
2.1.1 Methacrylic ionic monomers	148
2.1.2 Dipropargyl ionic monomers	150
2.2 Poly(ionic liquid)s (PIL)s	152
2.2.1 Triazole/triazolium PILs (PIL1-PIL9).....	152
2.2.2 Methacrylate based polyelectrolytes (PIL10-PIL29).....	154
2.2.3 Epichlorohydrin-derived PILs (PIL30-PIL37).....	171
2.3 Dynamic ion gels (DIG)s	180
3. Supercapacitors assembly and testing.....	180
V. Conclusions	182
VI. Acknowledgements	186
VII. Dissemination	186
VIII. References	191

List of Acronyms, Abbreviations and Symbols

AIBN - Azobisisobutyronitrile

AFM - Atomic Force Microscopy

Bu₄N - Tetrabutylammonium

Bu₄P - Tetrabutylphosphonium

BuIm - 1-Butylimidazolium

BuMeIm - 1-Methyl-3-butylimidazolium

CNT - Carbon nanotubes

CPDB - 2-Cyano-2-propyl benzodithioate

CPCP - 4-Cyano-4-(phenylcarbonothioylthio)pentanoic acid

CTA - Chain Transfer Agent

CV - Cyclic voltammogram

CuAAC - Copper (I) Catalyzed Azide–Alkyne Cycloaddition

DCM - Dichloromethane

DIPEA - N,N-Diisopropylethylamine

DIG - Dynamic Ion Gel

DMF - Dimethylformamide

DSC - Differential Scanning Calorimetry

EIS - Electrochemical Impedance Spectroscopy

ESW - Electrochemical Stability Window

FTIR - Fourier-Transform Infrared Spectroscopy

IL - Ionic Liquid

ILM - Ionic Liquid-Like Monomers

Me₃PrN - N,N,N-Trimethyl-N-propylamine

MeCN - Acetonitrile

Napht - (1-Naphthyl)methyl Methacrylate

NMR - Nuclear Magnetic Resonance

PEGM - Poly(ethylene glycol) Methyl Ether Methacrylate

PEDOT - poly(3,4-ethylenedioxythiophene)

PEO - poly(ethylene oxide)

PhEtM - 2-Phenylethyl Methacrylate

PhMe - Toluene (Methylbenzene)

PIL - Poly(ionic Liquid)s

PSBMA - poly(sulfobetainemethacrylamide)

PSS - poly(4-styrene sulfonate)

PS – Polystyrene

Py - Pyridine

RAFT - Reversible Addition-Fragmentation Chain Transfer

RGO - reduced graphene oxide

SAOS - Small Amplitude Oscillatory Shear

SC - Supercapacitor

SEC - Size Exclusion Chromatography

SPE - Solid Polymer Electrolytes

SST - Stainless steel

TFSI - Bis(trifluoromethylsulfonyl)imide

TGA - Thermogravimetric Analysis

TFM2B - 1,4-bis(trifluoromethyl)benzene

THF - Tetrahydrofuran

TMA - Thermomechanical Analysis

TTS - Time-Temperature Superposition

VFT - Vogel-Fulcher-Tammann

WLF - Williams-Landel-Ferry

a_T - Shift Factor

bp - Boiling Point

C_{SP} – Specific capacity

E – Energy density

d - density

G' and **G''** - Storage Modulus and Loss Modulus

η - dynamic viscosity

ε_r - Relative Permittivity (Dielectric Constant)

M_n - Number-Average Molecular Weight

M_w - Weight-Average Molecular Weight

M_w/M_n - Polydispersity Index

q – Conversion

σ – Ionic conductivity

P – power density

T_g - Glass Transition Temperature

T_{HDT} - Heat Distortion Temperature

T_{onset} - Onset Temperature

T_m - Melting Temperature

ω - Angular frequency



I. Thesis goal and objectives

The goal of this thesis is a development of solid polymer electrolytes (SPE) with an unprecedented combination of mechanical (G') and electrochemical (σ , ESW) properties. It is hypothesized that this goal can be realised through the creation of a new family of polymer materials termed **dynamic ion gels (DIGs)** via the coacervation of oppositely charged building blocks (Figure I). This approach involves blending complementary polycationic and polyanionic poly(ionic liquid)s (PIL)s and/or ionic silica nanoparticles. The gelation process occurs via the creation of dynamic ionic cross-links through an ion metathesis with the concomitant in situ generation of highly ion conducting ionic liquids (IL)s. Thus, DIGs should combine the ion-conducting properties of ionic liquids with the solidity and toughness of dynamic polymer networks and nanocomposites.

To achieve these goals, the following research objectives were established:

- 1) The design and synthesis of novel ionic liquid like monomers (ILM)s toward the formation of PILs with the highest ionic conductivity.
- 2) The copolymerization of the novel ILMs and the investigation of the properties of the resulting copolymers.
- 3) The preparation of novel PILs via chemical modification and investigation of their properties.
- 4) The synthesis of model **DIG1** through the coacervation of **PIL33TFSI** and **PIL13**, the optimization of synthetic conditions and the confirmation of ionic cross-links formation and IL generation.
- 5) The combination of various building blocks to obtain the most highly conductive and mechanically robust DIGs, the establishment of structure/properties relationship and the determination of the most promising DIG candidates for further application in supercapacitors
- 6) The application of selected DIGs in all-solid-state supercapacitors and evaluation of their characteristics (C_{SP} , E, P).

The manuscript is structured as a monograph thesis and divided into four chapters (Figure I). At the beginning thorough review of methods to enhance the ionic conductivity and mechanical properties of polyelectrolytes is presented.

Chapter 1 provides a detailed description of the design and synthesis of two groups of ILMs, as well as their thermal and electrochemical properties. The first group comprises two ionic methacrylate-based monomers (anionic **ILM1** and cationic **ILM2**, Figure 1.1), which were further used

in Reversible Addition-Fragmentation Chain Transfer (RAFT) polymerization. These monomers have similar structures, differing only in the ionic group attached to the spacer. The second group includes four dipropargyl ionic monomers intended for Cu(I)-catalyzed azide–alkyne polyaddition with neutral diazide. All of these monomers are cationic, but they differ in the number and nature of the cations included in the structure.

Chapter 2 aligns with Objectives 2 and 3 and is dedicated to the synthesis of five novel families of PILs by three synthetic approaches (Figure I). The thermal, electrochemical, and rheological properties of all obtained polyelectrolytes are discussed in detail. The first family of PILs, obtained by Cu(I)-catalyzed azide–alkyne polyaddition of previously developed dipropargyl ionic monomers and subsequent n-alkylation reactions, consists of 9 polymers with repeat units containing one to four ion pairs (Scheme 2.1). The variation in the number of ion pairs in the repeat unit and the nature of cations involved allowed for the investigation of the influence of these structural factors on ionic conductivity and mechanical properties. The best polymer from this series is **PIL9**, containing two 1,2,3-triazolium cations separated by an oxyethylene spacer, which exhibited an ionic conductivity of $1.8 \times 10^{-5} \text{ S cm}^{-1}$ at 25 °C and a storage modulus of 0.1 kPa at 25°C and 1 rad s⁻¹.

The second, third, and fourth families were obtained by RAFT copolymerization of various methacrylic neutral monomers with one commercial (**ILM7**) and two novel methacrylic monomers (**ILM1** and **ILM2**) presented in the second chapter (Scheme 2.2). This resulted in 16 random and 8 block copolymers with a wide range of properties. The ionic conductivity varied between $1.9 \times 10^{-7} \text{ S cm}^{-1}$ and $1.8 \times 10^{-5} \text{ S cm}^{-1}$ at 25 °C and reached a maximum for **PIL14**. The storage modulus at 25°C and 1 rad s⁻¹ varied from 0.5 to 1680 kPa, reaching the maximum for block copolymer **PIL25**. Based on this series of copolymers, the influence of polymer morphology, charge delocalization, and the structure of cations and anions on mechanical properties and ionic conductivity is discussed.

The last family of PILs consists of 12 polymers synthesized through the chemical modification of a neutral polymer. The influence of the nature and length of substituents on the imidazolium cation, as well as the asymmetry and charge delocalization of the counter anion, on the properties of PILs, is discussed in detail. **PIL33BF(CN)₃** exhibited a storage modulus of 22 kPa at 25°C and 1 rad s⁻¹ and the highest ionic conductivity in the family ($1.0 \times 10^{-5} \text{ S cm}^{-1}$ at 25 °C).

Chapter 3 discusses the concept of DIGs in more details and is devoted to the synthesis and investigation of DIGs, thus addressing Objective 4 and 5. It begins by presenting a model **DIG1** which helps to determine the optimal synthetic conditions for preparing DIGs, including the choice of solvent and the order of mixing. The application of various methods confirms the occurrence of ion exchange between two PILs and the formation of dynamic cross-links with *in-situ* generation of ionic liquid. Following this foundation, the chapter expands by discussing and comparing a wider range of DIGs incorporating specific structural features, such as localized charges and block copolymers. These

materials are comprehensively characterized through thermal, rheological, and electrochemical analyses. Finally based on the obtained results the last iteration of DIG structure optimization led to the development of **DIG14** which exhibited an ionic conductivity of $8.2 \times 10^{-6} \text{ S cm}^{-1}$ at 25 °C and a storage modulus of 214.5 kPa at 25°C and 1 rad s⁻¹.

The final chapter, **Chapter 4**, explores the application of the most promising **DIG14** as an polyelectrolyte for supercapacitors. For comparative purposes, two additional supercapacitors utilizing PILs are also examined. The specific capacitance, energy and power density, and capacitance retention of these devices are analyzed and compared. The results demonstrate that the supercapacitor with **DIG14** outperforms the others, exhibiting the following characteristics: $C_{\text{SP}} 19.6 \text{ F g}^{-1}$, $E 10.9 \text{ Wh kg}^{-1}$, and $P 97.7 \text{ W kg}^{-1}$.

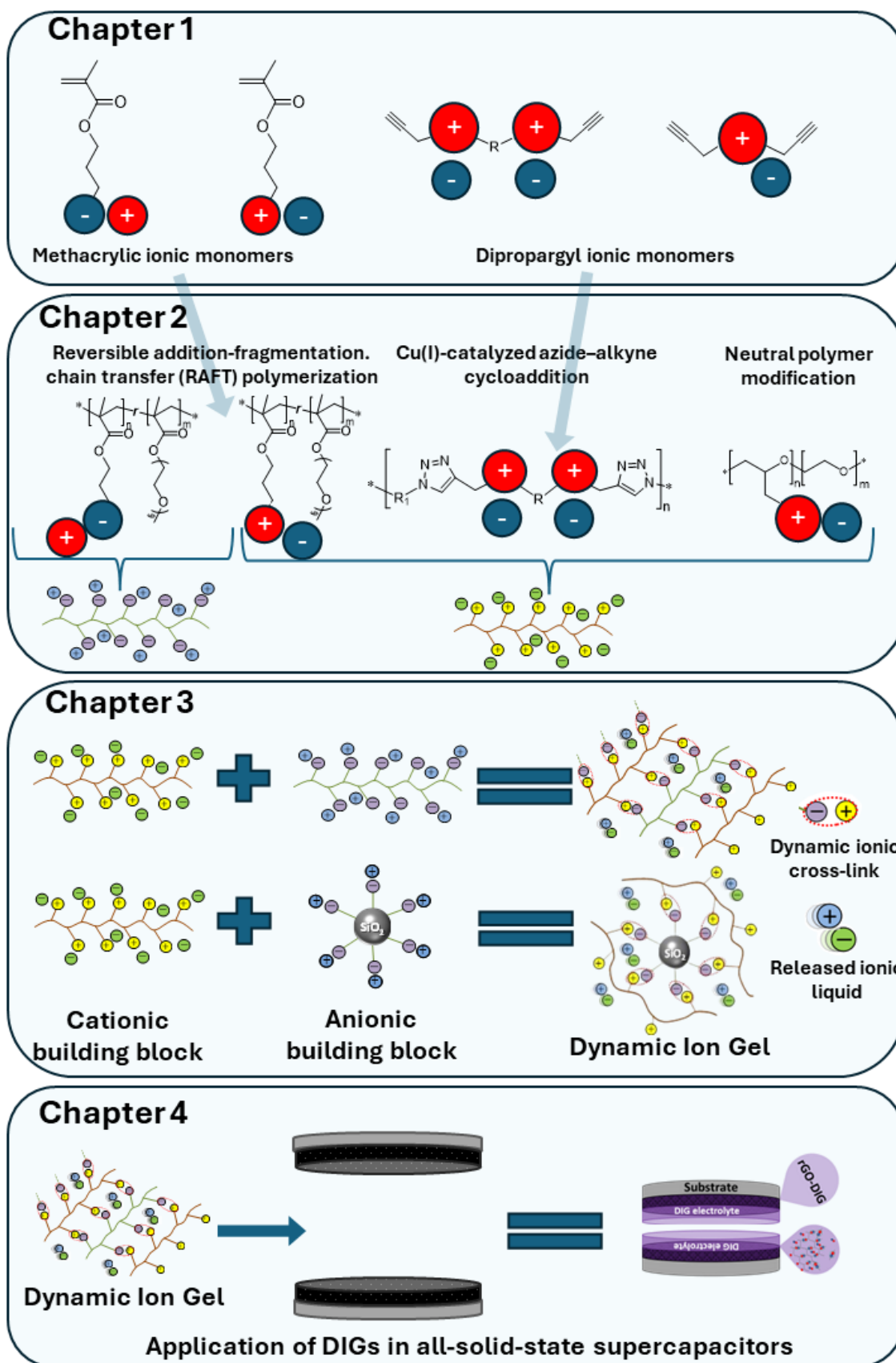


Figure I Thesis roadmap



II. Literature review

In recent decades, the landscape of electrochemical device development has undergone a profound and far-reaching transformation, motivated by the dual imperatives of enhancing both safety and performance. Electrochemical devices, such as batteries, fuel cells, and supercapacitors, play an indispensable role in modern society, powering everything from portable electronics to electric vehicles and renewable energy systems. Traditionally, these devices have relied on liquid electrolytes, which have been the cornerstone of electrochemical systems for many years. Liquid electrolytes have facilitated the efficient movement of ions between electrodes, thereby enabling the energy conversion and storage processes that are fundamental to the operation of these devices. However, despite their widespread use and effectiveness, liquid electrolytes are not without significant drawbacks¹.

One of the most pressing issues associated with liquid electrolytes is their inherent flammability. Most liquid electrolytes are composed of organic solvents, which, while effective at dissolving salts and promoting ionic conductivity, are also highly volatile and combustible. This flammability poses a serious safety risk, particularly in high-energy-density applications like lithium-ion batteries, where thermal runaway can lead to catastrophic failures, including fires and explosions². In addition to their flammability, liquid electrolytes are prone to leakage, which can result in the degradation of device components and reduced operational lifespan³. Furthermore, the chemical stability of liquid electrolytes is often compromised under extreme conditions, such as high temperatures or prolonged cycling, leading to the formation of harmful by-products that can deteriorate device performance^{4,5}.

These concerns have increasingly driven the research community to seek out safer, more reliable alternatives to traditional liquid electrolytes. In response to the growing demand for enhanced safety and performance, a significant shift in focus has occurred within the field of electrochemical materials research. Scientists and engineers have turned their attention to the development of both solid polymer electrolytes (SPEs) and polyelectrolytes. SPEs, composed of polymer matrices that are typically non-volatile and non-flammable, are designed to maintain structural integrity under a wide range of operating conditions. This makes them inherently safer and more stable, addressing many of the critical safety issues associated with liquid electrolytes. On the other hand, polyelectrolytes, which consist of polymers with ionizable groups, offer unique advantages due to their ability to form charged polymer backbones with mobile counterions^{6,7}. This characteristic allows polyelectrolytes to interact strongly with other ions and molecules, facilitating innovative approaches to energy storage and conversion technologies⁵.

Both SPEs and polyelectrolytes offer compelling properties that make them highly attractive for use in next-generation electrochemical devices. SPEs are known for their superior safety profile and mechanical robustness, which are crucial for the long-term durability of devices⁸. The polymeric nature of these electrolytes allows for flexibility in material design, enabling the creation of thin, lightweight, and flexible devices that are well-suited for modern applications⁹. Similarly, polyelectrolytes can form thin films or multilayer structures that are particularly useful in applications in batteries and other devices. The charged nature of polyelectrolytes also allows for extensive chemical modification, enabling the design of highly specialized systems tailored to specific functions. The versatility of polymers in both SPEs and polyelectrolytes allows for a wide range of chemical modifications and processing techniques, optimizing the performance of the electrolytes for various applications.

As the demand for safer, more efficient, and more reliable energy storage and conversion technologies continues to grow, the development and optimization of both solid polymer electrolytes and polyelectrolytes will play an increasingly critical role. SPEs, with their ability to overcome the limitations of traditional liquid electrolytes, have the potential to revolutionize electrochemical devices by providing safer and more durable energy storage solutions. Concurrently, polyelectrolytes, with their unique ionic properties and structural flexibility, offer innovative possibilities for enhancing the performance and functionality of these devices. Together, these materials are paving the way for the next generation of energy storage solutions that are not only safer and more reliable but also more adaptable to the evolving needs of modern society.

1. Poly(ionic liquid)s (PIL)s

Poly(ionic liquid)s (PIL)s are a distinct subclass of polyelectrolytes, characterized by the incorporation of ionic liquid moieties into the polymer backbone or side chains (Figure II.1). Over the last 25 years these materials have garnered significant attention from various scientific communities due to their exceptional potential in electrochemical applications. It happened due to the fact that PILs uniquely combine the high ionic conductivity and electrochemical stability of ionic liquids with the processability and mechanical flexibility of polymers^{7,10}. Additionally, PILs offer several other advantages, including extensive structural design freedom, which allows for the customization of their physical and chemical properties to meet specific application requirements.

For PILs to be effectively utilized in modern electrochemical devices, they must meet several critical criteria. First, they should exhibit an ionic conductivity greater than $10^{-5} \text{ S cm}^{-1}$ at 25°C , which is essential for efficient ion transport in electrochemical applications^{10,11}. Second, PILs must maintain sufficient mechanical stability to endure mechanical stresses and preserve structural integrity during operation^{10,12}. Thus, achieving a balance between mechanical strength and ionic conductivity is vital for

the development of high-performance PILs that can meet the stringent demands of modern electrochemical applications.

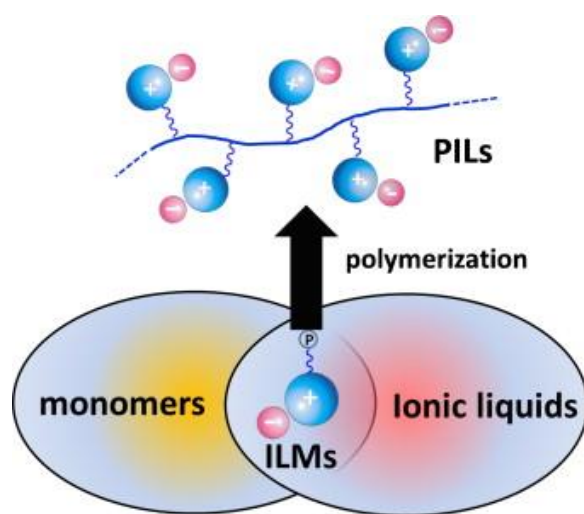


Figure II.1 Illustration of the relationship between ILs and PILs⁷.

However, a significant challenge in the development of PILs lies in the inverse relationship between these two critical properties^{13,14} (Figure II.2). High mechanical stability in PILs typically requires a high glass transition temperature (T_g) and/or a degree of crystallinity. Materials with a high T_g are generally more rigid and mechanically robust, which enhances structural integrity. However, this rigidity can restrict the segmental motion of polymer chains, which is crucial for fast ion transport and achieving high ionic conductivity. Conversely, to attain high ionic conductivity, PILs need a low T_g , which allows for greater segmental motion within the polymer matrix. This increased flexibility at lower T_g facilitates ion mobility, leading to improved ionic conductivity. Unfortunately, the trade-off is that these low T_g , amorphous polymers often lack the mechanical strength and dimensional stability required for certain applications.

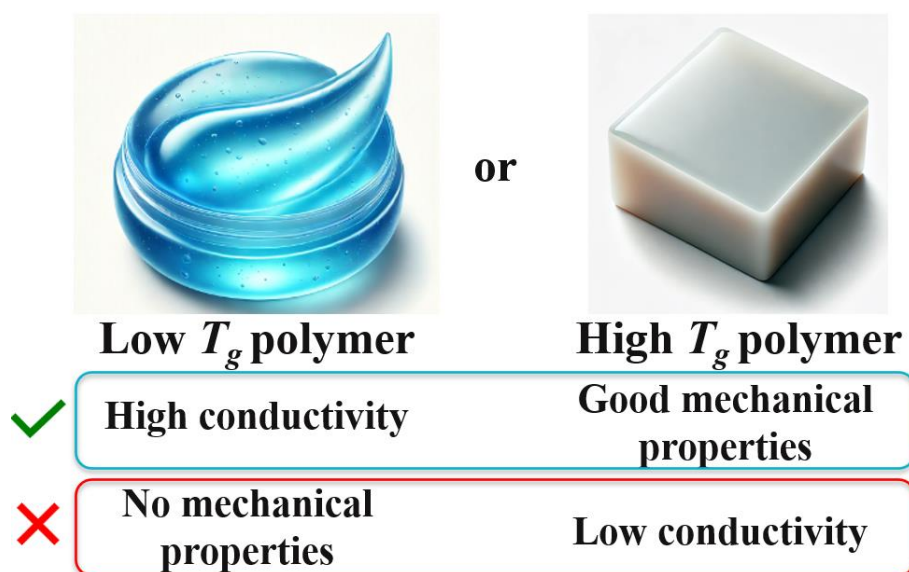


Figure II.2 Visual comparison of PILs with different T_g s

To address this challenge, classical approaches involve sophisticated polymer structure design^{10,15}. By introducing specific structural scaffolds, altering charge density, and adjusting molecular weight, it is possible to influence the balance between ionic conductivity and T_g . One of the most promising design strategies involves modifying polymer architecture and forming block copolymers. In some cases, block copolymers exhibit phase separation, leading to the formation of ionic channels within the material, which facilitates faster ion movement while also creating stiff regions that contribute to mechanical stability¹⁶. However, it is important to note that even with these design strategies, the most highly conductive PILs still tend to appear as oils or cold-flowing viscous liquids (Table II.1).

In addition to structural design, many methods involve adding specific additives to PILs to improve their properties. For instance, to enhance ionic conductivity, one common approach is the addition of ionic liquids, resulting in the formation of iongels^{17,18}. Ionic liquids, acting as plasticizers, facilitate both chain and ion mobility and also participate directly in ion transport. This results in improved ionic conductivity which can reach $10^{-3} \text{ S cm}^{-1}$ at 25°C ¹⁴. However, achieving this level of conductivity often requires high IL loadings, which consequently leads to a significant decrease in the mechanical properties of the ion gels¹⁸.

To improve the mechanical properties and processability, the mixing of PILs with other polymers is frequently reported in the literature^{19,20}. Specifically, the formation of polyelectrolyte complexes (PECs) from two oppositely charged polyelectrolytes has proven to be an effective method for enhancing polymer processability. However, this method has never been used to improve the ionic conductivity of polyelectrolytes.

Table II.1 Overview of the most highly conductive linear PILs reported to date (updated in February, 2024).

17

29		2.4×10^{-5}	30	23.0	from purple sticky soft solid to cross-linked soft self-standing films (maximum stress and the elongation at break (tensile testing, 25°C): 0.17 MPa and 170%)
30		2.5×10^{-5}	30	26.8	yellow viscous oil (n.d.)
31		2.3×10^{-5}	25	45.0	viscous liquid (n.d.)
32		1.8×10^{-5}	25	71.7	brown gummy sticky solid (n.d.)
33		1.2×10^{-5}	30	-	brown viscous oil (n.d.)
34		1.1×10^{-5}	30	113.6	orange viscous material (n.d.)
35		1.0×10^{-5}	25	44.0	dark brown viscous gummy solid (n.d.)
36		7.7×10^{-6}	30	252 ⁴	yellow viscous oil (n.d.)
37		6.9×10^{-6}	25	194	transparent cold flowing viscous mass (n.d.)
38		6.3×10^{-6}	27	99.5	(n.d.)

¹Ionic conductivity under anhydrous conditions at 25 or 30°C. ²Temperature at which σ was measured. ³Number-average molar mass. ⁴Number-average molar mass measured for neutral precursor. ⁵n.d.=not determined.

1.1 Design of poly(ionic liquids)

The design of new PILs (Figure II.3) can be based on tuning the following parameters that are known to influence the bulk ionic conductivity of a polyelectrolyte: the anion's and cation's nature (1),

the architecture of the polymer backbone (2), the length and the nature of the spacer (3) between chemically bonded ion and main polymer chain^{14,39}. The influence of each of these parameters on ionic conductivity of PILs will be discussed in detail below.

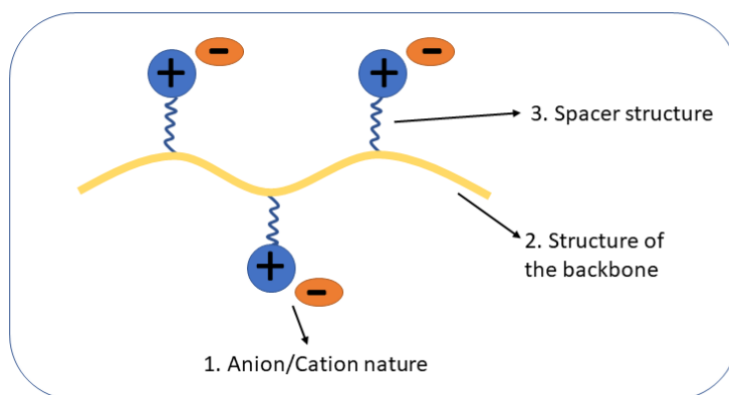


Figure II.3 Schematic illustration of PILs and structural factors affecting their ionic conductivity.

1.1.1 The type of organic cation.

Cation's structure, in particular its type and the substituents, showed a strong influence on ionic conductivity of PILs. Among the vast number of cations, polyelectrolytes with positively charged imidazolium heterocycles demonstrated the best performance in terms of conductivity and may be considered as the most promising candidates for further investigation^{40,41}. At the same time, the study of substitutes influence or side chains in imidazolium ring on PIL's bulk ionic conductivity was mainly limited to the negligible variation in length⁴⁰⁻⁴³ and isomerism⁴³ of hydrocarbon chains (Figure II.4, a-c). In spite of the similarity in PILs structures, the results obtained by several research groups were contradictory. Thus, Ohno et al.⁴⁰ revealed the extremal character of ionic conductivity in TFSI based PILs during the transfer from methyl to *n*-butyl substitute in imidazolium cation (Figure II.4, a):

$$\sigma \text{ (25 } ^\circ\text{C, S cm}^{-1}\text{): } \text{-CH}_3 \text{ (} 4.4 \times 10^{-5} \text{)} < \text{-CH}_2\text{CH}_3 \text{ (} 1.4 \times 10^{-4} \text{)} > \text{-(CH}_2\text{)}_3\text{CH}_3 \text{ (} 4.1 \times 10^{-5} \text{)}$$

Contrary, in a very similar imidazolium PILs, the increase in the substituent's length from methyl⁴¹ to *n*-butyl⁴² group led to the linear growth in ionic conductivity from 7.4×10^{-10} to 8.5×10^{-7} S cm⁻¹ at 25 °C (Figure II.4, b). Another trend was observed in the recent publication of Ikeda et al.⁴³, where the conductivity of PILs was firstly increasing by half order of magnitude with the transfer from methyl to ethyl substitute and then became constant independently of the substitute's length (Figure II.4, c):

$$\sigma \text{ (30 } ^\circ\text{C, S cm}^{-1}\text{): } \text{-CH}_3 \text{ (} 5.0 \times 10^{-6} \text{)} < \text{-CH}_2\text{CH}_3 \text{ (} 1.5 \times 10^{-5} \text{)} \approx \text{-(CH}_2\text{)}_2\text{CH}_3 \text{ (} 1.3 \times 10^{-5} \text{)} \approx \text{-CH(CH}_3\text{)}_2 \text{ (} 1.1 \times 10^{-5} \text{)} \approx \text{-(CH}_2\text{)}_3\text{CH}_3 \text{ (} 1.5 \times 10^{-5} \text{)}$$

At this, the influence of imidazolium substituents containing heteroatoms (Si, F, O, etc.) on ionic conductivity of PILs practically was not studied. Although some reports discussing such PILs

appeared recently⁴⁴⁻⁴⁶, they were mainly dedicated to the elaboration of the synthetic pathways for the preparation of imidazolium PILs with fluorinated, silyl or siloxane substituents, while the conductivity of resultant polymers was not measured. Only one study of Detrembleur and Drockenmuller et al.⁴⁷ can show the indirect comparison of the influence of fluorinated substituents on the conductivity of imidazolium PILs (Figure II.4, d). The introduction of the side fluorinated chain along with triethylene glycol pendant groups in imidazolium cations resulted in higher ionic conductivity in comparison with homopolymer analogue bearing hydrocarbon substitute (3.0×10^{-7} and 2.5×10^{-11} S cm⁻¹ (30°C), respectively)⁴⁸. However, the observed increase in overall conductivity may also be related solely to the presence of triethylene glycol pendant groups in the third block, known to promote the conductivity of PILs⁴⁹.

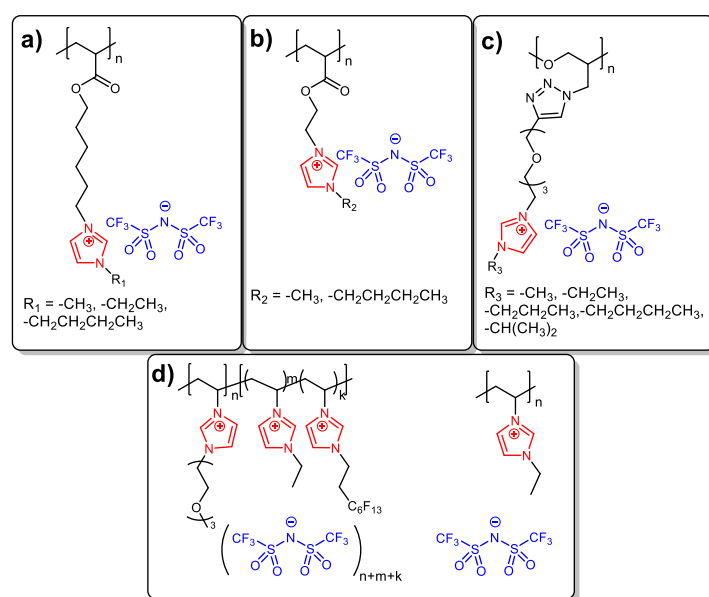


Figure II.4 Examples of PILs illustrating the influence of substituent in the cation on bulk polymer ionic

1.1.2 Polymer backbone.

Polymer backbone is another important factor to consider when designing highly conductive PILs^{48,50-55}. The direct comparison of conductivity in PILs having various backbones such as methacrylate, acrylate, siloxane, norbornene, etc. represents a known problem as it is quite hard to find the examples of PILs with similar cations, anions and spacers, although differ only by the nature of the main chain. However, it is possible to postulate some common trends. Firstly, the main chain of a PIL should be flexible as the ionic conductivity crucially depends on PIL's glass transition temperature. As a rule of thumb, polyelectrolytes with lower T_g show higher ionic conductivity^{48,52,55,56}. It is important to note, that this rule is only valid if the difference between the glass transition temperature and the temperature at which the ionic conductivity is measured does not exceed 30-35°C¹⁰. Secondly, the presence of alkylene oxide fragments was found to be beneficial for conductivity of PILs as they

promote ion solvation and as a result increase the ion mobility and ionic conductivity^{49,57,58}. Thus, PILs with flexible polyethylene oxide (Figure II.5, a-c) or poly(propylene oxide) (Figure II.5, d) backbones were capable to show significantly high ionic conductivities. Baker et al.⁵⁹ prepared a set of polyethylene oxide PILs with the molecular weights ranging from 21000 to 76000 g mol⁻¹ via ring opening polymerization of epichlorohydrin and subsequent polymer quaternization. These oligomeric PILs demonstrated relatively high ionic conductivity being above 10⁻⁶ S cm⁻¹ (Figure II.5, a). Further on, Shaplov et al.⁶⁰ suggested to quaternize poly(epichlorohydrin-co-ethylene oxide) copolymer having high molar mass of 8.7×10⁶ g mol⁻¹ with N-methyl imidazole (Figure II.5, b). This approach allowed to “dilute” the charge carriers with additional ethylene oxide (EO) units, helping their dissociation and providing the ionic conductivity up to 8.4×10⁻⁷ S cm⁻¹ at 25°C and simultaneously to improve the mechanical properties of PILs due to their high molecular weight of the precursor (Figure II.5, b). Later on, Baker et al.⁶¹ proposed to copolymerize epichlorohydrin with 2-((2-(2-(2-methoxyethoxy)ethoxy)ethoxy)methyl) oxirane in different ratios. The quaternization of obtained copolymers with N-butyl imidazole and subsequent ion metathesis provided PILs with ionic conductivities up to 1.2×10⁻⁴ S cm⁻¹ (25°C) at equimolar ratio of comonomers (n:m = 1:1). Such an improvement in conductivity can be explained by introduction of EO containing side so-called “dangling” chains, additional “dilution” of charges with EO units and relatively low M_n (2.2×10³ g mol⁻¹). Finally, PILs having poly(propylene oxide) backbone (Scheme 3, d) were synthesized by Matsumoto et al.^{62,63} via ring opening polymerization of ionic monomers with four-membered cyclic ether oxetanyl moieties. These PILs showed only moderate ionic conductivity of 2.0×10⁻⁸ S cm⁻¹ (25°C) that can be explained by analogy with the difference in conductivity between polymer electrolytes based on poly(ethylene oxide) and poly(propylene oxide) filled with Li salts^{64,65}: the presence of the ethyl groups prevents coordination of anions with oxygens thus disrupting the hopping mechanism of ions mobility.

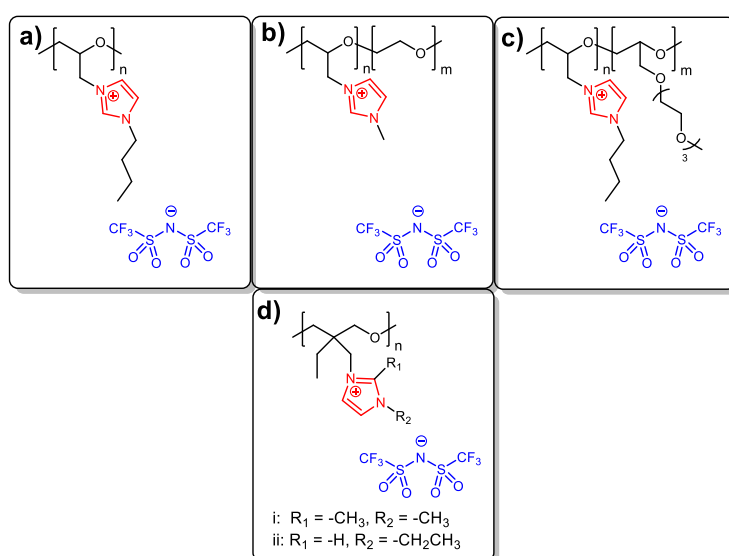


Figure II.5 Examples of PILs with alkylene oxide main chains.

1.1.3 The type of anion.

Anion structure also shows the great impact on PILs properties: the reduction in size and increase in charge delocalization are the most powerful tools for the improvement of PILs ionic conductivity¹⁰. Although the direct influence of anion's structure on ionic conductivity of PILs can be found in a variety of published works^{42,66–72}, the majority of them was dedicated to the study of only four anions, namely of TFSI, PF₆, BF₄ and CF₃SO₃. For example, for poly(1-[(2-methacryloyloxy)ethyl]-3-butylimidazolium)s (Figure II.6, a) the following order of conductivity values with respect to chemical structure of the counter anions was found:

$$\sigma (30^{\circ}\text{C}, \text{S cm}^{-1}): (\text{CF}_3\text{SO}_2)_2\text{N} (4.0 \times 10^{-4}) > \text{CF}_3\text{SO}_3 (1.5 \times 10^{-5}) > \text{BF}_4 (6.5 \times 10^{-6}) > \text{PF}_6 (3.8 \times 10^{-6})$$

In the work of Buchmeiser et al⁷¹ a series of polynorbornene derivatives with different anions were synthesized and investigated. Similarly, the transition from PF₆ to BF₄ and further to more delocalized TFSI anion led to the increase in ionic conductivity:

$$\sigma (25^{\circ}\text{C}, \text{S cm}^{-1}): (\text{CF}_3\text{SO}_2)_2\text{N} (4.2 \times 10^{-7}) > \text{BF}_4 (9.8 \times 10^{-9}) > \text{PF}_6 (3.8 \times 10^{-11})$$

In a number of polyvinyl imidazoles the significant increase in conductivity was achieved by application of a small delocalized dicyanamide anion⁶⁹. At the same time, PIL bearing TFSI anion demonstrated only moderate conductivity increase⁶⁹ in comparison with BF₄ and CF₃SO₃ anions.

$$\sigma (25^{\circ}\text{C}, \text{S cm}^{-1}): (\text{CN})_2\text{N} (1.4 \times 10^{-5}) >> (\text{CF}_3\text{SO}_2)_2\text{N} (2.5 \times 10^{-11}) > \text{CF}_3\text{SO}_3 (4.9 \times 10^{-12}) > \text{BF}_4 (< 10^{-12})$$

Starting from 2000s, the introduction of the asymmetry principle in anions structure has become a very successful approach for the synthesis of ionic liquids with lowest melting points and viscosities and as a result with highest known ionic conductivity^{73,74}. However, such novel anions were practically not tested with PILs and to the best of our knowledge only one report describing the comparison of PILs with asymmetric anions is existing to date⁶⁶. In this paper Shaplov and Drockenmuller synthesized a series of PILs having triazolium cation and five different anions. PILs under investigation demonstrated nearly similar ionic conductivities with TFSI-based PILs outmatching those bearing the asymmetric TFSAM anion by half order of magnitude. The observed conductivity trend at 30°C can be represented by the raw below:

$$\sigma (30^{\circ}\text{C}, \text{S cm}^{-1}): (\text{CF}_3\text{SO}_2)_2\text{N} (8.5 \times 10^{-6}) > (\text{C}_2\text{F}_5\text{SO}_2)_2\text{N} (6.2 \times 10^{-6}) > (\text{CN})_2\text{N} (5.8 \times 10^{-6}) > (\text{FSO}_2)_2\text{N} (3.5 \times 10^{-6}) > (\text{CF}_3\text{SO}_2)(\text{CN})\text{N} (1.8 \times 10^{-6})$$

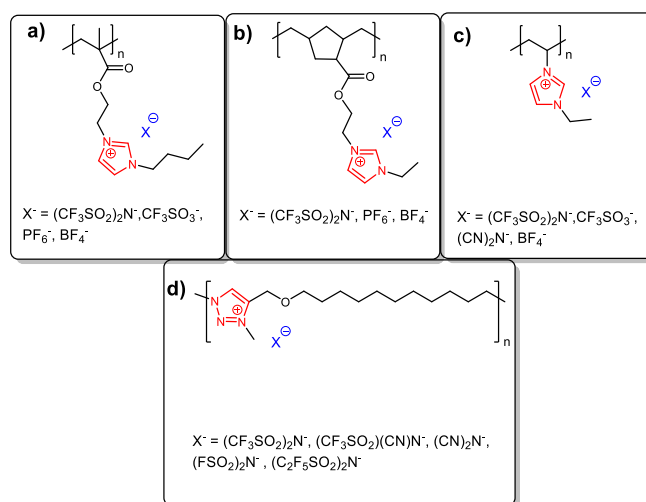


Figure II.6 Examples of PILs illustrating the influence of the anion's structure on bulk polymer ionic conductivity.

1.1.4 Block copolymers.

Another critical structural factor in the design of PILs is the polymer architecture, which plays a significant role in determining the material's physical, chemical, and mechanical properties. A particularly effective type of architecture for enhancing the mechanical properties of PILs without sacrificing ionic conductivity is block copolymers^{16,75,76}. Block copolymers consist of two or more chemically distinct polymer blocks that are typically immiscible, leading to microphase separation. This phase separation is crucial to their functionality, as one block can be engineered to be soft and flexible, providing pathways for ion transport, while the other block is more rigid, enhancing the material's overall mechanical strength.

Phase separation in block copolymers can result in various morphologies, including lamellar, cylindrical, gyroidal, and spherical structures (Figure II.7)⁷⁷. The type of phase separation and the resulting morphology depend heavily on the specific polymer structure, including the volume fraction of the blocks and the degree of polymerization^{16,77}. For instance, when the blocks are arranged to maximize the interfacial area between them, a lamellar structure typically forms. Conversely, when one block forms small, discrete domains within a continuous matrix of the other block, spherical or cylindrical morphologies may be observed. The gyroid morphology, a more complex bicontinuous structure, can also form under certain conditions, providing a three-dimensional network.

Among the various morphologies, lamellar and gyroid structures stand out as particularly favorable for use in solid-state electrolytes due to their ability to balance ionic conductivity and mechanical strength^{16,78,79}. The lamellar structure, characterized by alternating layers of different blocks, provides continuous pathways for ion transport in two directions while maintaining structural integrity (Figure II.7, d). In contrast, gyroid morphologies offer a three-dimensional network of interconnected

pathways, significantly enhancing ionic conductivity while still preserving mechanical robustness (Figure II.7, c).

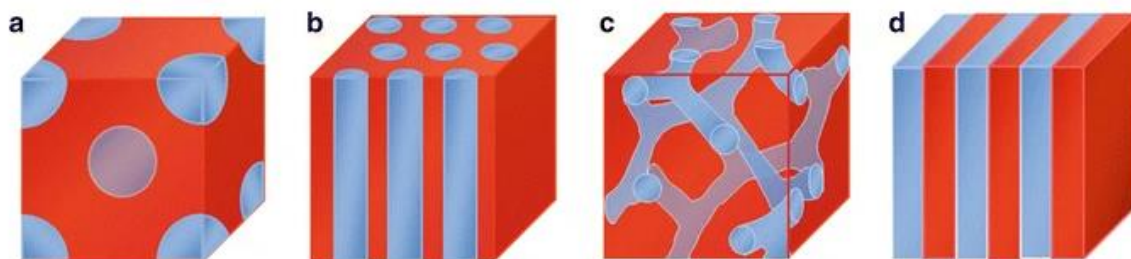


Figure II.7 Types of microphase separation: spheres (a), hexagonally packed cylinders (b), gyroids (c) and lamellar (d) ⁷⁷.

In one of the pioneering works by Elabd et al.⁸⁰, the favourable effect of block copolymer formation was demonstrated by comparing random and block copolymers of methyl methacrylate and 1-[(2-methacryloyloxy)ethyl]-3-butylimidazolium bis(trifluoromethanesulfonyl)imide (Figure II.8, a). The block copolymer exhibited weak microphase separation but showed two orders of magnitude higher ionic conductivity than the random copolymer with a similar composition.

Later, a series of poly[(styrene)-b-(1-((2-acryloyloxy)ethyl)-3-butylimidazolium bis(trifluoromethanesulfonyl)imide)] block copolymers was investigated (Figure II.8, b)⁷⁹. These copolymers exhibited a variety of self-assembled nanostructures, including hexagonally packed cylindrical, lamellar, and coexisting lamellar and network morphologies. The conductivities of an acrylate-based PIL block copolymer with strong microphase separation were approximately 1.5–2 orders of magnitude higher than those of a methacrylate-based PIL block copolymer with weak microphase separation at a comparable PIL composition. It was concluded that strong microphase separation resulting from a higher degree of incompatibility between blocks improves ion transport properties in PIL block copolymers.

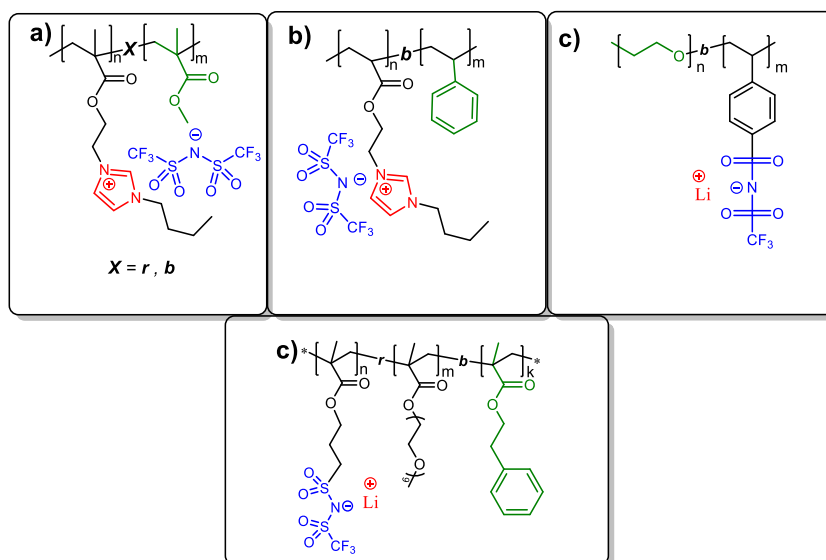


Figure II.8 An overview of PIL block copolymers (r-random copolymer; b-block copolymer).

In contrast to cationic PIL block copolymers, anionic PIL block copolymers are less studied in the literature, with most examples containing Li^+ as a counterion^{81–83}. For instance, Balsara et al.⁸⁴ reported A–B type poly(ethylene oxide)-b-poly(styrenesulfonyllithium(trifluoromethylsulfonyl)imide) (PEO-b-PSLiTFSI) copolymers. At moderate temperatures, these copolymers exhibited lamellar phase separation, but the ionic conductivity was very low ($10^{-8} \text{ S cm}^{-1}$). High conductivity of $10^{-4} \text{ S cm}^{-1}$ was achieved when heating above 50°C ; however, this increase in conductivity was accompanied by the mixing of the two blocks and the elimination of the morphology, resulting in a deterioration of mechanical properties.

To improve ionic conductivity at room temperature while preserving the obtained morphology, a different block copolymer architecture was proposed by Lozinskaya et al.⁸⁵. The group investigated a series of $[\text{MLiTFSI}_n\text{-r-PEGM}_m]\text{-b-(PhEtM)}_k$ copolymers with a second high T_g block based on 2-phenylethyl methacrylate (PhEtM). Polymers with hexagonally packed cylinders and lamellar morphologies were observed, with ionic conductivity reaching $3.6 \times 10^{-7} \text{ S cm}^{-1}$ at 25°C . Additionally, several interesting structural factors affecting phase separation were discovered. It was found that lamellar morphology occurred only when high molecular weight block copolymers ($M_n = 50\text{--}90 \text{ kDa}$) were targeted, with the ion-containing block being at least twice as large as the neutral block by weight, and with a PEGM:ILM ratio of approximately 5:1 by mole.

2. Ion gels

The enhancement of ionic conductivity of poly(ionic liquid)s can be further achieved through the development of ion gels. Ion gels, also known as ionic liquid gels are a type of materials in which the liquid phase, percolating through the solid polymeric matrix, is an ionic liquid (Figure II.9). Ion gels

represent a novel class of materials when compared to more traditional gels like hydrogels, where the liquid phase is water, or organogels, where the liquid phase is an organic solvent.

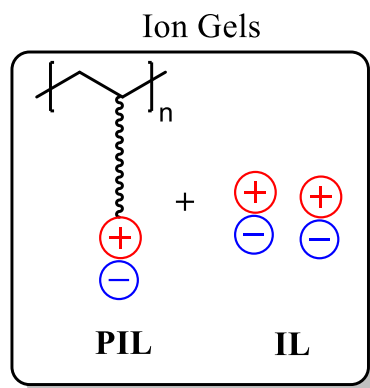


Figure II.9 Graphical representation of ion gels

The ionic conductivity in these materials arises from the transport of both the cations and anions of the IL, and PIL counter-ions and as a result can reach up to $10^{-3} \text{ S cm}^{-1}$ at 25°C . Furthermore, ion gels retain the unique and desirable properties of ionic liquids, including a broad electrochemical stability window, negligible vapor pressure, non-flammability, and high thermal stability. These attributes are typically preserved within ion gels, making them highly attractive and versatile materials for various electrochemical applications.

Typically, ion gels are composed of a substantial amount of ionic liquid (IL), usually around 30-50 wt%. At this concentration, the ionic conductivity of the gel can achieve values between 10^{-4} and $10^{-6} \text{ S cm}^{-1}$ at 25°C , while still retaining some of the mechanical properties inherent to neat poly(ionic liquid)s. However, to make these materials viable for use in electrochemical devices, higher levels of ionic conductivity are often required, necessitating an increase in IL content.

When the IL content exceeds 60 wt%, the ionic conductivity can rise significantly, potentially reaching up to $10^{-3} \text{ S cm}^{-1}$ at 25°C , which is ideal for applications demanding high ionic transport efficiency. However, this increase in IL content also leads to considerable plasticization of the polymer matrix, resulting in a loss of mechanical stability. This plasticization makes ion gels more susceptible to issues such as IL loss, extraction, or leakage over time, especially under external conditions like the application of compressive forces. As a result, while higher IL loads improve conductivity, they also pose challenges for maintaining the material's structural integrity in practical applications.

3. Polyelectrolyte complexes

Another approach to enhancing the mechanical properties of PILs is the formation of polyelectrolyte complexes (PECs). The term “PEC” was first introduced by Bungenberg de Jong and Kruyt to differentiate the coacervation between two polyelectrolytes from that between a polyelectrolyte

and a small molecule⁸⁶. Polyelectrolyte complexes are association complexes formed between oppositely charged polyelectrolytes, driven by electrostatic interactions between their oppositely charged polyions. Thus, in PECs, two polymer chains are connected by dynamic ion bonds rather than covalent bonds, as seen in crosslinked polymers.

Dynamic ion bonds in PECs differ significantly from covalent bonds in several key ways. While covalent bonds involve the sharing of electron pairs between atoms, creating strong and permanent connections within a molecule, ionic bonds are based on electrostatic interactions between oppositely charged ions, and are weaker and reversible. This reversibility allows ion bonds to break and reform in response to environmental changes, providing PECs with flexibility, self-healing abilities, and responsiveness to stimuli⁸⁷.

PECs can exhibit a wide range of elastic behaviors, from soft and flexible to relatively stiff, depending on the composition and environmental conditions. For instance, PECs formed from highly charged polyelectrolytes may exhibit greater stiffness due to stronger electrostatic interactions between the oppositely charged chains, while PECs with lower interaction energy between two polymer chains form softer and more flexible materials. This tunability makes PECs suitable for various applications, including the formation of fibers⁸⁸ and coatings⁸⁹. Fibers produced from PECs often possess high tensile strength and durability, making them suitable for applications where mechanical robustness is essential, such as in biomedical scaffolds or filtration membranes. Similarly, PEC coatings can be engineered to provide strong adhesion, mechanical resilience, and flexibility, which are critical for protective coatings, surface modification.

However, it should be noted that while PECs have been extensively studied, particularly in their hydrated state, investigations under anhydrous conditions remain limited, despite their significant potential in various applications. For example, Maaskant et al. studied polyester-based polyelectrolytes and their corresponding polyelectrolyte complexes (Figure II.10, a)⁹⁰. The resulting complexes exhibited a glass transition temperature of approximately 50°C and demonstrated thermoplastic properties, with storage moduli ranging from 800 to 1800 MPa at 25°C. Similarly, Lange et al. reported on the thermoplastic properties of PECs based on two polystyrene-based polyelectrolytes (Figure II.10, b)⁹¹. These materials exhibited storage moduli around 600 MPa at room temperature (25°C), highlighting their potential as mechanically robust materials. However, the T_g of these complexes was not determined, leaving some aspects of their thermal behavior unexplored.

One more widely known example of PEC formation is the coacervation between poly(3,4-ethylenedioxythiophene) (PEDOT) and poly(4-styrene sulfonate) (PSS) which results in PEDOT:PSS complex (Figure II.10, c). This coacervation process significantly enhances the mechanical properties and film-forming ability of PEDOT, which on its own tends to be brittle and insoluble. The resulting

PEDOT complex not only presents flexibility but also greatly enhances the material's processability, enabling it to form uniform, conductive films. These improvements have made PEDOT:PSS a cornerstone in the field of organic electronics, where it is valued for its versatility in applications ranging from transparent conductive films to flexible electronic devices^{92,93}.

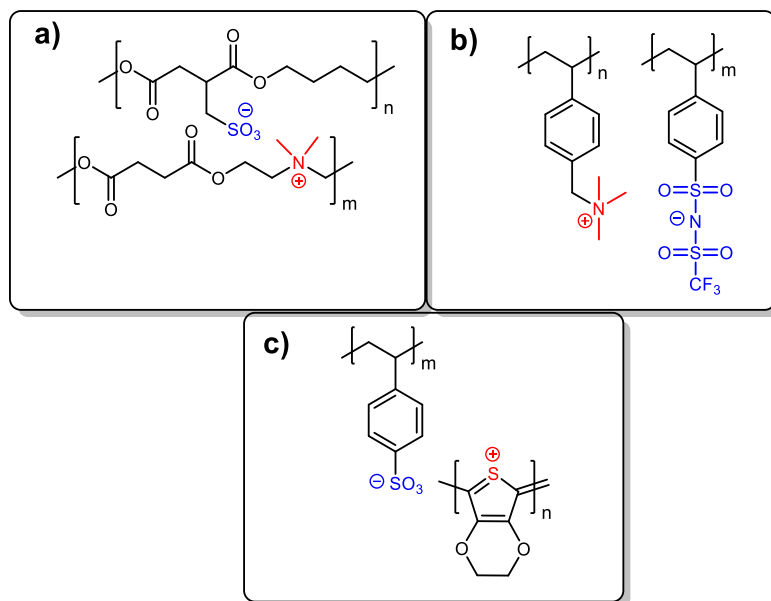


Figure II.10 Examples of polyelectrolyte complexes.

4. Conclusions

Poly(ionic liquid)s show significant potential for electrochemical applications due to their unique combination of ionic conductivity and viscoelastic properties. However, a major challenge in their development lies in the inverse relationship between these two attributes. PILs with high ionic conductivity often appears as cold flowing viscous liquids, while mechanically stable PILs generally exhibit low ionic conductivity. The design of polymer structures cannot successfully address this challenge, making it necessary to explore alternative solutions.

In this context, the concepts of ion gels and polyelectrolyte complexes have been explored as potential methods to improve the properties of PILs. Ion gels can enhance conductivity but often compromise mechanical stability. On the other hand, the formation of PECs can improve mechanical properties, but it does not inherently improve ionic conductivity. As a result, a solution that effectively balances high ionic conductivity with robust mechanical stability has yet to be found.

To address this challenge, the following chapters present the development of a new family of polymer materials, termed **dynamic ion gels (DIGs)**, created through complex coacervation. It is hypothesized that DIGs will achieve an unprecedented combination of mechanical and electrochemical properties due to the formation of dynamic ionic cross-links between oppositely charged building blocks and the *in situ* generation of highly conductive ionic liquid.

A key distinction between DIGs and PECs should be noted. In PECs, the ion exchange between two polyelectrolytes typically results in the formation of a low molecular weight inorganic salt (e.g., CsCl, NaCl), which is usually washed out before the final utilization of the material. In contrast, DIGs are designed so that the oppositely charged polyelectrolytes generate a highly conductive ionic liquid during the coacervation process. Importantly, this ionic liquid remains within the material, contributing to its enhanced conductivity.



III. Results and discussions

1. Design and synthesis of ionic liquid like monomers (ILM)s

Based on the first research objective, this chapter presents the development of two distinct groups of ionic liquid like monomers.

The first group comprises ionic methacrylate-based monomers for Reversible Addition Fragmentation Chain Transfer (RAFT) polymerization. It includes two “mirrored” monomers: anionic **ILM1** and cationic **ILM2**. Both monomers feature a flexible spacer and incorporate bis(trifluoromethylsulfonyl)imide (TFSI) and imidazolium motifs (Figure 1.1).

The second group consists of dipropargyl ionic monomers intended for Cu(I)-catalyzed azide-alkyne polyaddition in combination with neutral diazide to form triazole-based polymers. These polymers were further quaternized by methyl iodide and underwent ion metathesis with LiTFSI to obtain multicationic PILs. This group includes two monocationic (**ILM3**, **ILM4**) and two dicationic (**ILM5**, **ILM6**) varieties with ammonium and imidazolium scaffolds (Figure 1.1).

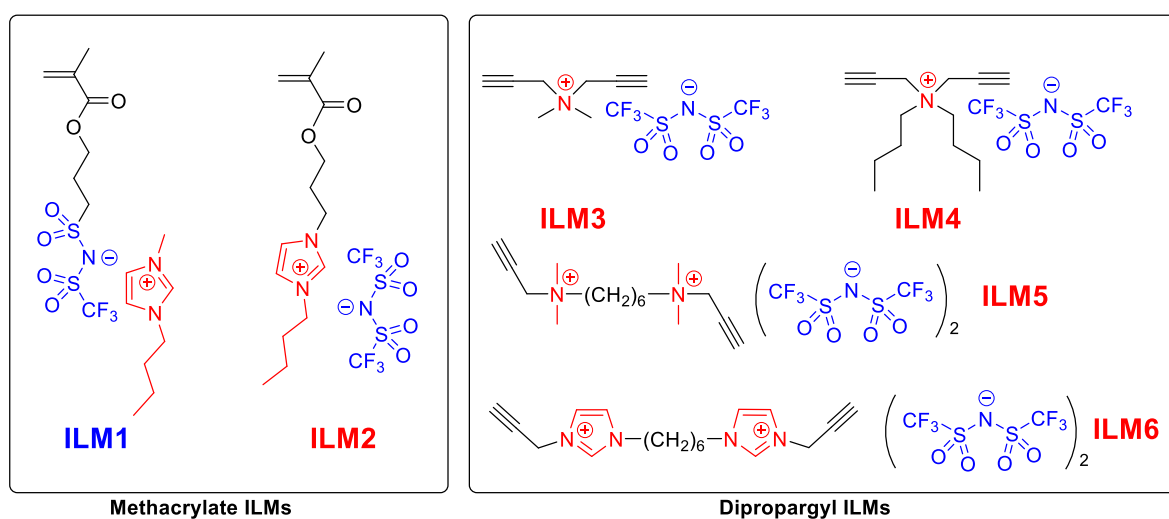


Figure 1.1 Two groups of ionic liquid like monomers

1.1 Methacrylic ionic monomers

1.1.1 Design and selection

The ionic conductivity of poly(ionic liquid)s is highly influenced by the structural features of the monomer units. Therefore, a key strategy for obtaining highly conductive PILs involves designing ionic liquid like monomers with specific structural frameworks. Based on the literature review presented in the first chapter, these frameworks should include: (1) reactive groups capable of forming flexible

polymer chains during the polymerization process; (2) highly delocalized and/or asymmetric ionic centers located at the end of the comb-like side chains; (3) flexible spacers between the main polymer chain and the attached ion⁹⁴.

Keeping this in mind, three structural motifs were used for the design of the first group of monomers (Figure 1.2). Methacrylate was selected as the reactive group due to its well-known advantages: ease of radical polymerization, resistance to the presence of ionic groups^{94,95}, and its ability to produce high molecular weight polymers with a narrow polydispersity index. The propyl group was chosen as a spacer for two reasons. Firstly, ionic monomers with a propyl spacer demonstrated a sharp increase in ionic conductivity compared to those with an ethyl spacer^{10,14,94}. Secondly, the precursors for its synthesis are commercially available and incorporating the propyl group into the monomer does not require any additional steps. To enhance ionic conductivity, highly delocalized and ion conductive TFSI⁹⁶ and imidazolium^{97,98} moieties were placed at the end of the propyl spacer. According to the literature, monomers and polymers with these structural fragments typically exhibit the highest ionic conductivity. The length of the substituent on the imidazolium cation was also optimized, being set to four carbon atoms. Studies on polymers synthesized from similar ionic monomers have shown that increasing the substituent length from methyl⁹⁸ to n-butyl⁹⁹ results in three orders of magnitude increase in ionic conductivity at 25 °C (Figure 1.5). Lastly, both monomers were designed to be identical to facilitate the comparison of the obtained polymers after RAFT polymerization.

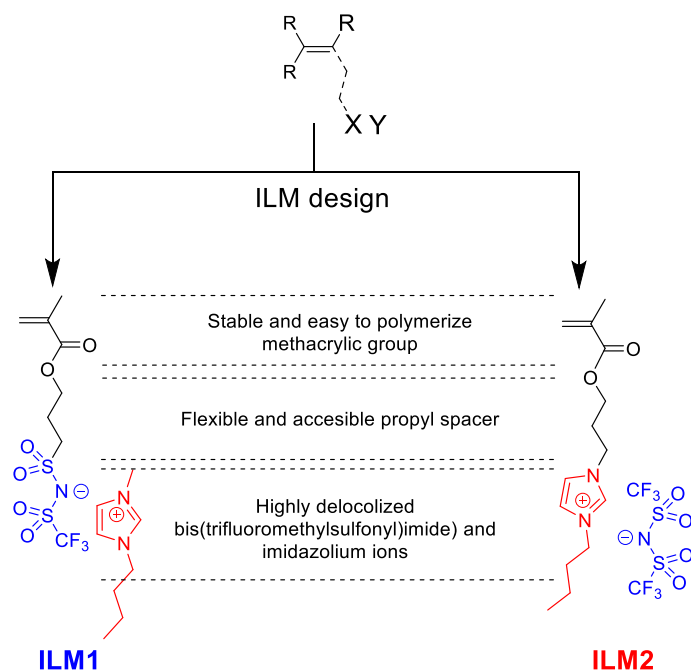


Figure 1.2 Structures of ILMs.

As a result, 2 “mirrored” methacrylic ILMs (Figure 1.2), cationic 3-butyl-1-(3-(methacryloyloxy)propyl)imidazolium bis((trifluoromethyl) sulfonyl)imide (**ILM2**) and anionic 1-

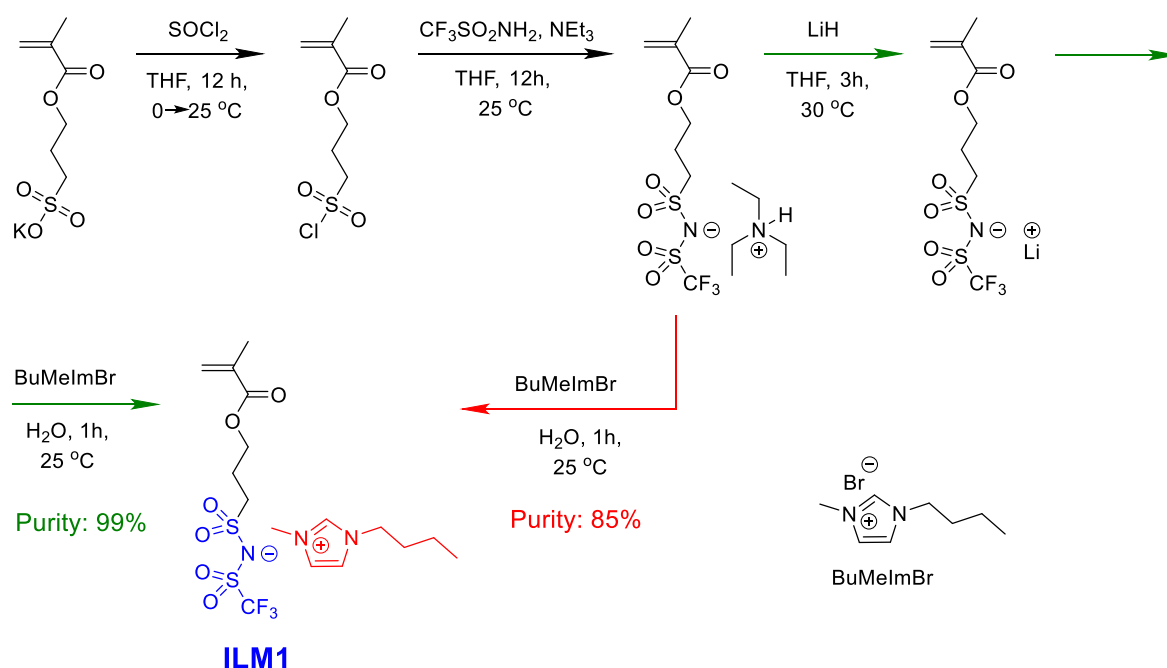
butyl-3-methylimidazolium 1-[3-(methacryloyloxy)propylsulfonyl]-1-(trifluoromethanesulfonyl)imide (**ILM1**) were designed and synthesized in large quantities.

1.1.2 Synthesis and characterization

1.1.2.1 1-butyl-3-methylimidazolium 1-[3-(methacryloyloxy)propylsulfonyl]-1-(trifluoromethanesulfonyl)imide (**ILM1**) synthesis

ILM1 was synthesized in 4 steps, as shown in Scheme 1.1. The first three steps, which produce lithium 1-[3-(methacryloyloxy)propylsulfonyl]-1-(trifluoromethanesulfonyl)imide, have been previously discussed by our group¹⁰⁰. The final step, involving ion metathesis with 1-methyl-3-butylimidazolium bromide (BuMeImBr), was introduced here for the first time.

In the initial step, reaction between potassium 3-(methacryloyloxy)propane-1-sulfonate and thionyl chloride was carried out in THF and was catalysed by DMF. The desired sulfonyl chloride derivative was isolated by pouring the resultant slurry into ice water, effectively removing all unreacted starting materials and solvents, and yielding the product quantitatively.



Scheme 1.1 Synthetic pathway for the preparation of **ILM1**.

In the second step, 3-(chlorosulfonyl)propyl methacrylate reacted with trifluoromethanesulfonamide in the presence of a 2.2 molar excess of triethylamine. The excess of triethylamine was necessary because in case of equimolar ratio, the mixture of compounds was obtained. The third step of the proposed synthetic pathway involved the interaction of triethyl ammonium 1-[3-(methacryloyloxy)propylsulfonyl]-1-(trifluoromethane-sulfonyl)imide with an excess of lithium hydride in anhydrous THF at 30°C. This elevated temperature was required, as it was discovered that the reaction proceeded very slowly at temperatures below 30°C.

The desired **ILM1** monomer was obtained from the lithium salt via an ion metathesis reaction with an excess of 1-methyl-3-butyylimidazolium bromide in an aqueous medium. The driving force of this reaction is the hydrophobic nature of **ILM1**, which causes its precipitation from the water solution. This approach allowed to obtain the monomer with 99% purity, which was crucial for further RAFT polymerization. Since **ILM1** contains a highly reactive methacrylic group that can lead to unwanted polymerization upon heating, a radical inhibitor (3-methoxyphenol) was added at each reaction step before solvent evaporation. Additionally, solvent removal was performed at temperatures below 30°C, and the obtained products were stored in the fridge to prevent premature polymerization.

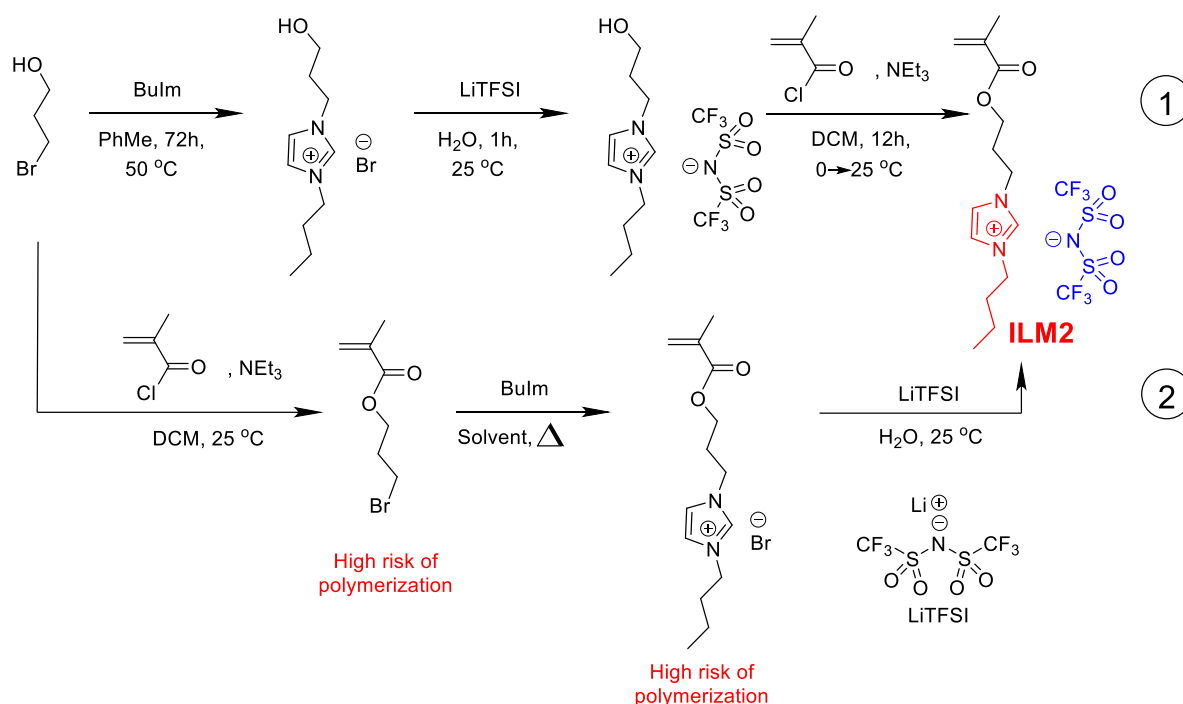
To decrease the amount of reaction steps direct ion exchange between triethyl ammonium 1-[3-(methacryloyloxy)propylsulfonfyl]-1-(trifluoromethane-sulfonfyl)imide and 1-metyl-3-butyylimidazolium bromide was attempted. However, due to the more hydrophobic nature of the triethyl ammonium counter cation in comparison to lithium, ion metathesis was incomplete, resulting in a product purity of only 85%.

1.1.2.2 3-butyl-1-(3-(methacryloyloxy)propyl)imidazolium bis((trifluoromethyl)sulfonfyl)imide (**ILM2**) synthesis

For the synthesis of methacrylate based cationic ILMs two approaches that differ by the sequence of chemical reaction can be found in the literature (Scheme 1.2). The first one includes the formation of bromide ionic liquid with the hydroxyl group, the ion exchange to the desired anion and subsequent reaction of 3-butyl-1-(3-hydroxypropyl)imidazolium bis((trifluoromethyl)sulfonfyl)imide with methacryloyl chloride^{98,101}. The advantages of this method are quantitative yields and high purity of the first two reaction steps. However, the only issue is the complicated purification procedure in the final step due to the generation of ionic by-products during the reaction.

The second approach introduced by Ohno group¹⁰², relies on the reverse reaction order in which acylation reaction happens first and resultant bromalkane methacrylate undergoes the quaternization with substituted cyclic amine (imidazole, pyrrolidine, ...). Such approach allows to carry out the acylation reaction between two neutral compounds, providing more opportunities for purification. However, the key concern regarding this strategy is the high risk of polymerization of the two intermediate products containing active methacrylic groups. Consequently, there are several documented instances in the literature of premature polymerization of bromalkane methacrylates^{6,102,103}.

After evaluating all the proc and cons, it was decided to use the first synthetic path to decrease the possibility premature polymerization. Thus, 3-butyl-1-(3-(methacryloyloxy)propyl) imidazolium bis((trifluoromethyl)sulfonfyl)amide (**ILM2**) was synthesized in three steps, as presented in Scheme 1.2, path 1.



Scheme 1.2 Synthetic pathway for the preparation of **ILM2**.

The first step included the quaternization of 1-butylimidazole by 3-bromo-1-propanol in toluene (PhMe). Achieving high conversion required long reaction time. The use of PhMe as a solvent facilitated the production of a high-purity product with nearly quantitative yield without the need for purification, as the neutral starting materials remained dissolved in the solvent, while the desired ionic liquid precipitated as a yellowish oil. Later ion metathesis with LiTFSI was performed in aqueous medium to obtain more hydrophobic TFSI ionic liquid with the hydroxyl group as a transparent liquid with quantitative yields.

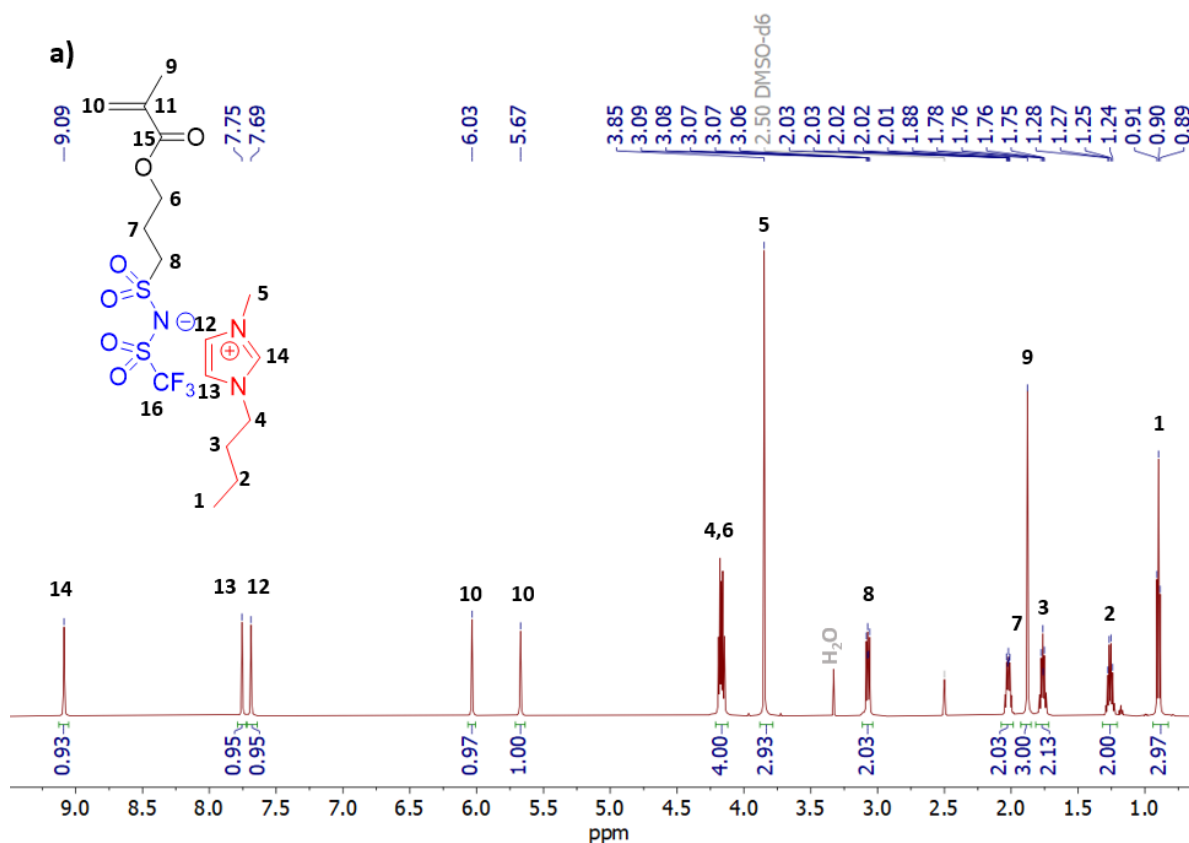
In the final step, 3-butyl-1-(3-hydroxypropyl)imidazolium bis((trifluoromethyl)sulfonyl)imide was reacted with methacryloyl chloride in the presence of 1.6 triethylamine equivalents in DCM. The triethylamine acted as a base and as HCl acceptor, facilitating the removal of dissolved HCl in the form of triethylammonium hydrochloride (NEt_3HCl) and thus improving the reaction conversion. Preliminary purification, consisting in washing with Et_2O , removed unreacted methacryloyl chloride and resulted in a product containing ~15 mol% of NEt_3HCl . To further purify the product from the ammonium salt, three methods were applied. First, the sample was dissolved in anhydrous THF which resulted in precipitation and subsequent filtration of ~7 mol% of NEt_3HCl . Next, the concentrated solution of the monomer in DCM was passed through 5 ml silica gel pad, removing ~5 mol% of NEt_3HCl . The final step involved mixing the monomer with decolorizing charcoal in a polar solvent (MeOH), removing the remaining ~3 mol% of NEt_3HCl . This sophisticated procedure ensured the attainment of **ILM2** with $\geq 99\%$ purity in the form of yellowish oil. Similar to **ILM1**, cationic **ILM2**

also contains prone to polymerization methacrylic group, thus the obtained monomer was stored in the refrigerator.

1.1.2.3 Spectroscopic analysis of ILMs

The structures and purity of **ILM1** and **ILM2** were confirmed by FTIR, ^1H , ^{13}C and ^{19}F NMR spectroscopy and elemental analysis. The detailed signal assignments for both monomers are discussed below and presented in the following figures: ^1H NMR in Figure 1.3, ^{13}C NMR in Figure 1.4, ^{19}F NMR in Figure 1.5 and FTIR in Figure 1.6.

Both monomers showed similar spectroscopic appearance with minor shifts of signal frequencies. For example, both FTIR spectra (Figure 1.6) had the following absorption bands: ~ 3130 , $2990\text{--}2930\text{ cm}^{-1}$ that were assigned to CH_2 stretching; $\sim 1710\text{ cm}^{-1}$ ($\text{C}=\text{O}$ stretching); $\sim 1630\text{ cm}^{-1}$ ($\text{C}=\text{C}$ stretching); $\sim 1455\text{ cm}^{-1}$ (CH bending); $\sim 1330\text{ cm}^{-1}$ (asymmetric $\text{S}=\text{O}$ stretching); $\sim 1160\text{ cm}^{-1}$ (CF stretching); $\sim 1110\text{ cm}^{-1}$ (symmetric $\text{S}=\text{O}$ stretching); $\sim 1050\text{ cm}^{-1}$ (CF stretching). Moreover, the characteristic signal of CF_3 group is seen in ^{13}C NMR as quadruplet at $\sim 120\text{ ppm}$ and as a singlet in ^{19}F NMR spectra around -80 ppm .



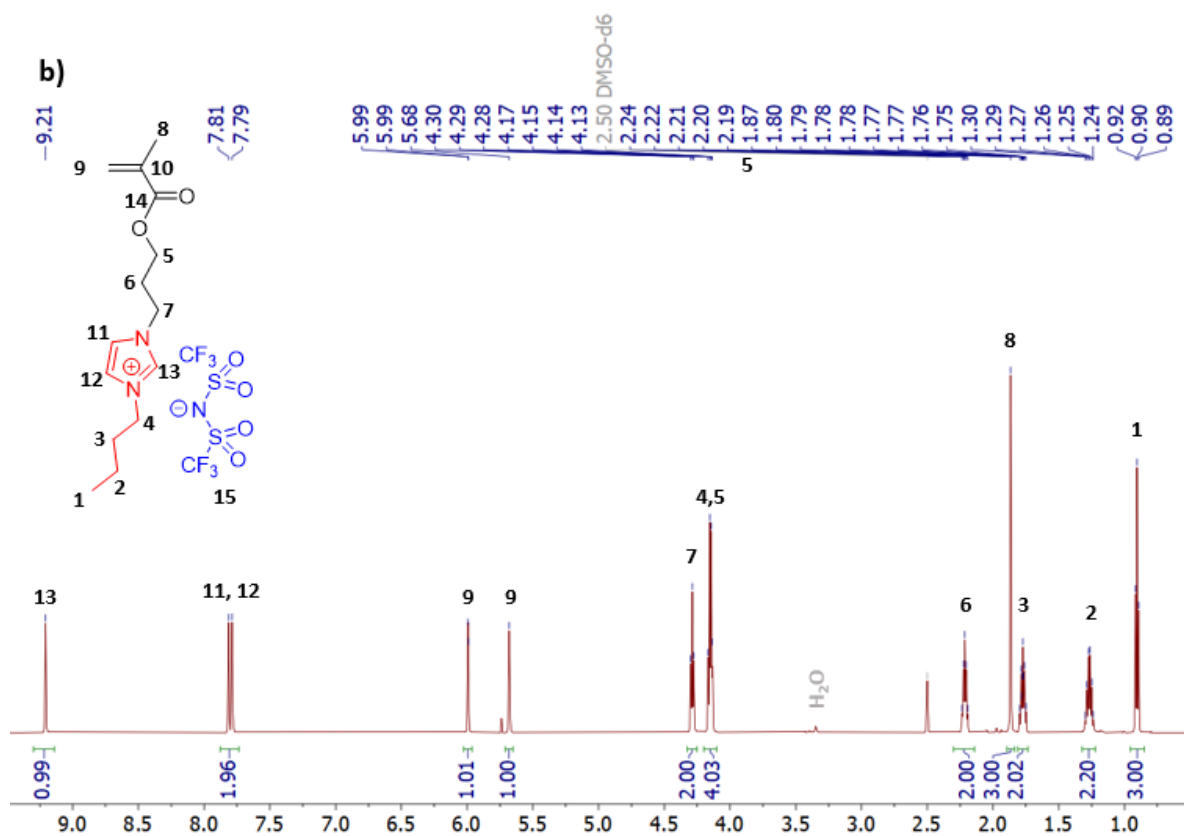


Figure 1.3 ¹H NMR of **ILM1** (a) and **ILM2** (b) (25 °C, DMSO-d₆).

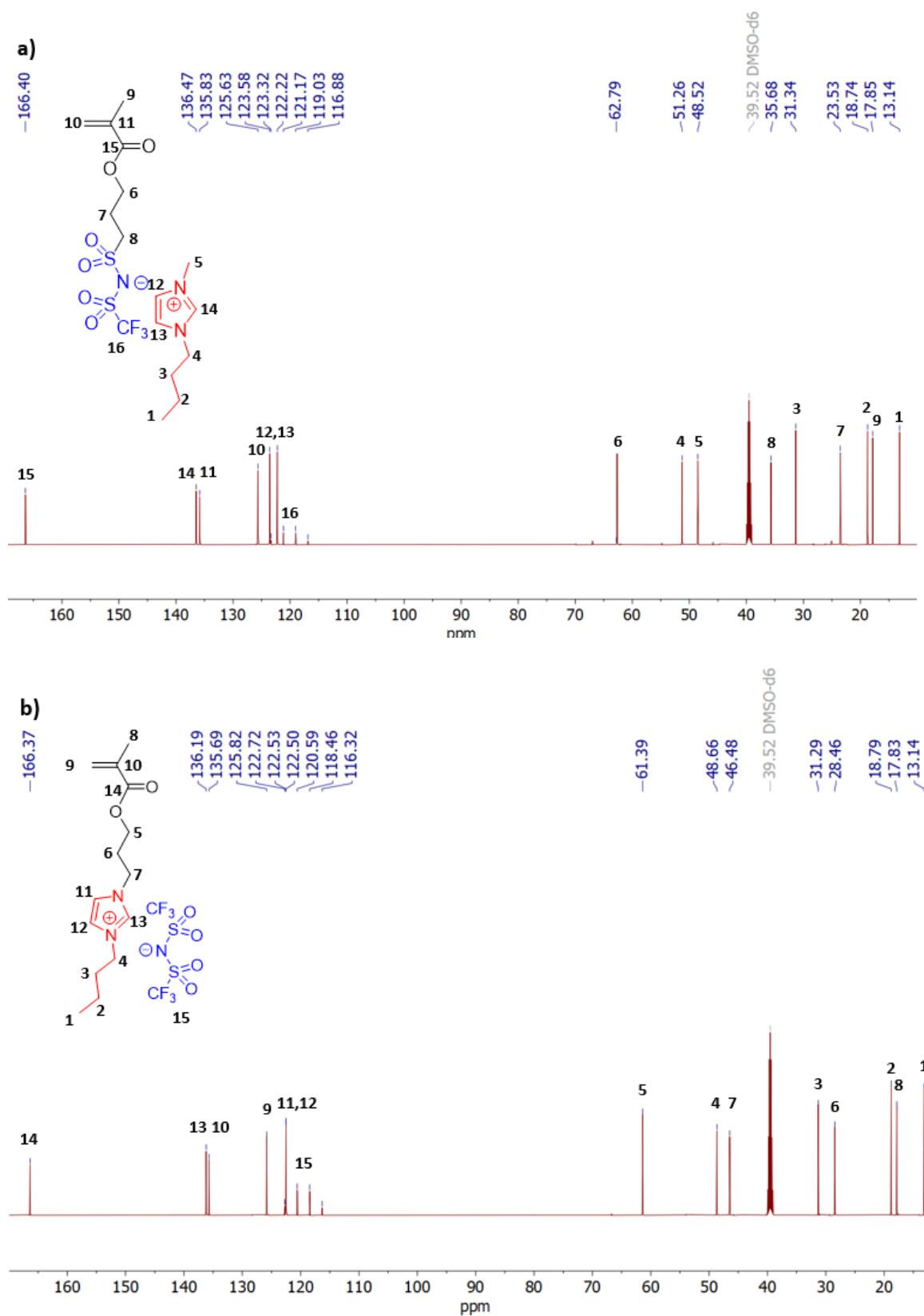


Figure 1.4 ^{13}C NMR of **ILM1** (a) and **ILM2** (b) (25 °C, DMSO- d_6).

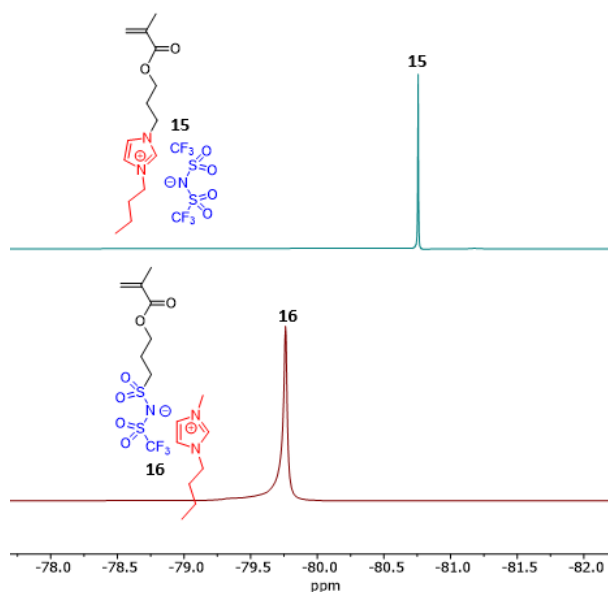


Figure 1.5 Comparison of ^{19}F NMR of **ILM1** (red) and **ILM2** (green) (25 °C, DMSO- d_6).

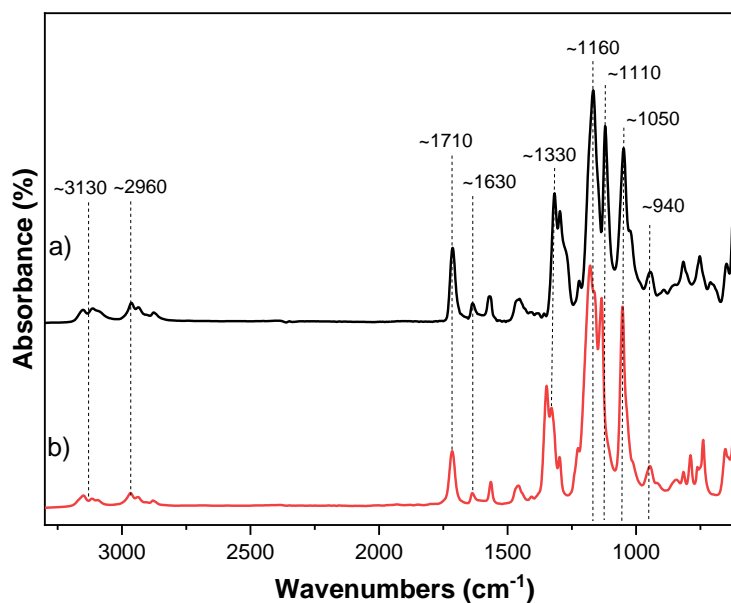


Figure 1.6 Comparison of FTIR of **ILM2** (a) and **ILM1** (b).

1.1.3 Selected properties of ILMs

Properties of ILMs are summarized in Table 1.1. Thermal properties were assessed via differential scanning calorimetry (DSC) and thermogravimetric analysis (TGA). Both ILMs displayed solely a glass-transition temperature (T_g) without any evidence of melting or crystallization processes even at very low (2 K min^{-1}) heating/colling rates. **ILM2** exhibited a slightly lower T_g , of -70°C , while **ILM1** demonstrated -63°C . TGA revealed nearly identical degradation behaviour for both ILMs (Figure 1.7), with **ILM2** showing a 20°C higher T_{onset} .

Table 1.1 Selected properties of ILMs

ILM	d at 25°C (g ml ⁻¹)	η at 25°C (cP)	σ at 25°C (S cm ⁻¹)	T_g (°C) ¹	T_{onset} (°C) ²
ILM1	1.31	504	2.4×10^{-4}	-63	225
ILM2	1.36	213	4.1×10^{-4}	-70	245

¹Obtained by DSC 2 K min⁻¹. ²Onset loss temperature obtained by TGA.

Interestingly, despite their very similar densities, a significant difference in viscosity was observed. **ILM1** exhibited a viscosity of 504 cP, while **ILM2** showed a viscosity more than twice as low, at 213 cP. This phenomenon can be explained by the varying levels of ionic interactions within the ion pairs. Probably, in cationic **ILM2**, the two bulky substituents on the imidazole ring hinder the approach of the anion, thereby decreasing the interaction energy between the charged units, while in **ILM1** only one side of the cation is hindered with butyl substituent. Ionic conductivity of ILMs was measured over a temperature range from 20 to 100 °C using electrochemical impedance spectroscopy (EIS) (Figure 1.8). The conductivity increased with increasing temperature and did not follow a linear Arrhenius behavior. Within the whole temperature range **ILM2** consistently maintained a slightly higher conductivity than **ILM1**. At 25 °C, both ILMs displayed conductivities in 10^{-4} S cm⁻¹ region, with **ILM2** reaching a higher value of 4.1×10^{-4} S cm⁻¹ compared to 2.4×10^{-4} S cm⁻¹ for **ILM1**. This observation can likely be attributed to the significantly higher viscosity (504 cP) of **ILM1**.

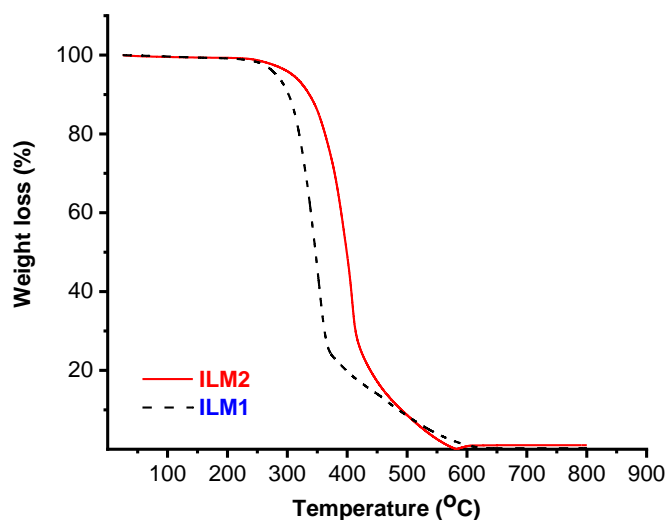


Figure 1.7 TGA traces of ILMs (5°C min⁻¹, under air).

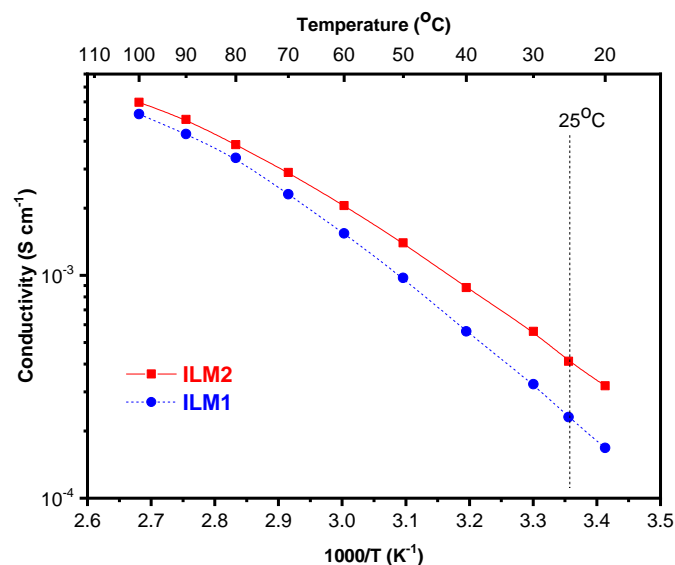


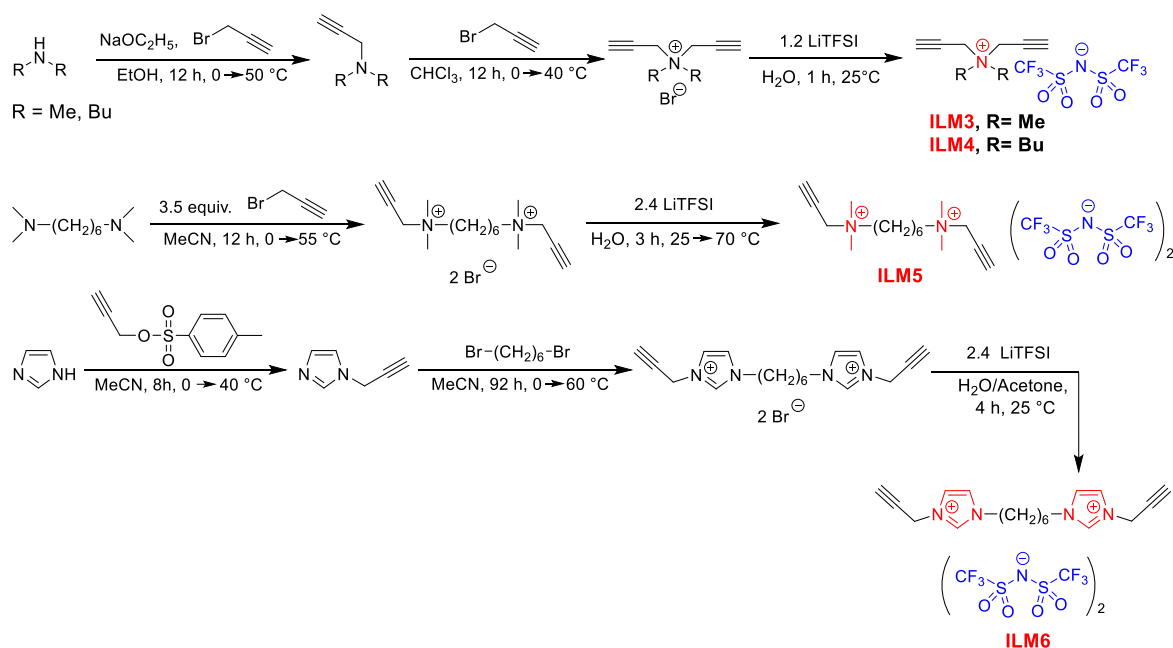
Figure 1.8 Ionic conductivity vs temperature dependence for ILMs.

1.2 Dipropargyl ionic monomers

1.2.1 Design and selection

In addition to the structural factors discussed earlier, the repeat unit charge density plays a crucial role in determining the ionic conductivity of PILs. Although numerous studies have explored PILs with varying charge densities per unit, the relationship between structure and conductivity often remains inconsistent and unclear. To address this gap in knowledge, 1,2,3-triazolium-based PILs synthesized via copper(I)-catalyzed azide-alkyne cycloaddition (CuAAC) were identified as an ideal platform for the synthesis and study of a library of monocationic and heterodicationic PILs with adjustable repeat unit charge density.

For this purpose, neutral 1,11-diazido-3,6,9-trioxaundecane was selected as the commercially available diazide monomer, while all dipropargyl ionic monomers containing varying numbers of ion pairs were designed and synthesized as part of this thesis (Scheme 1.3). Consequently, two monocationic dipropargyl monomers and two dipropargyl monomers containing two cations with a flexible n-hexyl spacer were developed. Both monocationic monomers incorporated ammonium cations with different substituents and a TFSI counter-anion. The dicationic monomers featured either ammonium or imidazolium cations, also paired with a TFSI counter-anion. The introduction of the n-hexyl spacer between the two cations aimed to enhance the flexibility of the polymer chain after polymerization.



Scheme 1.3 Synthesis of dipropargyl ionic monomers.

1.2.2 Synthesis and characterisation

1.2.2.1 N,N-Dimethyl-N,N-dipropargylammonium Bis(trifluoromethylsulfonyl)imide (**ILM3**) and N,N-Dibutyl-N,N-dipropargylammonium Bis(trifluoromethylsulfonyl)imide (**ILM4**)

The synthesis of ionic N,N-dipropargylammonium salts was carried out utilising a procedure previously developed by our group¹⁰⁴. The first step entailed the deprotonation of the secondary amine with sodium ethanolate followed by alkylation with propargyl bromide. The resulting tertiary amine was then quaternized with propargyl bromide in chloroform. To mitigate the exothermic effect during both alkylation steps, the reactions were carried out in a solvent with a gradual increase in temperature. This approach yielded high-purity bromide-based ionic liquids as colorless solid products. Finally, the last step included ion exchange with LiTFSI in aqueous medium.

1.2.2.2 N,N,N',N'-tetramethyl-N,N'-dipropargyl-hexane-1,6-diammonium bis(trifluoromethylsulfonyl)imide (**ILM5**)

The synthetic strategy for the preparation of diammonium based dipropargyl ionic monomer included N-alkylation of N,N,N',N'-tetramethyl-1,6-hexanediamine by propargyl bromide and an ion exchange reaction with an excess of LiTFSI. During the initial step, it was discovered that at ambient temperatures the reaction was not complete and monoquaternized product was precipitating. Therefore, to increase the solubility and promote the alkylation of the second amine group, the temperature was increased to 55°C and a 3.5 equivalent excess of propargyl bromide was used. Moreover, the temperature was increased gradually to mitigate the exothermic effect. The same issue of precipitation of the mono-exchanged product was observed during the ion metathesis step. To achieve quantitative

conversion, it was necessary to heat the reaction to 70°C and use a significant excess of LiTFSI. As a result, **ILM5** was obtained as a white crystalline solid in near quantitative yields.

1.2.2.3 1,1'-(hexane-1,6-diyl)bis(3-propargyl-imidazolium) bis(trifluoromethylsulfonyl)imide (**ILM6**)

For the **ILM6** monomer the reaction pathway contained three steps: (1) synthesis of N-propargyl imidazole through N-alkylation of imidazole with propargyl tosylate, (2) Quaternization of N-propargyl imidazole by 1,6-dibromohexane and (3) ion exchange with an excess of LiTFSI. During the initial step, unwanted double alkylation of imidazole was possible. To minimize this, double excess of imidazole relative to propargyl tosylate was used. To purify the product, vacuum distillation was applied, however the distillate still contained 10 mol% of imidazole. The remaining impurities were removed by treatment with concentrated HCl solution, resulting in $\geq 99\%$ pure N-propargyl imidazole with a yield of around 40%. To reach full conversion in the next reaction step with dibromohexane, a long reaction time (92 hours) and a high temperature (70°C) were required. The purification procedure of 1,1'-(hexane-1,6-diyl) bis(3-propargylimidazolium) bromide only involved crystallization from a MeCN/H₂O mixture. On the last step, the desired **ILM6** monomer was obtained *via* ion metathesis reaction with a small excess of LiTFSI in the aqueous medium as a slightly viscous yellow oil.

1.2.3 Thermal properties

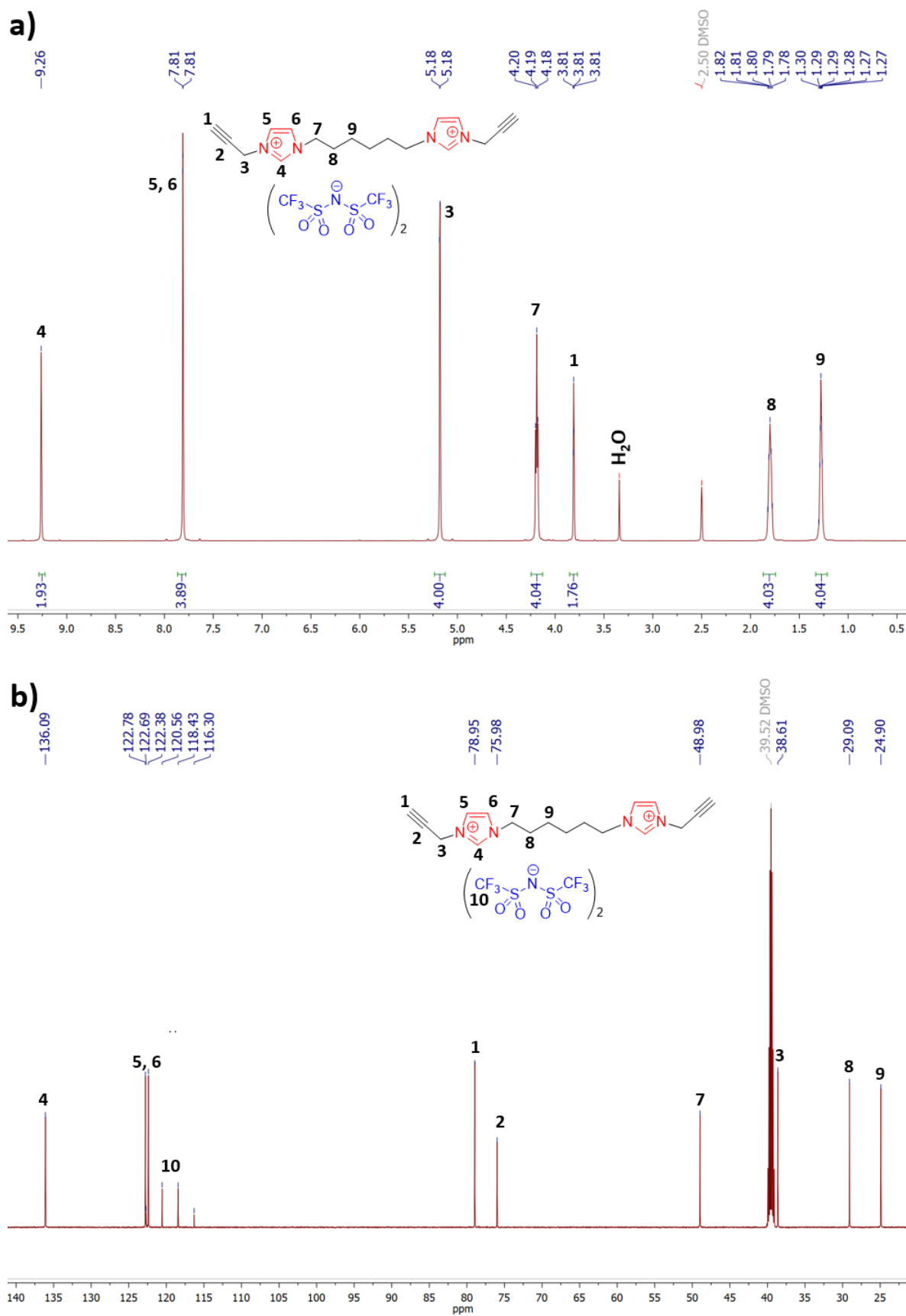
The thermal properties of the obtained monomers were assessed by differential scanning calorimetry. The monocationic monomers (**ILM3**, **ILM4**) each showed a single transition, attributed to their melting temperatures. **ILM3** exhibited a melting temperature of 49°C, while **ILM4**, with longer butyl substituents, had lower melting temperature of 40°C.

For the diammonium **ILM5**, DSC analysis revealed two phase transitions: a glass transition temperature of -45°C and a melting point of 69°C. In contrast, **ILM6** exhibited only $T_g = -56^\circ\text{C}$, confirming its glassy behavior.

1.2.4 Spectroscopic analysis of dipropargyl ionic monomers

The structure and purity of **ILM5** and **ILM6** were confirmed by ¹H, ¹³C and ¹⁹F NMR spectroscopy, FTIR spectroscopy and elemental analysis (Figure 1.9 - Figure 1.11).

The FTIR spectra of the monomers (Figure 1.11) showed absorption bands at ~ 3250 , 2990-2930 and 2880–2850 cm⁻¹ that were assigned to CH₂ stretching. The absorption bands at 3310–3250 (ν_{CH}), 2140 ($\nu_{\text{C}\equiv\text{C}}$) and ~ 615 (δ_{CH}) cm⁻¹ were identified as characteristic bands of alkyne groups. The characteristic bands of the TFSI anion were observed at ~ 1350 (asymmetric S=O), ~ 1190 (CF), ~ 1130 (symmetric S=O) and ~ 1050 (CF) cm⁻¹. Furthermore, ¹⁹F NMR spectra showed the singlet at -78.7 ppm assigned to trifluoromethyl groups, while ¹³C NMR spectra contained characteristic trifluoromethyl quadruplets at ~ 120 ppm.



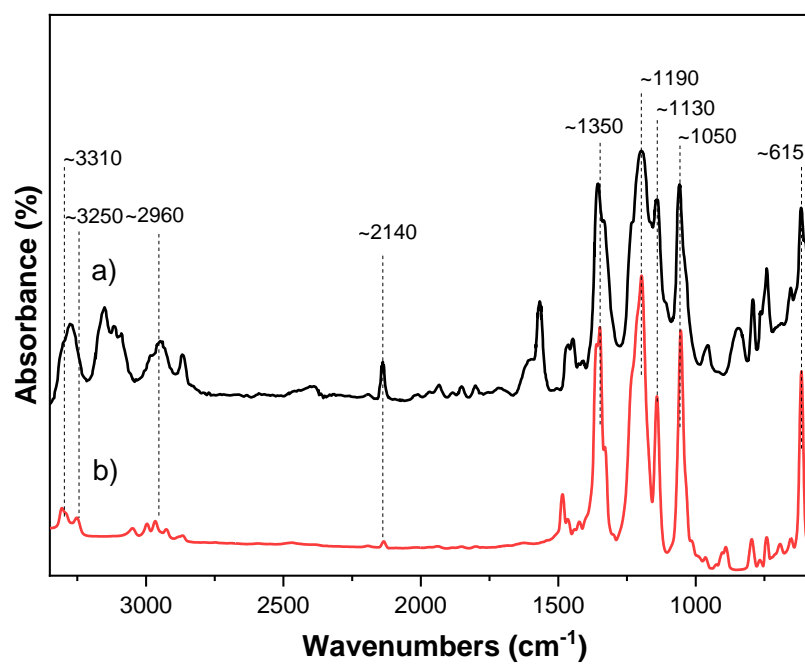


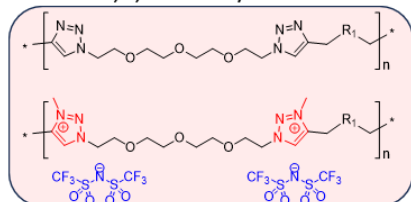
Figure 1.11 Comparison of FTIR spectra of **ILM6** (a) and **ILM5** (b).

2. Synthesis of poly(ionic liquid)s (PIL)s

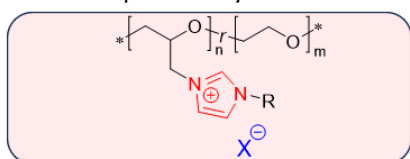
To fulfil the second and third objectives of this thesis and obtain highly conductive cationic and anionic polymeric building blocks necessary for the formation of dynamic ion gels, 5 families of poly(ionic liquid)s were developed (Figure 2.1):

- 1) Cationic 1,2,3-triazol/triazolium PILs synthesized *via* Cu(I)-catalysed azide–alkyne cycloaddition of **ILM3** - **ILM6** with subsequent alkylation;
- 2) Cationic methacrylic coPILs and cationic block copolymers obtained by reversible addition-fragmentation chain transfer (RAFT) polymerization of **ILM2** and different methacrylic neutral monomers;
- 3) Anionic methacrylic coPILs and anionic block copolymers obtained by reversible addition-fragmentation chain transfer polymerization of **ILM1** and different methacrylic neutral monomers;
- 4) Anionic methacrylic coPILs obtained by reversible addition-fragmentation chain transfer polymerization of **ILM7** with subsequent ion exchange.
- 5) Cationic PILs prepared via modification of a neutral epichlorohydrin-derived polymer.

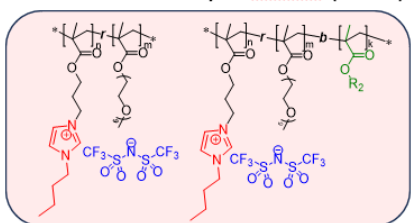
Cationic 1,2,3-triazol/triazolium PILs(**ILM3-ILM6**)



Cationic epichlorohydrin based PILs

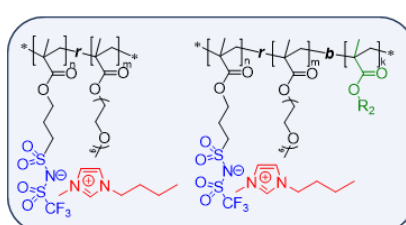


Cationic methacrylic coPILs (**ILM2**)



Polymeric building
blocks for the
formation of
dynamic ion gels
(DIG)s

Anionic methacrylic coPILs (**ILM1**)



Anionic methacrylic coPILs (**ILM7**)

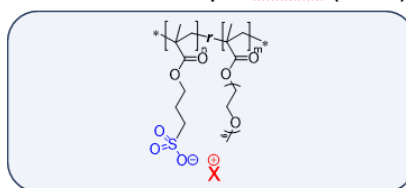


Figure 2.1 Various families of PILs synthesized in course of PhD thesis work.

A diverse range of PIL families with significant structural variations was synthesized to explore several under-researched factors affecting ionic conductivity, mechanical stability and other critical

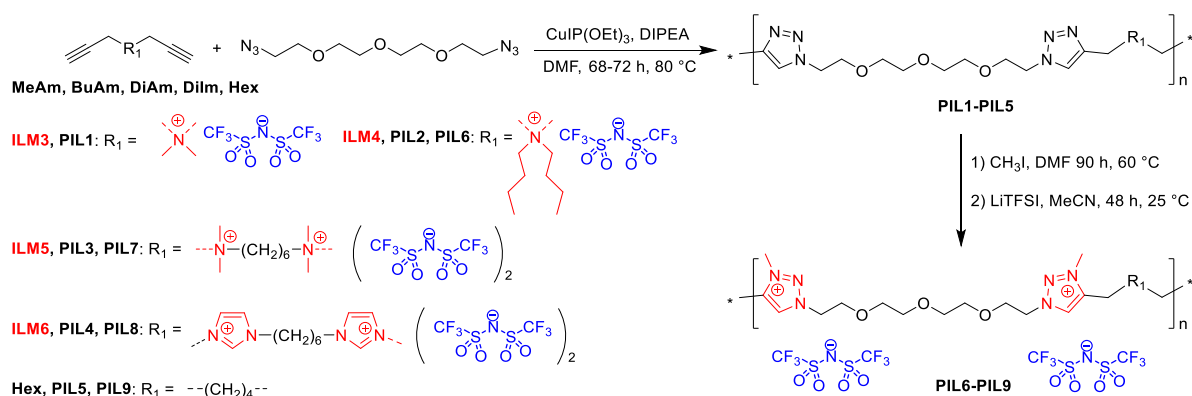
properties of PILs. The influence of repeat unit charge density on the bulk ionic conductivity was studied using a series of 1,2,3-triazole/triazolium cationic PILs. The effect of polymer morphology and block copolymer formation on mechanical properties was examined in cationic and anionic methacrylic coPILs derived from **ILM2** and **ILM1**. The dependence of ionic conductivity on counter cation nature was evaluated using a series of **ILM7** methacrylic coPILs. Lastly, the impact of substituents on the imidazolium cation, as well as the nature of counter anions on PILs properties, was investigated using cationic epichlorohydrin derived PILs.

2.1 Triazole/triazolium PILs (PIL1-PIL9)

2.1.1 Polyaddition of ionic monomers

All ionic dipropargyl monomers were first polymerized with 1,11-diazido-3,6,9-trioxaundecane by AA + BB CuAAC polyaddition in DMF (Scheme 2.1). In order to obtain high molar mass PILs, optimal conditions, including the utilization of CuIP(OEt)₃ as a catalyst and concentrated solutions of the monomers (20 wt.%), were applied as determined in previous studies^{35,105,106}. In contrast to previously reported procedure, the utilization of CH₂Cl₂ was not possible due to the precipitation of the formed ionic polymers at the beginning of the reaction. To increase the solubility of ionic triazole polymers the more polar DMF was used as the reaction solvent. The application of above-mentioned reaction conditions to the polyaddition of ionic dipropargyl monomers (**ILM3** – **ILM6**) with diazide resulted in the preparation of PILs having one (Scheme 2.1, **PIL1** and **PIL2**) or two (Scheme 2.1, **PIL3** and **PIL4**) ion pairs per repeat unit.

The molar mass of obtained polymers was estimated by size exclusion chromatography (SEC). It was revealed that in all cases CuAAC polyaddition resulted in the formation of high molar mass polymers, with number average molar masses (M_n) ranging from 50 to 120 kDa for **PIL2-PIL5** (Table 2.1). **PIL4**, based on bisimidazolium monomer, showed the highest M_n value.

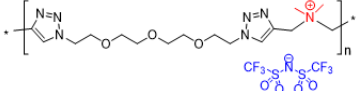
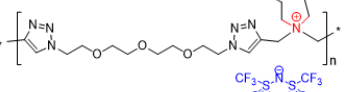
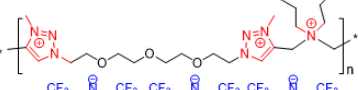
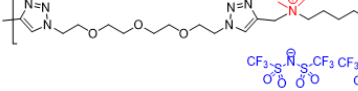
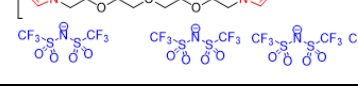
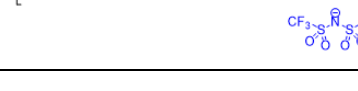


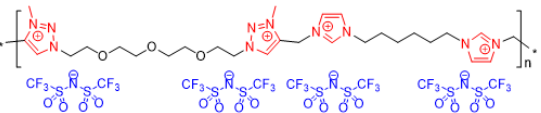
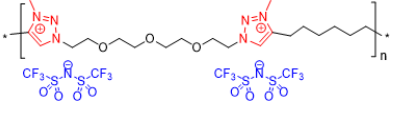
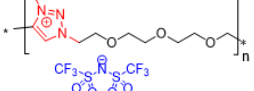
Scheme 2.1 Synthetic pathway for the preparation of 1,2,3-triazol/triazolium based cationic PILs.

2.1.2 Transformation of triazole polymers into triazolium PILs with charge density increase

To increase repeat unit charge density the poly(1,2,3-triazole)s (**PIL2-PIL5**) were further subjected to modification and transformed into 1,2,3-triazolium analogues (**PIL6-PIL9**) (Scheme 2.1). The modification involved two steps: N-alkylation using iodomethane and ion exchange with LiTFSI. **PIL1** was not considered further due to its limited solubility, which prevented the quantitative N-alkylation of 1,2,3-triazole groups. It should be mentioned that the previously developed single step method consisting in N-alkylation of poly(1,2,3-triazole)s **PIL2-PIL5** by N-methyl bis(trifluoromethylsulfonyl)imide³⁵ could not be performed quantitatively even after 72 h at 90 °C. Probably this can be explained by steric hindrance neighbouring the 1,2,3-triazole rings due to the near proximity of an ammonium or imidazolium cation and a bulky TFSI anion. Optimization of the reaction duration (90 hours) and the amount of CH₃I (10 equivalents) allowed to achieve nearly quantitative N-alkylation of the 1,2,3-triazole groups as confirmed by ¹H NMR. Further ion exchange reaction with excess LiTFSI in aqueous medium led to the preparation of **PIL6-PIL9** having from two to four ion pairs per repeat unit.

Table 2.1 Selected properties of poly(1,2,3-triazole)s and poly(1,2,3-triazolium)s

Polymer	M _n (SEC) (kDa) ¹	M _w /M _n (SEC) ¹	T _g (°C) ²	T _{onset} (°C) ³	σ at 25 °C (S cm ⁻¹)	ESW (V) ⁴	Charge density (mmol g ⁻¹)
Structure	PIL						
	PIL1	50.5	2.8	13	235	9.8×10 ⁻¹⁰	- ⁵ 1.55
	PIL2	62.8	1.9	8	220	2.8×10 ⁻⁹	4.0 1.37
	PIL6	19.9	1.1	15	175	4.9×10 ⁻¹⁰	3.3 2.27
	PIL3	57.4	1.8	3	270	5.8×10 ⁻⁸	4.3 1.90
	PIL7	56.2	1.2	8	230	8.3×10 ⁻⁹	3.3 2.43
	PIL4	119.0	1.8	-11	290	6.0×10 ⁻⁷	3.9 1.82

	PIL8	121.9	1.5	-1	265	4.2×10^{-7}	3.1	2.37
	PIL9	71.7	2.6	-32	280	1.8×10^{-5}	4.8	2.06
		- ⁶	-	-	-35	-	9.0×10^{-6}	1.97

¹Obtained by GPC in 0.1M LiTFSI in DMF at 50 °C with polystyrene standards calibration. ²Obtained by DSC 5 K min⁻¹. ³Obtained by TGA. ⁴Obtained by cyclic voltammetry at 70 °C (stainless steel as working electrode and Li foil as counter and reference electrodes, scan rate 0.5 mV s⁻¹). ⁵Not determined due to the very low conductivity. ⁶For comparison.

2.1.3 Spectroscopic analysis

The structure of the polymers, their composition and purity were supported by ¹H, ¹³C and ¹⁹F NMR and FTIR spectroscopy as well as by elemental analysis.

¹H NMR (Figure 2.2) corroborated the quantitative N-alkylation of the 1,2,3-triazole groups in **PIL6-PIL9** by: 1) the appearance of the N-3 methyl signal at 4.34 ppm; 2) the shift from 4.55 to 4.83 ppm of the N-1 methylene signal; 3) the shift from 8.22 to 8.97 ppm for the signal of the 1,2,3-triazole and 1,2,3-triazolium protons, respectively. The quantitative formation of 1,2,3-triazolium rings in **PIL6-PIL9** was also supported by elemental analysis. All ¹³C NMR spectra (Figure 2.3) contained characteristic trifluoromethyl quadruplets at ~ 120 ppm while ¹⁹F NMR spectra showed singlets at -78.7 ppm assigned to trifluoromethyl groups.

Finally, Figure 2.4 shows FTIR spectrum of **PIL9** which contains aliphatic CH groups (3140, 2960 cm⁻¹) and the bands related to the TFSI anion (1346, 1328, 1175, 1131 and 1050 cm⁻¹).

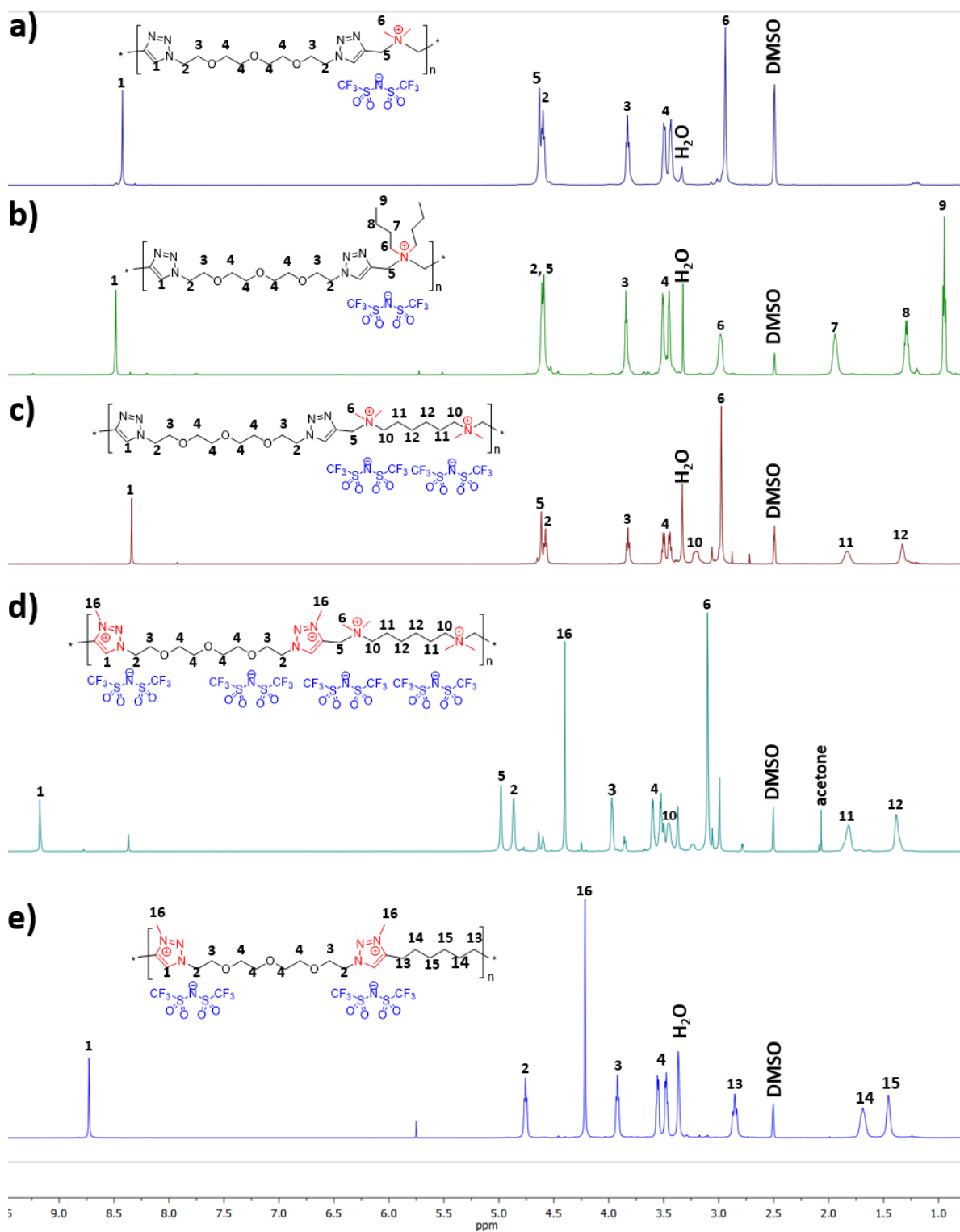


Figure 2.2 ^1H NMR of polymers **PIL1** (a), **PIL2** (b), **PIL3** (c), **PIL7** (d) and **PIL9** (e) (25°C , DMSO-d_6).

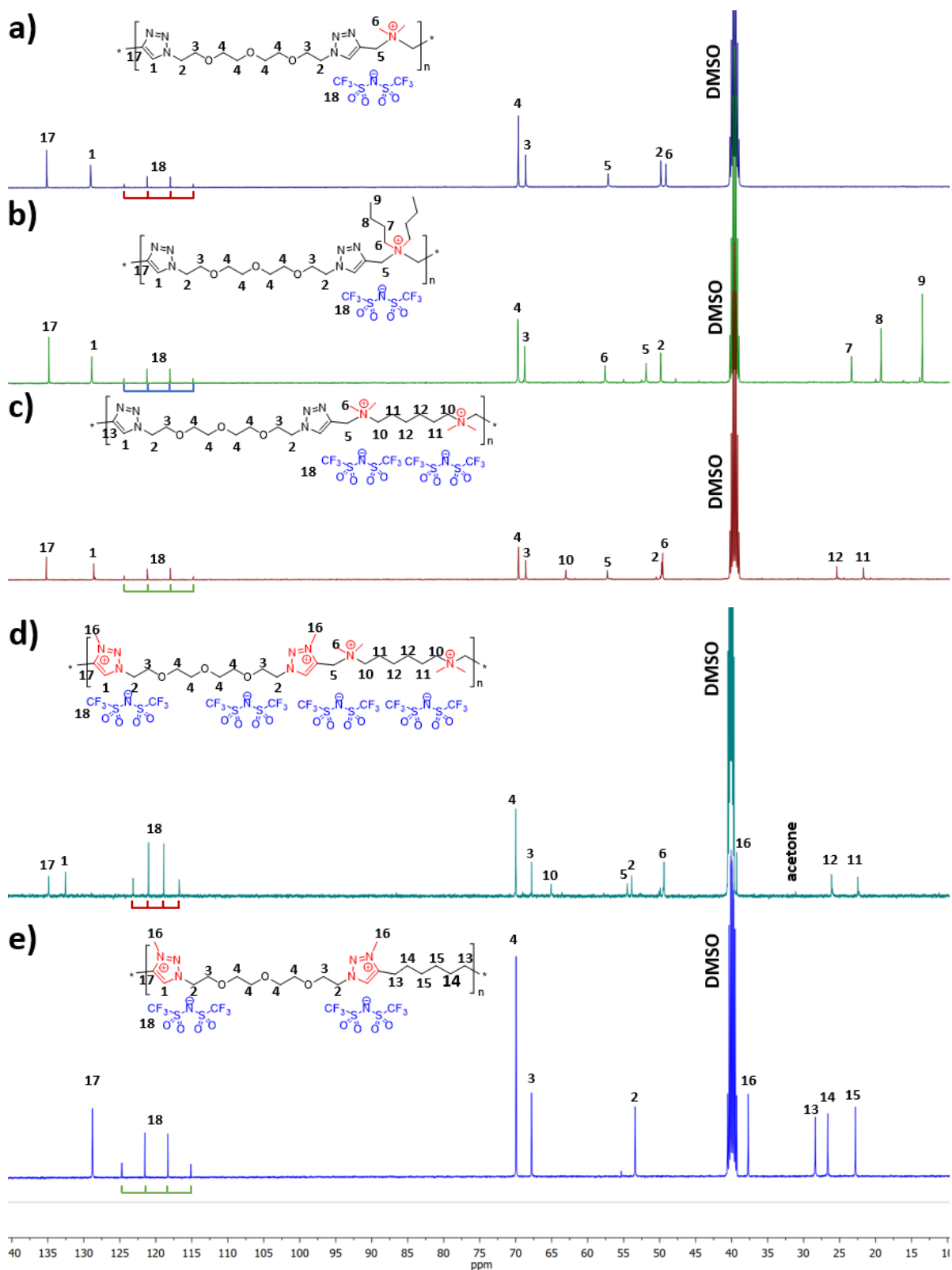


Figure 2.3 ^{13}C NMR of polymers **PIL1** (a), **PIL2** (b), **PIL3** (c), **PIL7** (d) and **PIL9** (e) (25 $^\circ\text{C}$, DMSO-d_6).

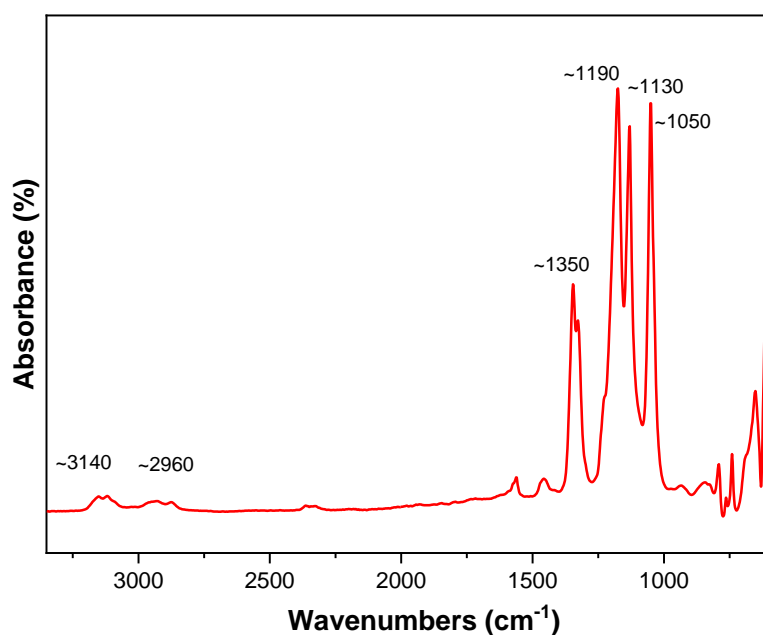


Figure 2.4 FTIR spectrum of **PIL9**.

2.1.4 Thermal properties

2.1.4.1 Glass-transition temperature

Thermal properties of **PIL1-PIL4** and **PIL6-PIL9** were assessed via differential scanning calorimetry (DSC). By analysing the T_g values of PILs, several interconnections with their structure can be identified:

- 1) The increase in the length of side chains in the ammonium cations affords a decrease in T_g (**Table 2.1**, **PIL1** and **PIL2**). This tendency fully correlates with the melting point variation observed in ILs¹⁰⁷ where T_m is dependent on the length of alkyl side chain.
- 2) The separation of the ammonium cations by a flexible aliphatic spacer increases the flexibility of the polymer backbone and thus reduces T_g (**Table 2.1**, polymers **PIL1** and **PIL3**).
- 3) The transition from ammonium to imidazolium cations results in the lowering of PILs heat resistance (**Table 2.1**, **PIL3** and **PIL4**, **PIL7** and **PIL8**), that was found to be in a full agreement with data reported for (meth)acrylate based PILs^{98,108}.
- 4) The correlation between repeat unit charge density and T_g can be summarized as follows:

T_g (°C): **PIL1** (1 charge, 13) > **PIL7** (4 charges, 8) > **PIL3** (2 charges, 3)

T_g (°C): **PIL6** (3 charges, 15) > **PIL2** (1 charge, 8)

Thus, it can be concluded that with the exception of **PIL1**, which does not contain flexible spacer between ammonium and 1,2,3-triazole groups, the increase in repeat unit charge density induces a rise in T_g . This reduction of polymer chains mobility is most likely due to electrostatic repulsions.

2.1.4.2 Onset temperature of weight loss

Thermal stability of PILs under air was found to be strongly dependent on the cation's structure (Figure 2.5). The overall evolution of thermal stability of PILs (T_{onset} values) according to the cation's nature can be summarized as follows:

T_{onset} (°C): **PIL4** (imidazolium cations, 290) > **PIL9** (1,2,3-triazolium cations, 280) > **PIL3** (ammonium cations, 270)

As generally observed for ILs¹⁰⁸ and methacrylate PILs⁹⁸, the imidazolium **PIL4** demonstrates higher thermal stability than **PIL1-PIL3** having ammonium cations (**Table 2.1**). The transition to 1,2,3-triazolium cations in **PIL9** results in lowering of T_{onset} value in comparison with imidazolium analogue **PIL4**. Thermal stability of PILs decreased following the orders below with respect to the repeat unit charge density:

T_{onset} (°C): **PIL3** (2 charges, 270) > **PIL1** (1 charge, 235) \approx **PIL7** (4 charges, 230)

T_{onset} (°C): **PIL2** (1 charge, 220) > **PIL6** (3 charge, 175)

T_{onset} (°C): **PIL4** (2 charges, 290) > **PIL8** (4 charges, 265)

Analysing the thermal stability data mentioned above, it is possible to summarize that the increase in repeat unit charge density of PILs affords a decrease in their decomposition temperatures. This is mainly due to the limited thermal stability of the 1,2,3-triazolium cation towards de-*N*-alkylation¹⁰⁹.

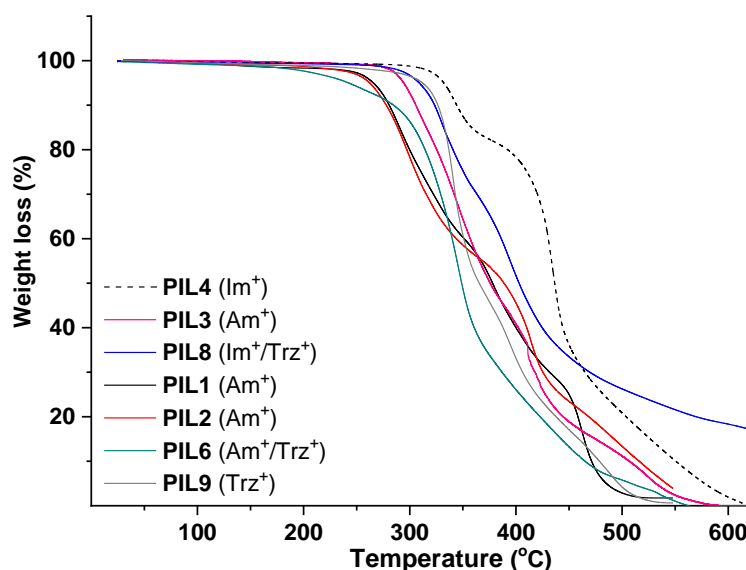


Figure 2.5 TGA traces of 1,2,3-triazolium/1,2,3-triazole PILs (5 K min⁻¹, under air). Imidazolium – **Im**⁺, ammonium – **Am**⁺, 1,2,3-triazolium – **Trz**⁺.

2.1.5 Electrochemical properties

2.1.5.1 Ionic Conductivity

Ionic conductivities of polymer electrolytes were investigated as a function of temperature by electrochemical impedance spectroscopy (Figure 2.6). Depending on the chemical nature of the cations and the repeat unit charge density the σ values determined at 25 °C under anhydrous conditions for synthesized PILs varied from 9.8×10^{-10} to 1.8×10^{-5} S cm⁻¹. The influence of the cation's chemical structure on ionic conductivity of monocationic PILs can be ranked as follows:

σ (25 °C, S cm⁻¹): **PIL9** (1,2,3-triazolium, 1.6×10^{-5}) >> **PIL4** (imidazolium, 6.0×10^{-7}) > **PIL3** (ammonium, 5.8×10^{-8})

This order fully correlates with the previously reported influence of cations structure on the conductivity of ILs^{110,111}. The insertion of side “dangling” chains decreases T_g and improves ionic conductivity as it can be concluded from the comparison of **PIL1** and **PIL2**. Such an increase in ionic conductivity can be explained by the decrease in packing density of the corresponding polyelectrolyte¹⁴. The separation of cations by an aliphatic spacer in **PIL3** increases the solvation of ions and thus triggers their dissociation and improves ionic conductivity (**Table 2.1**, **PIL1** and **PIL3**). Finally, the influence of repeat unit charge density on ionic conductivity of PILs can be ranked in the following decreasing orders:

σ (25 °C, S cm⁻¹): **PIL3** (2 charges (Am⁺), 5.8×10⁻⁸) > **PIL7** (4 charges (Trz⁺/Am⁺), 8.3×10⁻⁹) > **PIL1** (1 charge (Am⁺), 9.8×10⁻¹⁰)

σ (25 °C, S cm⁻¹): **PIL4** (2 charges (Im⁺), 6.0×10⁻⁷) > **PIL8** (4 charges (Trz⁺/Im⁺), 4.2×10⁻⁷)

σ (25 °C, S cm⁻¹): **PIL9** (2 charges (Trz⁺), 1.8×10⁻⁵) > **REF** (1 charge (Trz⁺), 9.6×10⁻⁶)

Taking these data into account it is possible to conclude that the repeat unit charge density vs conductivity dependence is passing through the maximum at PILs carrying two ion pairs. There are several possible explanations of the observed phenomenon. Possibly, the initial increase in number of cations leads to the increase in the repeat unit charge density or in the concentration of free anions and results in the conductivity magnification. However, at some point in a solid polymer, only the surrounding atoms/groups can solvate the ions, the ratio between the number of charges and the solvating groups becomes too low for efficient dissociation and the conductivity starts to decrease. Following this assumption, the dilution of ions by incorporation of an aliphatic spacer leads to an immediate rise in ionic conductivity (**Table 2.1**, **PIL1** and **PIL3**). Another explanation can be connected with the highly documented influence of the PILs structure/composition on T_g ¹⁴. As the increase in repeat unit charge density generally induces a rise of T_g and as ionic conductivity has an inverse relationship with the later¹⁴, it becomes obvious that the increase in the number of charges will reduce the ionic conductivity of PILs. In accordance with this assumption the transfer from monocationic or dicationic PILs (**PIL2-4**) to tricationic or tetracationic ones (**PIL6-8**) is accompanied by an increase in T_g and as a result in a decrease in ionic conductivity. Finally, it can be concluded that among studied cations, the 1,2,3-triazolium cation shows the highest ionic conductivity which is in a full agreement with the literature²³.

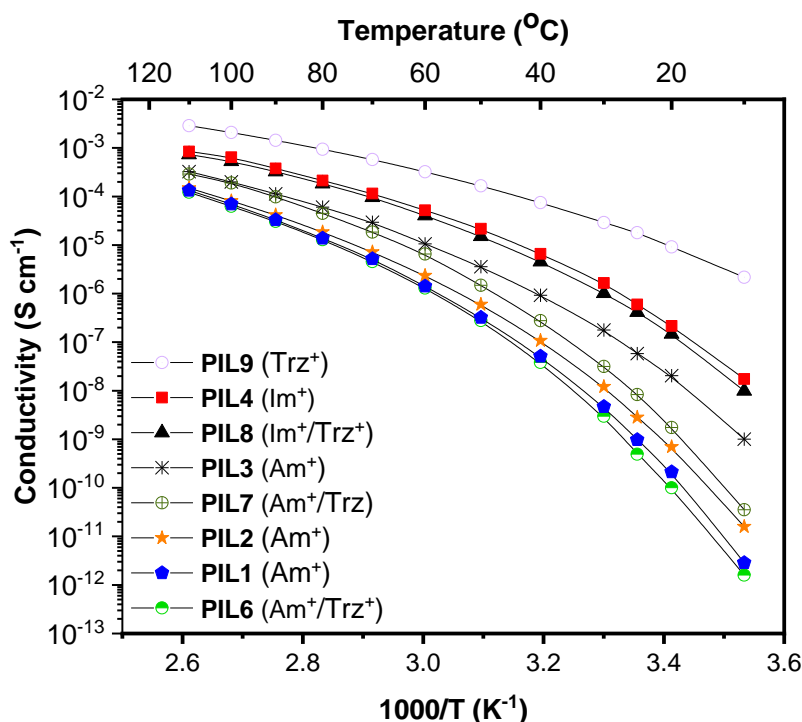


Figure 2.6 Evolution of ionic conductivity with inverse temperature for 1,2,3-triazolium/1,2,3-triazole PILs. Imidazolium – Im^+ , ammonium – Am^+ , 1,2,3-triazolium – Trz^+ .

The conductivity of PILs as a function of inverse temperature between 10 and 110 °C is shown on Figure 2.6. Independently on the repeat unit charge density and the nature of the cations, the ionic conductivity of all studied PILs increased with increasing temperature and reached a level ranging from ca. 5×10^{-6} to $6 \times 10^{-4} \text{ S cm}^{-1}$ at 70 °C. The temperature dependence of conductivity did not follow linear Arrhenius behaviour indicating that anion diffusion results from various mechanisms: hopping of TFSI anions along positively charged polymer backbone and local segmental motion of polymer chains.

2.1.5.2 Electrochemical stability

In addition to ionic conductivity, electrochemical stability (ESW) is another crucial property to consider for the practical application of PILs. Thus, ESW of PILs with the highest conductivity was evaluated against both Ag/Ag^+ and Li/Li^+ reference systems. This dual analysis provides a comprehensive understanding of their behavior in different electrochemical environments.

2.1.5.2.1 Ag/Ag^+ reference system

The electrochemical stability limits of **PIL9** were initially evaluated using cyclic voltammetry, with an Ag mesh serving as the reference electrode. Figure 2.7 presents the anodic and cathodic scans of **PIL9** at 25 °C. The oxidation potential of **PIL9** was determined to be 2.1 V, while the reduction potential was slightly lower at -1.4 V (Figure 2.7). Consequently, the total electrochemical stability

window was calculated to be 3.5 V. This value was slightly lower than what has been reported in the literature for triazole-based PILs³⁵.

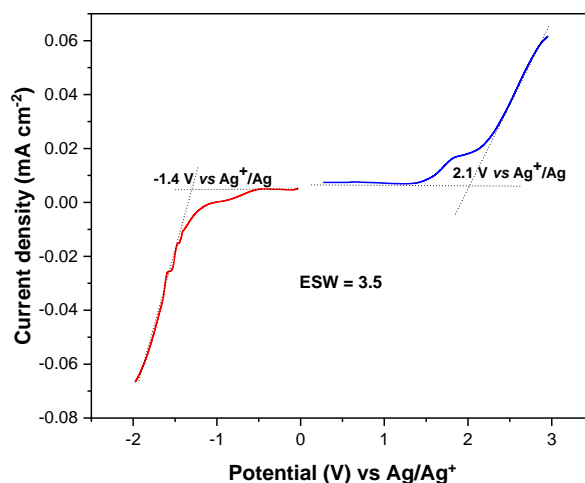
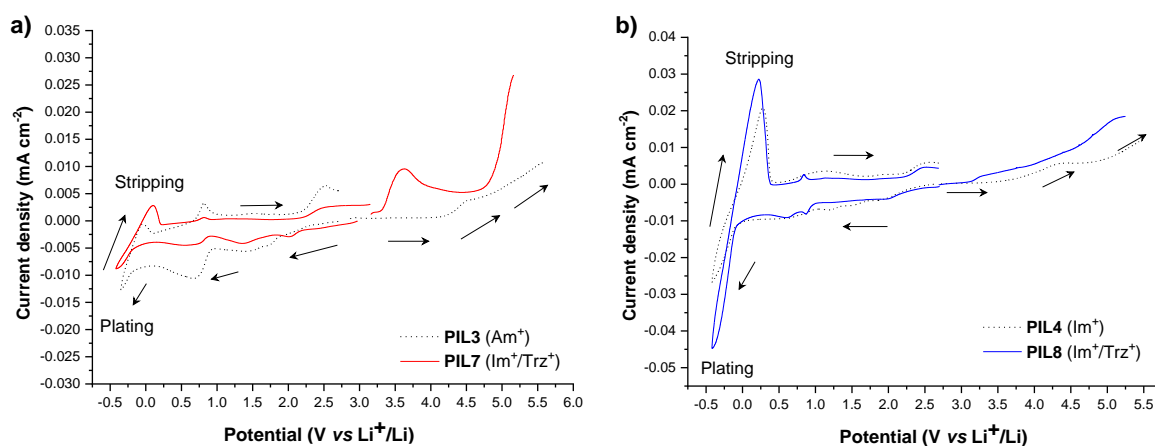


Figure 2.7 Electrochemical stability window for **PIL9** at 25 °C (Pt foils as the working and counter electrodes and Ag mesh as the reference electrode, scan rate 5 mV s⁻¹).

2.1.5.2.2 Li/Li⁺ reference systems

More detailed investigation of PIL's electrochemical stability windows was conducted versus Li/Li⁺. Figure 2.8 shows the anodic and cathodic scans at 70 °C of **PIL3**, **PIL 4**, **PIL7-PIL9**. For all PILs two reversible redox peaks at -0.45 V and between -0.05 and 0.30 V vs. Li⁺/Li were observed that are associated with the reversible lithium plating and stripping at the copper electrode surface. It should be noted that the intensity of the peaks was directly dependent on the ionic conductivity of polymers. The higher is the conductivity of PIL the better were the lithium plating and stripping processes.



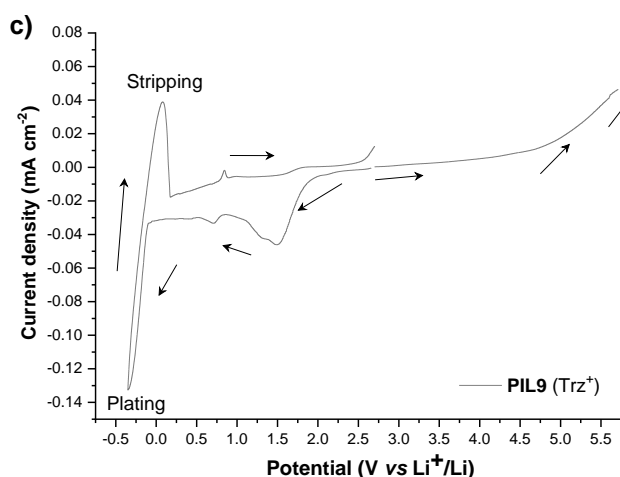


Figure 2.8 Electrochemical stability windows obtained by CV for (a) **PIL3** and **PIL7**, (b) **PIL4** and **PIL8** and (c) **PIL9** at 70°C (stainless steel as a working electrode and Li foil as counter and reference electrodes, scan rate 0.5 mV s⁻¹). Imidazolium – **Im**⁺, ammonium – **Am**⁺, 1,2,3-triazolium – **Trz**⁺.

Figure 2.8 suggests that the cathodic limit potential is mainly determined by the reduction of the respective cations. The irreversible oxidation peak at 1.5 V vs. Li⁺/Li found for **PIL9** (Figure 2.8, c) can be attributed to the partial degradation of the 1,2,3-triazolium cations as was observed previously³⁵. The increased cathodic stability up to -0.4 V vs. Li⁺/Li and observation for Li stripping and plating in comparison with previously reported 1,2,3-triazolium-based PILs may arise from the presence of the oxyethylene chain that could contribute to preventing the full reduction of the 1,2,3-triazolium cation. Similar influence of CH₂CH₂O groups on the cathodic limit of 1,2,3-triazolate anions was recently reported¹¹². It was previously observed that 1,2,3-triazolium cations exhibit lesser cathodic stability than quaternary ammonium and imidazolium cations. Following these observations for ILs, imidazolium-based **PIL4** shows better cathodic stability in comparison with **PIL9** and reveals no oxidation peaks until Li plating at -0.41 V (Figure 2.8, b and c). Surprisingly ammonium-based **PIL3** demonstrates two oxidation peaks at ca. 1.47 and 0.68 V (Figure 2.8, a). Although in PIL the ammonium cations are separated from the 1,2,3-triazole ring by a methylene group, these peaks can probably be attributed to the cleavage of the ring by Dimroth rearrangement. Interestingly, the presence of ammonium and imidazolium cations in heterocationic **PIL7** and **PIL8** fully suppresses the reduction of 1,2,3-triazolium cations, thus increasing the electrochemical stability of PILs (Figure 2.8, a and b).

The anodic limit potential of cationic PILs is commonly determined by the oxidation of the anion. As all studied PILs contain the same TFSI anion, their anodic stability was expected to be above 4.0 V vs. Li⁺/Li. Indeed, **PIL3** and **PIL9** demonstrate electrochemical stability windows up to 4.3 and 4.8 V, respectively (Figure 2.8, a and c). In accordance with what was observed previously for ILs, imidazolium-based **PIL4** shows a slightly reduced anodic limit equal to 3.9 V vs. Li⁺/Li (Figure 2.8, b). Unexpectedly, some irreversible reduction peaks at 3.6 and 3.3 V were found for **PIL7** and **PIL8**

having mixed cations (Figure 2.8, a and b). The reason for this phenomenon was unclear as usually the mixtures of Li salts either in EC-EMC solution or in polymer electrolyte are showing an improved stability in comparison with systems containing single salts.

2.1.6 Rheological properties

The rheological properties of 1,2,3-triazolium PILs were investigated using small amplitude oscillatory shear (SAOS) rheology, over a temperature range of -20 to 75°C, focusing on the most conductive **PIL9**. In order to facilitate the direct comparison of viscoelastic behaviour between PILs from different families, master curve was built through time-temperature superposition (TTS) using $T_0 = 25^\circ\text{C}$ as reference temperature (Figure 2.9, a). Figure 2.9 (a) shows that **PIL9** exhibits a short rubbery pseudo-plateau extending approximately 1-2 decades of frequency ($10^4 > \omega a_T > 10^2$), which is typical of entangled polymer chains. At 25°C and higher temperatures, **PIL9** displays a terminal regime evidenced by the evolution of loss and storage moduli following slopes as ω^1 and ω^2 , respectively. The shift factors a_T used in the TTS were determined (Figure 2.9, b) and it was verified that they present a temperature dependence that follows the Williams-Landel-Ferry (WLF) equation¹¹³ (equation 1.4).

Furthermore, to simplify the discussions, it was decided to investigate the dependence of mechanical properties of PILs on their structure by comparing only the storage modulus (G') at 25°C and 1 rad s⁻¹. This temperature was selected because, as it will be discussed in Section 4.1, the supercapacitor performance was evaluated at 25°C, while 1 rad s⁻¹ is the typical frequency at which the rheological behavior of polymers is studied¹¹⁴. Thus, **PIL9** exhibited a storage modulus of 0.1 kPa at 25°C and 1 rad s⁻¹, which was below average among all PILs under current investigation.

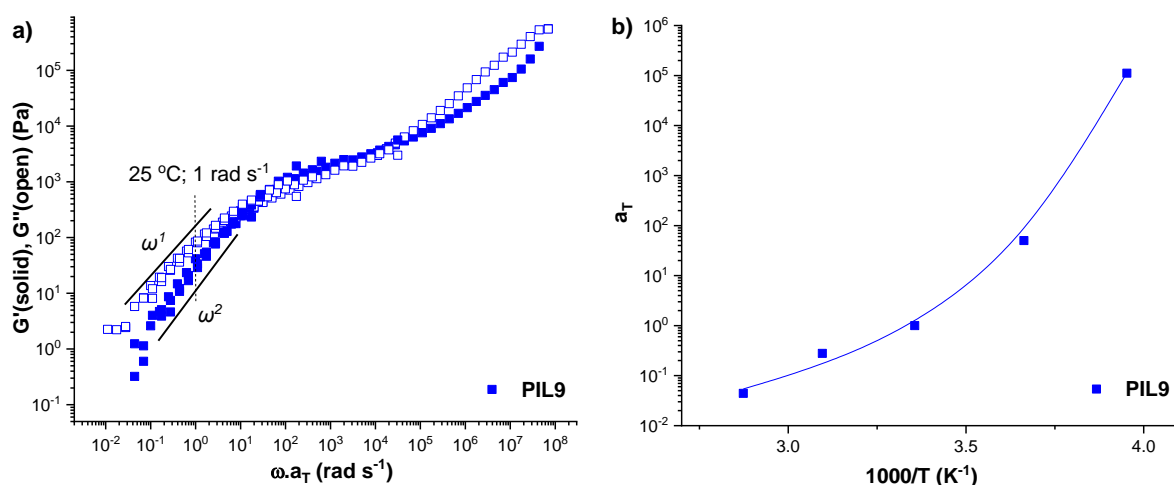


Figure 2.9 Time-temperature superposition (TTS) master curve of **PIL9** obtained by frequency sweep experiments performed from -20 to 75°C and referenced at $T_0 = 25^\circ\text{C}$ (a), corresponding a_T shift factors and WLF best fits at $T_0 = 25^\circ\text{C}$ for **PIL9** (b).

2.2 Methacrylate based polyelectrolytes (PIL10-PIL29) prepared by Reversible Addition Fragmentation chain Transfer (RAFT) polymerization

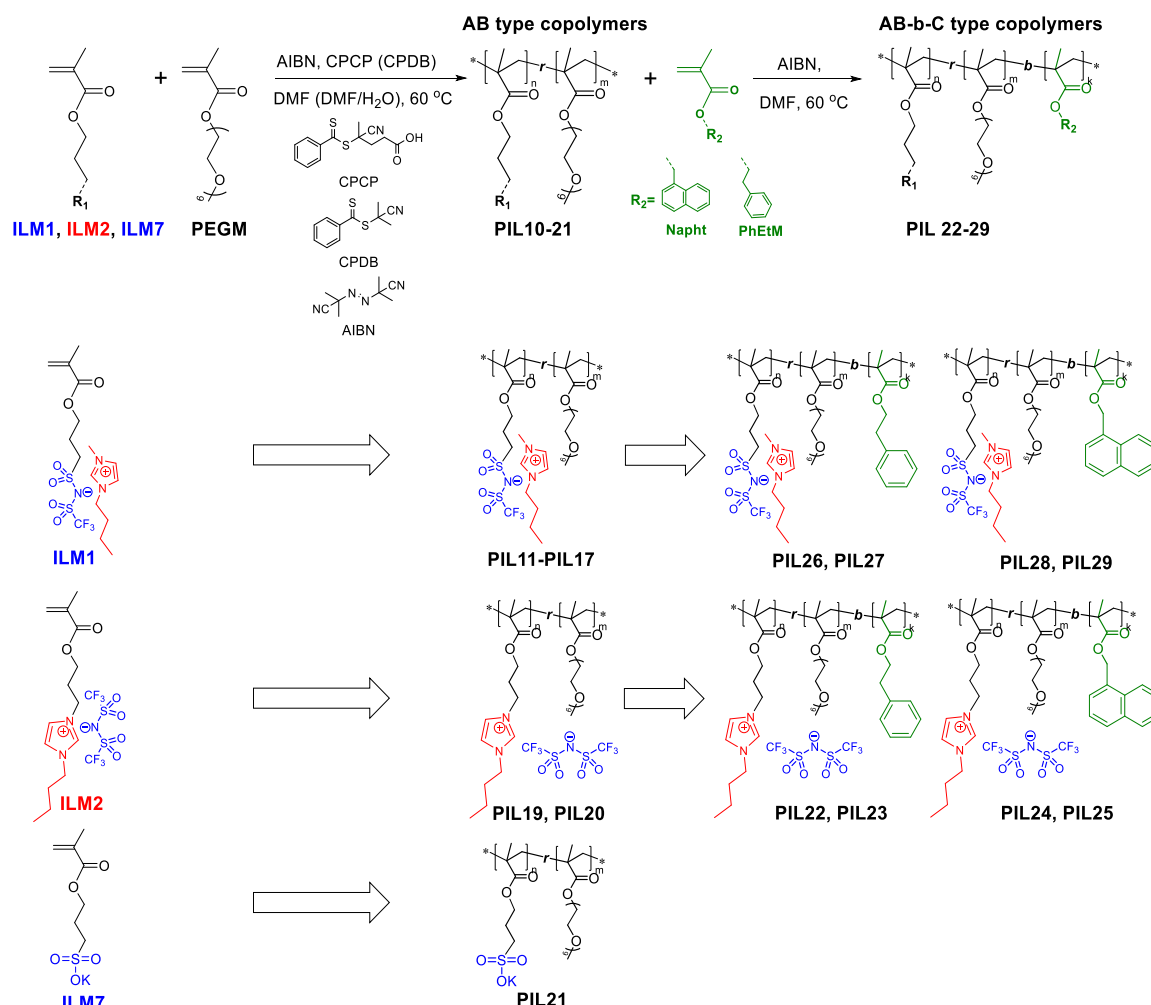
2.2.1 Synthesis and characterization

To prepare three families of methacrylate based random and block copolymers, three ionic monomers were utilized (Scheme 2.2). Along with synthesized in this work **ILM1** and **ILM2**, which contain the highly delocalized TFSI anion, the commercially available 3-sulfopropyl methacrylate potassium (**ILM7**), featuring a sulfonyl group was also used to evaluate the influence of charge delocalization on ionic conductivity and mechanical properties of PILs. For all ionic monomers mentioned above, poly(ethylene glycol) methyl ether methacrylate (**PEGM**) was used as a neutral comonomer. There were several reasons for this choice. Firstly, PEGM has the same methacrylate moiety which should provide similar to ILMs level of reactivity¹¹⁵. Furthermore, the introduction of the monomer with a long dangling chain significantly decreases the glass transition temperature of the resultant polymer, which beneficially affects the level of ionic conductivity^{11,12,116}. Additionally, the presence of oxyethylene fragments in PEGM facilitates ion pairs dissociation and promote the mobility of ions. The copolymerization of selected ionic and neutral monomers was conducted using the Reversible Addition-Fragmentation Chain Transfer (**RAFT**) method, resulting in the preparation of 10 **AB type** random copolymers (Scheme 2.2, Table 2.3, **PIL11-PIL17**, **PIL19-PIL21**). This approach allowed for controlled variation of the ratio between the ionic comonomer A and the neutral comonomer B, as well as the molecular weight (M_n) at a fixed comonomer ratio^{115,117}.

In the next step, the **AB-b-C type** block copolymers were prepared using previously synthesized random copolymers with **ILM1** and **ILM2** as macro-chain transfer agents (macro-CTAs) (Scheme 2.2). The goal for the preparation of these block copolymers was further improvement of the mechanical properties gained through a high T_g neutral block addition and phase separation of the material. To address this, two neutral monomers, 2-phenylethyl methacrylate (**PhEtM**, T_g (poly(**PhEtM**)) = 48°C) and (1-naphthyl)methyl methacrylate (**Napht**, T_g (poly(**Napht**)) = 111°C) were selected. Except for high T_g of corresponding polymers, the selection of these monomers was based on several considerations:

- 1) Commercial availability of these monomers;
- 2) The presence of the methacrylic functional group, being similar to **ILM1**, **ILM2**, and **PEGM**;
- 3) The existence of the aromatic moiety, which is known to be incompatible with ionic compounds, leading to a beneficial phase separation in the resulting block copolymers^{75,118}.

As a result, 8 ionically conductive and mechanically robust block copolymers with **AB-b-C** type architecture (Scheme 2.2, Table 2.4, **PIL22-PIL29**) were successfully synthesized and investigated.



Scheme 2.2 Synthesis of methacrylate based random and block copolymers.

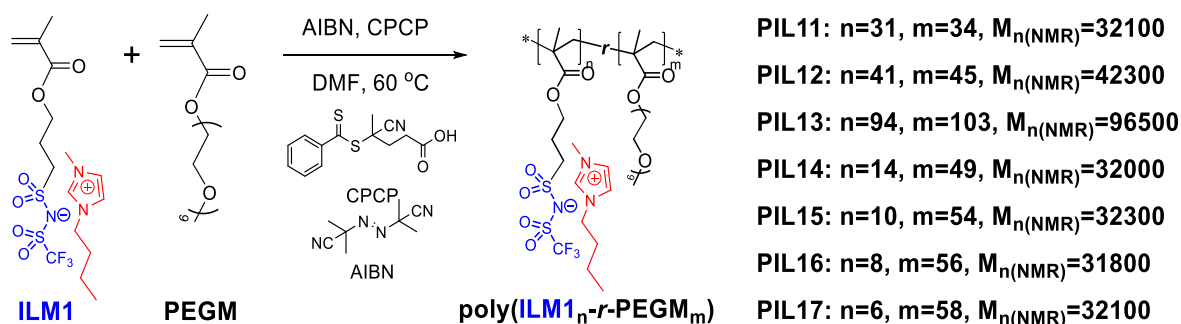
2.2.1.1 Random AB copolymers

2.2.1.1.1 Random copolymers based on ILM1

At first, the conditions for RAFT polymerization of **ILM1** and PEGM were fine-tuned. Building upon previous work by our group on analogous systems^{12,85,116}, DMF was chosen as the solvent due to its ability to form highly concentrated homogeneous solutions of ionic and neutral monomers (DMF:(ILM+PEGM) = 3:1 by weight) even at low temperatures. After determining that 60°C was the optimal reaction temperature for the successful polymerization, AIBN was selected as the thermal initiator. Dithiobenzoate-based 4-cyano-4-(phenylcarbonothioylthio)pentanoic acid (CPCP) was chosen as a suitable chain transfer agent (CTA) due to its high compatibility with ionic and neutral methacrylate monomers. A typical for RAFT CTA:initiator ratio of 5:1 (by mol) was used to balance the speed of the reaction and the livingness of the resulting polymeric chains¹¹⁵. Thus, the initial

conditions were established as follows: DMF as the solvent, AIBN as the initiator, CPCP as the CTA, with a CTA ratio of 5:1 (by mol), and a reaction temperature of 60°C (Scheme 2.3). It's worth to mention that polymers with molecular weight up to 35kDa (**PIL11**, **PIL14-PIL17**) required 12 h of synthesis, while to prepare high molecular weight **PIL13** (100 kDa) it was necessary to increase the reaction time to 72 h. The utilization of these conditions allowed for the synthesis of two groups of poly(**ILM1**_n-*r*-PEGM_m) random copolymers with high conversions (q) up to 90% (determined using equation 1.5) and molecular weights close to the target ones. The first group had fixed molecular weight (~35 kDa) and different PEGM:ILM ratios ranging from 1 to 10 (Scheme 2.3, Table 2.3, **PIL11**, **PIL14-PIL17**) and the second group had fixed PEGM:ILM ≈ 1:1 ratio and variable molecular weights (Scheme 2.3, Table 2.3, **PIL11-PIL13**).

The experimental values of n:m ratios were calculated using eqs. 1.6-1.10 and ¹H NMR of isolated copolymers. In all cases the values proved to be close to the ratio of monomers loading. Molar mass of obtained copolymers was determined by size exclusion chromatography (M_{n(SEC)}) and by NMR (M_{n(NMR)}) using equations 1.22-1.24 for the later. While the determined M_{n(NMR)} values for all poly(**ILM1**_n-*r*-PEGM_m) varied in the range of 31.8–96.5 kDa and were in a good agreement with targeted molecular weight, the M_{n(SEC)} values showed deviations (Table 2.3). Higher targeted molecular weight led to greater deviation of M_{n(SEC)} from M_{n(NMR)}, which was explained by the increase M_w/M_n ratio and the approach to the molecular weight limit for RAFT polymerization¹¹⁵.

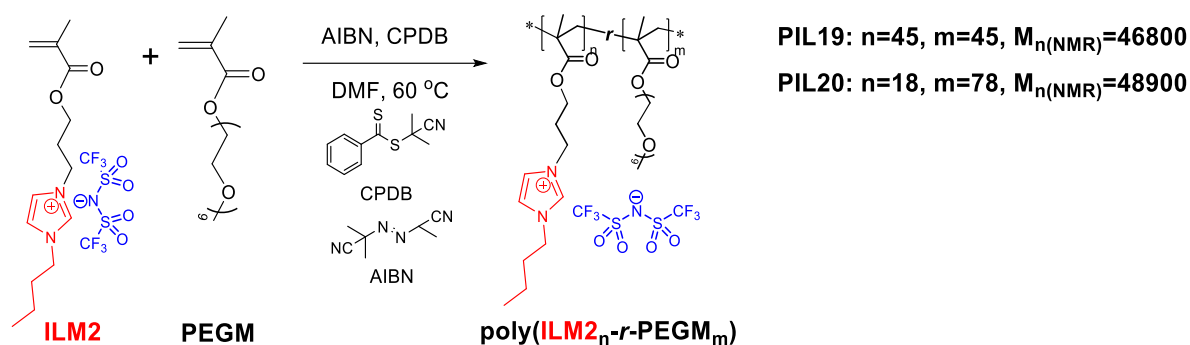


Scheme 2.3 Synthesis of poly(**ILM1**_n-*r*-PEGM_m).

2.2.1.1.2 Random copolymers based on ILM2

Contrary, copolymerization of the cationic monomer **ILM2**, under the aforementioned conditions resulted in a significantly lower conversion, which was only reaching 50%. This was probably attributed to the CTA's side reactions, as during the polymerization the noticeable colour change of the solution (from pink to brown) was observed. Consequently, CPCP with a carboxylic end group was replaced with a similar CPDB without reactive groups (Scheme 2.4). Keeping all other parameters constant, this change of the CTA improved the conversion up to 90%. Thus, applying these conditions a series of cationic poly(**ILM2**_n-*r*-PEGM_m) was synthesized with a fixed target molecular weight of 50 kDa and variable PEGM:**ILM2** ratio (from 1:1 to 5:1).

The actual *n*:*m* ratios were determined using eqs. 1.11-1.15 and ¹H NMR of isolated copolymers and were found to be 1:1 for **PIL19** and 1:4.4 for **PIL20** (Scheme 2.4). In analogy with poly(**ILM1**_{*n*}-*r*-PEGM_{*m*}), the molecular weight values of synthesized copolymers were determined by size exclusion chromatography (*M*_{n(SEC)}) and by NMR (*M*_{n(NMR)}). As a result, all synthesized cationic polymers showed a molecular weight of ~47 kDa and similarly to anionic PILs insignificant difference between *M*_{n(SEC)} and *M*_{n(NMR)} was observed.



Scheme 2.4 Synthesis of poly(**ILM2**_{*n*}-*r*-PEGM_{*m*}).

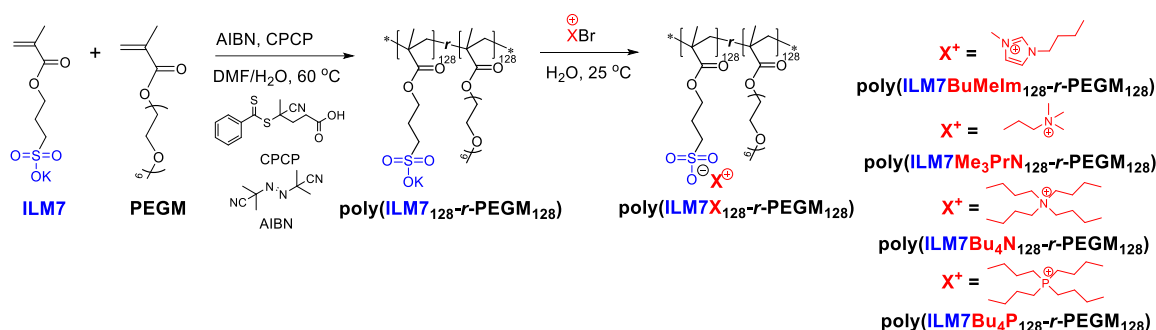
2.2.1.1.3 Random copolymers based on **ILM7**

To enhance the mechanical properties of the system through the introduction of highly localized ionic groups rather than by forming block copolymers, the last family of methacrylate-based random copolymers containing sulfonyl-based **ILM7** was synthesized. The procedure included two steps: the copolymerization of **ILM7** and PEGM and further ion exchange from poorly conductive potassium counter cation to various organic counter cations. The polymerization conditions previously developed for **ILM1** were not applicable for **ILM7** due to its low solubility in DMF. After several attempts to find a suitable solvent, a mixture of DMF and H₂O (3:2 by volume) was determined to be effective. Thus, by changing the solvent, poly(**ILM7**₁₂₈-*r*-PEGM₁₂₈), denoted as **PIL21**, was synthesized with conversion around 90% (Scheme 2.5). The *n*:*m* ratio, determined using NMR and equations 1.16-7.21, was 1:1, closely matching the monomers feed ratio. Molecular weight was determined only using NMR (*M*_{n(NMR)}) and equations 1.22-1.24 as **PIL21** was not soluble in the eluent (DMF), preventing the study of its molar mass by SEC.

On the next step, poly(**ILM7**₁₂₈-*r*-PEGM₁₂₈) containing potassium counter cations was subjected to ion metathesis with four different organic salts (Scheme 2.5). These salts featured a delocalized imidazolium cation, localized symmetric and asymmetric ammonium cations, and a symmetric phosphonium cation. This series of organic salts was selected to investigate several structural factors affecting the properties of the PILs. Utilization of 1-butyl-3-methylimidazolium bromide resulted in poly(**ILM7BuMeIm**₁₂₈-*r*-PEGM₁₂₈) (**PIL21I**). This PIL is an analog of poly(**ILM1**₉₄-*r*-PEGM₁₀₃) (**PIL13**) but features a localized sulfonyl group (Scheme 2.3, **PIL13**; Scheme 2.5, **PIL21I**).

The Comparison of these two polymers allows for evaluating the effect of anion charge delocalization on the properties of the PILs. The application of tetrabutylammonium and trimethylpropylammonium bromides resulted in poly(**ILM7Bu₄N**_{128-*r*}-PEGM₁₂₈) and poly(**ILM7PrMe₃**_{128-*r*}-PEGM₁₂₈), respectively (Scheme 2.5, **PIL21S**, **PIL21A**), and allowed for investigating the influence of cation charge delocalization and cation symmetry. Lastly, poly(**ILM7Bu₄P**_{128-*r*}-PEGM₁₂₈) (**PIL21P**), which was used to study the effect of the nature of the heteroatom on PIL properties, was obtained by ion metathesis with tetrabutylphosphonium bromide.

The completion of ion exchange was confirmed by NMR (Figure 2.11, c-f). Since the parent **PIL21** with potassium cation was not soluble in DMF, preventing the study of its molar mass by SEC, the imidazolium-substituted **PIL21I** which was readily soluble in organic solvents was investigated to determine $M_{n(SEC)}$ and the M_w/M_n ratio (Table 2.3).



Scheme 2.5 Synthetic pathway for the preparation of poly(**ILM7X**_{128-*r*}-PEGM₁₂₈).

2.2.1.2 Block AB-b-C copolymers

The creation of block copolymers is a well-established method in the literature for enhancing the mechanical properties of ionic polymers without compromising their ionic conductivity. This approach involves synthesizing block copolymers where one block is ionic, while the other block is typically neutral and possess high T_g . Due to partial incompatibility between these two blocks, a microphase-separated morphology emerges, forming two distinct domains: one ionic, with a high concentration of mobile ions and enhanced conductivity, and the other neutral, acting as stiffness ribs responsible for mechanical stability. Specifically, the self-assembly of block copolymers can result in a variety of nanostructures, such as body-centered cubic spheres, hexagonal packed cylinders, bicontinuous gyroid, and lamellar (Figure II.7). However, it was shown that the efficiency of charge transport in block copolymers increases as the morphology transitions from hexagonally packed cylinders to lamellar and to bicontinuous gyroid structures, thus making the last two the most favourable.

Consequently, to enhance the mechanical properties of **AB type** random copolymers comprising **ILM1** and **ILM2**, they were used as macro-chain transfer agents (macro-CTAs) for further

polymerization with neutral blocks to result **AB-b-C type** block copolymers (Scheme 2.2). To achieve beneficial morphology several structural factors previously discovered by our group on analogous polymers^{12,85,116} were considered.

- 1) High molecular weight block copolymers ($M_n = 50\text{--}90$ kDa) should be obtained
- 2) The ratio of molecular weight between the ion-containing block (AB) and neutral blocks (C) (M_{AB}/M_C) should be close to 2
- 3) The ratio of PEGM:ILM within ionic block (AB) should be around 5:1 by mol

Thus, poly(**ILM2**_{18-*r*}-PEGM₇₈) and poly(**ILM1**_{14-*r*}-PEGM₇₁) with PEGM:ILM \approx 5:1 and molecular weight around 45 kDa were chosen as macro-chain transfer agents for further copolymerization. However, considering that obtained block copolymers will be used in the preparation of DIGs, where the amount of released ionic liquid should play a crucial role in determining the ionic conductivity, polymers having higher ionic monomer content (poly(**ILM2**_{45-*r*}-PEGM₄₅) and poly(**ILM1**_{41-*r*}-PEGM₄₅)) were also included. 2-phenylethyl methacrylate (**PhEtM**, T_g (poly(**PhEtM**)) = 48°C) and (1-naphthyl)methyl methacrylate (**Napht**, T_g (poly(**Napht**)) = 111°C) were selected as neutral monomers with high T_g .

Therefore, four cationic (**PIL22-25**) and four anionic (**PIL26-29**) block copolymers (Table 2.2) were synthesized applying the conditions developed earlier: DMF as the solvent, AIBN as the initiator, macro-CTA, with a macro-CTA:initiator ratio of 5:1 (by mol) and a reaction temperature of 60°C. The conversion for both PhEtM and Napht monomers determined by ¹H NMR spectroscopy and eq. 1.25 was reaching \sim 75%.

Table 2.2 Characteristics of the synthesized poly[(**ILM**_{*n-r*}-PEGM_{*m*})-b-**Arm**_{*k*}] block copolymers

PIL	Poly[AB-b-C]	PEGM: ILM ¹	$\frac{M_{AB(NMR)}}{M_{C(NMR)}}$	M_n (Target) (kDa)	M_n (NMR) (kDa) ²	M_n (SEC) (kDa) ³	M_w/M_n (SEC) ³
22	poly[(ILM2 _{45-<i>r</i>} -PEGM ₄₅)-b-PhEtM ₉₉]	1.0	2.5	78.0	64.6	46.9	1.5
23	poly[(ILM2 _{17-<i>r</i>} -PEGM ₇₄)-b-PhEMt ₉₉]	4.4	2.4	79.5	65.0	54.7	1.4
24	poly[(ILM2 _{45-<i>r</i>} -PEGM ₄₅)-b-Napht ₉₀]	1.0	2.3	76.0	66.5	56.7	1.6
25	poly[(ILM2 _{17-<i>r</i>} -PEGM ₇₄)-b-Napht ₉₉]	4.4	2.1	77.5	68.5	48.6	1.5
26	poly[(ILM1 _{41-<i>r</i>} -PEGM ₄₅)-b-PhEtM ₉₄]	1.1	2.4	67.7	60.6	32.8	1.9
27	poly[(ILM1 _{12-<i>r</i>} -PEGM ₆₁)-b-PhEtM ₇₄]	5.1	2.6	60.8	50.6	53.5	1.7
28	poly[(ILM1 _{41-<i>r</i>} -PEGM ₄₅)-b-Napht ₇₇]	1.1	2.4	65.9	59.5	41.0	1.8
29	poly[(ILM1 _{14-<i>r</i>} -PEGM ₇₃)-b-Napht ₈₆]	5.2	2.2	60.8	62.6	46.6	1.8

¹By ¹H NMR. ²Defined by eqs. 1.28 and 1.31. ³Obtained by GPC in 0.1M LiTFSI in DMF at 50 °C with PMMA standards calibration.

Molar masses of the obtained copolymers were determined by NMR ($M_{n(\text{NMR})}$) using equations 1.28 for poly[(**ILM**_{n-r}-PEGM_m)-b-PhEtM] and 1.31 for poly[(**ILM**_{n-r}-PEGM_m)-b-Napht]. The determined $M_{n(\text{NMR})}$ values ranging between 50.6 and 68.5 kDa, thus the M_{AB}/M_C ratio was calculated to be 2.1–2.6 (Table 2.2). It should be mentioned that determined $M_{n(\text{NMR})}$ values were closely matching the targeted M_n . The investigation of the molar masses was repeated with SEC to provide $M_{n(\text{SEC})}$. Figure 2.10 presents the typical SEC chromatograms for both random and block copolymers. The chromatograms indicate that the obtained block copolymers possess higher $M_{n(\text{SEC})}$ values and similar or slightly higher M_w/M_n ratios (~1.4–1.9) compared to the parent poly(**ILM**_{n-r}-PEGM_m) macro-CTA, thus strongly supporting the successful formation of the desired block copolymers.

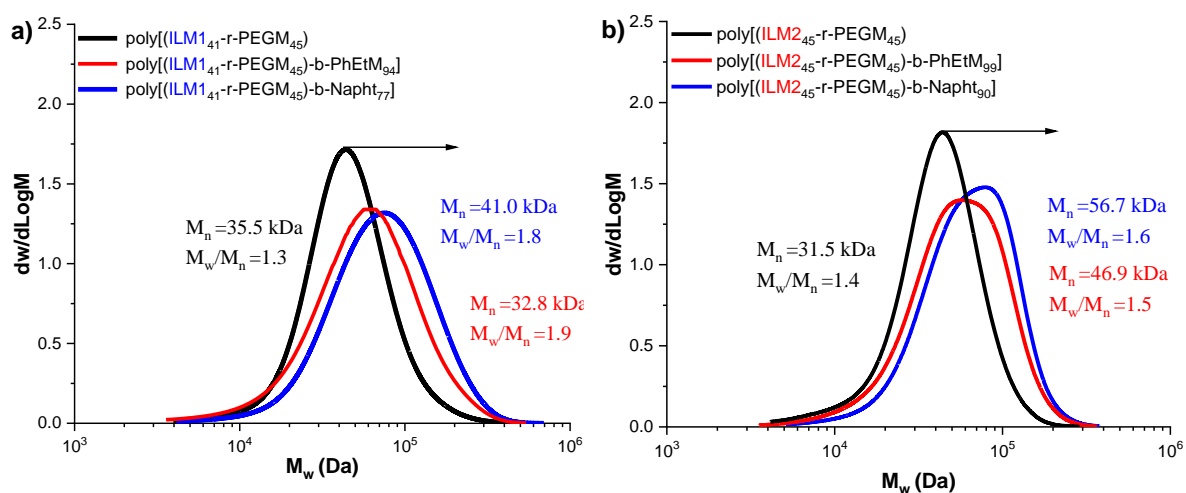


Figure 2.10 SEC traces of anionic (a) and cationic (b) macro-CTAs and block copolymers (0.1 M LiTFSI in DMF, 50°C, PMMA standards).

2.2.2 Spectroscopic analysis

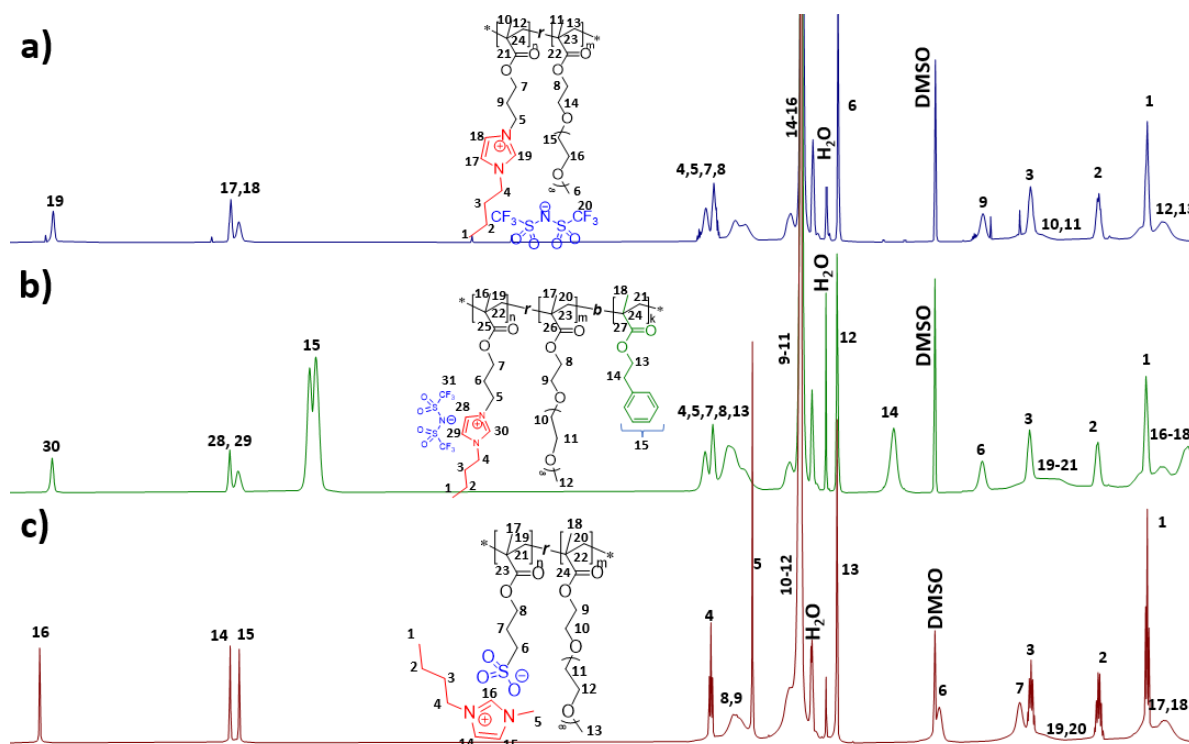
The structure of all random and block copolymers, their composition and purity were supported by ^1H , ^{13}C and ^{19}F NMR and FTIR spectroscopy as well as by elemental analysis.

The ^1H NMR spectra of poly[(**ILM2**_{45-r}-PEGM₄₅), shown in Figure 2.11(a), confirm the absence of methacrylic double bonds and other impurities. The comonomer ratio was determined using equations 1.11-1.15. The ^{13}C NMR spectra (Figure 2.12, d) display a characteristic trifluoromethyl quadruplet around 120 ppm, while the ^{19}F NMR spectra show a singlet at approximately -80.0 ppm, assigned to the trifluoromethyl group.

For poly(**ILM7X**_{128-r}-PEGM₁₂₈), ^1H NMR (Figure 2.11, c-f) confirmed quantitative ion exchange, indicated by the presence of signals from organic counter cations in a 1:1 ratio to the PEGM CH₃ end group. Elemental analysis further supported the completion of this reaction.

Figure 2.11(b) presents the ^1H NMR spectra of poly[(**ILM2**₄₅-*r*-PEGM₄₅)-*b*-PhEtM₉₉]. The spectra clearly show chemical shifts corresponding to both blocks, poly[(**ILM2**₄₅-*r*-PEGM₄₅) and poly(PhEtM₉₉), and confirm the absence of double bonds from the neutral comonomer and other impurities. Similar to the ionic random copolymers, the ^{13}C NMR signals (Figure 2.12, a-f) exhibit characteristic trifluoromethyl quadruplets, and the ^{19}F NMR spectra show singlet at around -80.0 ppm.

FTIR spectra (Figure 2.13) of random copolymers had the following absorption bands: $\sim 2930\text{ cm}^{-1}$ that was assigned to CH_2 stretching; $\sim 1730\text{ cm}^{-1}$ ($\text{C}=\text{O}$ stretching); $\sim 1630\text{ cm}^{-1}$ ($\text{C}=\text{C}$ stretching); $\sim 1455\text{ cm}^{-1}$ (CH bending); $\sim 1350\text{ cm}^{-1}$ (asymmetric $\text{S}=\text{O}$ stretching); $\sim 1160\text{ cm}^{-1}$ (CF stretching); $\sim 1110\text{ cm}^{-1}$ (symmetric $\text{S}=\text{O}$ stretching); $\sim 1055\text{ cm}^{-1}$ (CF stretching), while block copolymers also exhibited absorption bands attributed to aromatic rings: $\sim 1455\text{ cm}^{-1}$ ($\text{C}=\text{C}$ vibrations of the aromatic ring), ~ 775 , 745 cm^{-1} (CH -aromatic deformation).



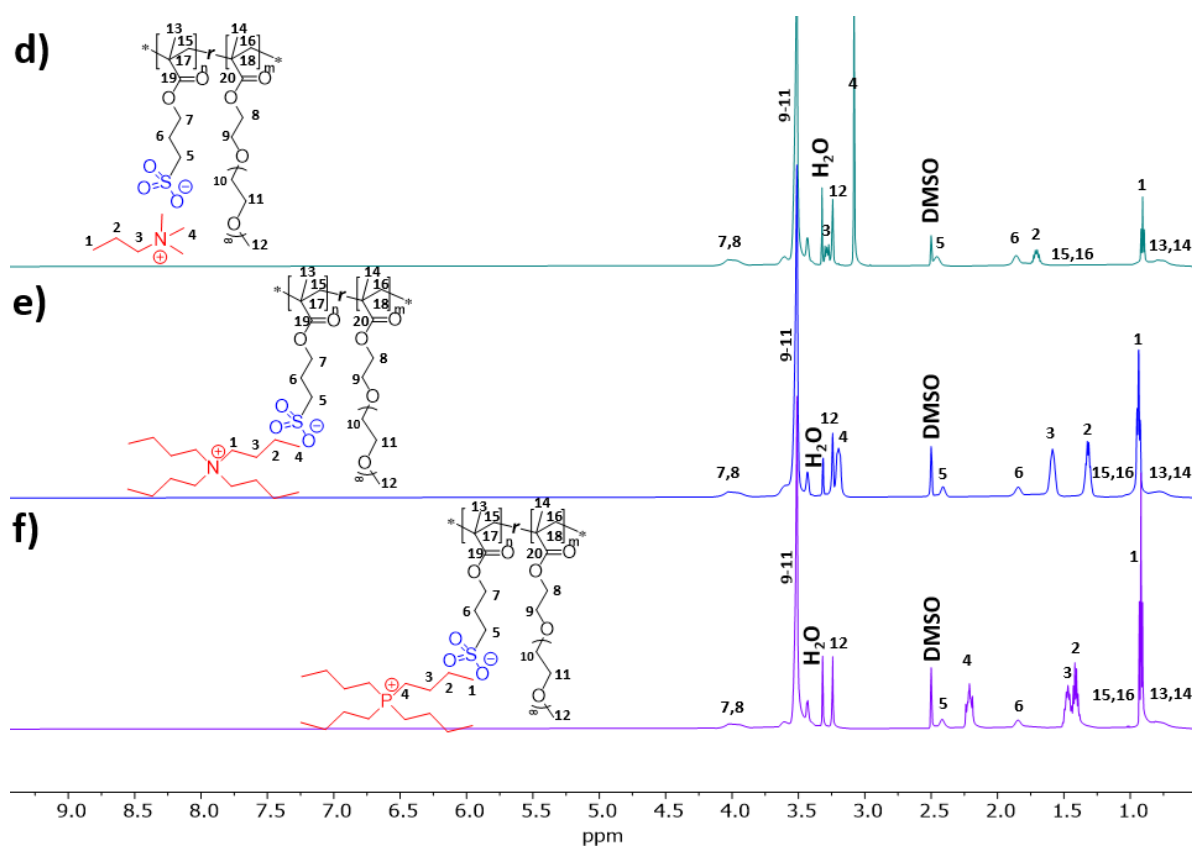
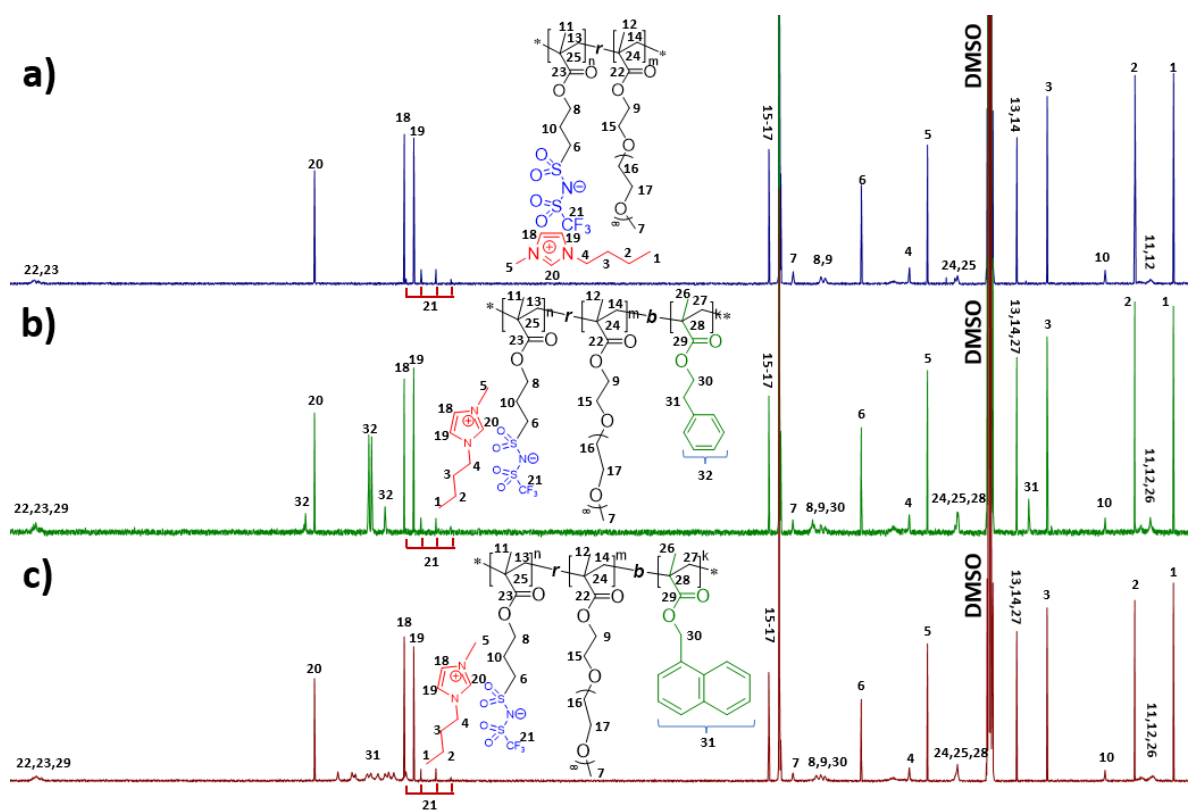


Figure 2.11 ^1H NMR of polymers PIL19 (a), PIL22 (b), PIL21I (c), PIL21A (d), PIL21S (e) and PIL21P (f) (25 $^\circ\text{C}$, DMSO-d_6).



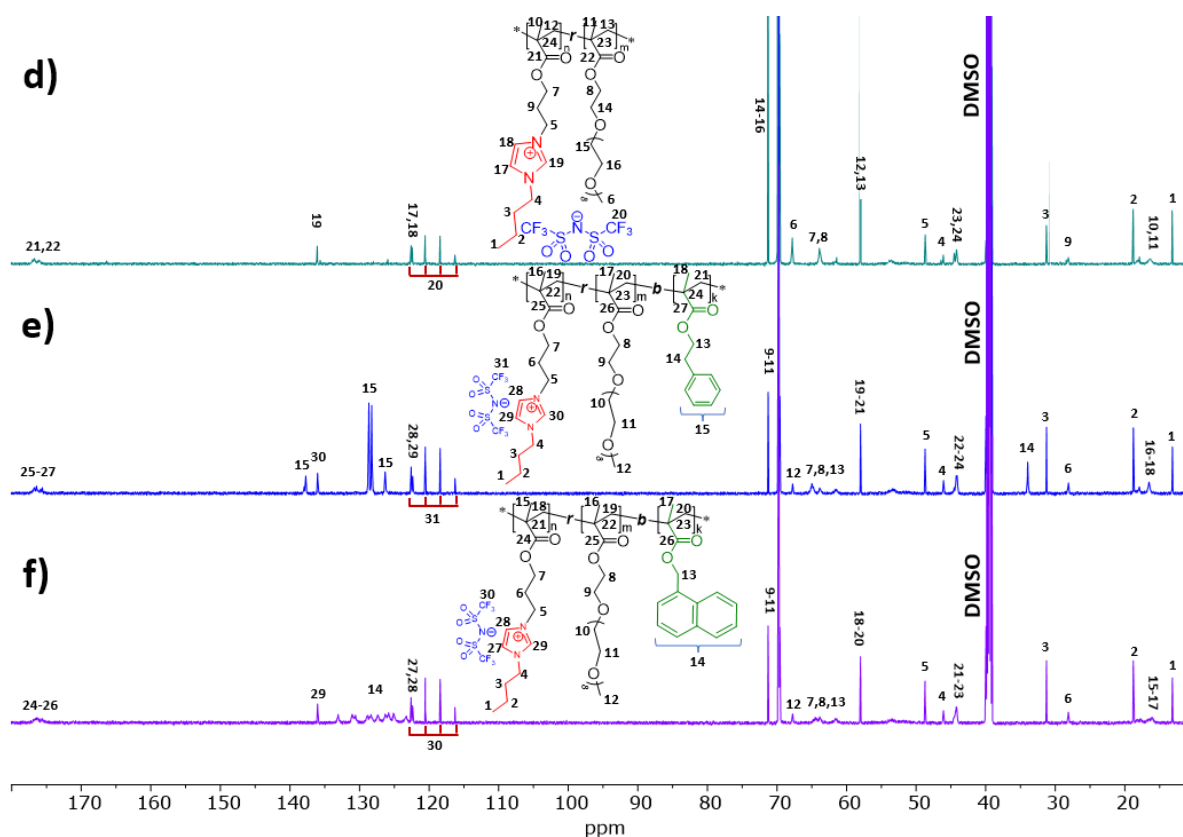


Figure 2.12 ^{13}C NMR of polymers **PIL12** (a), **PIL26** (b), **PIL28** (c), **PIL19** (d), **PIL22** (e) and **PIL24** (f) (25 °C, DMSO- d_6).

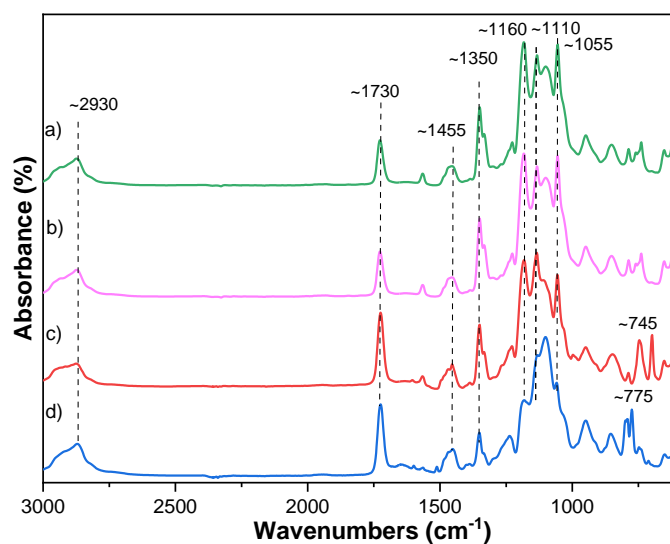


Figure 2.13 FTIR spectra of **PIL13** (a), **PIL18** (b), **PIL22** (c) and **PIL24** (d).

2.2.3 Thermal properties

2.2.3.1 Glass-transition temperature

2.2.3.1.1 Random copolymers poly(ILM_n-*r*-PEGM_m)

Thermal properties of all random copolymers were investigated via DSC. All of them demonstrated the presence of a single glass transition on the DSC curves.

It was observed that random copolymerization of **ILM1** and **ILM2** with PEGM in any ratios leads to the decrease in the T_g of polyelectrolytes in comparison with respective homopolymers (T_g **PIL10** = -13°C and T_g **PIL18** = -6°C, Table 2.3). The higher was the content of PEGM units in copolymers, the lower was the observed T_g (Figure 2.14, a). Consequently, the relationship between PEGM content in poly(**ILM**_n-*r*-PEGM_m) and T_g can be summarized as follows:

T_g (°C): **PIL10** (poly(**ILM1**₇₄), -13) > **PIL11** (PEGM:**ILM1** = 1.1, -40) > **PIL14** (PEGM:**ILM1** = 3.4, -54) > **PIL15** (PEGM:**ILM1** = 5.3, -57) > **PIL16** (PEGM:**ILM1** = 7.0, -58) > **PIL17** (PEGM:**ILM1** = 10.1, -62)

T_g (°C): **PIL18** (poly(**ILM2**₅₁), -6) > **PIL19** (PEGM:**ILM2** = 1.0, -38) > **PIL20** (PEGM:**ILM2** = 4.4, -57)

In the case of anionic polymers, an increase in PEGM content resulted in a decrease in T_g , shifting from -13°C for the **ILM1** homopolymer (**PIL10**) to -62°C for poly(**ILM1**₆-*r*-PEGM₅₈), eventually reaching the T_g of neat poly(PEGM) (Figure 2.14, a). Similarly, PILs incorporating cationic **ILM2** exhibited a comparable trend, with T_g values closely mirroring those of poly(**ILM1**_n-*r*-PEGM_m) (Figure 2.14, a). Interestingly to note that cationic homopolymer **PIL18** showed slightly higher T_g than its anionic analogue **PIL10**. However, with an increase in PEGM content in the respective copolymers, the effect of the monomer nature became insignificant.

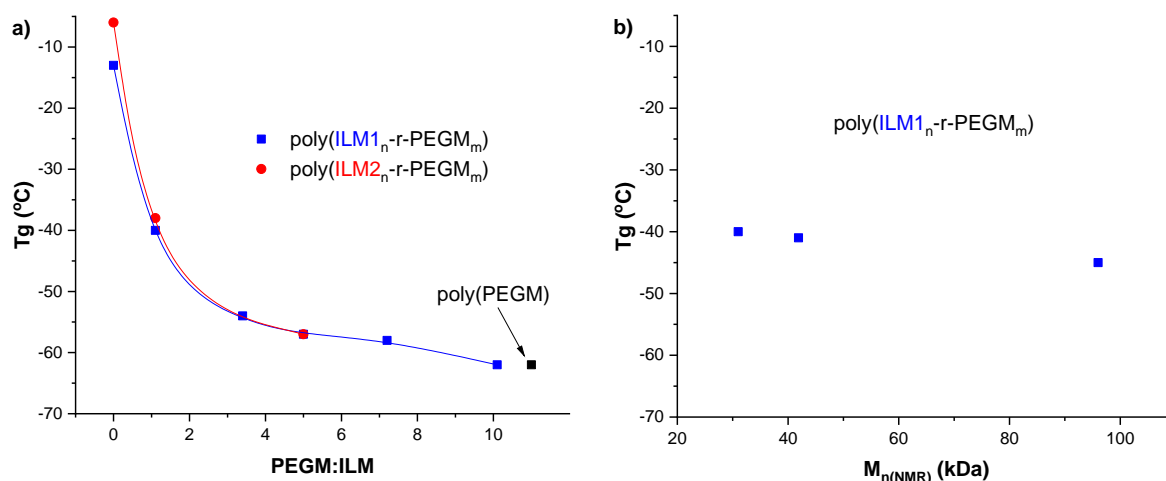


Figure 2.14 Glass transition temperature (T_g) dependence on PEGM content for poly(**ILM1**_n-*r*-PEGM_m) and poly(**ILM2**_n-*r*-PEGM_m) (a); T_g dependence on molecular weight ($M_{n(NMR)}$) for poly(**ILM1**_n-*r*-PEGM_m) (b).

Furthermore, in the series of anionic poly(**ILM1**_n-*r*-PEGM_m) with fixed PEGM:**ILM1** (**PIL11**-**PIL13**, Table 2.3) the effect of molecular weight on T_g was evaluated. It was shown that the rise of molecular weight from 30 kDa to 96 kDa only resulted in minor decrease in T_g , thus, proving independence of glass transition temperature from molecular weight in this range (Figure 2.14, b).

Table 2.3 Selected properties of methacrylic random copolymers

PIL	Poly(A)/Poly(AB)	PEGM : ILM ¹	M _n (^{NMR}) (kDa) ²	M _n (^{SEC}) (kDa) ³	M _w /M _n (^{SEC}) ³	σ at 25°C (S cm ⁻¹)	T _g (°C) ⁴	T _{onset} (°C) ⁵
10	poly(ILM1 ₇₄)	-	-	35.5	1.5	3.6×10 ⁻⁷	-13	275
11	poly(ILM1 _{31-<i>r</i>} -PEGM ₃₄)	1.1	32.1	31.0	1.2	7.5×10 ⁻⁶	-40	165
12	poly(ILM1 _{41-<i>r</i>} -PEGM ₄₅)	1.1	42.3	35.5	1.3	5.2×10 ⁻⁶	-41	-
13	poly(ILM1 _{94-<i>r</i>} -PEGM ₁₀₃)	1.2	96.5	72.1	1.4	5.9×10 ⁻⁶	-46	-
14	poly(ILM1 _{14-<i>r</i>} -PEGM ₄₉)	3.4	32.0	31.3	1.2	1.2×10 ⁻⁵	-54	160
15	poly(ILM1 _{10-<i>r</i>} -PEGM ₅₄)	5.4	32.3	30.6	1.2	6.6×10 ⁻⁶	-57	160
16	poly(ILM1 _{8-<i>r</i>} -PEGM ₅₆)	7.0	31.8	31.0	1.2	5.2×10 ⁻⁶	-58	160
17	poly(ILM1 _{6-<i>r</i>} -PEGM ₆₀)	10.1	32.1	31.2	1.2	3.9×10 ⁻⁶	-62	160
18	poly(ILM2 ₅₁)	-	-	27.1	1.4	4.4×10 ⁻⁷	-6	290
19	poly(ILM2 _{45-<i>r</i>} -PEGM ₄₅)	1.0	46.8	31.5	1.4	5.7×10 ⁻⁶	-38	160
20	poly(ILM2 _{18-<i>r</i>} -PEGM ₇₈)	4.4	48.9	36.4	1.3	1.2×10 ⁻⁵	-57	160
21	poly(ILM7 _{128-<i>r</i>} -PEGM ₁₂₈)	1.0	95.7	-	-	-	-	-
21I	poly(ILM7BuMeIm _{128-<i>r</i>} -PEGM ₁₂₈)	1.0	-	-	-	1.9×10 ⁻⁶	-40	190
21S	poly(ILM7Bu ₄ N _{128-<i>r</i>} -PEGM ₁₂₈)	1.0	-	-	-	9.0×10 ⁻⁸	-36	190
21A	poly(ILM7PrMe ₃ N _{128-<i>r</i>} -PEGM ₁₂₈)	1.0	-	-	-	4.8×10 ⁻⁷	-29	195
21P	poly(ILM7Bu ₄ P _{128-<i>r</i>} -PEGM ₁₂₈)	1.0	-	-	-	3.3×10 ⁻⁷	-52	200
-	poly(PEGM)	-	-	23.6	1.2	-	-62	160
-	poly(PhEtM)	-	-	17.1	1.2	-	48	200
-	poly(Napht)	-	-	5.0	1.1	-	111 ⁶	225

¹By ¹H NMR. ²Defined by eq 1.24. ³Obtained by GPC in 0.1M LiTFSI in DMF at 50 °C with PMMA standards calibration. ⁴Obtained by DSC (5 K min⁻¹). ⁵Onset loss temperature obtained by TGA. ⁶Obtained by TMA.

For the row of poly(ILM7X_{128-*r*}-PEGM₁₂₈) DSC investigation revealed the strong influence of counter-cation nature on T_g (Figure 2.15):

T_g (°C): **PIL21A** (PrMe₃N, -29) > **PIL21S** (Bu₄N, -36) > **PIL21I** (BuMeIm, -40) > **PIL21P** (Bu₄P, -52)

Both PILs with ammonium cations exhibited higher glass transition temperatures than **PIL21I**, which contains an imidazolium cation. This can be explained by the greater charge delocalization in the imidazolium cation. A similar trend is observed in ionic liquids¹¹⁹. **PIL21P**, which features a phosphonium cation, demonstrated the lowest T_g of -52°C. This is likely due to the larger atomic radius of phosphorus and the resulting weaker ion pairing compared to nitrogen.

The influence of anion charge delocalization on T_g can be seen when comparing **PIL13** and **PIL21I**, which have the same counter cation, molecular weight, and PEGM:ILM ratio but differ in their anionic groups:

$$T_g(^{\circ}\text{C}): \text{PIL21I} (\text{SO}_3^-, -40) > \text{PIL13} (\text{TFSI}^-, -46)$$

The TFSI anion, with its greater extent of charge delocalization, promotes ions dissociation thereby lowering the glass transition temperature.

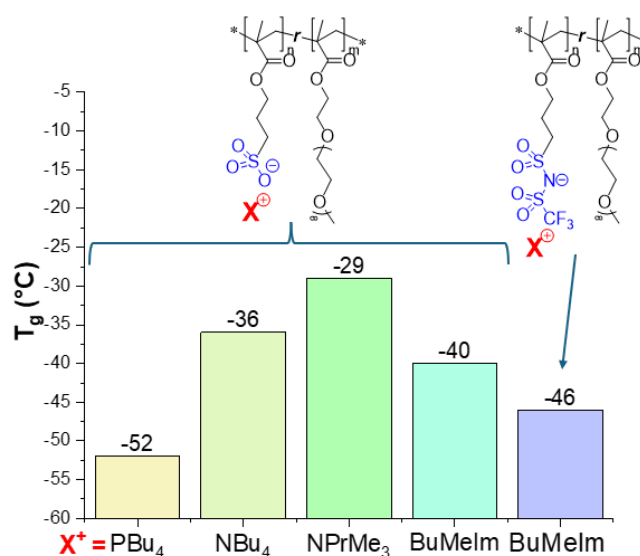


Figure 2.15 Glass transition temperature dependence on counter-cation nature for poly(**ILM7X**₁₂₈-*r*-**PEGM**₁₂₈)

2.2.3.1.2 Block copolymers poly[(ILM_n-*r*-PEGM_m)-*b*-Arm_k]

The DSC investigation of block copolymers revealed that samples with PEGM:ILM ratio 1:1 (Table 2.4, **PIL22**, **PIL24**, **PIL26**, **PIL28**) exhibited 2 glass transition temperatures. The first transition (T_{g1}) was attributed to the glass transition of the ionic random block and the second transition (T_{g2}) occurring above room temperature was assigned to the T_g of neutral blocks. In contrast samples with PEGM:ILM ratio 1:5 (Table 2.4, **PIL23**, **PIL25**, **PIL27**, **PIL29**) presented only the T_{g1} of ionic blocks. This phenomenon is likely connected with the higher plasticization effect in the samples with PEGM:ILM ratio = 1:5 and as a result lower heat response of the second phase transition. It was noticed that for all block copolymers T_{g1} of the ionic random block closely mirrored the T_g of the corresponding

macro-CTAs. Similarly to macro-CTAs (poly(**ILM_n**-*r*-PEGM_m)) increase in PEGM content led to a decrease in T_g .

To discuss the T_g of neutral blocks for all synthesized block copolymers it was decided to switch to thermomechanical analysis (TMA). In contrast to DSC, TMA measures the deformation of the samples under non-oscillating stress, offering greater sensitivity in many cases. Consequently, TMA revealed two glass transition temperatures for all synthesized block copolymers.

Similarly to DSC, T_{g1} coincided with T_g of the corresponding macro-CTAs and was around -40°C for block copolymers with PEGM:ILM ratio 1:1 and around -50°C for samples with higher PEGM content.

T_{g2} of neutral blocks, measured by TMA, in all cases was lower compared to T_g s of poly(PhEtM) and poly(Napht) homopolymers.

T_g (°C): **poly(PhEtM)** (57) > **PIL22** (PhEtM, PEGM:ILM = 1:1, 46) > **PIL23** (PhEtM, PEGM:ILM = 1:5, 44)

T_g (°C): **poly(Napht)** (111) > **PIL24** (Napht, PEGM:ILM = 1:1, 105) > **PIL25** (Napht, PEGM:ILM = 1:5, 85)

T_g (°C): **poly(PhEtM)** (57) > **PIL26** (Napht, PEGM:ILM = 1:1, 45) > **PIL27** (Napht, PEGM:ILM = 1:5, 67)

T_g (°C): **poly(Napht)** (111) > **PIL28** (Napht, PEGM:ILM = 1:1, 81) > **PIL29** (Napht, PEGM:ILM = 1:5, 46)

Except for **PIL26** and **PIL27**, an increase in PEGM content resulted in a decrease in the T_{g2} of the neutral block. This can be explained by the greater degree of plasticization of the neutral block by the ionic block with increased PEGM content.

Moreover, TMA curves revealed the presence of the third distinct transition, attributed to the heat distortion temperature (T_{HDT}) at which noticeable deformation (flow) was observed. This temperature was detected in all block copolymers with ILM:PEGM=1:1 and only in one with ILM:PEGM=1:5 (**PIL29**), varying from 91 to 150°C. Thus, it is reasonable to conclude that T_{HDT} is dependent on PEGM content and, with the exception of **PIL29**, was not visible in block copolymers with ILM= 1:5.

Overall, all three transition temperatures were found to be strongly dependent on the ILM:PEGM ratio. This observation can be summarized as follows: an increase in PEGM content led to (1) a decrease in T_{g1} ; (2) a decrease in T_{g2} (Table 2.4, with the sole exception of the pair **PIL26/PIL27**); (3) the disappearance of T_{HDT} (Table 2.4, with the sole exception of **PIL29**). Furthermore, the existence of two distinct T_g clearly demonstrated the presence of two segregated microphases in all poly[(**ILM_n**-*r*-PEGM_m)-*b*-**Arm_k**] block copolymers.

Table 2.4 Selected properties of poly(**ILM**_n-*r*-PEGM_m) and poly[(**ILM**_n-*r*-PEGM_m)-*b*-**Arm**_k] copolymers

PIL	Polymer structure	PEGM : ILM ¹	T_{g1} , (°C) ²	T_{g2} , (°C) ²	T_{g1} , (°C) ³	T_{g2} , (°C) ³	T_{HDT} , (°C) ³	T_{onset} , (°C) ⁴	σ at 25°C (S cm ⁻¹)	Type of morphology, domain length (nm) ⁵
19	poly(ILM2 ₄₅ - <i>r</i> -PEGM ₄₅)	1.0	-38	-	-	-	-	160	5.7×10 ⁻⁶	-
22	poly[(ILM2 ₄₅ - <i>r</i> -PEGM ₄₅)- <i>b</i> -PhEtM ₉₉]	1.0	-34	36	-33	46	91	170	5.6×10 ⁻⁷	L, 61.2 ± 3.0
23	poly[(ILM2 ₁₇ - <i>r</i> -PEGM ₇₄)- <i>b</i> -PhEMt ₉₉]	4.4	-55	-	-52	44	-	165	2.2×10 ⁻⁶	L, 33.3 ± 0.8
24	poly[(ILM2 ₄₅ - <i>r</i> -PEGM ₄₅)- <i>b</i> -Napht ₉₀]	1.0	-40	109	-37	105	147	190	1.9×10 ⁻⁷	L, ⁻⁷
25	poly[(ILM2 ₁₇ - <i>r</i> -PEGM ₇₄)- <i>b</i> -Napht ₉₉]	4.4	-50	-	-48	85	-	180	1.2×10 ⁻⁶	L, 35.7 ± 0.8
12	poly(ILM1 ₄₁ - <i>r</i> -PEGM ₄₅)	1.1	-41	-	-	-	-	165	5.2×10 ⁻⁶	-
26	poly[(ILM1 ₄₁ - <i>r</i> -PEGM ₄₅)- <i>b</i> -PhEtM ₉₄]	1.1	-40	34	-37	45	107	185	2.0×10 ⁻⁶	L, 45.9 ± 1.8
27	poly[(ILM1 ₁₂ - <i>r</i> -PEGM ₆₁)- <i>b</i> -PhEtM ₇₄]	5.1	-51	-	-46	67	-	160	1.6×10 ⁻⁶	L, 36.8 ± 1.4
28	poly[(ILM1 ₄₁ - <i>r</i> -PEGM ₄₅)- <i>b</i> -Napht ₇₇]	1.1	-40	88	-35	81	119	180	1.1×10 ⁻⁶	L, 37.5 ± 2.0
29	poly[(ILM1 ₁₄ - <i>r</i> -PEGM ₇₃)- <i>b</i> -Napht ₈₆]	5.2	-45	-	-42	46	150	180	4.4×10 ⁻⁷	Disordered
	poly(PhEtM) ⁶	-	-	48	-	57	110	200	-	-
	poly(Napht) ⁶	-	-	-	-	111	151	225	-	-
	poly(PEGM) ⁶	-	-62	-	-	-	-	160	-	-

¹By ¹H NMR. ²Obtained by DSC (5 Kmin⁻¹). ³Obtained by TMA. ⁴Onset loss temperature obtained by TGA. ⁵By AFM on block copolymer-coatings, L - lamellar. ⁶For comparison. ⁷Can not be calculated.

2.2.3.2 Onset temperature of weight loss

The thermal degradation behaviour of methacrylate based PILs was further studied via TGA. The weight loss profiles of the polymers, presented in Figure 2.16, revealed a one-step degradation behaviour for all studied samples, with T_{onset} ranging from 160°C to 290 °C.

For random poly(ILM_n-*r*-PEGM_m) containing ILM2 and ILM1 units, the T_{onset} values were strongly influenced by the presence of PEGM in the polymer chain (Figure 2.16, a). While the homopolymers poly(ILM1) and poly(ILM2) showed close onset weight loss temperatures of 275°C and 290°C respectively, all the random copolymerization of ILM1 and ILM2 with PEGM irrespectively of PEGM:ILM ratio led to the formation of copolyelectrolytes with T_{onset} of about 160°C. This was attributed to the thermal degradation oxyethylene chains¹²⁰. This conclusion was further support by the investigation of poly(PEGM) thermal behaviour. In a similar manner, the TGA curve of poly(PEGM) shows sharp decrease of mass at 160°C (Table 2.3).

The variation of counter-cations in poly(ILM7X₁₂₈-*r*-PEGM₁₂₈) had a moderate impact on the thermal stability of the polymers. The relationship between counter-cations and T_{onset} can be succinctly summarized as follows:

T_{onset} (°C): PIL21P (Bu₄P, 200) > PIL21A (PrMe₃N, 195) \approx PIL21S (Bu₄N, 190) = PIL21I (BuMeIm, 190)

It is evident that the transition from TFSI-based PIL13 to sulfonate-based PIL21I resulted in an increase in thermal stability, from 165 to 190°C. Sulfonate-based PILs with ammonium cations (PIL21A, PIL21S) demonstrated a similar level of thermal stability. In contrast, the exchange of the counter-cation from imidazolium to phosphonium led to a significant increase in thermal stability, consistent with existing data on ILs¹²¹ and PILs¹²². Phosphonium-based compounds generally exhibit higher thermal stability compared to their ammonium or imidazolium counterparts.

On next step the thermal properties of poly[(ILM_n-*r*-PEGM_m)-*b*-Arm_k] block copolymers were investigated. The incorporation of neutral blocks into the block copolymer structures led to a modest enhancement of thermal stability by 10-30 degrees. At this, the highest thermal stability has been demonstrated by PIL24 with T_{onset} reaching 190°C (Figure 2.16, c). The overall evolution of thermal stability in poly[(ILM_n-*r*-PEGM_m)-*b*-Arm_k] according to the neutral block nature can be summarized as follows:

T_{onset} (°C): PIL24 (poly[(ILM2₄₅-*r*-PEGM₄₅)-*b*-Napht₉₀], 190) > PIL26 (poly[(ILM1₄₁-*r*-PEGM₄₅)-*b*-PhEtM₉₄], 185) > PIL25 (poly[(ILM2₁₇-*r*-PEGM₇₄)-*b*-Napht₉₉], 180) = PIL28 (poly[(ILM1₄₁-*r*-PEGM₄₅)-*b*-Napht₇₇], 180) = PIL29 (poly[(ILM1₁₄-*r*-PEGM₇₃)-*b*-Napht₈₆], 180)

>PIL22 (poly[(ILM2₄₅-*r*-PEGM₄₅)-*b*-PhEtM₉₉], 170) >PIL23 (poly[(ILM2₁₇-*r*-PEGM₇₄)-*b*-PhEMt₉₉], 165) >PIL27 (poly[(ILM1₁₂-*r*-PEGM₆₁)-*b*-PhEtM₇₄], 160)

It is notable that, with exception of PIL26, ionic block copolymers with poly(Napht) block demonstrated higher thermal stability. This observation was assigned to higher thermal stability of the neat poly(Napht) compared to poly(PhEtM).

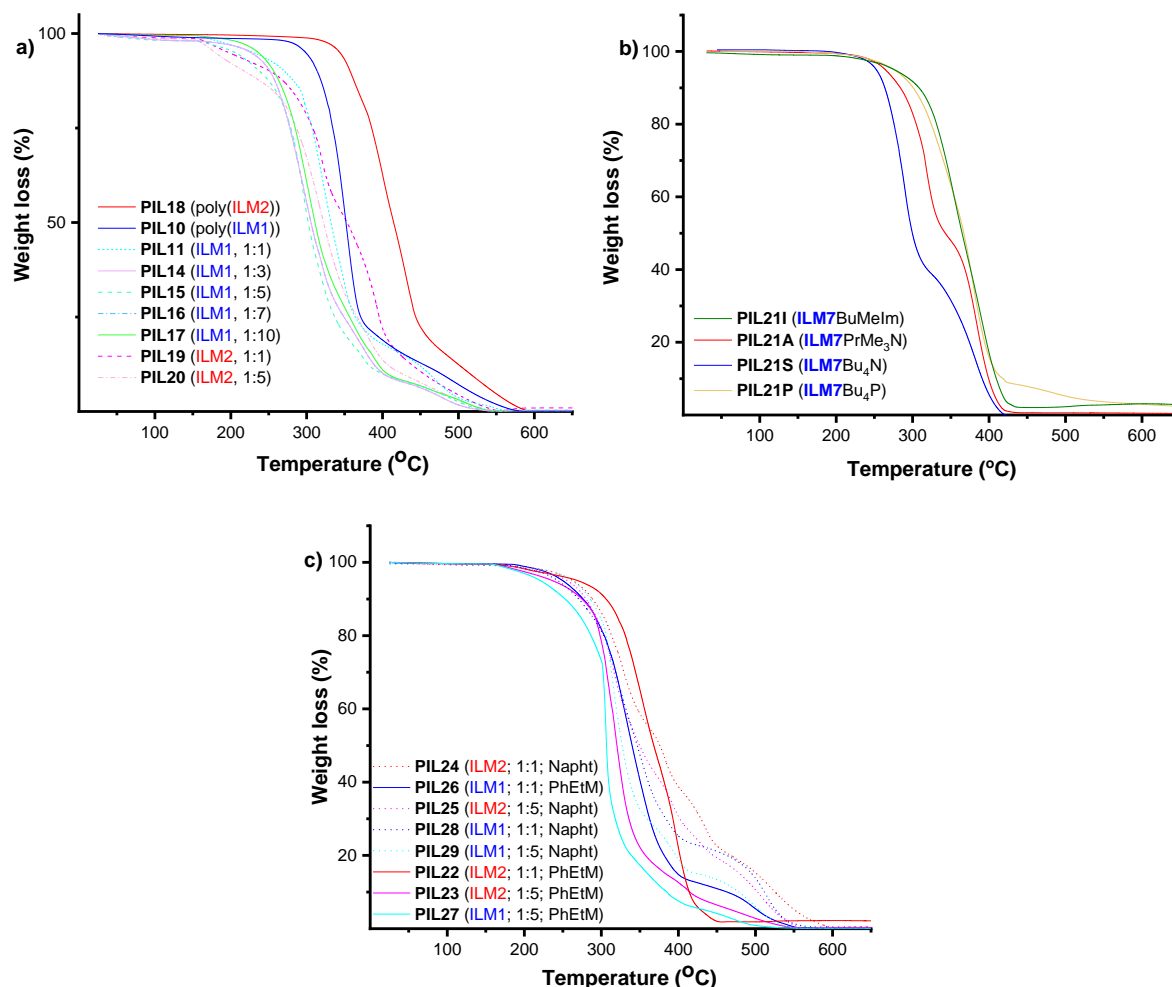


Figure 2.16 TGA traces of poly(ILM_n-*r*-PEGM_m) (a); poly(ILM7X₂₃₈-*r*-PEGM₁₂₈) (b); poly[(ILM_n-*r*-PEGM_m)-*b*-Arm_k] (c) (5°C min⁻¹, under air).

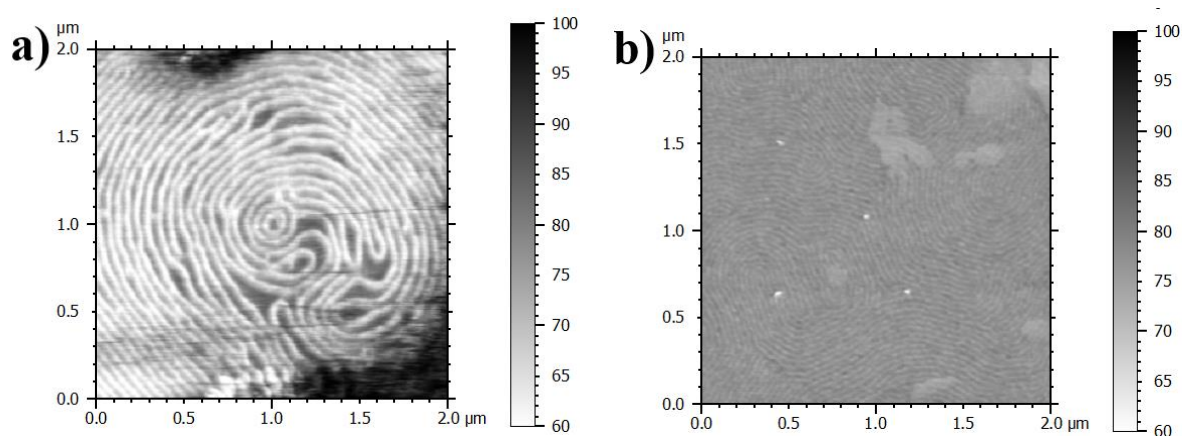
2.2.4 Morphological properties

TMA curves of all poly[(ILM_n-*r*-PEGM_m)-*b*-Arm_k] block copolymers clearly demonstrated the presence of two segregated microphases (see section 2.3.3.1.2). To visualize the block copolymer morphologies, thin films were casted from DMF solutions, then dried at $T > T_{g2}$ to enable polymer reorganization and the achievement of (near-) equilibrium morphologies and later on explored by atomic force microscopy (AFM). Thus, the AFM phase contrast images demonstrated that all block

copolymers, except for poly[(**ILM1**_{14-*r*}-PEGM₇₃)-*b*-Napht₈₆] (**PIL29**), exhibit lamellar morphologies (Figure. 3.17, Table 2.4). **PIL29** does not have any visible phase separation (Figure. 3.17, h), which can be attributed to the significant plasticization of the neutral block by the ionic block. This assumption is supported by the observed T_g value of the neutral poly(Napht) block in **PIL29** (T_g of poly(Napht) = 111°C, while T_{g2} of poly(Napht) block in poly[(**ILM1**_{14-*r*}-PEGM₇₃)-*b*-Napht₈₆] = 46°C, Table 2.4).

Subsequently, the domain length for all block copolymers exhibiting phase separation was measured and found to range between 61.2 and 33.3 nm (Table 2.4). However, it was not possible to determine the domain length for poly[(**ILM2**_{45-*r*}-PEGM₄₅)-*b*-Napht₉₀] because, in this case, the lamellar phase separation occurred parallel to the surface (Figure 2.17, c). Analysing the data, it was found that, the ILM:PEGM ratio had a more significant impact on domain size than the nature of the ionic and neutral monomers. Specifically, the decrease of PEGM content from 1:5 to 1:1 in the ILM:PEGM ratio led to an increase in domain size. For example, transitioning from poly[(**ILM2**_{17-*r*}-PEGM₇₄)-*b*-PhEMt₉₉] to poly[(**ILM2**_{45-*r*}-PEGM₄₅)-*b*-PhEMt₉₉] increased the domain length from 33.3 to 61.2 nm. Similarly, in anionic block copolymers, poly[(**ILM1**_{41-*r*}-PEGM₄₅)-*b*-PhEtM₉₄] had a domain size 15 nm larger than poly[(**ILM1**_{12-*r*}-PEGM₆₁)-*b*-PhEtM₇₄]. Additionally, as previously discussed, poly[(**ILM1**_{14-*r*}-PEGM₇₃)-*b*-Napht₈₆] showed no signs of phase separation, while poly[(**ILM1**_{41-*r*}-PEGM₄₅)-*b*-Napht₇₇] exhibited a lamellar morphology with a domain size of 37.5 nm.

In general, these results can be explained by the compatibility of the PEGM moiety with both ionic fragments and neutral aromatic fragments. Despite the incompatibility of ionic block with PEG side chains and the neutral block in block copolymers, an increase in PEGM content leads to higher plasticization or solubilization of the neutral block, that in its turn resulting in poorer phase separation.



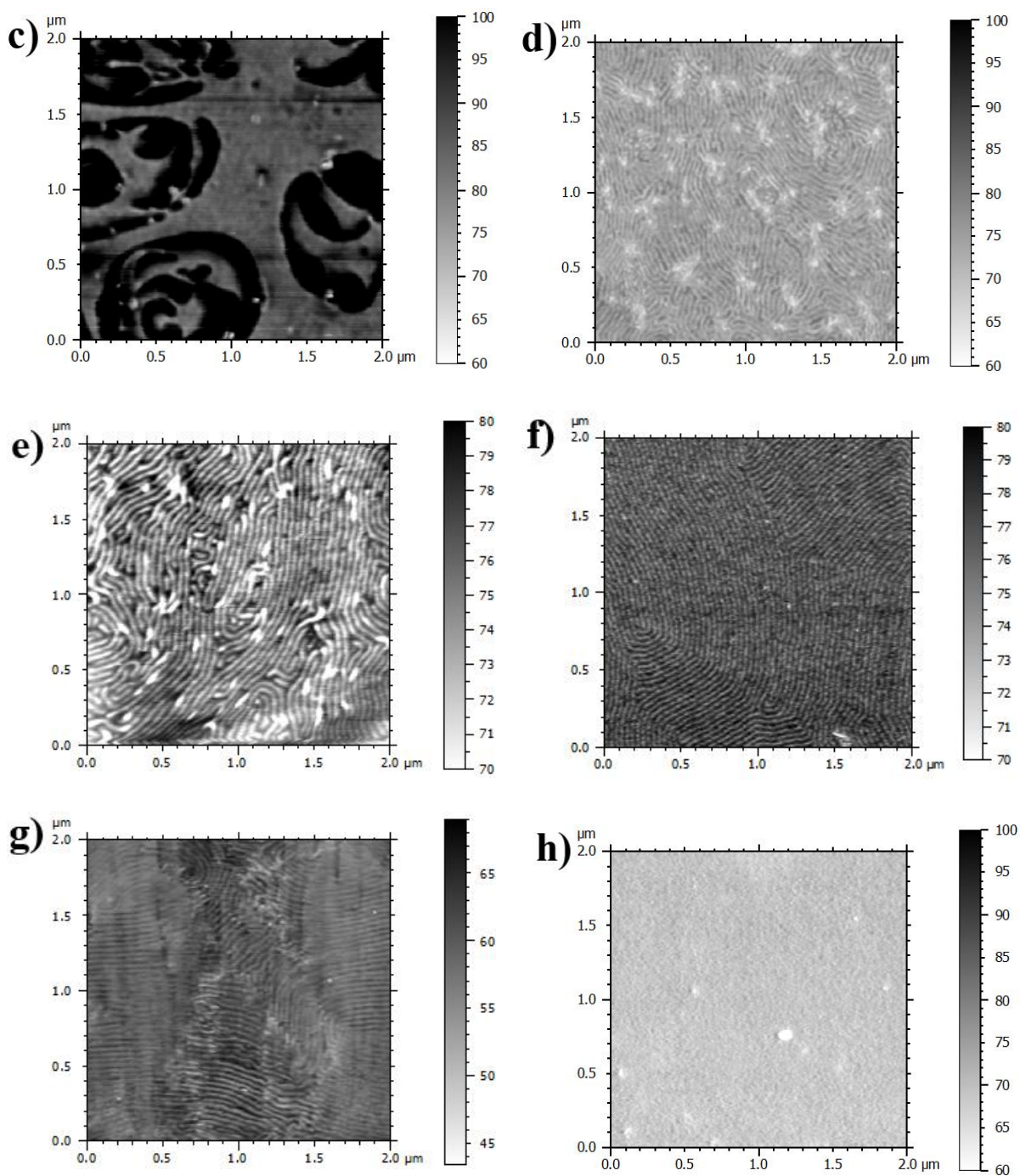


Figure 2.17 AFM images of **PIL22** (a), **PIL23** (b), **PIL24** (c), **PIL25** (d), **PIL26** (e), **PIL27** (f) **PIL28** (g) **PIL29** (h) films.

2.2.5 Electrochemical properties

2.2.5.1 Ionic Conductivity of random copolymers

The investigation of PILs electrochemical properties started from the study of ionic conductivity of random methacrylate-based copolymers. By applying electrochemical impedance spectroscopy (EIS), the following factors affecting ionic conductivity were discovered:

1) ILM:PEGM ratio in poly(ILM_n-r-PEGM_m)

Using **ILM1** monomer, one homopolymer and five random copolymers having the same molecular weight, but differing in PEGM:**ILM1** ratios were prepared. It was discovered that ionic conductivity strongly depends on PEGM content, varying from 1.2×10^{-5} to 3.6×10^{-7} S cm⁻¹ at 25°C (Figure 2.18, a). The overall evolution of ionic conductivity at 25°C according to the PEGM:**ILM1** ratio can be summarized as follows:

σ (25°C, S cm⁻¹): **PIL14** (PEGM:**ILM1**=3.4, 1.2×10^{-5}) > **PIL11** (PEGM:**ILM1**=1.1, 7.5×10^{-6}) > **PIL15** (PEGM:**ILM1**=5.4, 6.6×10^{-6}) > **PIL16** (PEGM:**ILM1**=7.0, 5.2×10^{-6}) > **PIL17** (PEGM:**ILM1**=10.1, 3.9×10^{-6}) >> **PIL10** (poly(**ILM1**₇₄), 3.6×10^{-7})

Taking these data into account it is possible to conclude that PEGM content vs. conductivity dependence passes through the maximum at PEGM:**ILM1** ratio equal to 3.4, which corresponds to **PIL14** (Figure 2.18, a). There are two opposite factors involved in the observed phenomenon. On one side, an increase in PEGM content decreases the glass transition temperature (T_g of poly(PEGM) = -62°C, while T_g of poly(**ILM1**₇₄) = -13°C (see Table 2.3)), thus enhancing ion mobility and ionic conductivity. On the other side, the excessive presence of neutral, non-conductive units reduces the number of conducting species, thereby decreasing overall ionic conductivity. The observed trend was in a full agreement with the data reported for cationic copolymers by Dutta et al.¹²³.

Similarly to anionic PILs, the ionic conductivity is dependent on PEGM content in cationic PILs comprising **ILM2** as well. At 25°C, it varied between 1.2×10^{-5} and 4.4×10^{-7} S cm⁻¹. The observed dependence of ionic conductivity on PEGM content in cationic copolymers can be summarized below:

σ (25°C, S cm⁻¹): **PIL20** (PEGM:**ILM2**=4.7, 1.2×10^{-5}) > **PIL19** (PEGM: **ILM2**=1.0, 5.7×10^{-6}) > **PIL15** (poly(**ILM2**₅₁), 4.4×10^{-7})

For cationic PILs, an increase in PEGM content led to an increase in ionic conductivity, eventually reaching a maximum of 1.2×10^{-5} at PEGM:**ILM2**=4.7 in **PIL20** (Figure 2.18, b). However, it is reasonable to suggest that further increases in PEGM content, similar to anionic PILs, will eventually result in a decrease in ionic conductivity due to the reduction in the number of conducting species.

Overall, the ionic conductivity of both poly(**ILM1**_n-r-PEGM_m) and poly(**ILM2**_n-r-PEGM_m), was 1.5 orders of magnitude higher at 25°C in comparison with the respective homopILs, thus highlighting the positive effect of the introduction of PEGM moiety.

2) Nature of ionic monomer in poly(ILM_n-r-PEGM_m)

It was found that ionic conductivity also depends on the nature of the ionic monomer. In the study of homopolymers, the conductivity of cationic **PIL18** was higher than that of anionic **PIL10**:

$$\sigma (25^{\circ}\text{C}, \text{S cm}^{-1}): \text{PIL18 (poly(ILM2}_{51}), 4.4 \times 10^{-7}) > \text{PIL10 (poly(ILM1}_{74}), 3.6 \times 10^{-7})$$

These results coincide with the data observed for the corresponding ILMs, where the cationic monomer **ILM2** also showed slightly higher conductivity in comparison with the anionic **ILM1** ($\sigma (25^{\circ}\text{C}, \text{S cm}^{-1}): \text{ILM2} (4.1 \times 10^{-4}) > \text{ILM1} (2.4 \times 10^{-4})$), that was explained by the significant difference in their viscosity ($\eta (25^{\circ}\text{C}, \text{cP}): \text{ILM1} (504) > \text{ILM2} (213)$). However, when **ILM1** and **ILM2** were copolymerized with PEGM, the influence of the nature of the ionic monomer became less prominent.

$$\sigma (25^{\circ}\text{C}, \text{S cm}^{-1}): \text{PIL12 (PEGM:ILM1}=1.1, 5.2 \times 10^{-6}) > \text{PIL19 (PEGM:ILM2}=1.0, 5.7 \times 10^{-6})$$

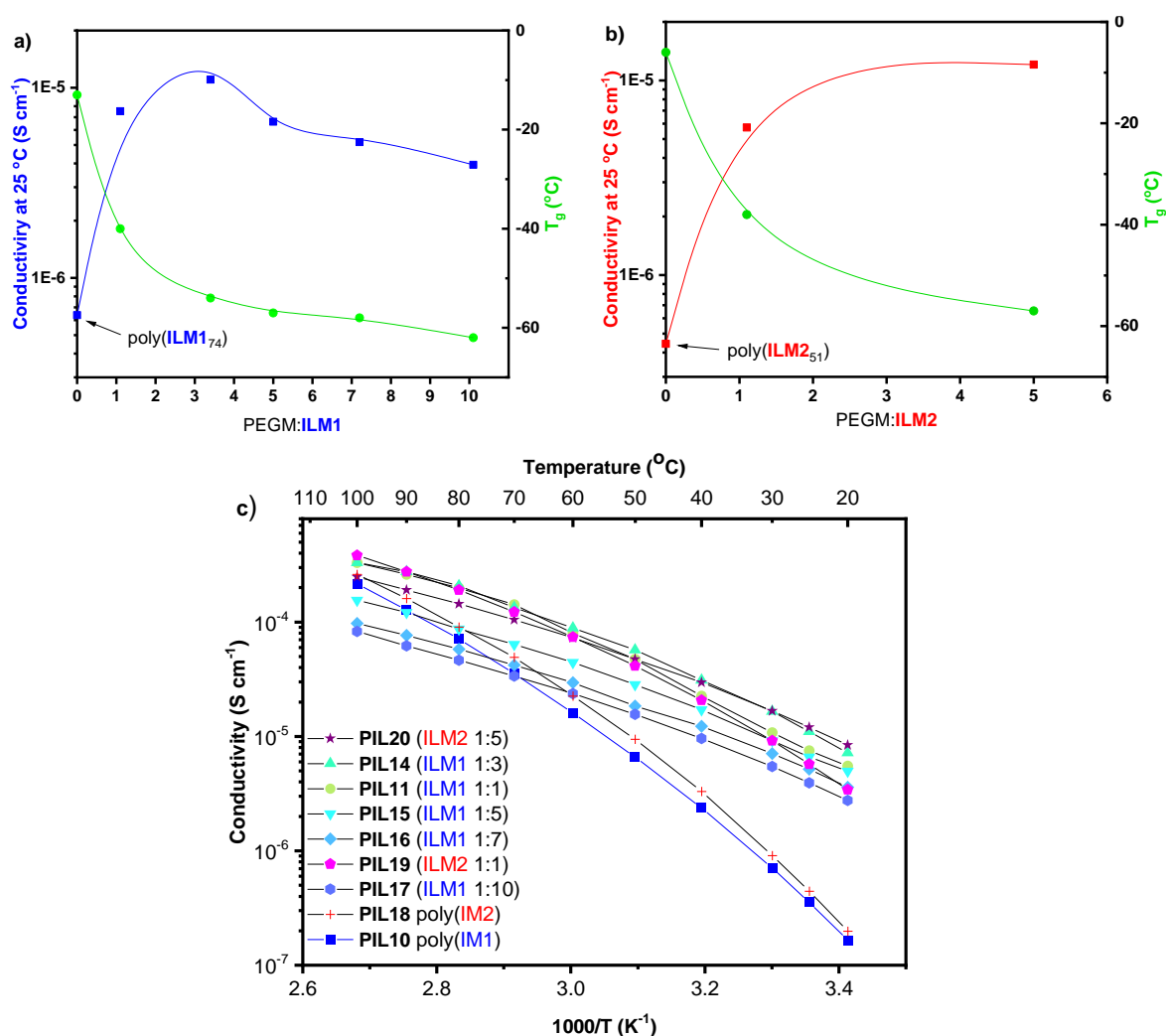


Figure 2.18 Dependence of ionic conductivity at 25°C on the ILM:PEGM ratio in poly(**ILM1**_{n-r}-PEGM_m) (a) and in poly(**ILM2**_{n-r}-PEGM_m) (b). The evolution of ionic conductivity with inverse temperature for poly(**ILM2**_{n-r}-PEGM_m) and poly(**ILM1**_{n-r}-PEGM_m) (c).

3) Anion charge delocalization

The influence of anion charge delocalization can be observed by comparing the ionic conductivity of **PIL13** and **PIL21I**, both having the same counter cation, molecular weight and ILM:PEGM ratio, but differing in the nature of the chemically bonded anions, namely having TFSI or sulfonate moieties:

σ (25°C, S cm⁻¹): **PIL13** (poly(**ILM1BuMeIm**₉₄-*r*-PEGM₁₀₃), TFSI, 5.9×10⁻⁶) > **PIL21I** (poly(**ILM7BuMeIm**₁₂₈-*r*-PEGM₁₂₈), SO₃, 1.9×10⁻⁶)

It is evident that the introduction of the more delocalized TFSI group increases the ionic conductivity by approximately half an order of magnitude. This result aligns with data presented in the literature for sulfonate and TFSI-based ILs¹¹⁹ and anionic PILs¹⁰.

4) Counter cation nature

A significant effect of counter cation on ionic conductivity was observed in sulfonate-based poly(**ILM7X**₁₃₈-*r*-PEGM₁₂₈) copolymers (Figure 2.19). The overall variation of counter-cations improved the conductivity by 2 orders of magnitude, namely from 9.0×10⁻⁸ to 1.9×10⁻⁶ S cm⁻¹ at 25 °C. The results can be summarized in the following decreasing order:

σ (25°C, S cm⁻¹): **PIL21I** (BuMeIm, 1.9×10⁻⁶) > **PIL21A** (PrMe₃N, 4.8×10⁻⁷) > **PIL21P** (Bu₄P, 3.3×10⁻⁷) > **PIL21S** (Bu₄N, 9.0×10⁻⁸)

Firstly, the transition from ammonium cation in **PIL21S** to phosphonium cation in **PIL21P** resulted in an improvement in ionic conductivity by half an order of magnitude thus highlighting the influence of the charged heteroatom in the cation. This can be explained by more diffused electron density of phosphorus compared to nitrogen and, as a result, lower binding energy within the ion pair.

Secondly, the change of symmetry in the ammonium cation from symmetric tetrabutylammonium (**PIL21S**) to asymmetric trimethylpropylammonium (**PIL21A**) led to 1.5 orders of magnitude increase in ionic conductivity. This effect of the improvement of conductivity by the application of asymmetric anions is known in literature for ILs^{119,124}, and appears due to the disruption of ions packing, decrease in viscosity and as a result increase in ions mobility.

Lastly, the introduction of the more delocalized imidazolium cation (**PIL21I**) compared to ammonium and phosphonium cations resulted in two orders of magnitude rise in ionic conductivity. This striking improvement can also be explained by decreased ions interactions and respectively by enhanced ion mobility.

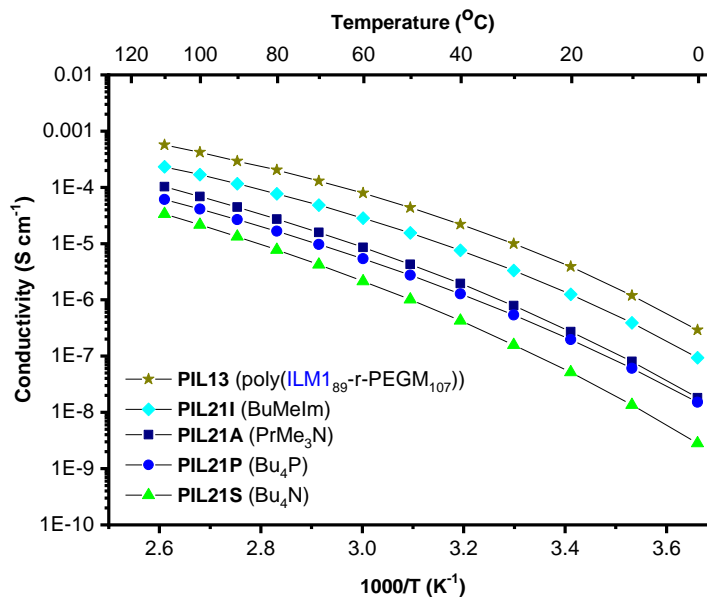


Figure 2.19 Evolution of ionic conductivity with inverse temperature for poly(**ILM7X**₂₃₈-*r*-PEGM₁₂₈).

5) Molecular weight

To investigate the influence of molecular weight on ionic conductivity three anionic poly(**ILM1**_{*n*}-*r*-PEGM_{*m*}) copolymers with fixed PEGM:ILM ratio and variable molar masses were synthesized. The obtained results at 25°C can be summarized in the following order:

σ (25°C, S cm⁻¹): **PIL11** (32.1 kDa, 7.5×10^{-6}) > **PIL13** (42.3 kDa, 5.9×10^{-6}) \approx **PIL12** (96.5 kDa, 5.2×10^{-6})

Although, the slight increase in conductivity was noticed for **PIL11**, it can be concluded that, within this *M_n* range, the ionic conductivity is nearly independent from the molecular weight.

6) Temperature

The ionic conductivity of poly(**ILM1**_{*n*}-*r*-PEGM_{*m*}), poly(**ILM7X**₂₃₈-*r*-PEGM₁₂₈) and poly(**ILM2**_{*n*}-*r*-PEGM_{*m*}) was measured as a function of inverse temperature in the range between 0 or 20 and 100°C (Figures 3.18, c and 3.19). For all PILs the observed conductivity increased with increasing temperature. At this, the temperature dependence did not follow the linear Arrhenius behaviour. This can be explained by the fact that the ions diffusion occurs via two different mechanisms: (1) hopping of the free ions between chemically bonded charges and (2) local segmental motion of polymer chains.

Overall, the charge delocalization in both cations and anions, along with the presence of short dangling PEO chains in the (co)polymer structure, were the factors mostly contributing to the

improvement in ionic conductivity. Specifically, at 25°C both anionic and cationic PEGM copolymers showed 1.5 orders of magnitude increase in ionic conductivity in comparison with respective homopolymers reaching an outstanding value of $1.2 \times 10^{-5} \text{ S cm}^{-1}$ (**PIL14**, **PIL20**, Table 2.3). At the same time, the transition from localized tetrabutylammonium cation to the more delocalized imidazolium cation in the series of poly(**ILM7X**₂₃₈-*r*-PEGM₁₂₈) copolymers resulted in a 2 orders of magnitude increase in ionic conductivity.

2.2.5.2 Ionic Conductivity of block copolymers

On the next step the ionic conductivity in methacrylic block copolymers (poly[(**ILM**_n-*r*-PEGM_m)-*b*-**Arm**_k]) was investigated (Figure 2.20, a). The obtained values varied between 2.2×10^{-6} and $1.9 \times 10^{-7} \text{ S cm}^{-1}$, predominantly maintaining the same order of magnitude as the parent poly(**ILM**_n-*r*-PEGM_m) block. The following parameters affecting the ionic conductivity of block copolymers could be further highlighted:

- 1) PEGM:ILM ratio in poly[(**ILM**_n-*r*-PEGM_m)-*b*-**Arm**_k] and 2) the nature of ionic monomer

Similarly to random poly(**ILM**_n-*r*-PEGM_m) copolymers, the ionic conductivity of poly[(**ILM**_n-*r*-PEGM_m)-*b*-**Arm**_k] block copolymers was found to be dependent on PEGM:ILM ratio (Figure 2.20, a). For anionic [poly[(**ILM1**_n-*r*-PEGM_m)-*b*-**Arm**_k] block copolymers, independently of the neutral block nature, the polymers with PEGM:ILM=1:1 ratio in the ionic block showed slightly higher ionic conductivity than those having PEGM:ILM=1:5 ratio:

σ (25°C, S cm^{-1}): **PIL26** (poly[(**ILM1**₄₁-*r*-PEGM₄₅)-*b*-PhEtM₉₄], 2.0×10^{-6}) > **PIL27** (poly[(**ILM1**₁₂-*r*-PEGM₆₁)-*b*-PhEtM₇₄], 1.6×10^{-6})

σ (25°C, S cm^{-1}): **PIL28** (poly[(**ILM1**₄₁-*r*-PEGM₄₅)-*b*-Napht₇₇], 1.1×10^{-6}) > **PIL29** (poly[(**ILM1**₁₄-*r*-PEGM₇₃)-*b*-Napht₈₆], 4.4×10^{-7})

Unexpectedly, the cationic poly[(**ILM2**_n-*r*-PEGM_m)-*b*-**Arm**_k] block copolymers showed the reverse dependence:

σ (25°C, S cm^{-1}): **PIL23** (poly[(**ILM2**₁₇-*r*-PEGM₇₄)-*b*-PhEMt₉₉], 2.2×10^{-6}) > **PIL22** (poly[(**ILM2**₄₅-*r*-PEGM₄₅)-*b*-PhEtM₉₉], 5.6×10^{-7})

σ (25°C, S cm^{-1}): **PIL25** (poly[(**ILM2**₁₇-*r*-PEGM₇₄)-*b*-Napht₉₉], 1.2×10^{-6}) > **PIL24** (poly[(**ILM2**₄₅-*r*-PEGM₄₅)-*b*-Napht₉₀], 1.9×10^{-7})

Such behaviour can be explained by the similar conductivity trend observed for corresponding ionic random copolymers (for clarity see Figure 2.18, a).

- 3) The nature of the neutral block

The influence of neutral block's nature in poly[(**ILM**_n-*r*-PEGM_m)-*b*-**Arm**_k] block copolymers on ionic conductivity can be summarised as follows:

σ (25°C, S cm⁻¹): **PIL26** (poly[(**ILM1**₄₁-*r*-PEGM₄₅)-*b*-**PhEtM**₉₄], 2.0×10^{-6}) \approx **PIL28** (poly[(**ILM1**₄₁-*r*-PEGM₄₅)-*b*-**Napht**₇₇], 1.1×10^{-6}) $>$ **PIL22** (poly[(**ILM2**₄₅-*r*-PEGM₄₅)-*b*-**PhEtM**₉₉], 5.6×10^{-7}) $>$ **PIL24** (poly[(**ILM2**₄₅-*r*-PEGM₄₅)-*b*-**Napht**₉₀], 1.9×10^{-7})

σ (25°C, S cm⁻¹): **PIL23** (poly[(**ILM2**₁₇-*r*-PEGM₇₄)-*b*-**PhEMt**₉₉], 2.2×10^{-6}) \approx **PIL27** (poly[(**ILM1**₁₂-*r*-PEGM₆₁)-*b*-**PhEtM**₇₄], 1.6×10^{-6}) \approx **PIL25** (poly[(**ILM2**₁₇-*r*-PEGM₇₄)-*b*-**Napht**₉₉], 1.2×10^{-6}) $>$ **PIL29** (poly[(**ILM1**₁₄-*r*-PEGM₇₃)-*b*-**Napht**₈₆], 4.4×10^{-7})

Based on this data it can be concluded that block copolymers with a poly(PhEtM) block exhibit higher ionic conductivity than those with a poly(Napht) block. This can be explained by the fact that, in the case of [(**ILM**_n-*r*-PEGM_m)-*b*-**PhEtM**_k], the high plasticization of the poly(PhEtM) by the ionic block causes a decrease in the T_{g2} of the neutral block (T_g of poly(PhEtM) = 48°C, while T_{g2} of poly(PhEtM) block in poly[(**ILM1**₄₁-*r*-PEGM₄₅)-*b*-**PhEtM**₉₄] = 36°C, Table 2.4) bringing it closer to the measurement temperature and thus increasing ionic conductivity. Although the plasticization effect is also visible in [(**ILM**_n-*r*-PEGM_m)-*b*-**Napht**_k], the T_{g2} of the poly(Napht) block still remains far from 25°C.

Ionic conductivity of poly[(**ILM**_n-*r*-PEGM_m)-*b*-**Arm**_k] was measured as a function of inverse temperature in the range between 20 and 100°C (Figure 2.20, b). Similarly to random copolymers, the ionic conductivity in block copolymers increased with increasing temperature and the temperature dependence was not following the Arrhenius behaviour.

Overall, while the transition from random copolymers to ionic block copolymers resulted in a slight decrease in ionic conductivity, it significantly enhanced their mechanical properties, as will be discussed in section 2.2.7

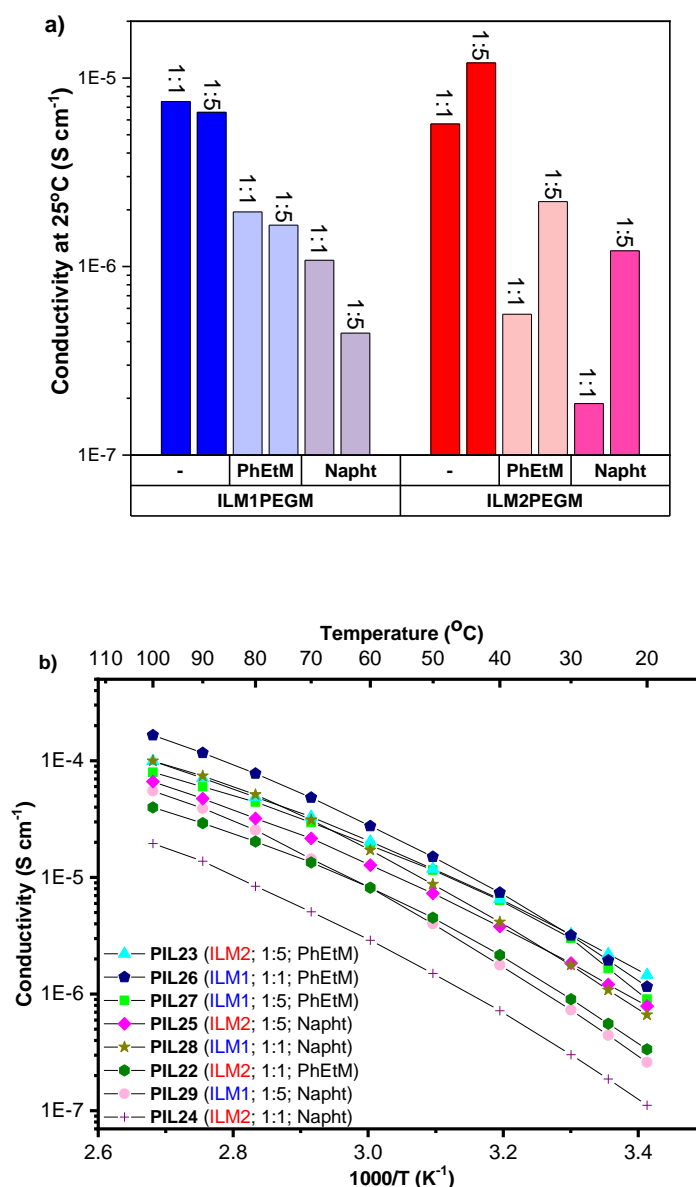


Figure 2.20 Dependence of ionic conductivity at 25°C on the structure of poly[(ILM_n-*r*-PEGM_m)-*b*-Arm_k] (a), evolution of ionic conductivity with inverse temperature for poly[(ILM_n-*r*-PEGM_m)-*b*-Arm_k] (b).

2.2.6 Electrochemical stability

Furthermore, the electrochemical stability limits of selected methacrylate based PILs were assessed via cyclic voltammetry. Figure 2.21 (a, b) shows the anodic and cathodic scans of anionic **PIL12** and cationic **PIL19** at 25 °C. The oxidation potential for **PIL19** was found to be higher than that of **PIL12** reaching the value of 2.6 V vs Ag⁺/Ag. Contrary, the reduction potential of **PIL12** was lower than of **PIL19**: -2.1 vs -1.2 V, respectively. The overall evolution of electrochemical stability of random methacrylate PILs can be summarized as follows:

ESW (25°C, V): **PIL12** (4.4) > ESW **PIL19** (3.8)

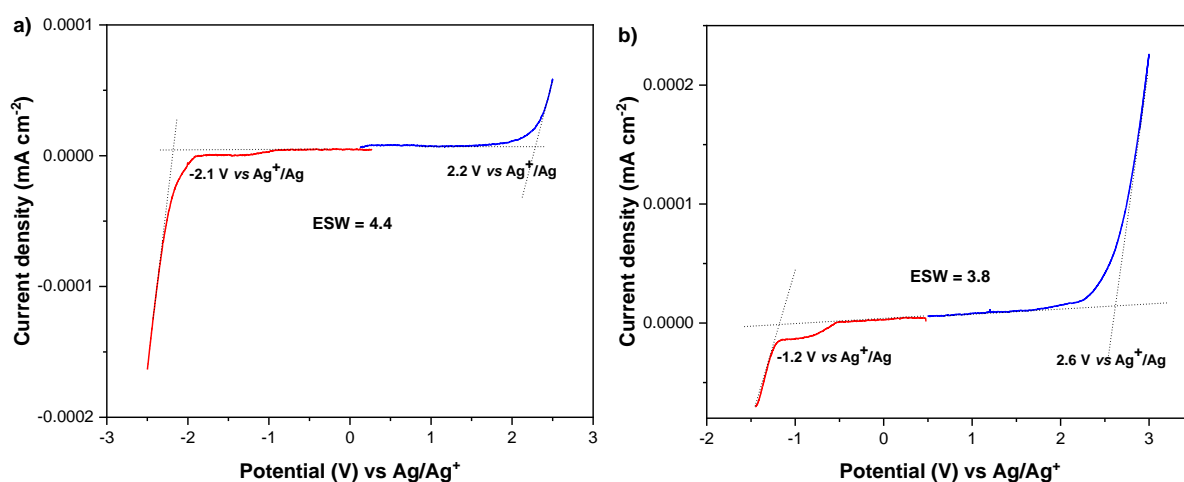


Figure 2.21 Electrochemical stability window for poly(**ILM1**₄₁-*r*-PEGM₄₅) (a), poly(**ILM2**₄₅-*r*-PEGM₄₅) (b) at 25 °C (Pt foils as the working and counter electrodes and Ag mesh as the reference electrode, scan rate 5 mV s⁻¹).

2.2.7 Rheological properties

The rheological properties of methacrylate-based PILs were investigated by small amplitude oscillatory shear (SAOS) rheology at temperatures ranging from -30 to 75°C. Master curves were built through time-temperature superposition (TTS) using $T_0 = 25^\circ\text{C}$ as reference temperature (Figure 2.22, a-c). The shift factors a_T used in the TTSs were determined and it was verified that they present a temperature dependence that follows the WLF equation¹¹³ (Figure 2.22, d and e).

First, the viscoelastic behavior of methacrylate-based PILs was studied. Random poly[(**ILM**_{*n*}-*r*-PEGM_{*m*})] copolymers based on **ILM1** and **ILM2** displayed viscoelastic behavior typical of unentangled polymer chains with terminal regimes evidenced by the evolution of loss (G'') and storage (G') moduli following ω^1 and ω^2 slopes, respectively (Figure 2.22, a and b). This behavior was observed over a range of frequencies at 25°C, confirming that poly(**ILM1**_{*n*}-*r*-PEGM_{*m*}) and poly(**ILM2**_{*n*}-*r*-PEGM_{*m*}) are cold flowing fluids at room temperature.

The terminal regime was also observed for all random poly(**ILM7X**₂₃₈-*r*-PEGM₁₂₈) copolymers with sulfonate group, however it was shifted to a low frequencies region compared to poly(**ILM1**_{*n*}-*r*-PEGM_{*m*}) (Figure 2.22, c). It is noteworthy that the magnitude of this shift depended on the structure of the counter cation and correlated with the T_g values for these copolymers. The results aligned with the visual appearance of poly(**ILM7X**₂₃₈-*r*-PEGM₁₂₈) copolymers which appeared as much more viscous cold flowing rubber materials in comparison to poly(**ILM1**_{*n*}-*r*-PEGM_{*m*}).

In contrast, the terminal regime was not observed for poly[(**ILM**_{*n*}-*r*-PEGM_{*m*})-*b*-**Arm**_{*k*}] block copolymer. Across the entire temperature range, these block copolymers predominantly remained in the

transition region. Additionally, some samples exhibited a plateau at elevated temperatures ($>25^{\circ}\text{C}$) which was associated with phase separation or PIL auto-organization. This behavior is exemplified in Figure 2.22 (a, b) for **PIL24** and **PIL28**. The viscoelastic properties of these block copolymers corresponded to their physical appearance, as they manifested as rubbery solid materials capable of withstanding a load of 10 g without deformation.

Next, simplified investigation of PIL's storage moduli at 25°C and 1 rad s^{-1} was conducted. For random poly[(**ILM**_n-*r*-PEGM_m) copolymers based on **ILM1** and **ILM2** the observed storage moduli were below 1 kPa (Figure 2.22, a-b), which was the lowest among investigated methacrylate PILs. In turn, random poly(**ILM7MeBuIm**₂₃₈-*r*-PEGM₁₂₈) copolymer, comprising localized sulfonate group, showed nearly six times increase of the storage modulus (from 0.5 kPa for poly[(**ILM1**₉₄-*r*-PEGM₁₀₃) to 2.9 kPa for poly(**ILM7MeBuIm**₂₃₈-*r*-PEGM₁₂₈) (Figure 2.22, a-b)

The successive investigation of the storage modulus in series of poly(**ILM7X**₂₃₈-*r*-PEGM₁₂₈) copolymers allowed to establish the following structure/mechanical properties dependencies:

1) Storage modulus vs counter cation nature

The storage modulus for poly(**ILM7X**₂₃₈-*r*-PEGM₁₂₈) was found to be strongly dependent on counter-cation nature and the observed trend can be summarized as follows:

G' (25°C ; 1 rad s^{-1} ; kPa): **PIL21S** (Bu₄N, 18.6) \approx **PIL21A** (PrMe₃N, 16.5) $>$ **PIL21P** (Bu₄P, 3.1) $>$ **PIL21I** (BuMeIm, 2.9)

While polymers with ammonium cation showed the storage modulus around 20 kPa polymers with imidazolium and phosphonium cations exhibited the values around 3 kPa. This tendency correlates with the values of their glass transition temperatures and can be explained by the cation charge delocalization and its symmetry, that effect the chains packing density and the interaction between ionic pairs (see section 2.2.3.1.1).

2) Storage modulus vs anion charge delocalization

As it was mentioned above, the beneficial effect of anion charge localization on mechanical properties of PILs can be seen by comparing **PIL13** with **PIL21I**, both having the same counter cation and ILM:PEGM ratio, but differ by charge delocalization at TFSI and sulfonate anions:

G' (25°C ; 1 rad s^{-1} ; kPa): **PIL21I** (SO₃BuMeIm, 2.9) $>$ **PIL13** (TFSIBuMeIm, 0.5)

The investigation of poly[(**ILM**_n-*r*-PEGM_m)-*b*-**Arm**_k] block copolymers, revealed (Figure 2.22, a-b) that they exhibit a significantly higher storage modulus compared to random poly[(**ILM**_n-*r*-PEGM_m) and poly(**ILM7X**₂₃₈-*r*-PEGM₁₂₈) copolymers. Overall, the observed storage modulus values

for poly[(**ILM**_{n-r}-PEGM_m)-*b*-**Arm**_k] block copolymers varied in the range between 82.1 and 1679.9 kPa and the following factors affecting the storage modulus can be distinguished:

1) PEGM:ILM ratio

In the case of anionic poly[(**ILM**₁_{n-r}-PEGM_m)-*b*-**Arm**_k] block copolymers the increase in PEGM:ILM ratio from 1:1 to 1:5 was leading to a decrease in mechanical properties:

G' (25°C; 1 rad s⁻¹; kPa): **PIL28** (poly[(**ILM**₁_{41-r}-PEGM₄₅)-*b*-Napht₇₇], 517.9) > **PIL29** (poly[(**ILM**₁_{14-r}-PEGM₇₃)-*b*-Napht₈₆], 170.8)

Contrary, for cationic poly[(**ILM**₂_{n-r}-PEGM_m)-*b*-**Arm**_k], the opposite trend was discovered on all compared pairs:

G' (25°C; 1 rad s⁻¹; kPa): **PIL23** (poly[(**ILM**₂_{17-r}-PEGM₇₄)-*b*-PhEMt₉₉], 1615.8) > **PIL22** (poly[(**ILM**₂_{45-r}-PEGM₄₅)-*b*-PhEtM₉₉], 512.2)

G' (25°C; 1 rad s⁻¹; kPa): **PIL25** (poly[(**ILM**₂_{17-r}-PEGM₇₄)-*b*-Napht₉₉], 1679.9) > **PIL24** (poly[(**ILM**₂_{45-r}-PEGM₄₅)-*b*-Napht₉₀], 492.8)

2) The nature of the ionic monomer

The influence of ionic monomer nature on mechanical properties can be summarized as follows:

G' (25°C; 1 rad s⁻¹; kPa): **PIL28** (poly[(**ILM**₁_{41-r}-PEGM₄₅)-*b*-Napht₇₇], 517.9) > **PIL24** (poly[(**ILM**₂_{45-r}-PEGM₄₅)-*b*-Napht₉₀], 492.8)

G' (25°C; 1 rad s⁻¹; kPa): **PIL25** (poly[(**ILM**₂_{17-r}-PEGM₇₄)-*b*-Napht₉₉], 1679.9) > **PIL29** (poly[(**ILM**₁_{14-r}-PEGM₇₃)-*b*-Napht₈₆], 170.8)

G' (25°C; 1 rad s⁻¹; kPa): **PIL23** (poly[(**ILM**₂_{17-r}-PEGM₇₄)-*b*-PhEtM₉₉], 1615.8) > **PIL27** (poly[(**ILM**₁_{12-r}-PEGM₆₁)-*b*-PhEtM₇₄], 82.1)

3) The nature of the neutral block

It was found that at 25°C, the nature of the neutral block was affecting the mechanical properties of block copolymers at a lesser extent than at elevated temperatures (≥45°C). The higher was the temperature the greater was the observed difference in the mechanical properties of block copolymers with different neutral blocks.

At 25°C the following comparison can be done:

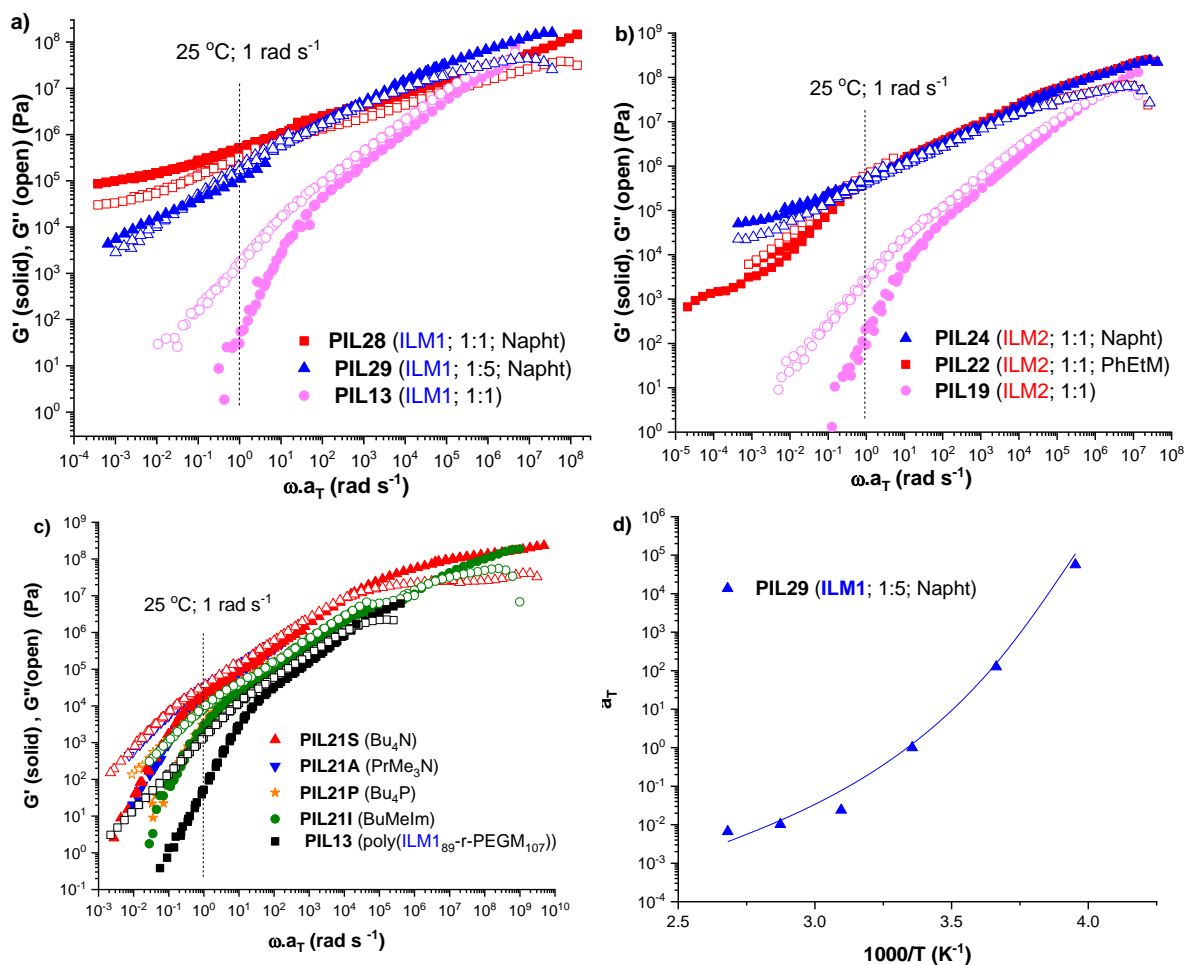
G' (25°C; 1 rad s⁻¹; kPa): **PIL29** (poly[(**ILM**₁_{14-r}-PEGM₇₃)-*b*-Napht₈₆], 170.8) > **PIL27** (poly[(**ILM**₁_{12-r}-PEGM₆₁)-*b*-PhEtM₇₄], 82.1)

G' (25°C; 1 rad s⁻¹; kPa): **PIL25** (poly[(**ILM2**₁₇-*r*-PEGM₇₄)-*b*-Napht₉₉], 1679.9) > **PIL23** (poly[(**ILM2**₁₇-*r*-PEGM₇₄)-*b*-PhEtM₉₉], 1615.8)

G' (25°C; 1 rad s⁻¹; kPa): **PIL22** (poly[(**ILM2**₄₅-*r*-PEGM₄₅)-*b*-PhEtM₉₉], 512.2) > **PIL24** (poly[(**ILM2**₄₅-*r*-PEGM₄₅)-*b*-Napht₉₀], 492.8)

In general, block copolymers with poly(Napht) block showed higher mechanical performance in comparison with their poly(PhEtM) based analogues. This behavior can be explained by the fact that poly(PhEtM) block in poly[(**ILM**_{*n*}-*r*-PEGM_{*m*})-*b*-PhEtM_{*k*}] block copolymers shows the T_g of 36°C, that is very close to the temperature of storage modulus investigation (25°C) and results in its partial softening. While the poly(Napht) block in poly[(**ILM**_{*n*}-*r*-PEGM_{*m*})-*b*-Napht_{*k*}] block copolymer demonstrates a T_g of >80°C, that being far above the examination temperature (25 °C) allows it to perfectly reinforce the material.

To sum up, it is worth noting that the complex dependence of mechanical properties on the structure of poly[(**ILM**_{*n*}-*r*-PEGM_{*m*})-*b*-Arm_{*k*}] block copolymers can be explained by the interconnected nature of all the aforementioned factors, which collectively influence the storage modulus.



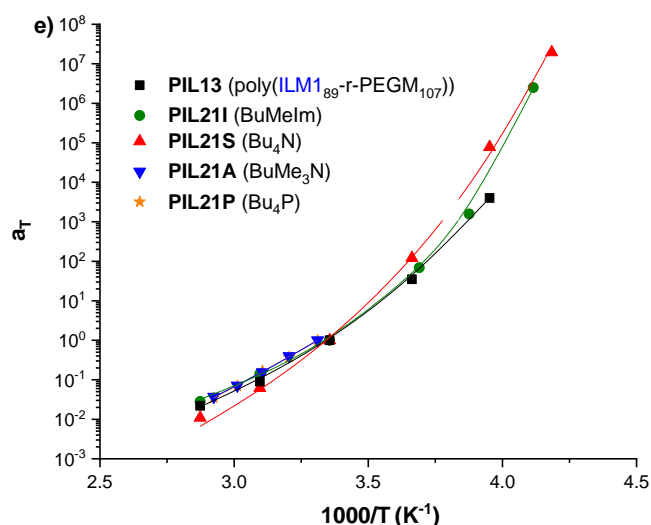


Figure 2.22 TTS master curves of poly[(**ILM1**_n-*r*-PEGM_m)] and poly[(**ILM1**_n-*r*-PEGM_m)-*b*-**Arm**_k] (a), TTS master curves of poly[(**ILM2**_n-*r*-PEGM_m)] and poly[(**ILM2**_n-*r*-PEGM_m)-*b*-**Arm**_k] (b), TTS master curves of poly(**ILM7X**₁₃₁-*r*-PEGM₁₃₁) (c) obtained by frequency sweep experiments performed from –30 to 75 °C and referenced at T₀ = 25 °C. Corresponding a_T shift factors and WLF best fits at T₀ = 25 °C for **PIL29** (d), and poly(**ILM7X**₁₃₁-*r*-PEGM₁₃₁) (e).

2.3 Epichlorohydrin-derived PILs prepared by chemical modification of a neutral polymer (PIL30-PIL37)

The last family of polymers, comprising twelve cationic PILs, was synthesized through a straightforward modification of a commercially available poly(epichlorohydrin-co-ethylene oxide) copolymer. This modification involved the incorporation of various N-substituted imidazoles, followed by ion metathesis reactions. The variation in substituents allowed for the investigation of the side chain's influence on the properties of the TFSI based PILs and the identification of the best-performing polymer in terms of ionic conductivity. Subsequently, the most highly conducting PIL underwent ion metathesis with various salts containing symmetric and asymmetric anions, enabling the exploration of the dependence of PIL properties on different counter-anions (Figure 2.23).

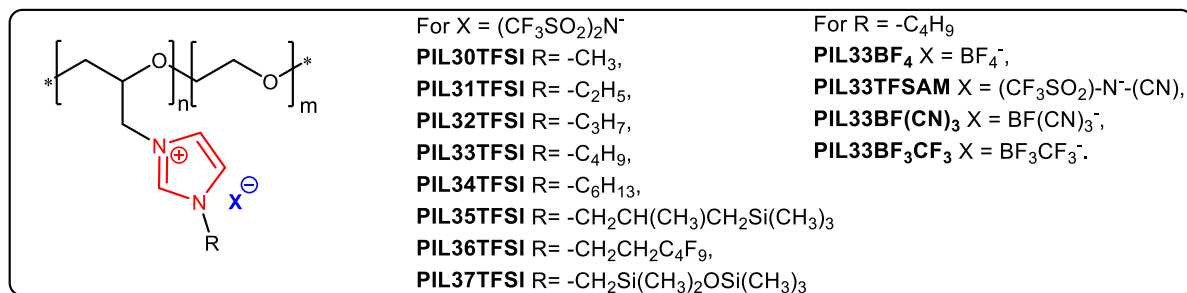
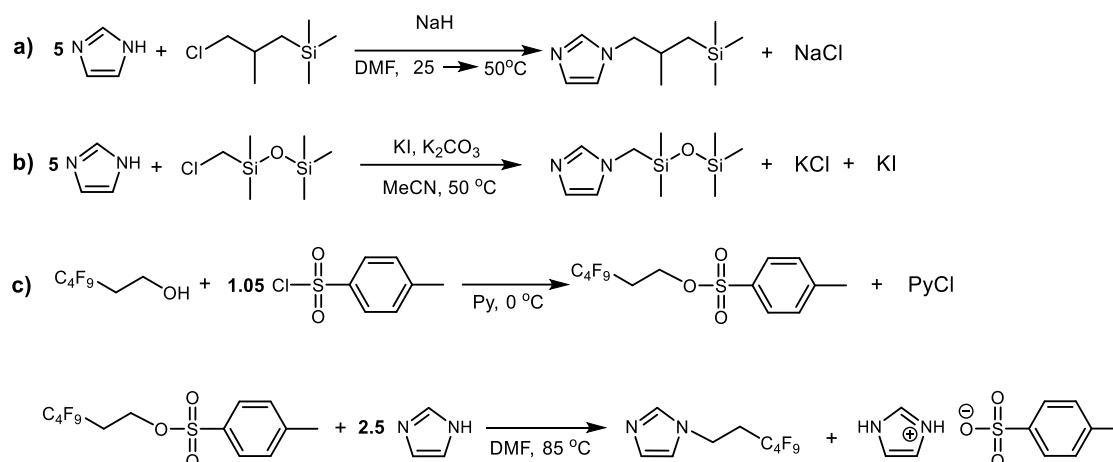


Figure 2.23 Epichlorohydrin-derived PILs

2.3.1 Synthesis and characterization

2.3.1.1 Synthesis of mono N-substituted imidazoles



Scheme 2.6 Synthetic pathways for the preparation of N-substituted imidazoles

The research on this family of polyelectrolytes began with the choice or design of N-substituted imidazoles. Firstly, a series of N-alkyl substituted imidazoles was selected to investigate the influence of alkyl side chain and its length on the ionic conductivity of the resultant PILs. All of the applied N-alkyl imidazoles, namely N-methyl-, N-ethyl-, N-propyl-, N-butyl- and N-hexylimidazoles were obtained from commercial sources.

Secondly, the N-(2-methyl-3-(trimethylsilyl)propyl) imidazole, N-((1,1,3,3,3-pentamethyldisiloxanyl)methyl) imidazole and N-(3,3,4,4,5,5,6,6,6-nonafluorohexyl) imidazole were chosen to study the effect of silyl-based, siloxane and perfluorinated side chains or in the other words the influence of the various heteroatomic chains. These N-substituted imidazoles were synthesized in accordance with the developed pathways depicted on Scheme 2.6 and their synthesis will be described in details below.

The synthesis of N-(2-methyl-3-(trimethylsilyl)propyl) imidazole consisted in two reaction steps: deprotonation of imidazole with NaH in DMF and subsequent alkylation of sodium imidazol-1-ide with (3-chloro-2-methylpropyl)-trimethylsilane (Scheme 2.6, a). The isolation of the product and its purification via extraction method provided a yellowish liquid in nearly quantitative yield (94%).

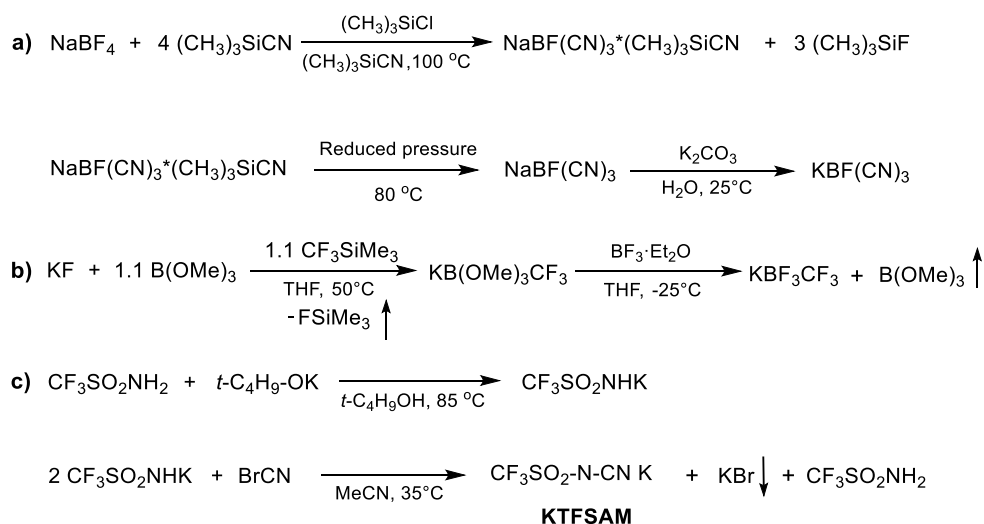
The same procedure was not applicable for the synthesis of N-((1,1,3,3,3-pentamethyldisiloxanyl)methyl) imidazole (Scheme 2.6, b) as the siloxane fragment in the alkylating agent was easily undergoing alcoholysis in the presence of a strong base such as sodium imidazol-1-ide. Switching to a less basic K_2CO_3 was not efficient as the nascent intermediate, namely potassium imidazol-1-ide, was still partially attacking both the alkylating agent and the final product. Thus, it was necessary to increase the rate of the main reaction and to suppress the side alcoholysis reaction. For that reason, firstly, a small amount of KI was added to perform in situ the exchange of chloride atom to the

iodide one in the alkylating agent and to enhance its reactivity. Secondly, the amount of K_2CO_3 was decreased to reduce the formation of potassium imidazol-1-ide. Simultaneous application of both approaches, namely the transition to 1-(iodomethyl)-1,1,3,3,3-pentamethyldisiloxane with higher reactivity and the decrease in the excess of the potassium imidazol-1-ide allowed for the preparation of targeted N-((1,1,3,3,3-pentamethyldisiloxan-1-yl)methyl) imidazole as a colorless liquid in 40% yield.

Due to the commercial availability of 3,3,4,4,5,5,6,6,6-nonafluorohexan-1-ol, the N-(3,3,4,4,5,5,6,6,6-nonafluorohexyl) imidazole was synthesized via another route (Scheme 2.6, c). On the first step the activated 3,3,4,4,5,5,6,6,6-nonafluorohexyl-4-methylbenzenesulfonate was obtained by the reaction of 4-toluenesulfonyl chloride with 3,3,4,4,5,5,6,6,6-nonafluorohexan-1-ol. Pyridine was used in this reaction simultaneously as a solvent, a catalyst and HCl acceptor. The second step involved the alkylation of imidazole with 3,3,4,4,5,5,6,6,6-nonafluorohexyl-4-methylbenzenesulfonate in anhydrous DMF. Imidazole was taken in excess to form the desired N-(3,3,4,4,5,5,6,6,6-nonafluorohexyl) imidazole and to act as a scavenger of 4-methylbenzenesulfonic acid. The product was obtained in 70% yield as a white waxy solid.

The structure and purity of all synthesized mono N-substituted imidazoles were confirmed by 1H , ^{13}C , ^{19}F NMR and IR spectroscopy as well as by elemental analysis (see IV.2.2.3).

2.3.1.2 Synthesis of potassium salts with asymmetric anions



Scheme 2.7 Synthetic pathways for the preparation of potassium salts with asymmetric anions.

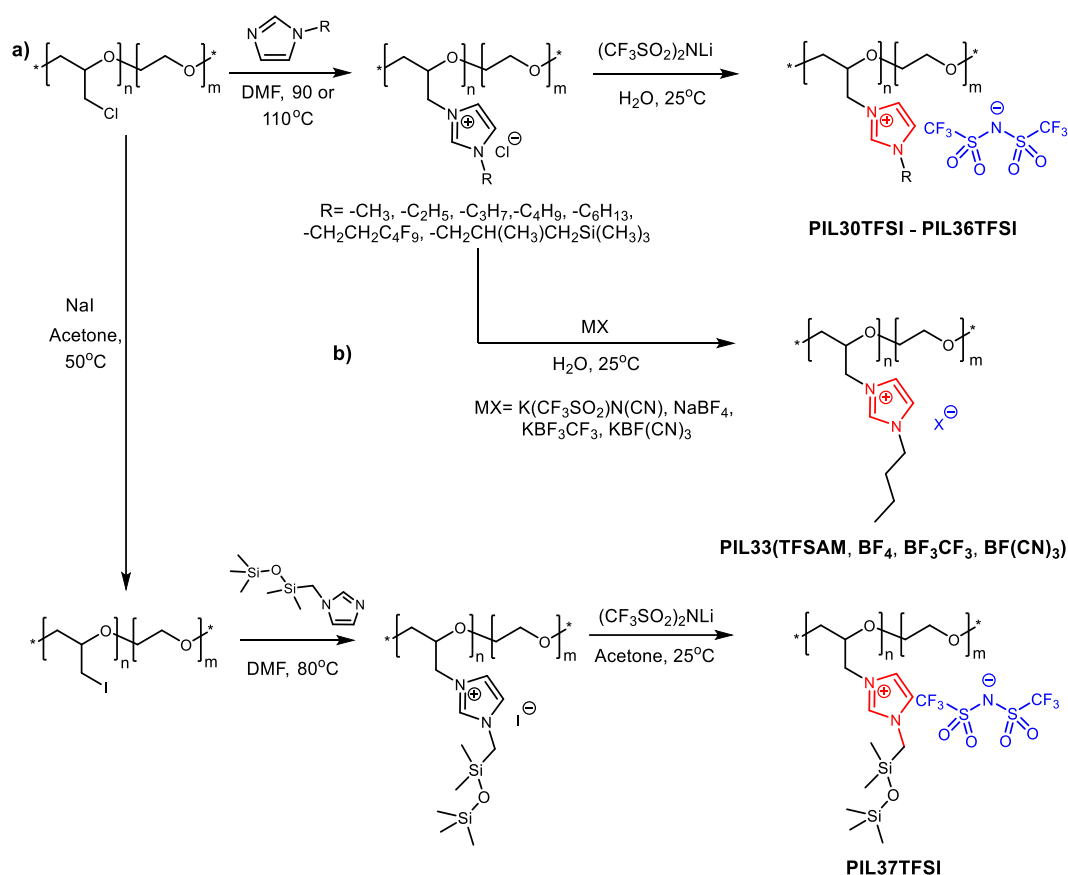
Three potassium salts with various asymmetric anions were prepared using synthetic routes depicted on Scheme 2.7. The $KBF(CN)_3$ was synthesized using the method reported by Ignatiev et al¹²⁵. The first step involved the substitution reaction between sodium tetrafluoroborate and trimethylsilyl cyanide in the presence of a trimethylsilyl chloride as a catalyst (Scheme 2.7, a). Solvate-free high purity potassium salt was obtained by heating to 80°C under reduced pressure and subsequent treatment with aqueous hydrogen peroxide and K_2CO_3 solutions.

The KBF_3CF_3 was synthesized using improved procedure proposed by our group recently (Scheme 2.7, b)¹²⁶. It included two steps: the formation of so-called “ate” complex, and its subsequent reaction with $\text{BF}_3\cdot\text{Et}_2\text{O}$, followed by the removal of $\text{B}(\text{OCH}_3)_3$ by distillation. The main advantage of the suggested method is the substitution of the corrosive HF with more benign $\text{BF}_3\cdot\text{Et}_2\text{O}$ complex as a source of fluorine atoms.

Finally, the KTFSAM ($\text{CF}_3\text{SO}_2\text{-N-CNK}$) salt was synthesized in accordance with the procedure developed by our group previously (Scheme 2.7, c)⁷⁴. It consists of the two reaction steps, namely the reaction of the trifluorosulfoneamine with potassium tert-butoxide and further interaction of the as prepared $\text{CF}_3\text{SO}_2\text{NHK}$ salt with BrCN in acetonitrile solution.

All potassium salts used in this study were characterized by elemental analysis, NMR and IR spectroscopy. Their spectroscopic data were in a full accordance with the data reported in the literature^{74,126,125} (see IV.2.2.3).

2.3.1.3 Synthesis of the halide PILs



Scheme 2.8 Synthesis of cationic PILs via modification of poly(epichlorohydrin-co-ethylene oxide).

Commercially available Hydrin® poly(epichlorohydrin-co-ethylene oxide) copolymer with high molecular weight was selected as a starting material for the synthesis of PILs as the presence of

additional ethylene oxide fragments in the backbone in comparison with epichlorohydrin homopolymer allows to reduce charge density, increase back-bone flexibility, to promote additional ion solvation, and thus to increase ion mobility. The general reaction pathway for the synthesis of novel cationic PILs consisted in two steps (Scheme 2.8): 1) the quaternization reaction of poly(epichlorohydrin-co-ethylene oxide) with an excess of respective mono N-substituted imidazole in DMF and 2) ion metathesis between the obtained chloride PIL and selected metal salt in aqueous medium. The quaternization degree of all PILs was determined using NMR spectroscopy (Figure IV.5) and equations 1.32-1.35.

The study of the temperature effect on the completeness of the quaternization step revealed that 80 °C is the minimum required temperature to achieve modification degree above 85%. For the short alkyl chains (from N-methyl to N-propyl imidazole) the performing of the reaction at 90 °C was sufficient to reach 93-95% degree of quaternization, while for long substitutes the temperature of 110 °C was necessary to gain comparable modification. Next, the influence of N-substituted imidazole excess on quaternization degree was investigated. It was found that for the achievement of high reaction conversions the ten-fold excess of the respective N-substituted imidazole is required. Finally, the application of the determined optimized reaction conditions (ten-fold excess of N-substituted imidazole, 80 °C for N-methyl-, N-ethyl- and N-propyl imidazoles, 110 °C for other N-substituted imidazoles) allowed to reach 93-95% quaternization degree for all synthesized chloride PILs.

The same conditions were not applicable for the synthesis of the halide precursor of **PIL37TFSI** (Figure 2.23) with siloxane side chain as the excess of mono substituted imidazole even in the presence of traces of water at high temperatures was leading to the hydrolysis of siloxane bonds and further polymer degradation. For that reasons, the excess of N-((1,1,3,3,3-pentamethyldisiloxanyl)methyl) imidazole was reduced from 10 to 1.3 equivalents, the temperature was decreased to 80°C and more reactive poly(epichlorohydrin-co-ethylene oxide) was used. These precautions provided the respective iodide PIL with a degree of quaternization equal to 60%.

2.3.1.4 Ion metathesis

To obtain PILs with TFSI anions (Scheme 2.8, **PIL30TFSI** – **PIL36TFSI**) the ion metathesis with LiTFSI salt was conducted in aqueous medium. The application of a 2-equivalent excess of LiTFSI and the hydrophobic nature of the formed polyelectrolytes resulted in quantitative ion exchange. The subsequent additional precipitation from acetone solution into the excess of water provided the desired **PIL30TFSI** – **PIL36TFSI** in 80-90% yield with high purity. Depending on the substituents at the imidazolium cation the **PIL30TFSI** – **PIL36TFSI** represented yellowish cold flowing rubbers with various viscosity.

At this, the ion metathesis in aqueous medium was not applicable for the synthesis of **PIL37TFSI** with siloxane side chain (Scheme 2.8). To avoid the degradation in water the ion exchange with LiTFSI was conducted in the anhydrous acetone and the final product was precipitated into the excess of anhydrous Et₂O. This allowed to obtain fully exchanged **PIL37TFSI** with 50% yield.

Finally, the **PIL33Cl** with n-butyl substituted imidazolium cation has been selected for the ion exchange with potassium salts bearing various symmetric and asymmetric anions (Scheme 2.8). Such choice was driven by the fact that **PIL33TFSI** was demonstrating the highest ionic conductivity among the synthesized TFSI-based PILs (see section 2.3.2.1). The ion metathesis with potassium salts in aqueous medium resulted in the isolation of high purity PILs in the sufficient yields of 86-92%. Both **PIL33TFSAM**, **PIL33BF₃CF₃** and **PIL33BF(CN)₃** were precipitated in course of the ion exchange reaction. It is necessary to mention that neither BF₃CF₃ nor BF(CN)₃ anions were previously used for the preparation of PILs, thus making **PIL33BF₃CF₃** and **PIL33BF(CN)₃** the first examples in the field.

The absence of the chloride anions after ion metathesis was confirmed by a qualitative test with silver nitrate.

2.3.2 Spectroscopic analysis

The structure of the polymers, their composition and purity were supported by ¹H, ¹³C and ¹⁹F NMR and FTIR spectroscopy as well as by elemental analysis.

The detailed assignation of ¹H NMR spectra of PILs is shown on Figure 2.24. Similar to ILs⁹⁹, the significant change in chemical shift for protons of the imidazolium cation was observed after the ion exchange from the chloride anion. All PILs with delocalized anions (TFSI, TFSAM, BF₄, BF₃CF₃ and BF(CN)₃) showed the chemical shift of the imidazolium ring protons compared to the chloride precursor, although this shift was nearly identical. ¹³C NMR spectra of TFSI and TFSAM based PILs (Figure 2.25, a-d) contained characteristic trifluoromethyl quadruplets at ~ 120 ppm while **PIL33BF(CN)₃** exhibited broad multiplet at ~ 120 ppm assigned to CN group (Figure 2.25, e). The comparison of the fluorine chemical shifts in ¹⁹F NMR spectra of synthesized PILs is shown on Figure 2.26. As the negative inductive effect of the substituent on the boron atom increases, the chemical shift of the fluorine moves to the higher field reaching approximately -211 ppm for **PIL33** with BF(CN)₃ anion (Figure 2.26, e). A similar dependence can be seen for **PIL33TFSI** and **PIL33TFSAM** showing the transition from -80.9 to -79.9 ppm for TFSI and TFSAM anions, respectively (Figure 2.26, b and c).

PILs were further characterized by IR spectroscopy (Figure 2.27). Characteristic bands for imidazolium ring (red dashed lines) at ~740 (ν(CH₂(N))), ~1337 (ν(CN_{ring})) and ~1568 (ν(CC_{ring})) cm⁻¹ as well as for ester groups (green dashed lines) at ~1165 (ν(COC)) cm⁻¹ were found in all analysed samples¹²⁷. Polymers **PIL33BF₄**, **PIL33BF₃CF₃** and **PIL33BF(CN)₃** with boron-based anions showed

the signals at ~ 1062 ($\nu(\text{BF})$) cm^{-1} . In addition to that, **PIL33BF₃CF₃** and **PIL33BF(CN)₃** demonstrated a signal at ~ 940 cm^{-1} , attributed to the B-C bond vibration. The signal at ~ 2200 cm^{-1} assigned to the vibration of the C-N group was found for **PIL33TFSAM** and **PIL33BF(CN)₃**^{127,128}. The characteristic bands of sulfonylimide anions were observed in **PIL33TFSI** at ~ 1332 (asymmetric SO₂), ~ 1187 (CF), ~ 1136 (symmetric SO₂) and ~ 1056 (SNS) cm^{-1} , correspondingly. At the same time for **PIL33TFSAM** the signal at 1060 cm^{-1} was absent and the CF stretching signal was shifted to 1218 cm^{-1} , in a full agreement with published reports^{74,127}.

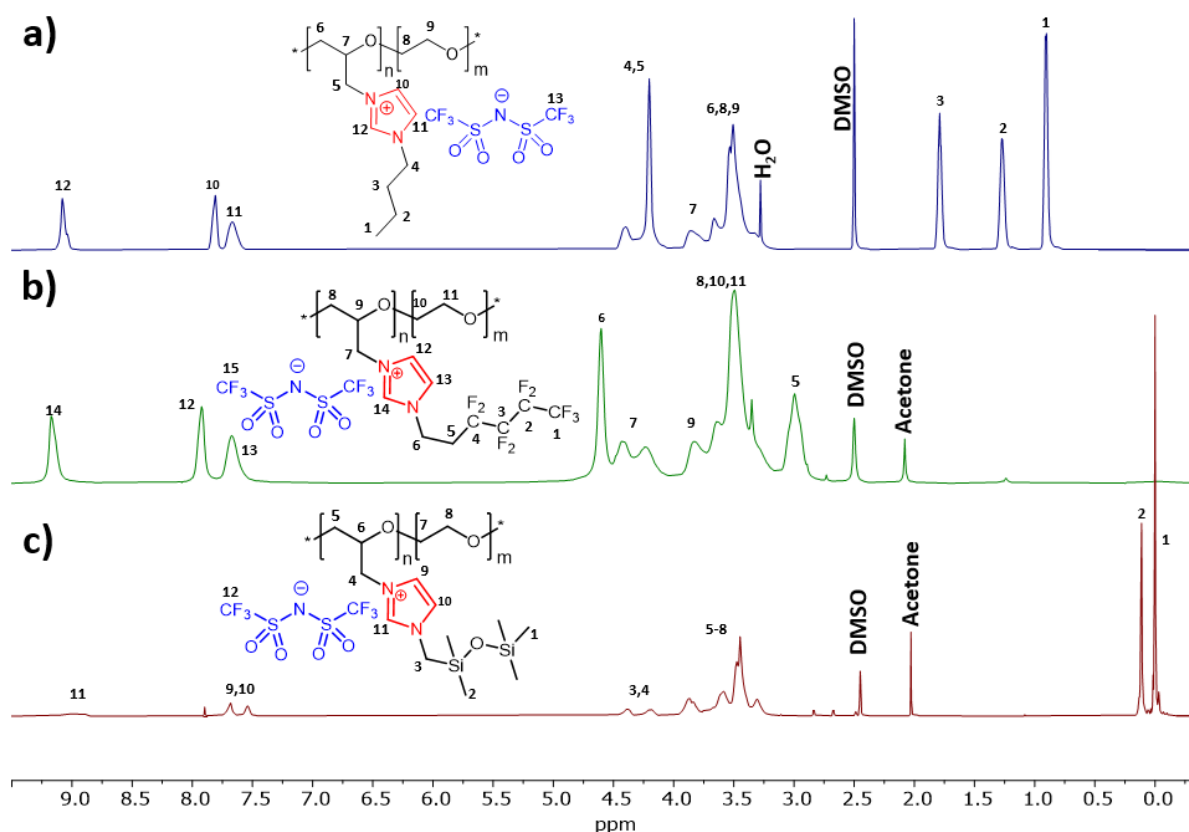


Figure 2.24 ^1H NMR of polymers **PIL33TFSI** (a), **PIL36TFSI** (b), **PIL37TFSI** (c) (25 °C, DMSO- d_6).

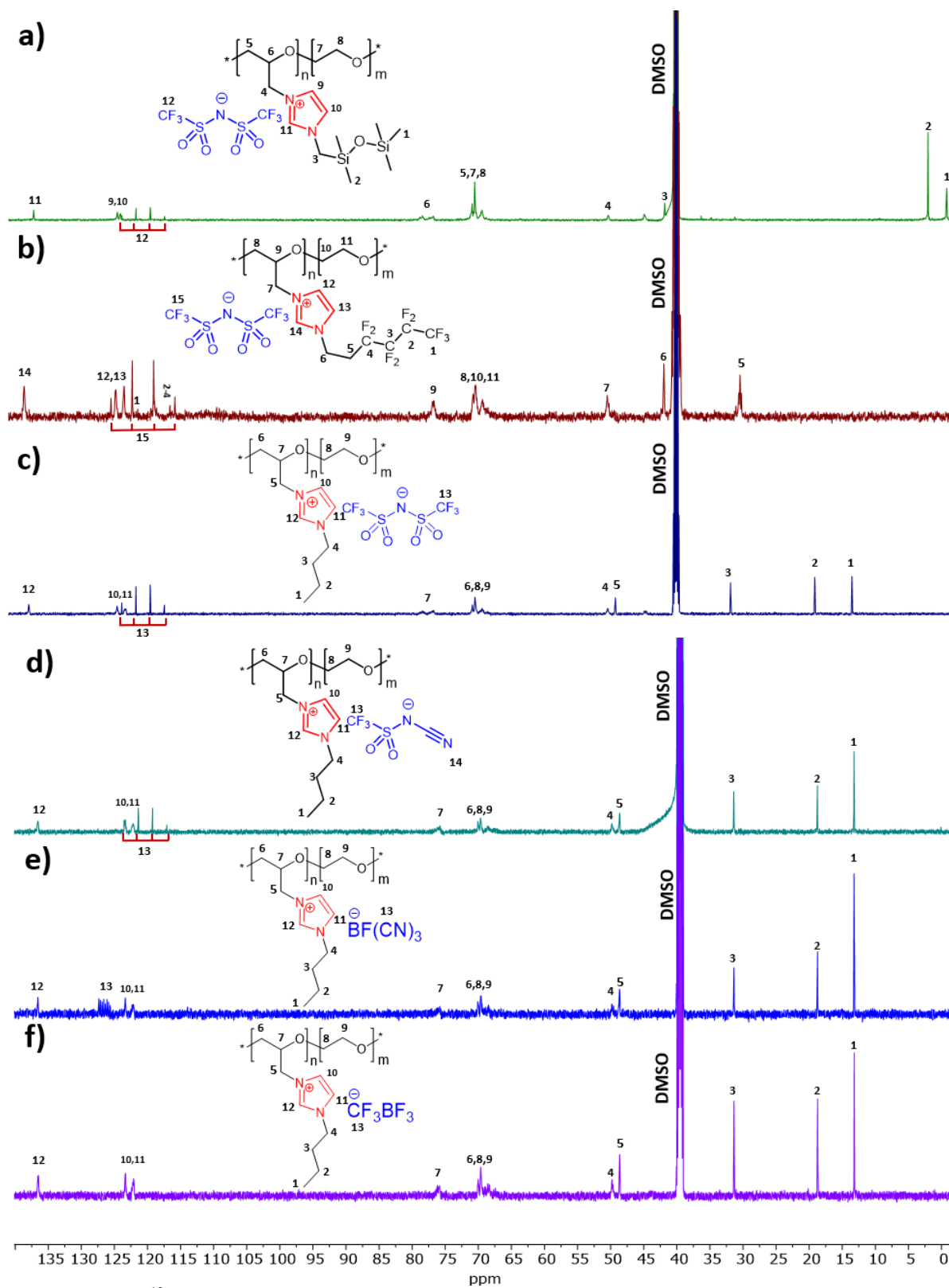


Figure 2.25 ^{13}C NMR of polymers **PIL37TFSI** (a), **PIL36TFSI** (b), **PIL33TFSI** (c), **PIL33TFSAM** (d), **PIL33BF(CN) $_3$** (e) and **PIL33CF $_3$ BF $_3$** (f) (25°C , $\text{DMSO}-d_6$).

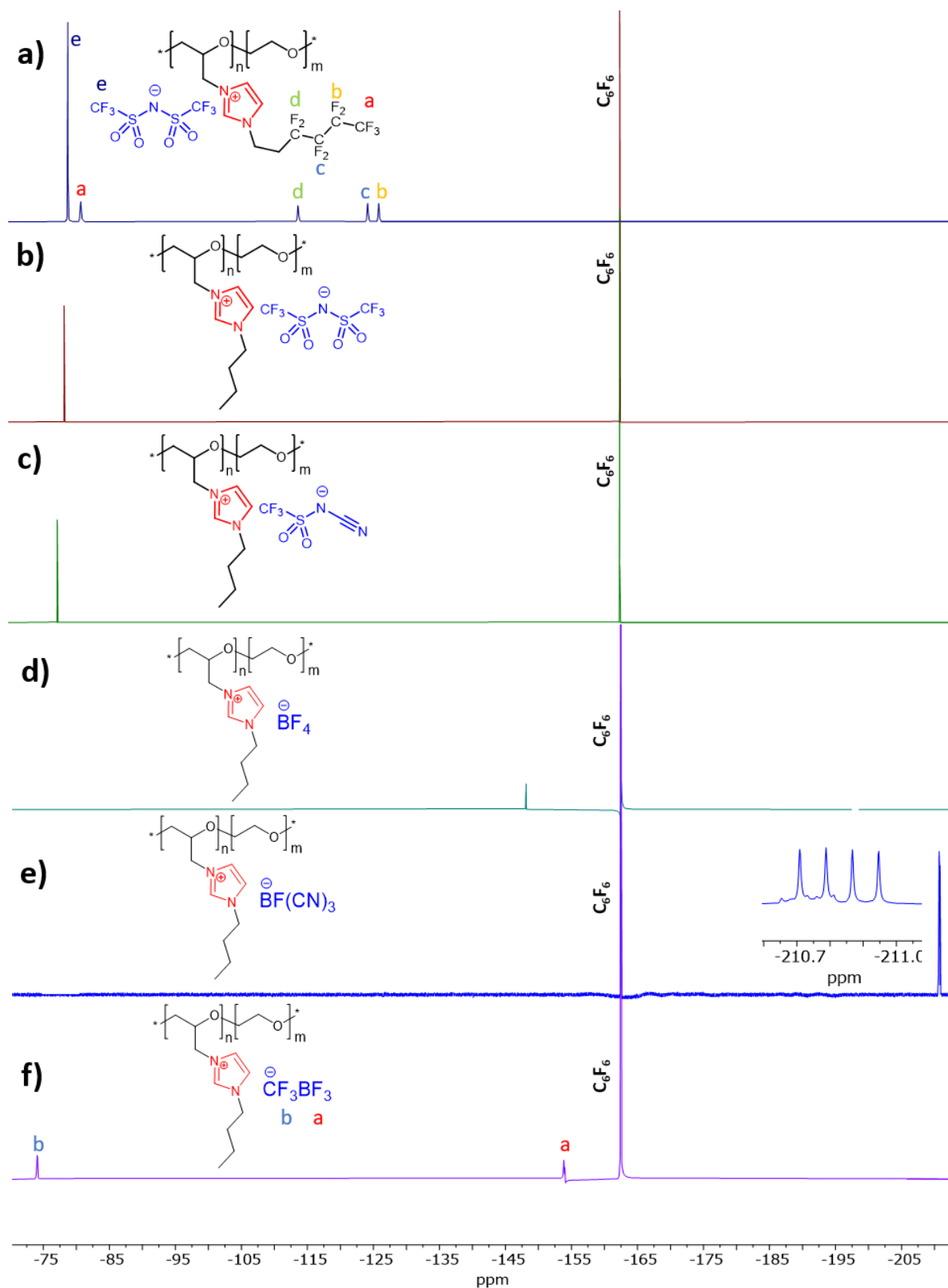


Figure 2.26 ^{19}F NMR of polymers **PIL36TFSI** (a), **PIL33TFSI** (b), **PIL33TFSAM** (c), **PIL33BF $_4$** (d), **PIL33BF(CN) $_3$** (e) and **PIL33CF $_3$ BF $_3$** (f) (25 $^\circ\text{C}$, DMSO-d_6).

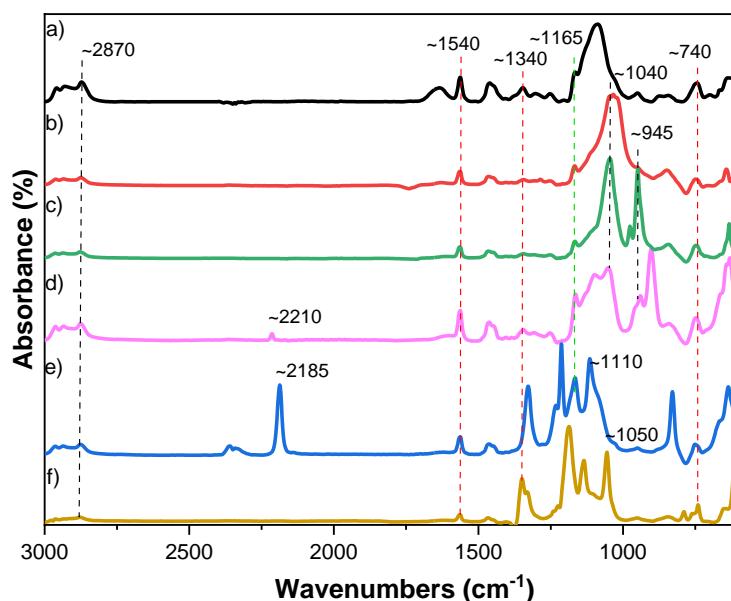


Figure 2.27 FTIR spectra of **PIL33Cl** (a), **PIL33BF₄** (b), **PIL33CF₃BF₃** (c), **PIL33BF(CN)₃** (d), **PIL33TFSAM** (e) and **PIL33TFSI** (f).

2.3.1 Thermal properties

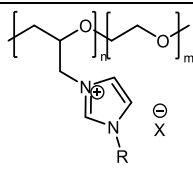
2.3.1.1 Glass-transition temperature

DSC was used to determine the glass transition temperature of PILs (Table 2.5). The T_g values of TFSI-based PILs with alkyl side chains are shown on Figure 2.28 (a). The observed trend displays a minimum, with the T_g of the PILs first decreasing with increasing alkyl side chain length up to $n = 4$ ($T_g = -25^\circ\text{C}$) for **PIL33TFSI**, then increasing at $n = 6$ (Figure 2.28, a). The same trend was observed previously for hexafluorophosphate imidazolium ionic liquids¹²⁹, with T_g decreasing until $n = 6$, at which point an increase was observed. This may be explained by improved chain packing and an associated increase in interchain interactions once the alkyl substituents are sufficiently long. The glass transition temperatures of all PILs with TFSI anions can be arranged in the following order:

T_g ($^\circ\text{C}$): **PIL36TFSI** (CF_3 , 6) > **PIL37TFSI** (SiOSi , -2) > **PIL35TFSI** ($\text{Si}(\text{CH}_3)_3$, -6) > **PIL30TFSI** (C_1 , -10) > **PIL31TFSI** (C_2 , -16) > **PIL32TFSI** (C_3 , -20) > **PIL34TFSI** (C_6 , -21) > **PIL33TFSI** (C_4 , -25)

PIL35TFSI, **PIL36TFSI** and **PIL37TFSI** with heteroatoms in the side chain demonstrated T_g values of -6°C , 6°C and -2°C respectively. Thus, all PILs with side chains containing heteroatoms showed higher T_g s in comparison with analogous PILs having alkyl substituents. Finally, among studied TFSI-based PILs the **PIL36TFSI** with fluorinated chain possesses the highest overall T_g .

Table 2.5 Selected properties of epichlorohydrin derived PILs

Polymer			T_{onset} (°C) ¹	T_g (°C) ²	σ (S cm ⁻¹)	
Sample					at 25 °C	at 70 °C
	R-	X				
PIL30TFSI	-CH ₃	(CF ₃ SO ₂) ₂ N	290	-10	8.4×10 ⁻⁷	2.2×10 ⁻⁴
PIL31TFSI	-C ₂ H ₅	(CF ₃ SO ₂) ₂ N	290	-16	3.3×10 ⁻⁶	2.8×10 ⁻⁴
PIL32TFSI	-C ₃ H ₇	(CF ₃ SO ₂) ₂ N	290	-20	2.6×10 ⁻⁶	1.9×10 ⁻⁴
PIL33TFSI	-C ₄ H ₉	(CF ₃ SO ₂) ₂ N	310	-25	4.7×10 ⁻⁶	2.5×10 ⁻⁴
PIL34TFSI	-C ₆ H ₁₃	(CF ₃ SO ₂) ₂ N	320	-21	2.4×10 ⁻⁶	2.0×10 ⁻⁴
PIL35TFSI	CH ₂ CH(CH ₃)CH ₂ Si(CH ₃) ₃	(CF ₃ SO ₂) ₂ N	285	-6	2.0×10 ⁻⁷	4.5×10 ⁻⁵
PIL36TFSI	-CH ₂ CH ₂ C ₄ F ₉	(CF ₃ SO ₂) ₂ N	280	6	1.6×10 ⁻⁸	9.7×10 ⁻⁶
PIL37TFSI	CH ₂ Si(CH ₃) ₂ OSi(CH ₃) ₃	(CF ₃ SO ₂) ₂ N	185	-2	8.0×10 ⁻⁸	3.8×10 ⁻⁵
PIL33BF ₄	-C ₄ H ₉	BF ₄	270	-4	1.2×10 ⁻⁸	6.4×10 ⁻⁶
PIL33TFSAM	-C ₄ H ₉	CF ₃ SO ₂ -N-CN	260	-30	4.3×10 ⁻⁶	2.1×10 ⁻⁴
PIL33BF(CN) ₃	-C ₄ H ₉	BF(CN) ₃	250	-31	1.0×10 ⁻⁵	4.5×10 ⁻⁴
PIL33BF ₃ CF ₃	-C ₄ H ₉	BF ₃ CF ₃	185	-16	3.9×10 ⁻⁷	4.7×10 ⁻⁵

¹Onset mass loss temperature by TGA in air at a heating rate of 5°C min⁻¹. ²By DSC in N₂ at a heating rate of 5°C min⁻¹.

The influence of the anion structure on PILs glass transition temperature is represented below by the following order:

T_g (°C): **PIL33BF₄** (-4) > **PIL33BF₃CF₃** (-16) > **PIL33TFSI** (-25) > **PIL33TFSAM** (-30) ≈ **PIL33BF(CN)₃** (-31)

As stated before in the literature review (see section II.1.1.3), the symmetry of the anion and the charge delocalization have a great impact on PILs T_g . The transition from symmetric BF₄ to asymmetric BF₃CF₃ and then to BF(CN)₃ with higher delocalization led to the decrease in T_g from -4 to -16 and further down to -31°C, respectively. Similar decrease of T_g can be seen by replacing symmetric TFSI anion with the asymmetric TFSAM one. Thus, both the asymmetry and the charge delocalization of the anion are effecting the T_g of PILs, imparting the lowest values to **PIL33TFSI** (-25°C) and **PIL33BF(CN)₃** (-31°C) among investigated polymers.

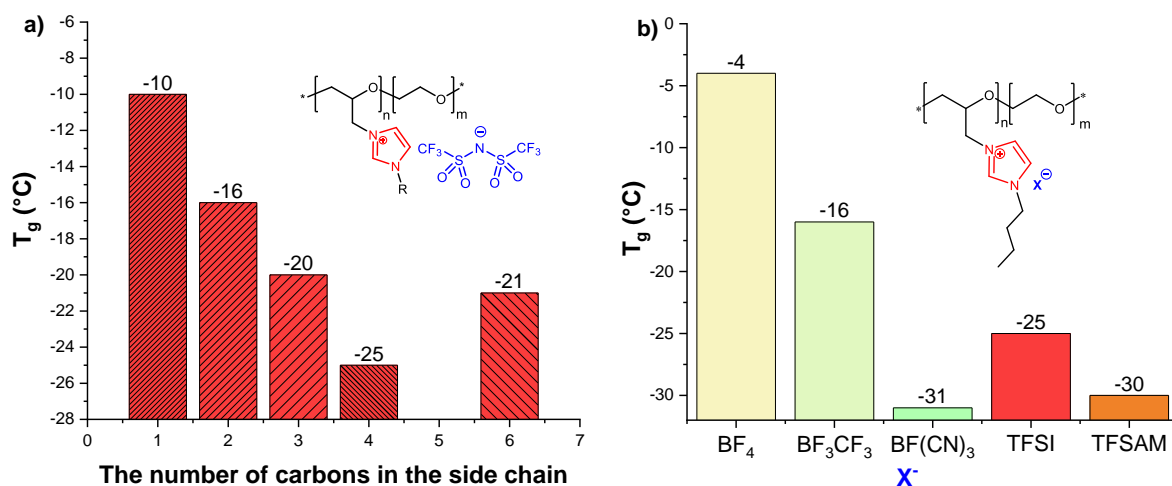


Figure 2.28 Glass transition temperature dependence on the structure for TFSI PILs with different alkyl substituents (a) and for n-butyl substituted PILs with various anions (b).

2.3.1.2 Onset temperature of weight loss

Thermal degradation behavior of PILs was investigated by thermo-gravimetric analysis in air (Figure 2.29 and Table 2.5). For the TFSI-based PILs the decomposition temperatures with respect to the chemical structure of the side chains are represented below by the following order:

T_{onset} (°C): **PIL34TFSI** (C_6 , 320) > **PIL33TFSI** (C_4 , 310) > **PIL32TFSI** (C_3 , 290) \approx **PIL31TFSI** (C_2 , 290) \approx **PIL30TFSI** (C_1 , 290) > **PIL35TFSI** ($\text{Si}(\text{CH}_3)_3$, 285) > **PIL36TFSI** (CF_3 , 280) > **PIL37TFSI** (SiOSi , 185)

Among TFSI PILs, all samples with alkyl side chains showed satisfactory thermal stability with onset thermal degradation ranging from 290 to 320 °C (Table 2.5). In contrast, polymers with heteroatoms in the side chains demonstrated slightly decreased thermal stability with the lowest one $T_{\text{onset}} = 185^\circ\text{C}$ for **PIL37TFSI** having siloxane side chain (Table 2.5). The later is in a full agreement with the thermal behavior of linear or branched polydimethylsiloxanes, that commonly possess T_{onset} of around 150°C ¹³⁰. The transfer from TFSI to BF_4 anion in **PIL33** was accompanied by a decrease in the onset weight loss temperature from 310 to 270°C , that was in agreement with the data published for PILs previously⁹⁹. The introduction of the CN group into the anions structure resulted in further decrease of PILs thermal stability from 310 to 260°C for TFSI and TFSAM representatives and from 270 to 250°C for BF_4 and $\text{BF}(\text{CN})_3$ based PILs (Table 2.5). Finally, **PIL33BF₃CF₃** showed the lowest thermal stability possibly due to a high tendency of BF_3CF_3 anion towards elimination of the CF_2 moiety and formation of BF_4 anion along with other byproducts¹³¹. The decomposition temperatures of PILs with respect to the chemical structure of their anions can be represented by the following order:

T_{onset} (°C): **PIL33TFSI** (310) > **PIL33BF₄** (270) > **PIL33TFSAM** (260) > **PIL33BF(CN)₃** (250) > **PIL33BF₃CF₃** (185)

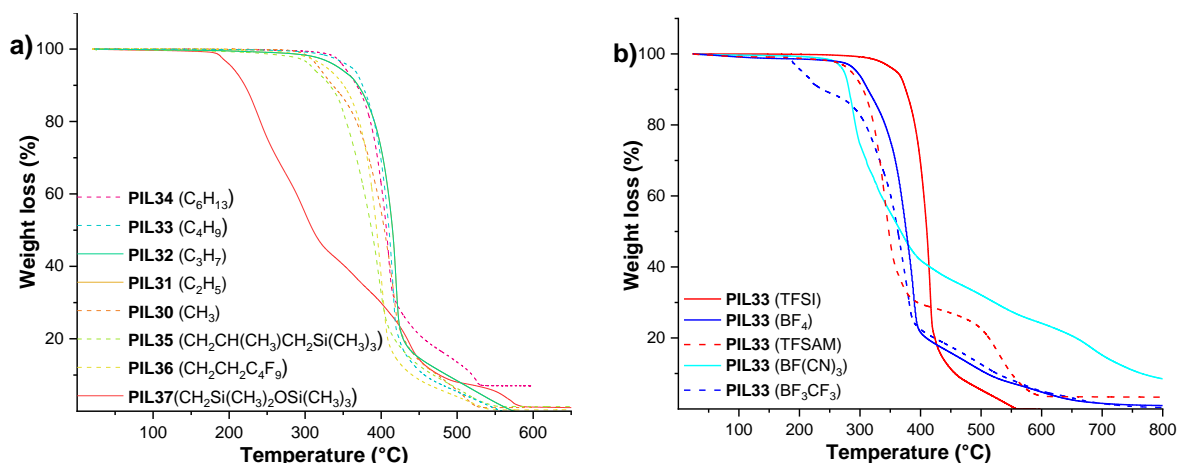


Figure 2.29 Comparison of TGA traces TFSI PILs with different alkyl substituents (a) and for *n*-butyl substituted PILs with various anions (b) (5°C min⁻¹, under air).

2.3.2 Electrochemical properties

2.3.2.1 Ionic conductivity

Ionic conductivity of PILs was measured over a wide temperature range (Figure 2.30). For all PILs the ionic conductivity increased with increasing temperature, however, the temperature dependence did not follow the linear Arrhenius behavior. This can be explained by the fact that the anions diffusion occurs via two different mechanisms: (1) hopping of the anions between chemically bonded cations and (2) local segmental motion of polymer chains with coordinative oxyethylene fragments. The determination of ionic conductivity at 25 °C revealed 3 orders of magnitude difference in σ of PILs (Figure 2.30 and Table 2.5). This difference was levelled out with the rise in temperature.

For TFSI-based PILs the conductivity values increased from 8.0×10^{-8} to 4.7×10^{-6} S cm⁻¹ and can be ranked in the following decreasing order:

σ (25°C, S cm⁻¹): **PIL33TFSI** (C₄, 4.7×10^{-6}) > **PIL31TFSI** (C₂, 3.3×10^{-6}) > **PIL32TFSI** (C₃, 2.6×10^{-6}) > **PIL34TFSI** (C₆, 2.4×10^{-6}) > **PIL30TFSI** (C₁, 8.4×10^{-7}) > **PIL35TFSI** (Si(CH₃)₃, 2.0×10^{-7}) > **PIL37TFSI** (SiOSi, 8.0×10^{-8}) > **PIL36TFSI** (CF₃, 1.6×10^{-8})

Within the whole temperature range **PIL33TFSI** with *n*-butyl side chain showed the highest conductivity values, while **PIL36TFSI** with fluorinated chain demonstrated the lowest conductivity (Figure 2.30, a). For polymers with alkyl substituents, the general trend of increasing conductivity with decreasing T_g is observed, with one exception – **PIL31TFSI** shows a higher than expected conductivity given its T_g . Otherwise, **PIL33TFSI** with the lowest T_g exhibited the highest conductivity, while **PIL30TFSI**, with highest T_g showed the lowest conductivity. Moreover, PILs with heteroatoms in the side chain (**PIL35TFSI** – **PIL37TFSI**) possessed one order of magnitude lower ionic conductivity in comparison with analogous PILs having alkyl substituents, that was found to be in correlation with their higher glass transition temperatures.

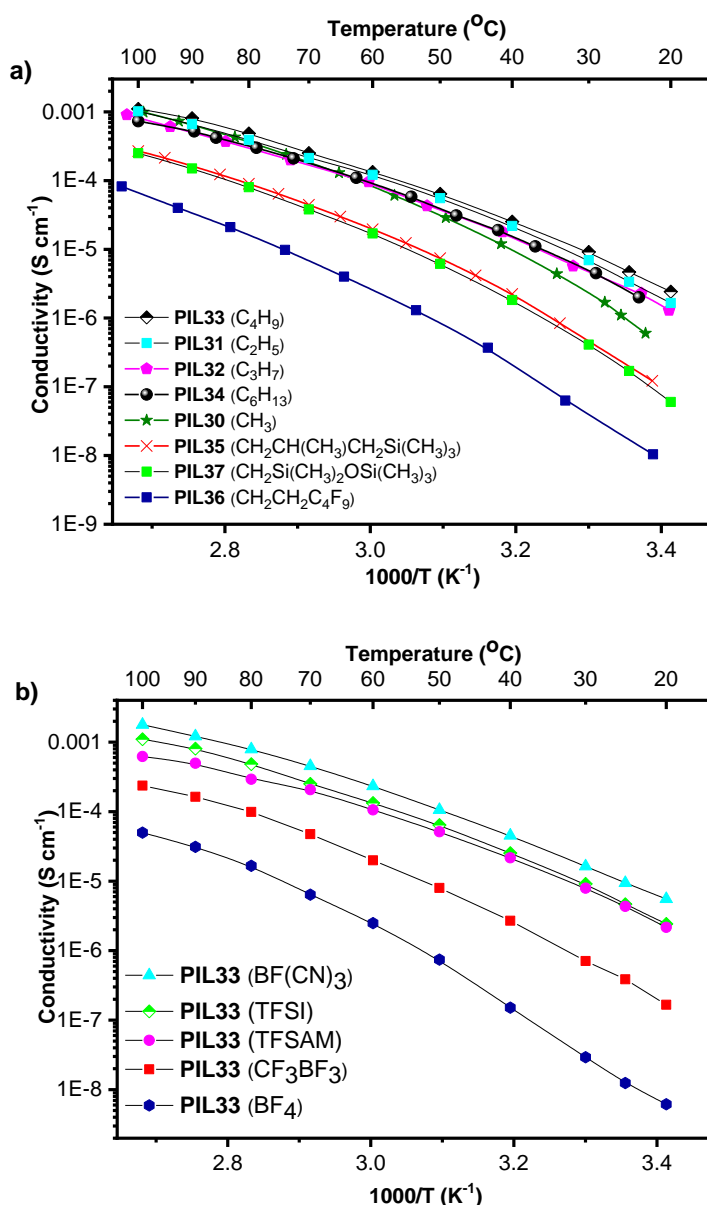


Figure 2.30 Temperature dependence of bulk ionic conductivity for TFSI PILs with different side chains (a) and for *n*-butyl substituted PILs with various anions (b).

The effect of the counter anion's structure on PILs ionic conductivity was even higher and resulted in three orders of magnitude difference (Figure 2.30, b). The conductivity trend for PILs with different anions at 25°C is represented below:

$$\sigma \text{ (25°C, S cm}^{-1}\text{): PIL33BF(CN)}_3 (1.0 \times 10^{-5}) > \text{PIL33TFSI} (4.7 \times 10^{-6}) \approx \text{PIL33TFSAM} (4.3 \times 10^{-6}) > \text{PIL33BF}_3\text{CF}_3 (3.9 \times 10^{-7}) > \text{PIL33BF}_4 (1.2 \times 10^{-8})$$

The transfer from symmetric BF_4 anion to asymmetric BF_3CF_3 and BF(CN)_3 anion resulted in nearly three orders of magnitude increase in ionic conductivity from 1.2×10^{-8} to $1.0 \times 10^{-5} \text{ S cm}^{-1}$ (25°C). Contrary, the introduction of smaller and asymmetric TFSAM anion was practically not affecting ionic

conductivity of **PIL33TFSI** in comparison with **PIL33TFSI**, that was in agreement with the work published previously by Drockemuller et al.⁶⁶ It can be concluded that among PILs synthesized in the current study the **PIL33TFSI** and **PIL33BF(CN)₃** demonstrated the highest ionic conductivities. It is worth noting that, the value of $1.0 \times 10^{-5} \text{ S cm}^{-1}$ found for **PIL33BF(CN)₃** at 25°C can be ranked among TOP15 PILs with highest conductivities published to date.

2.3.2.2 Electrochemical stability

Lastly, the electrochemical stability limits of PILs with highest ionic conductivity were assessed via cyclic voltammetry. Figure 2.31 shows the anodic and cathodic scans of **PIL33TFSI** and **PIL33BF(CN)₃** at 25 °C. The oxidation potential for **PIL33TFSI** against the platinum electrode was found to be higher than that of **PIL33BF(CN)₃** reaching the value of 2.7 V vs Ag⁺/Ag. Contrary, the reduction potential of **PIL33TFSI** was lower than of **PIL33BF(CN)₃**: -1.5 vs -2.0 V, respectively (Figure 2.31). For **PIL33BF(CN)₃** an additional irreversible peak was found at -2.4 V, which can be attributed to the oxidation processes of carbon atoms in the anion. The overall evolution of electrochemical stability of PILs can be summarized as follows:

ESW (25°C, V): **PIL33TFSI** (4.2) > ESW **PIL33BF(CN)₃** (3.2).

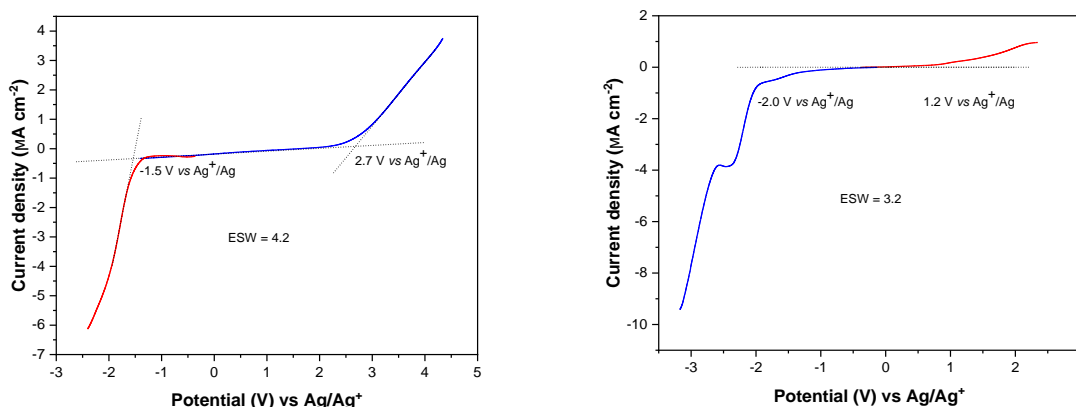


Figure 2.31 Electrochemical stability window for **PIL33TFSI** (a) and **PIL33BF(CN)₃** (b) at 25 °C (Pt foils as the working and counter electrodes and Ag mesh as the reference electrode, scan rate 5 mV s⁻¹).

2.3.3 Rheological properties

The viscoelastic properties of epichlorohydrin derived PILs were investigated by examples of **PIL33TFSI** and **PIL33BF(CN)₃** via small amplitude oscillatory shear (SAOS) rheology in a temperature range from -20 to 100°C. As shown in Figure 2.32, both polymers exhibit a rubbery pseudo-plateau spanning approximately 2-3 decades of frequency, which is typical of entangled polymer chains. This region includes the data measured at 25°C, demonstrating that both polymers exhibit solid-like

behavior at room temperature. At higher temperatures, **PIL33BF(CN)₃** transitions to a liquid state, as evidenced by the presence of a terminal regime where the loss (G'') and storage (G') moduli follow ω^1 and ω^2 slopes, respectively. The shift factors used in the TTS of **PIL33TFSI** and **PIL33BF(CN)₃** obey a WLF law (Figure 2.32, b, Equation 1.4).

To evaluate the mechanical properties of PILs, their storage modulus values at 25°C; 1 rad s⁻¹ were compared:

$$G' (25^\circ\text{C}; 1 \text{ rad s}^{-1}; \text{kPa}): \text{PIL33TFSI} (46.9) > \text{PIL33BF(CN)}_3 (22.0)$$

PIL33TFSI shows two times higher storage modulus which can be explained by higher T_g in comparison to **PIL33BF(CN)₃**.

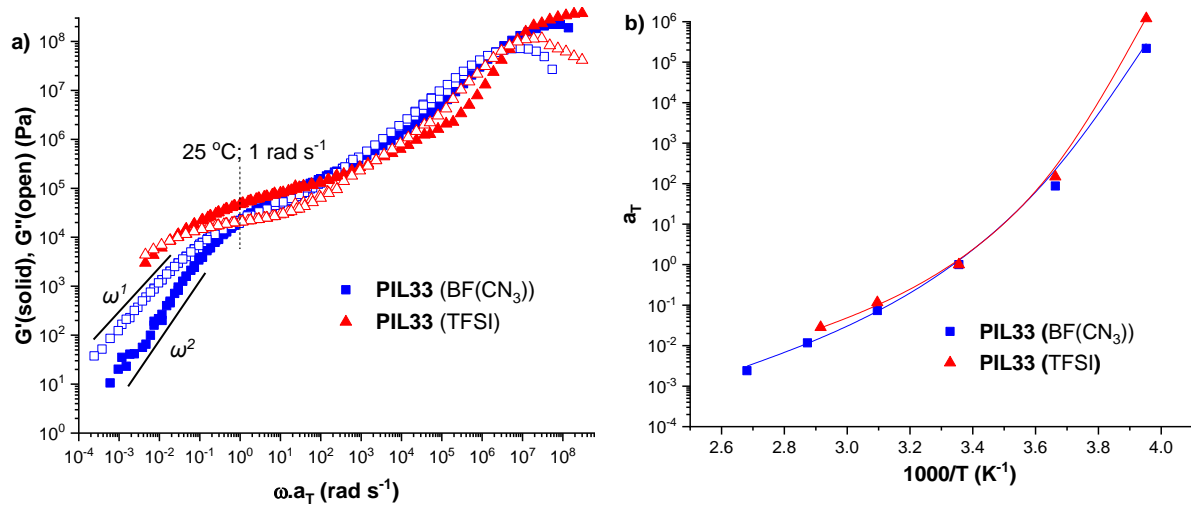
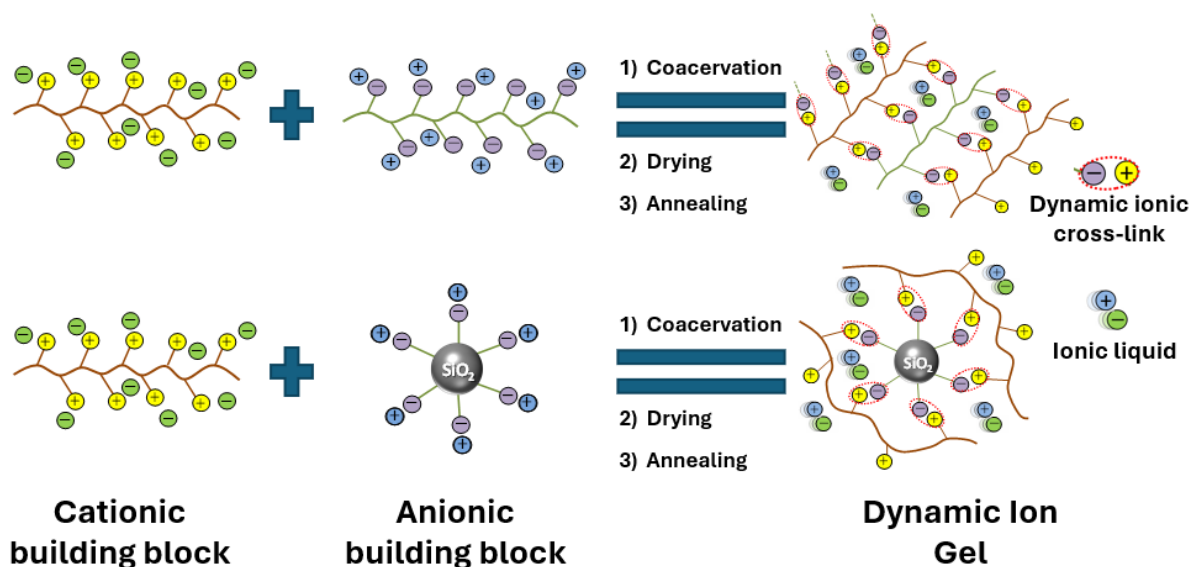


Figure 2.32 TTS master curves of **PIL33TFSI** and **PIL33BF(CN)₃** obtained by frequency sweep experiments performed from –20 to 100 °C and referenced at $T_0 = 25^\circ\text{C}$ (a). Corresponding a_T shift factors and WLF best fits at $T_0 = 25^\circ\text{C}$ for **PIL33TFSI** and **PIL33BF(CN)₃** (b).

3. Development of dynamic ion gels (DIG)s

“**Dynamic ion gels**” (DIG)s – a new term introduced by us, relate to a new generation of highly conductive and at the same time mechanically stable solid polymer electrolytes obtained via coacervation of oppositely charged building blocks. These building blocks can either be oppositely charged poly(ionic liquid)s, which leads to organic/organic materials, or a combination of oppositely charged poly(ionic liquid) and ionic silica nanoparticles, resulting in hybrid organic/inorganic materials (Figure 3.1). The dynamic gelation process between the complimentary building blocks proceeds *via* the creation of **dynamic ionic crosslinks** through ion metathesis with the concomitant *in situ* **generation of highly ion conducting ionic liquid** (Figure 3.1). Thus, this approach enables the creation of materials combining high ionic conductivity with the solidity and toughness of polymer networks or nano-composites. Additionally, the ability to mix-and-match various building blocks enables an unprecedented level of compositional freedom, providing the means to produce materials highly optimized for a variety of applications.

It also can be said that DIGs are an advanced materials that builds on the strengths of ion gels and of polyelectrolyte complexes, achieving a synergistic combination of their beneficial features. DIGs have dynamic ionic cross-links, like those in polyelectrolyte complexes, to enhance mechanical strength. Simultaneously, they possess *in-situ* generated ionic liquid, significantly boosting their ionic conductivity.



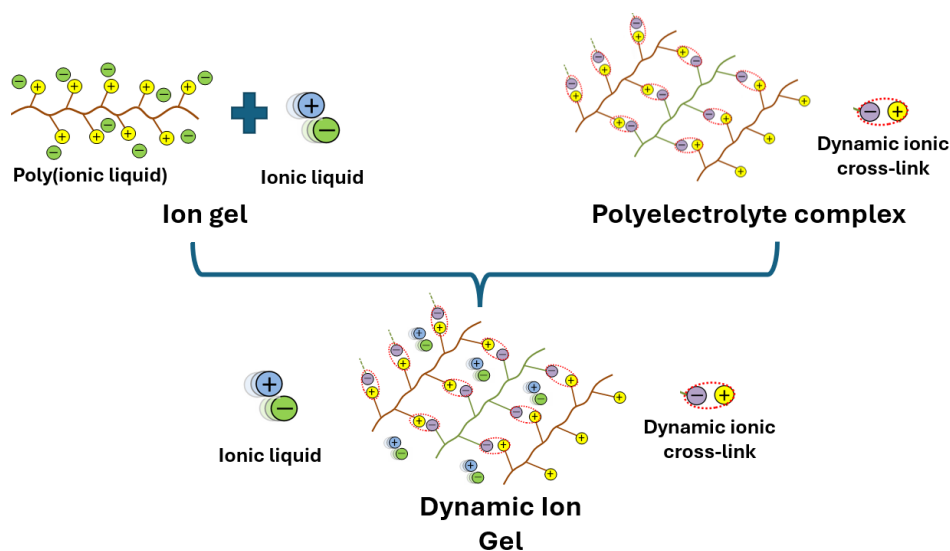


Figure 3.1 Concept of Dynamic Ion Gels (DIG)s

3.1 Model Dynamic Ion Gel DIG1 (proof-of-concept)

3.1.1 Synthesis and characterization

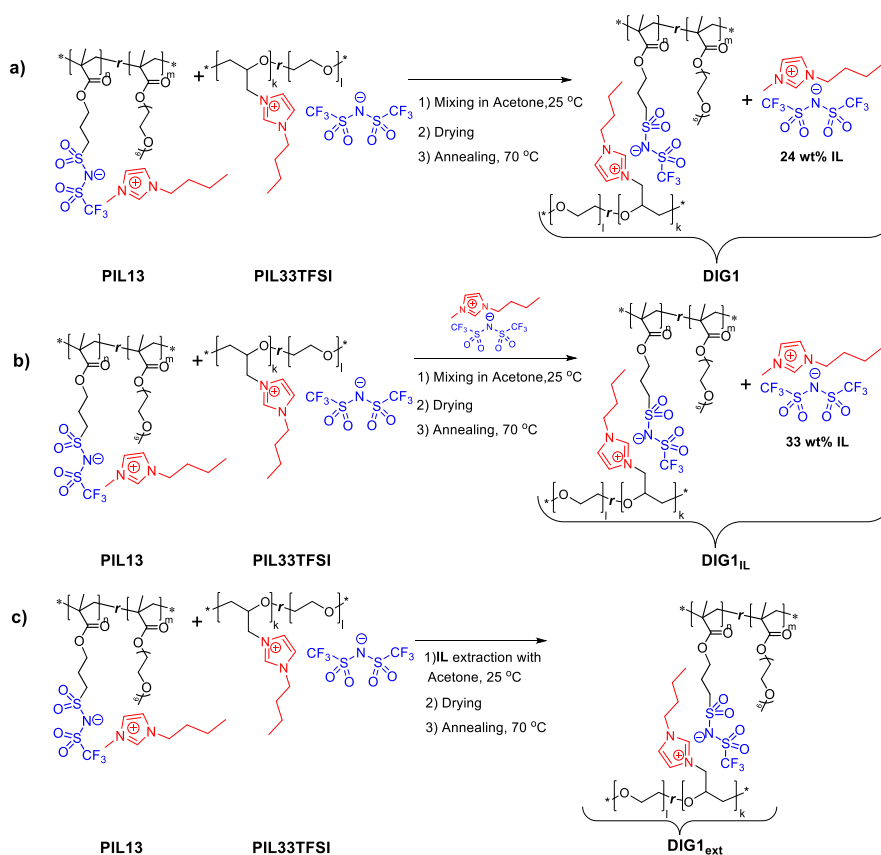
The choice of the PILs for the preparation of the model **DIG1** was governed by the following factors:

- 1) overall high ionic conductivity at 25°C;
- 2) the presence of highly delocalized and ion conductive 1-butyl-3-methylimidazolium and bis-(trifluoromethylsulfonyl)imide (TFSI) moieties in the structure of PILs (to form one of the most conductive IL, namely **BuMeImTFSI**, as a result of ion metathesis between oppositely charged PILs);
- 3) the easiness of PIL's synthesis and possibility to prepare them in large quantities.

Taking into account the above-mentioned requirements **PIL33TFSI** ($4.7 \times 10^{-6} \text{ S cm}^{-1}$) and **PIL13** ($5.9 \times 10^{-6} \text{ S cm}^{-1}$) were used to prepare **DIG1** (Scheme 3.1, a) through complex coacervation in acetone, which was in its turn selected for its low boiling point and the ability to dissolve both PILs and **BuMeImTFSI**. The coacervation was carried out by gradually adding a solution of **PIL33TFSI** in acetone to a solution of **PIL13** in acetone targeting the stoichiometry between ion pairs from each PIL. The formation of a hazy precipitate was immediate, with further vortexing yielding, depending on the solid content, either a single phase translucent gel-like coacervate (for a concentration of 20% wt./vol.) or a phase-separated mixture of a translucent elastic solid and a clear liquid (for a concentration of 3.4% wt./vol.) (Figure 3.2). Acetone was further evaporated under reduced pressure and the subsequent annealing for 24 h at 70 °C under vacuum yielded a **DIG1** through the formation of dynamic ionic cross-links and the release of 1-butyl-3-methylimidazolium and bis-(trifluoromethylsulfonyl)imide

(Scheme 3.1, a). Despite containing 67 wt% of the unentangled **PIL13**, model **DIG1** appeared as a rubbery solid, visually similar to **PIL33TFSI** (Figure 3.2).

Notably, **DIGs** with identical T_g and σ values (see sections 3.1.3 and 3.1.4) were obtained regardless of whether anionic **PIL13** was added to cationic **PIL33TFSI** or **PIL33TFSI** was added to **PIL13** during the coacervation step. The same results were also observed when polymer concentrations were varied from 1% to 20% (wt./vol.), and when acetone ($\epsilon_r = 20.7$, $b_p = 56^\circ\text{C}$)^{132–136} was substituted with higher dielectric constant solvents such as methanol ($\epsilon_r = 32.6$, $b_p = 65^\circ\text{C}$) or acetonitrile ($\epsilon_r = 36.0$, $b_p = 82^\circ\text{C}$). Although coacervates with different visual appearances (solid-like precipitates, liquid-like, colloidal, etc.) and colloidal properties (diameter of particles from several nanometers to several micrometers) were formed under the aforementioned conditions, the thermal annealing steps erased the processing history, thus yielding **DIGs** with identical physical, thermal and ion conducting properties in the end.



Scheme 3.1 Formation of model **DIG1**, **DIG1_{IL}** and **DIG1_{ext}**.

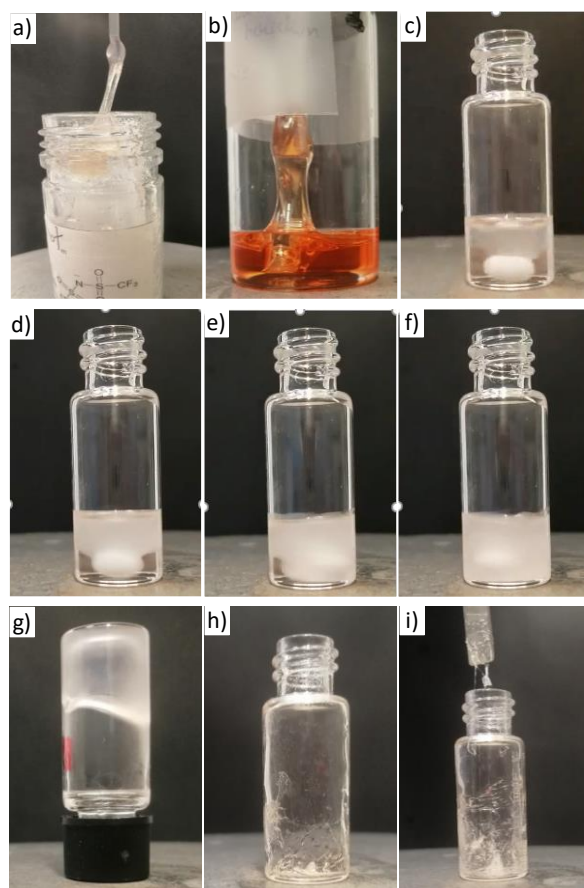


Figure 3.2 Optical images of **PIL33TFSI** (a, elastic solid), **PIL13** (b, viscous liquid), solid like coacervate (c to g) and the resulting **DIG1** (h and i, elastic solid).

3.1.2 Proof of dynamic ion exchange

The effective formation of ionic cross-links in model **DIG1** was then corroborated by the quantification of the amount of **BuMeImTFSI** released both by solvent extraction (*ex-situ* measurement) and quantitative ^{19}F NMR spectroscopy (*in-situ* measurement). For that reason, two additional DIG samples were prepared (Scheme 3.1, b and c). One sample, doped with extra IL and containing 33 wt% of IL in total (**DIG1_{IL}**), was synthesized by adding the supplementary amount of **BuMeImTFSI** to **PIL13** acetone solution before complex coacervation with **PIL33TFSI** solution (Scheme 3.1, b). The second sample (**DIG1_{ext}**) was obtained by the extensive extraction of the as formed **DIG1** with acetone and further drying under vacuum, thus yielding a coacervate-rich solid fraction (Scheme 3.1, c). While the obtained coacervate-rich solid fraction (**DIG1_{ext}**) amounted to 75.4 wt% of the initial PIL mixture, the extracted liquid fraction comprised 24.6 wt%.

The investigation of the extracted liquid phase from the formation of **DIG1_{ext}** by ^1H NMR spectroscopy confirmed that it consists exclusively of the released **BuMeImTFSI** and that no signals characteristic of **PIL33TFSI** or **PIL13** could be detected. This represents a first indication of the occurrence of an interchain ion exchange reaction between **PIL33TFSI** and **PIL13** leading to the

formation of ionic crosslinks and concomitant release of free IL. Moreover, the amount of extracted **BuMeImTFSI** was very close (i.e. 93.9%) to the theoretical amount of ion pairs that can be provided by **PIL33TFSI** and **PIL13**, thus again proving the completeness of the interchain ion exchange reactions.

In order to confirm that such efficient release of IL is not a consequence of the extraction process itself, the quantitative ^{19}F NMR spectroscopy was carried out *in-situ* on a **DIG1** prepared directly inside an NMR tube by mixing acetone- d_6 solutions of **PIL33TFSI** and **PIL13** while targeting a 1:1 stoichiometry between complementary ion pairs and using 1,4-bis(trifluoromethyl)benzene (TFM2B) as an internal standard (Figure 3.3). At a concentration of 3.4 wt./vol., the coacervation led to phase separation and precipitation of the polymer-rich complex coacervate at the bottom of the NMR tube, allowing for analysis of the supernatant solution alone. The comparison of ^{19}F NMR spectra for **PIL33TFSI**, and **PIL13**, **BuMeImTFSI** and **DIG1** corroborates the exclusive presence of **BuMeImTFSI** in the supernatant and the absence of any signal corresponding to **PIL33TFSI** or **PIL13**. The integration of ^{19}F signals of the released **BuMeImTFSI** and the TFM2B internal standard (at -78.8 and -62.7 ppm, respectively) suggests that ca. 90.8% of ion pairs of **PIL33TFSI** and **PIL13** have gone through interchain ion metathesis (i.e., corresponding to ca. 23.8 wt% of released IL) to form the **DIG1** through complex coacervation. This result is in a good agreement with the value determined by solvent extraction (i.e., 24.6 wt%, see *vide supra*). Besides experimental error, this rather small difference might also result from the fact that quantifications by ^{19}F NMR and solvent extraction were carried out before and after the annealing step of the coacervate, respectively.

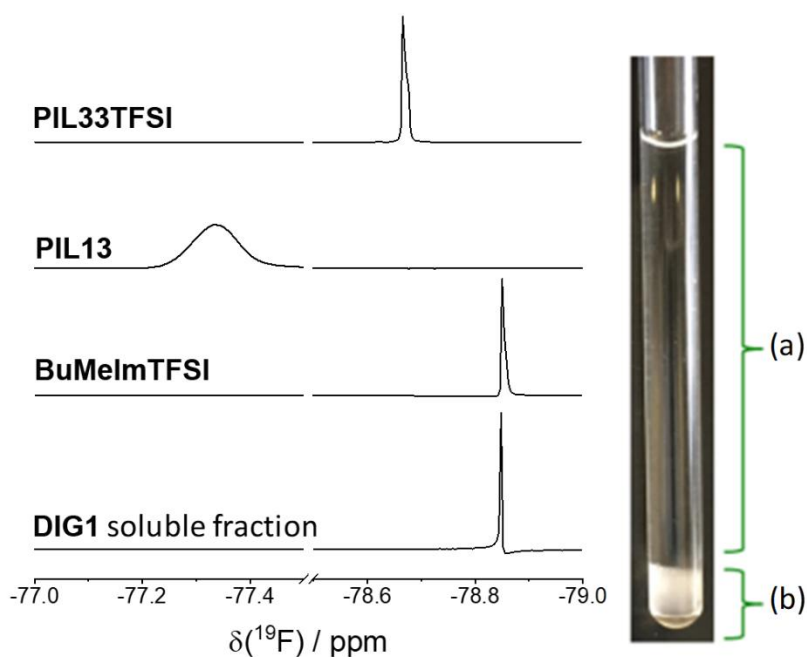


Figure 3.3 Stack of ^{19}F NMR spectra (acetone- d_6) of **PIL33TFSI**, **PIL13**, **BuMeImTFSI** and the soluble fraction of the **DIG1** coacervate; digital image of the NMR tube showing the analysis zone of the **DIG1** soluble fraction (a) and the phase-separated coacervate (b).

3.1.3 Thermal properties

3.1.3.1 Glass-transition temperature

The investigation of **DIG1** thermal properties started with the study of its glass transition temperature and the comparison with the thermal properties of the parent PILs (Table 3.1). The T_g of **DIG1** ($T_g = -39^\circ\text{C}$) falls between the T_g s of **PIL33TFSI** and **PIL13** ($T_g = -25$ and -46°C , respectively), aligning well with the value predicted by the Fox equation ($T_g = -40^\circ\text{C}$). Although this result might suggest a simple mixing behavior between the two polymers, the earlier findings (see section 3.1.2) strongly indicate that ion exchange between **PIL13** and **PIL33TFSI** leads to the formation of transient ionic crosslinks and the release of **BuMeImTFSI**. Thus, this intermediate T_g value can be explained by two opposing effects: an increase in T_g due to ionic crosslinks formation via ion metathesis, and a decrease in T_g due to the plasticizing effect of the released IL on the ionic network. The plasticizing effect of **BuMeImTFSI** becomes more pronounced when comparing the T_g values of DIGs with varying IL content:

T_g (IL content (wt%)): **DIG1_{ext}** (-30°C , 0 wt%) > **DIG1** (-39°C , 24 wt%) > **DIG1_{IL}** (-49°C , 33 wt%)

As the IL content in the DIG increases, the glass transition temperature progressively decreases.

Table 3.1 Selected properties of PILs, IL and DIGs

Sample	IL content (wt%)	T_g ($^\circ\text{C}$) ¹	T_{onset} ($^\circ\text{C}$) ²	σ at 25°C (S cm^{-1}) ³	G' at 25°C , 1 rad s^{-1} (kPa)
PIL33TFSI	0	-25	310	4.7×10^{-6}	46.9
PIL13	0	-46	165	5.9×10^{-6}	0.5
DIG1	23.8 ⁵ /24.6 ⁶	-39	250	7.2×10^{-6}	26.4
DIG1_{IL}	33 ⁵	-49	250	2.9×10^{-5}	3.7
DIG1_{ext}	0	-30	220	4.8×10^{-8}	157.3
BuMeImTFSI	100	-87 ⁴	330	3.3×10^{-3}	-

¹Determined by DSC. ²Determined by TGA. ³Determined by BDS. ⁴Reported by MacFarlane and Forsyth¹³⁷.

⁵Determined by quantitative ^{19}F NMR. ⁶Determined by gravimetry after solvent extraction.

3.1.3.2 Onset temperature of weight loss

The thermal degradation behavior of model DIGs and parent PILs was examined using TGA in air (Figure 3.4 and Table 3.1). **PIL13** exhibits the lowest thermal stability with T_{onset} of 165°C due to the presence of mobile oligoether side chains. **PIL33TFSI** with polyether backbone demonstrates a

higher T_{onset} value of 310 °C. Being a mixture of both PILs, **DIG1** shows thermal stability in between that of **PIL13** and **PIL33TFSI** (Table 3.1).

BuMeImTFSI composed of the same ion pairs as **PIL33TFSI**, but devoid of aliphatic ether fragments, exhibits the highest thermal stability with T_{onset} of 330 °C. The positive effect of IL presence on thermal stability of DIGs can be revealed through comparison of T_{onset} values for **DIG1_{ext}**, **DIG1** and **DIG1_{IL}**. The T_{onset} for **DIG1_{ext}** was found to be 30 °C lower than that of DIGs containing IL (**DIG1** and **DIG1_{IL}**).

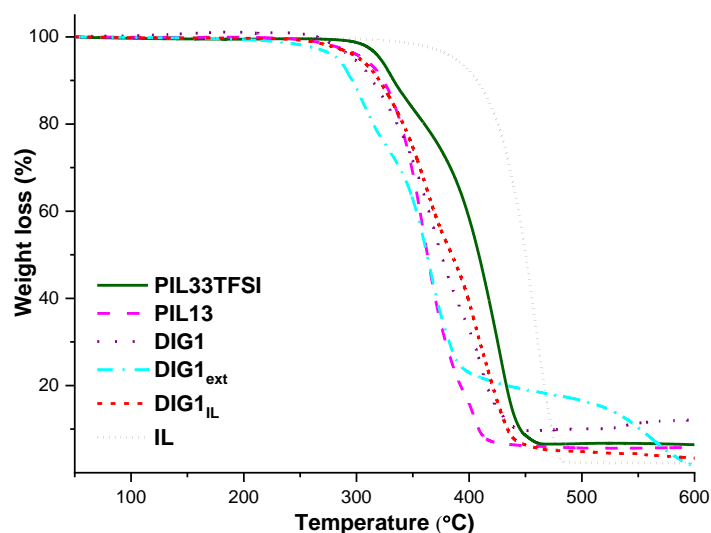


Figure 3.4 TGA curves of PILs, IL and DIGs (5°C min⁻¹, under air).

3.1.4 Ionic conductivity

The bulk anhydrous ionic conductivity of model DIGs was evaluated as a function of temperature using BDS (Figure 3.5, a). Similar to the parent PILs, the conductivity-temperature relationship did not exhibit linear Arrhenius behavior but could be accurately modelled using the Vogel–Fulcher–Tammann (VFT) equation. At 25 °C, the ionic conductivity of **DIG1** ($\sigma = 7.2 \times 10^{-6}$ S cm⁻¹) exceeds that of both **PIL13** (67 wt%, $\sigma = 5.9 \times 10^{-6}$ S cm⁻¹) and **PIL33TFSI** (33 wt%, $\sigma = 4.7 \times 10^{-6}$ S cm⁻¹). Further on, **DIG1** also demonstrates conductivities that surpass those of **PIL13** and **PIL33TFSI** at all but the highest temperatures (Figure 3.5, a).

To investigate the role of IL content on the ionic conductivity of DIGs, conductivity values for doped and extracted DIGs were compared:

$$\sigma (25^\circ\text{C}, \text{S cm}^{-1}): \mathbf{DIG1_{IL}} (2.9 \times 10^{-5}) > \mathbf{DIG1} (7.2 \times 10^{-6}) > \mathbf{DIG1_{ext}} (4.8 \times 10^{-8})$$

The results at 25 °C show that the ionic conductivity of **DIG1_{ext}** is more than two orders of magnitude lower than that of **DIG1**, highlighting that the ionic conductivity is primarily dominated by the release of free IL. Respectively, a significant 4-fold increase in conductivity is observed from **DIG1** to **DIG1_{IL}**, while adding extra amount of IL. While the resultant conductivity of **DIG1_{IL}** is still below

that of the neat **BuMeImTFSI** ($3.3 \times 10^{-3} \text{ S cm}^{-1}$), it is significantly higher than that of both neat **PIL13** and **PIL33TFSI**. The attempts to produce a **DIG_{IL}** having an overall **IL** content of 50 wt% yielded partial exudation of the **IL** from the **DIG** network, revealing the limits of this approach for **DIG1** system.

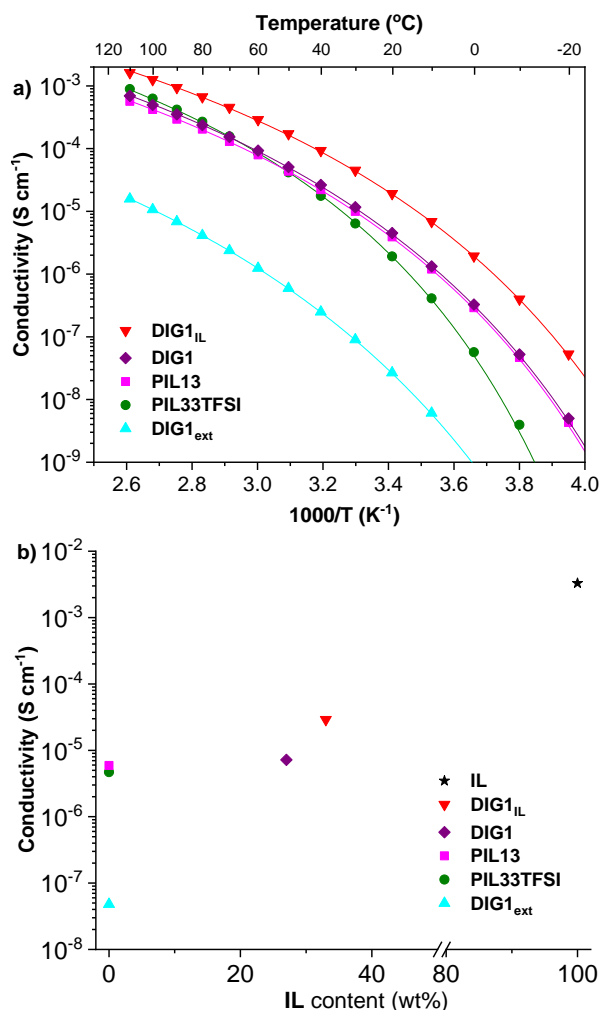


Figure 3.5 Bulk ionic conductivity for DIGs, PILs and IL as a function of reciprocal temperature (a) and **IL** content (b).

3.1.5 Rheological properties

The viscoelastic properties of **DIG1**, **DIG_{1ext}** and **DIG_{1IL}** were measured between -15 and 75 $^{\circ}\text{C}$ and master curves were built through time-temperature superposition using a reference temperature of $T_0 = 25^{\circ}\text{C}$. While **DIG1** has a macroscopic (visual) appearance comparable to **PIL33TFSI** (Figure 3.2), it exhibits specific rheological features distinct from **PIL33TFSI** (Figure 2.32, a) and **PIL13** (Figure 2.22, a). At high frequencies ($10^0 < \omega \cdot a_T < 10^3$), the storage (G') and loss (G'') moduli of **DIG1** nearly overlap, with a $\omega^{0.5}$ dependence in a range of frequencies spanning over seven decades. At lower frequencies ($10^{-5} < \omega \cdot a_T < 10^0$), they follow the typical disentanglement behavior already seen for **PIL13**, with the exception that the plateau moduli (**DIG1**: $G_N \approx 80 \text{ kPa}$) become significantly higher for **DIG_{1ext}** ($G_N \approx 100 \text{ kPa}$) and lower for **DIG_{1IL}** ($G_N \approx 36 \text{ kPa}$). These results are consistent with the

plasticization and dilution of entanglements caused by the presence of **BuMeImTFSI**. The $\omega^{0.5}$ dependence is typical of a near-critical gel in the vicinity of the sol–gel transition^{138,139}, and indicates that the formation of ion pairs across the backbones of PILs results in the transient crosslinks with a large distribution of lifetimes in the range from 1 ms to 1 s at the reference temperature. Similar near-critical gel behavior was previously observed for complex coacervates resulting from inorganic anionic polytungstate $\{W_{12}\}(\text{Li}_6\text{H}_2\text{W}_{12}\text{O}_{34})$ and zwitterionic poly(sulfobetainemethacrylamide) (PSBMA) in aqueous solutions of LiCl with concentrations ranging between 0.2 and 0.5 M^{138,140,141}. The significant left-shift of the TTS for lower amounts of IL may not be due to the plasticization effect of **BuMeImTFSI** alone, as the master curves are already referenced at $T_0 = 25^\circ\text{C}$. The presence of IL also strongly decreases the lifetime of transient ionic crosslinks, as evidenced by the increase in crossover frequency (by a factor ca. 60 from **DIG1_{IL}** to **DIG1_{ext}**). Although the presence of extra IL in **DIG1_{IL}** enhanced the ion conducting properties ($\sigma = 2.9 \times 10^{-5} \text{ S cm}^{-1}$ at 25°C) compared to **DIG1** ($\sigma = 7.2 \times 10^{-6} \text{ S cm}^{-1}$ at 25°C), it also leads to the decrease in stiffness (G' for **DIG1_{IL}** at 25°C and $1 \text{ rad s}^{-1} \sim 4 \text{ kPa}$ is six times lower than for **DIG1**) (Figure 3.6, c).

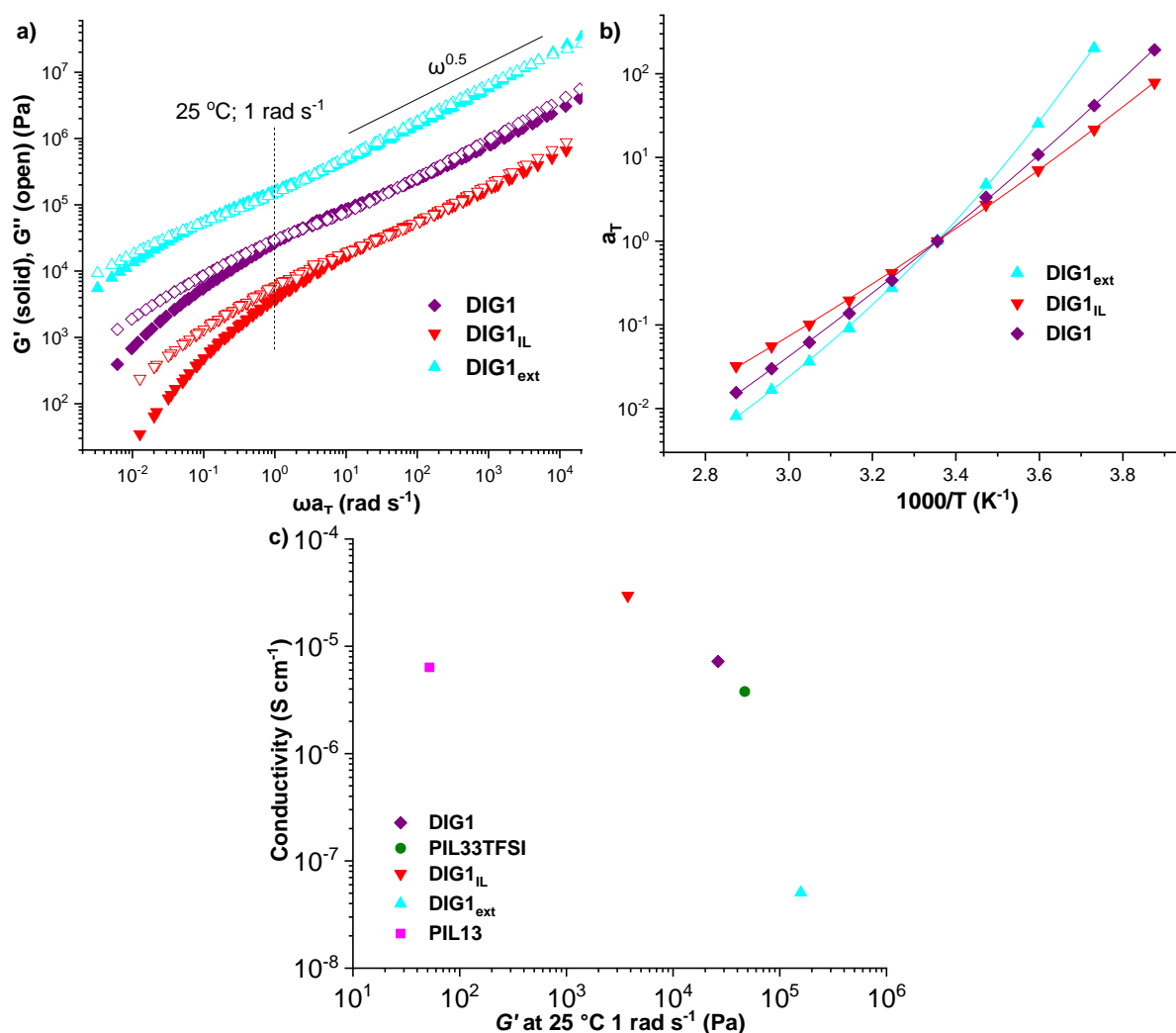


Figure 3.6 TTS master curves referenced at $T_0 = 25\text{ }^{\circ}\text{C}$ for DIGs obtained by SAOS rheology at temperatures ranging from -15 to $75\text{ }^{\circ}\text{C}$ **(a)**, corresponding a_T shift factors and WLF best fits at $T_0 = 25\text{ }^{\circ}\text{C}$ for DIGs **(b)**, ionic conductivity at $25\text{ }^{\circ}\text{C}$ as a function of the storage modulus (G') obtained at $25\text{ }^{\circ}\text{C}$ and 1 rad s^{-1} **(c)**.

3.2 Approaches for further improvement of DIGs properties

Although the model **DIG1** has demonstrated an increase in ionic conductivity in comparison with parent PILs (see section 3.1.4) that can serve as a proof-of-concept for the realization of the aim of the work, the mechanical properties of **DIG1** (see section 3.1.5) were lower than expected. Thus, two new approaches for the improvement of the viscoelastic properties of DIGs have been further suggested (Figure 3.7).

The first proposed approach involves the introduction of the PIL building blocks with sulfonate (SO_3^-) anions differ from TFSI analogue by the small size of the ion and charge localization (Figure 3.7). Respectively, the sulfonate anion has significantly stronger ion interaction with counter cations compared to the TFSI moiety¹⁴². Therefore, the incorporation of PILs with SO_3 anions into DIGs should result in the formation of much stronger dynamic ionic cross-links and should lead to the enhancement of the viscoelastic properties. Following this approach, four DIGs (**DIG2-DIG5**) containing PILs with sulfonate anion and different counter cations were prepared and investigated (see section 3.3. and Scheme 3.2).

The second suggested approach is based on the utilization of ionic **AB-b-C** type block copolymers as building blocks in the preparation of DIGs (Figure 3.7). At this, the AB-block was formed by random copolymerization of highly conductive anionic or cationic monomers with poly(ethylene glycol) methyl ether methacrylate, while the C-block was obtained by post polymerization of 2-phenylethyl methacrylate or (1-naphthyl)methyl methacrylate (see Scheme 3.3). The partial incompatibility between ionic and neutral blocks in suggested ionic **AB-b-C** type block copolymers should result in a microphase-separated morphology, where the neutral high T_g domains will be responsible for the mechanical properties, while the soft ionic domains with low T_g will possess elevated concentration of mobile ions and will enhance the ionic conductivity of the system. Similar to parent ionic block copolymers, the prepared DIGs are also expected to show the microphase segregation as well as the enhanced stiffness. Consequently, seven DIGs (**DIG6-DIG13**) composed of ionic block copolymers were synthesized and studied (see section 3.4. and Scheme 3.3).

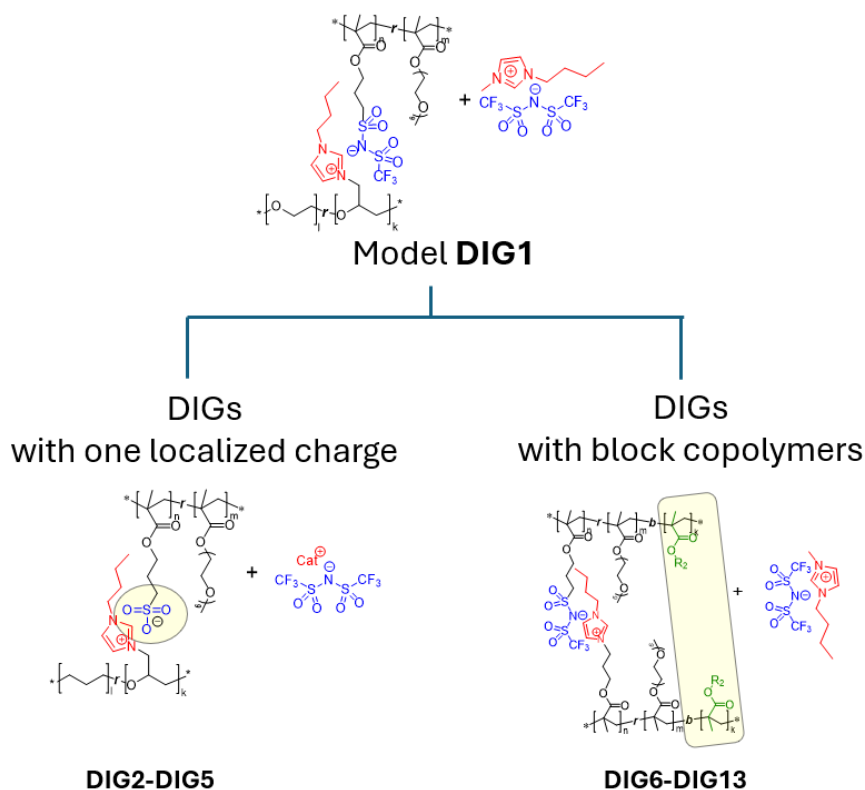


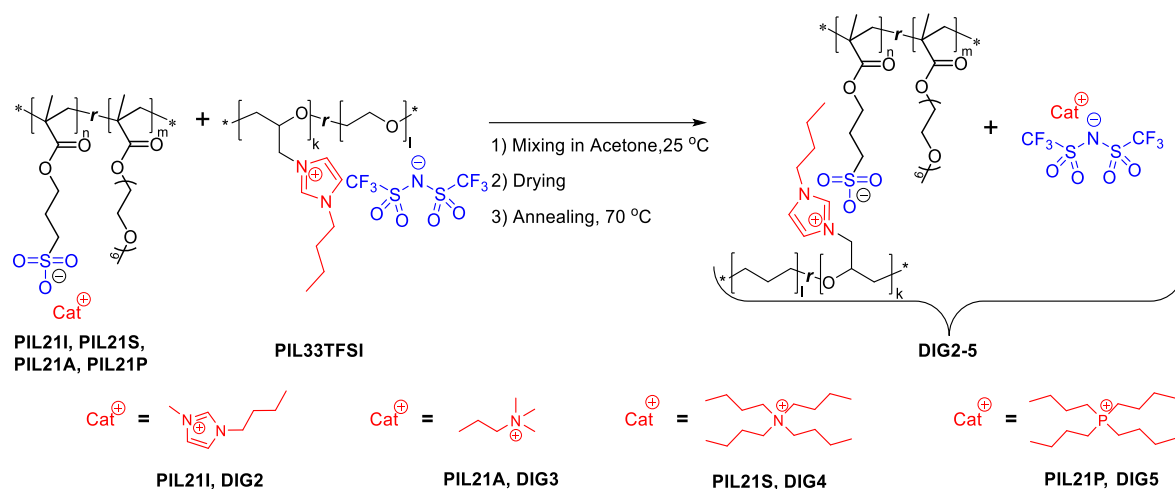
Figure 3.7 Suggested approaches for the improvement of DIGs viscoelastic properties.

3.3 1st approach for the improvement of DIGs - introduction of one localized charge (DIG2-DIG5)

3.3.1 Synthesis and characterization

Similarly to **DIG1**, the dynamic ion gels **DIG2-DIG5** were synthesized in acetone by complex coacervation of oppositely charge PILs (Scheme 3.2). **PIL33TFSI** was used as cationic building block, while one of the four sulfonate PILs (**PIL21I**, **PIL21S**, **PIL21A**, and **PIL21P**) having the same structure of the main chain, identical molecular weight, but differ in the nature of the counter cation were used as the anionic building block. Thus, the four obtained DIGs (**DIG2-DIG5**) differed by the structure of the *in-situ* generated TFSI ILs (Table 3.3). In its turn, this allowed for the investigation of two factors affecting the DIGs properties: 1) the strength level of ion pairing between oppositely charged polymer chains when chemically bonded TFSI anion in **PIL13** was substituted by SO_3 anion in **PIL21I**, **PIL21S**, **PIL21A**, and **PIL21P**; 2) the influence of the released IL structure. The effective formation of ionic cross-links in **DIG2-DIG5** was further confirmed by quantitative ^{19}F NMR spectroscopy similar to **DIG1**. The analysis revealed that coacervation of various **PIL21** with **PIL33TFSI** results in the release of 75-90% of respective IL. Such difference within a series of **DIG2-DIG5** and between these DIGs and **DIG1** can be explained by the influence of the following factors: 1) the dissociation of the ion pairs in solution (for example, the level of dissociation between chemically bonded SO_3 anion and bulky asymmetric BuMelm cation in **PIL21I** will be higher in comparison with

PIL21A possessing small ammonium cation with localized charge); 2) the solubility of the polymer-rich complex coacervate in acetone- d_6 and its degree of precipitation.



Scheme 3.2 Synthetic route for the preparation of **DIG2-DIG5**.

3.3.2 Thermal properties

3.3.2.1 Glass-transition temperature

The DSC investigation of DIGs revealed that **DIG2** and **DIG3** exhibited only one transition temperature, while **DIG4** and **DIG5** showed two distinct transitions (Table 3.3). The first transition observed at negative temperatures for all DIGs was associated with their glass transition temperature and was strongly dependent on the nature of the *in-situ* generated IL. This dependence can be summarized as follows:

T_g (°C): **DIG3** (PrMe₃NTFSI, -22) > **DIG4** (Bu₄NTFSI, -37) > **DIG2** (BuMeImTFSI, -43) > **DIG5** (Bu₄PTFSI, -49)

A comparison of these results with the T_g values of parent PILs provides further insights. First, this trend is consistent with the T_g s observed for the parent anionic PILs **PIL21A-PIL21P** (Table 3.2): the highest T_g was found for PILs with ammonium counter cations, followed by **PIL21A** with imidazolium cation, and **PIL21P** with phosphonium cation finishing the row. Second, **DIG2** and **DIG4** exhibited T_g values lower than both parent materials, while **DIG5** had a T_g in between the parent PILs, similar to the model **DIG1**. Finally, **DIG3** displayed a T_g higher than that of both parent PILs. As discussed in Section 3.1.3.1, the observed T_g values result from the interplay of two opposing factors. The first factor is the effective formation of ionic crosslinks between the two oppositely charged building blocks, which tends to increase the overall T_g of the material by the formation of the double-stranded or ladder-type polymer. The second factor is the plasticizing effect of the *in-situ* generated ILs, which has the exact opposite effect, i.e. decreasing of polymer glass transition temperature. A more detailed analysis of these factors would require the measurement of the T_g for the generated ILs, as well as for the neat polymer coacervate. Without such investigation, the observed trend can also be

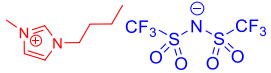
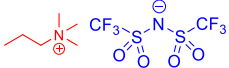
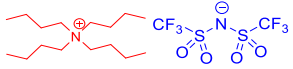
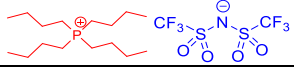
attributed to the increase in the ionic radius of the cations in the respective ILs. As the ionic radius increases from small, asymmetric ammonium to bulkier tetrabutylammonium and imidazolium cations, and eventually to tetrabutylphosphonium one, there is a reduction in oppositely charged polymer chains interactions and an increase in polymer free volume¹⁴³, that in its turn contributes to the decrease in T_g .¹⁴⁴

Table 3.2 Comparison of T_g s for **DIG3-DIG5** and their parent PILs.

T_g (°C)		PIL21A	PIL21S	PIL21I	PIL21P
		-29	-36	-40	-52
PIL33TFSI	-25	-22 DIG3	-37 DIG4	-43 DIG2	-49 DIG5

The second transition, which occurs above room temperature at 92 and 61°C in **DIG4** and **DIG5** respectively, was attributed to the melting process of the *in-situ* formed ILs. Thus, the melting temperature observed for **DIG4** at 92°C aligns precisely with that reported for the neat Bu₄NTFSI¹⁴⁵. Similarly, the melting temperature of 61°C observed in **DIG5** is perfectly matching the melting point of neat Bu₄PTFSI (65°C) reported previously¹⁴⁶.

Table 3.3 Selected properties of DIGs with sulfonate group

DIG		DIG properties				
Sample	IL generated <i>in situ</i>	G' at 29°C, 1 rad s ⁻¹ (kPa)	σ at 25°C (S cm ⁻¹)	T_g , (°C) ¹	T_m , (°C) ¹	T_{onset} , (°C) ²
DIG2		61.9	5.7×10^{-6}	-43	-	205
DIG3		34.6	2.4×10^{-6}	-22	-	205
DIG4		295.2	1.4×10^{-7}	-37	90	210
DIG5		142.3	5.6×10^{-7}	-49	61	210

¹Determined by DSC (5 K min⁻¹). ²Determined by TGA (5 K min⁻¹).

3.3.2.2 Onset temperature of weight loss

The thermal degradation behaviour of **DIG2-DIG5** was studied via TGA. The T_{onset} values for **DIG3-DIG5** were falling within a narrow range of 205 to 210°C and were practically independent of the nature of the *in situ* formed ILs:

T_{onset} (°C): **DIG5** (Bu₄PTFSI, 210) \approx **DIG4** (Bu₄NTFSI, 210) $>$ **DIG2** (BuMeImTFSI, 205) \approx **DIG3** (PrMe₃NTFSI, 205)

This trend was found to coincide with the behavior observed in parent anionic PILs, where T_{onset} was only moderately influenced by the nature of the counter cation (see section 2.2.3). Although, it is noteworthy that DIGs demonstrated a small improvement in thermal stability compared to their parent anionic PILs.

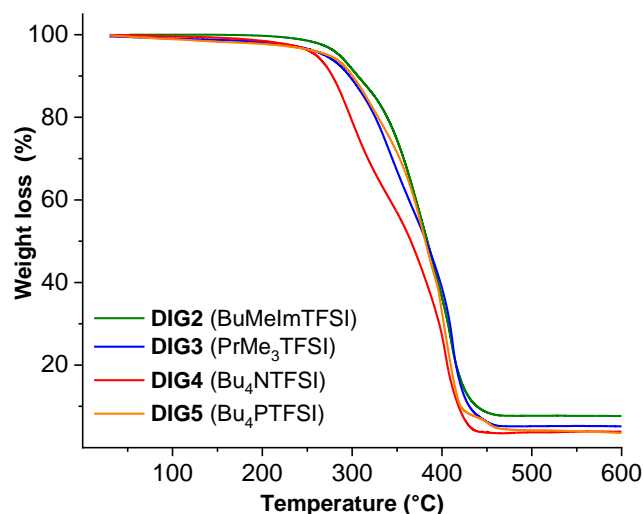


Figure 3.8 TGA traces of **DIG2-DIG5** ($5^{\circ}\text{C min}^{-1}$, under air).

3.3.3 Ionic conductivity

The ionic conductivity of DIGs was investigated as a function of temperature (Table 3.3 and Figure 3.9). The observed values varied from 5.7×10^{-6} to $1.4 \times 10^{-7} \text{ S cm}^{-1}$ at 25°C and were influenced by the nature of the *in situ* formed IL:

σ (25°C , S cm^{-1}): **DIG2** (BuMeImTFSI, 5.7×10^{-6}) > **DIG3** (PrMe₃NTFSI, 2.4×10^{-6}) > **DIG5** (Bu₄PTFSI, 5.6×10^{-7}) > **DIG4** (Bu₄NTFSI, 1.4×10^{-7})

DIG2 and **DIG3** showed one order of magnitude higher ionic conductivity than **DIG4** and **DIG5**. This difference can be attributed to the physical state of the *in situ* formed IL at the temperature of ionic conductivity measurement (25°C): the Bu₄NTFSI and Bu₄PTFSI ILs are crystalline (that can also be seen from the DSC traces of **DIG5** and **DIG4**), whereas BuMeImTFSI and PrMe₃NTFSI ILs remain liquid. The order of **DIG2** – **DIG4** conductivity is fully consistent with previously reported data on the conductivity of the respective neat ionic liquids^{137,145–147}. As in the case of model **DIG1**, it was of high importance to further compare the conductivity of **DIG2** – **DIG4** with that of their parent PILs (Table 3.4). It can be concluded that the conductivity trend observed in these DIGs is coinciding with the that identified for the parent anionic PILs (Table 3.4). In contrast to **DIG1**, the conductivity of **DIG3**, **DIG4** and **DIG5** was not exceeding the conductivity of both parent PILs. While their conductivity was higher than that of anionic PILs component, it was still inferior to the conductivity of the cationic PIL33TFSI. Only **DIG2** was capable to deliver the ionic conductivity which was higher in comparison with ionic conductivities of both parent PILs (Table 3.4). This result can be explained by the physical state (see *vide supra*) and the conductivity of the *in situ* formed IL.

σ (25°C, S cm⁻¹): BuMeImTFSI (8.9×10^{-3}) > PrMe₃NTFSI (3.3×10^{-3}) > Bu₄PTFSI (not measured, solid) > Bu₄NTFSI (not measured, solid)

This finding suggests that by special design of the PILs building blocks it is possible to generate highly conductive ionic liquids during complex coacervation, and thus to create materials with ionic conductivity exceeding both parent polyelectrolytes.

Table 3.4 Comparison of ionic conductivity for **DIG2-DIG5** and parent PILs at 25°C.

σ at 25°C (S cm ⁻¹)		PIL21I	PIL21A	PIL21P	PIL21S
		1.9×10^{-6}	4.8×10^{-7}	3.3×10^{-7}	9.0×10^{-8}
PIL33TFSI	4.7×10^{-6}	5.7×10^{-6} DIG2	2.4×10^{-6} DIG3	5.6×10^{-7} DIG5	1.4×10^{-7} DIG4

The influence of the ionic crosslinks strength on ionic conductivity was evaluated by comparison of **DIG1** and **DIG2**. The transition from **DIG1** to **DIG2**, both having the same **BuMeImTFSI** IL inside, but differ in the nature of the chemically bonded ion (TFSI and SO₃ anions in **DIG1** and **DIG2**, respectively) in the anionic building block, resulted only in a minor decrease in ionic conductivity from 7.2×10^{-6} to 5.7×10^{-6} S cm⁻¹ at 25°C. Thus, it can be concluded that the nature of the *in situ* formed IL plays a more significant role in ionic conductivity of a DIG than the type of the ions chemically bonded to the polymer main chain.

Further, the ionic conductivity of **DIG2 – DIG4** was measured across a temperature range of 0 to 110°C (Figure 3.9). The ionic conductivity of all studied DIGs was increasing with the rise in temperature. It is noteworthy that while **DIG2** and **DIG3** followed a Vogel-Fulcher-Tammann (VFT) dependence, **DIG4** and **DIG5**, which contain crystalline ILs, did not obey the VFT equation. This deviation is evidenced by the inflections in their conductivity curves in the 60-70°C region.

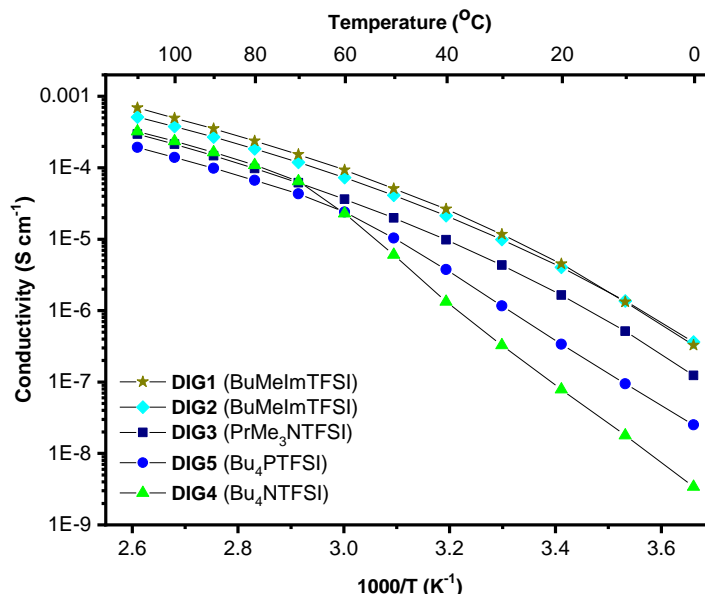


Figure 3.9 Ionic conductivity measured by BDS as a function of reciprocal temperature for **DIG2-DIG5**.

3.3.4 Rheological properties

The rheological behaviour of **DIG2-DIG5** was investigated between 25 and 100°C via analysis of TTS master curves referenced at $T_0 = 29^\circ\text{C}$ (Figure 3.10, a). Examining TTS plots, the $\omega^{0.5}$ dependence was observed for all four synthesized DIGs, thus confirming the successful gel formation. **DIG4** and **DIG5** with crystalline ILs, exhibited $\omega^{0.5}$ dependence on the whole range of applied frequencies ($10^{-5} < \omega \cdot a_T < 10^3$). Contrary, DIGs with liquid ILs (**DIG2** and **DIG3**) had similar behaviour only at high frequencies ($10^0 < \omega \cdot a_T < 10^3$). In the lower frequency region ($10^{-5} < \omega \cdot a_T < 10^0$), they followed the typical disentanglement behavior already seen and discussed for **DIG1** (see section 3.1.5). The shift factors (a_T) used in the TTSs for all DIGs obeyed the WLF law (Figure 3.10, b).

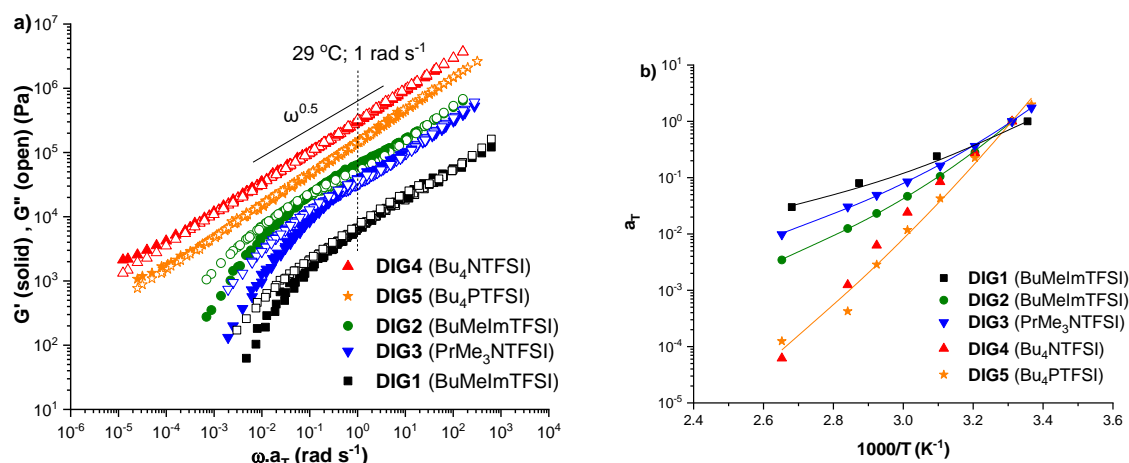
To simplify the comparison of DIGs mechanical properties it was decided to compare the values of their storage modulus (G') at 29°C and a frequency of 1 rad s⁻¹. The correlation of G' for **DIG2-DIG5** revealed that all sulfonate-based DIGs exhibited higher mechanical properties than model **DIG1** (Figure 3.10, a). This result can be attributed to the stronger dynamic crosslinks in **DIG2-DIG5** in comparison with **DIG1** due to the substitution of the chemically bonded and highly delocalized TFSI anion by the small SO₃ anion with localized charge. As in the case of **DIG2-DIG5** and **DIG1** the generated ILs are different, the influence of interaction between the two oppositely charged polymer chains on the viscoelastic properties of DIGs can be isolated by comparing **DIG1** and **DIG2**, in which the same **BuMeImTFSI** IL is formed *in situ* during complex coacervation. It can be concluded that the more intense is the interaction between the two oppositely charged PILs the higher is the observed storage modulus ($G' = 26.4$ and 61.9 Pa for **DIG1** and **DIG2**, respectively).

It was found that the mechanical properties of DIG, and particularly the storage modulus, are influenced by the nature of the released IL as well. This relationship can be summarized as follows:

G' (kPa, 29°C, 1 rad s⁻¹): **DIG4** (Bu₄NTFSI, 295.2) > **DIG5** (Bu₄PTFSI, 142.3) > **DIG2** (BuMeImTFSI, 61.9) > **DIG3** (PrMe₃NTFSI, 34.6) > **DIG1** (BuMeImTFSI, 26.4)

In the case of **DIG4** and **DIG5**, the enhancement of G' can be explained by the generation of solid ionic liquids during complex coacervation. From one hand, due to the interaction with polymer chains such crystalline compounds can reinforce the material. From another, ILs being in the solid state stop plasticizing the polymer matrix.

According to the thesis goals both the viscoelastic properties and the ionic conductivity of DIGs are the crucial factors for their application in supercapacitors (see section I). Thus, the comparison of DIGs was further continued by plotting the the ionic conductivity at 25°C as a function of the storage modulus (G') for **DIG2-DIG5** and their respective parent PILs (Figure 3.10, c). Notably, **DIG2** exhibited both enhanced ionic conductivity and improved stiffness relative to its parent PILs, underscoring the advantageous effect of DIG formation and establishing a record among studied DIGs.



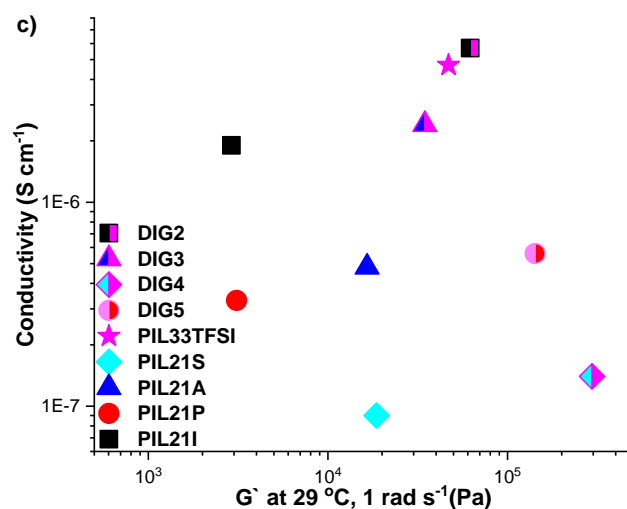
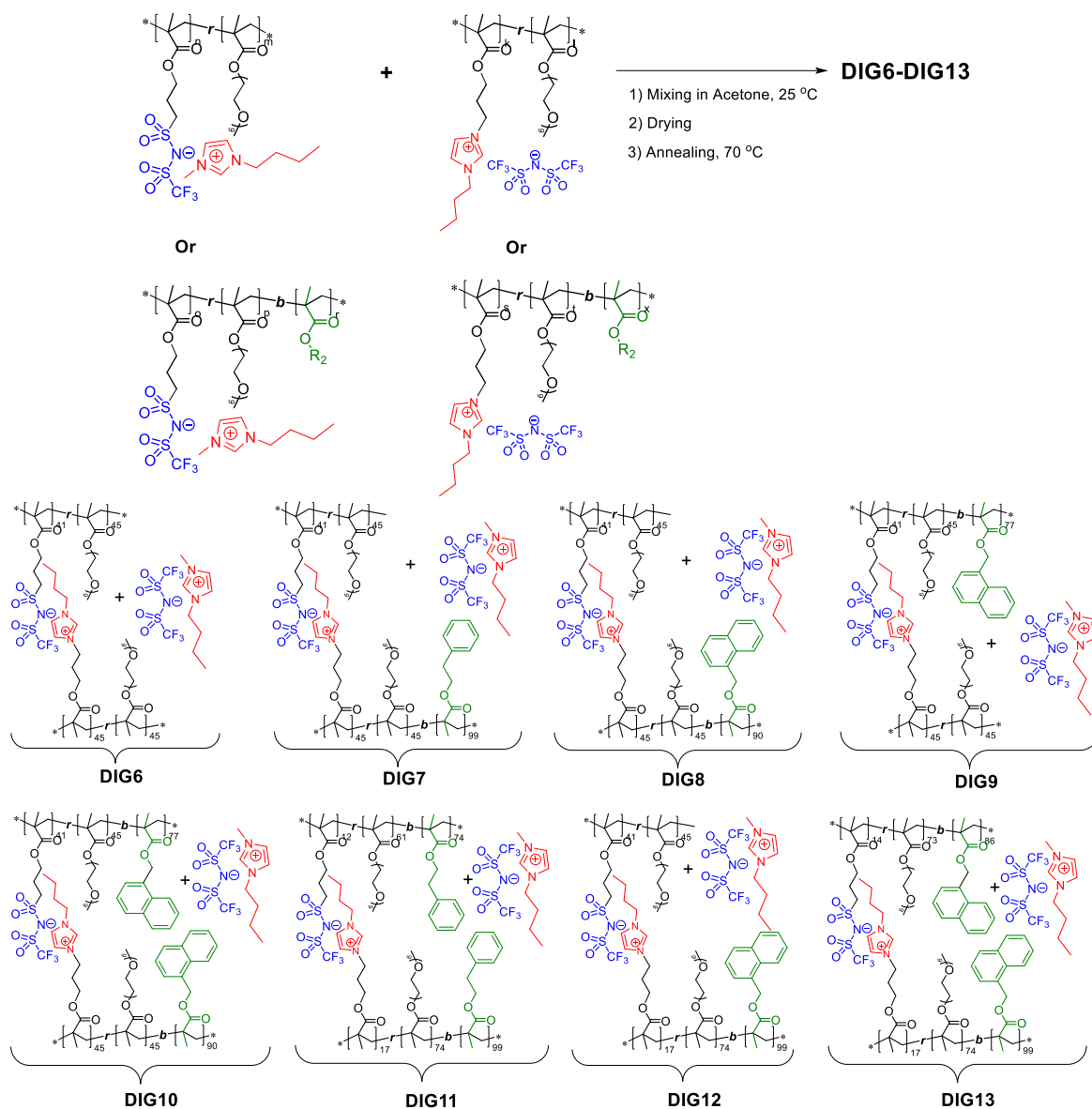


Figure 3.10 TTS master curves of DIGs obtained by frequency sweep experiments performed from 25 to 100 °C and referenced at $T_0 = 29$ °C (a), corresponding a_T shift factors and WLF best fits at $T_0 = 29$ °C for DIGs (b). Ionic conductivity at 25 °C as a function of the storage modulus (G') obtained at 29 °C and 1 rad s⁻¹ (c).

3.4 2nd approach for the improvement of DIGs - introduction of block copolymers (DIG6-DIG13)

3.4.1 Synthesis and characterization

DIGs with block copolymers were obtained using the same procedure described previously for **DIG1-DIG5** (Scheme 3.3). **PIL19**, **PIL22-PIL25** were used as the cationic building blocks, while **PIL12**, **PIL26-PIL29** having similar structures, but oppositely charged were applied as anionic building blocks. Their solution mixing in stoichiometric ratios resulted in the formation of seven DIGs entirely composed of block copolymers (**DIG7-DIG13**) and one DIG (**DIG6**) derived from mixing of random copolymers, which later served as a reference (Scheme 3.3, Table 3.5). The effective formation of ionic cross-links in **DIG6-DIG13** was again confirmed by quantitative ¹⁹F NMR spectroscopy (*in-situ* measurement). It was found that the coacervation of oppositely charged block copolymers provides the release of 85-92% of respective IL. This result is in agreement with what was observed for the model **DIG1** and may be a consequence of the facts that the same anionic monomer **ILM1** was used for the preparation of the block copolymers **PIL12**, **PIL26-PIL29** as well as that the cationic monomer **ILM2** produced copolymers with a structure close to **PIL33TFSI**.



Scheme 3.3 Synthetic route for the preparation of **DIG6-DIG13**

Table 3.5 Selected properties of **DIG6-DIG13**

DIG	PEGM : ILM	Anionic PIL	Cationic PIL	G' at 25°C, 1 rad s ⁻¹ (kPa)	σ at 25°C (S cm ⁻¹)	T _{g1} , (°C) ¹	T _{g2} , (°C) ¹	T _{onset} , (°C) ²	Domain length (nm) ³
DIG6	1:1	poly(ILM1 ₄₁ - <i>r</i> -PEGM ₄₅)	poly(ILM2 ₄₅ - <i>r</i> -PEGM ₄₅)	0.9	1.0×10 ⁻⁵	-48	-	160	-
DIG7		poly(ILM1 ₄₁ - <i>r</i> -PEGM ₄₅)	poly[(ILM2 ₄₅ - <i>r</i> -PEGM ₄₅)- <i>b</i> -PhEtM ₉₉]	7.9	5.8×10 ⁻⁷	-49	31	185	HPC, 59.0±9.8
DIG8		poly(ILM1 ₄₁ - <i>r</i> -PEGM ₄₅)	poly[(ILM2 ₄₅ - <i>r</i> -PEGM ₄₅)- <i>b</i> -Napht ₉₀]	21.5	2.7×10 ⁻⁷	-47	83	160	HPC, 55.6±3.1
DIG9		poly[(ILM1 ₄₁ - <i>r</i> -PEGM ₄₅)- <i>b</i> -Napht ₇₇]	poly(ILM2 ₄₅ - <i>r</i> -PEGM ₄₅)	18.4	1.1×10 ⁻⁶	-45	77	200	Disordered
DIG10		poly[(ILM1 ₄₁ - <i>r</i> -PEGM ₄₅)- <i>b</i> -Napht ₇₇]	poly[(ILM2 ₄₅ - <i>r</i> -PEGM ₄₅)- <i>b</i> -Napht ₉₀]	160.3	6.5×10 ⁻⁷	-43	78	180	L, 68.0±13.0
DIG11	1:5	poly[(ILM1 ₁₂ - <i>r</i> -PEGM ₆₁)- <i>b</i> -PhEt ₇₄]	poly[(ILM2 ₁₇ - <i>r</i> -PEGM ₇₄)- <i>b</i> -PhEtM ₉₉]	90.6	2.1×10 ⁻⁶	-55	-	170	L, 33.9±1.0
DIG12		poly(ILM1 ₄₁ - <i>r</i> -PEGM ₄₅)	poly[(ILM2 ₁₇ - <i>r</i> -PEGM ₇₄)- <i>b</i> -Napht ₉₉]	49.9	2.0×10 ⁻⁶	-49	-	190	L, 42.3±3.6
DIG13		poly[(ILM1 ₁₄ - <i>r</i> -PEGM ₇₃)- <i>b</i> -Napht ₈₆]	poly[(ILM2 ₁₇ - <i>r</i> -PEGM ₇₄)- <i>b</i> -Napht ₉₉]	1826.8	7.5×10 ⁻⁷	-54	-	185	L/HPC, 40.0±4.1

¹Determined by DSC (5 K min⁻¹). ²T_{onset} determined by TGA (5 K min⁻¹). ³By AFM on block copolymer-coatings, L – lamellar, HPC - hexagonally packed cylinders.

3.4.2 Thermal properties

3.4.2.1 Glass-transition temperature

Through DSC analysis, it was determined that all DIGs based on block copolymers with a PEGM:ILM ratio = 1:1 exhibited two distinct transition temperatures, while DIGs with PEGM:ILM ratio = 5:1 demonstrated only one transition (Table 3.5). This behavior was similar to that observed in the parent block copolymers and can be identically explained by plasticization of hard segments with side oligomeric PEG chains, when the concentration of the later was significantly increased (see section 2.3.3.1.2). The observed low-temperature transition was associated with the glass transition temperature of the soft ionic segment (T_{gl}). Three key insights can be drawn from the obtained data (Table 3.5):

1. The presence of only one transition in this temperature region confirms the successful coacervation of the two oppositely charged ionic copolymers.
2. All T_{gl} values observed in DIGs were lower than or equal to those of the parent random or block copolymers, which can be attributed to the plasticizing effect of the *in situ* formed IL. For example, **DIG10** exhibited a T_{gl} of -43°C, while the parent poly[(**ILM1**₄₁-*r*-PEGM₄₅)-*b*-Napht₇₇] and poly[(**ILM2**₄₅-*r*-PEGM₄₅)-*b*-Napht₉₀] both showed T_{gl} attributed to the ionic segments at -40°C.
3. DIGs derived from copolymers with PEGM:ILM ratio = 5:1 showed lower T_{gl} in comparison to those composed of copolymers with PEGM:ILM ratio = 1:1 (Table 3.5, **DIG6-DIG10** and **DIG11-DIG13**).

The second transition was associated with the glass transition temperature of the neutral segment (T_{g2}). Similarly to T_{gl} , the presence of only one T_{g2} confirmed the successful coacervation of the two block copolymers. Several dependences can be pointed out:

1. DIGs derived from block copolymers showed lower T_{g2} in comparison with parent PILs that can also be explained by plasticization of polymer chains by the *in situ* formed IL.
2. DIGs based on block copolymers with poly(PhEtM) blocks commonly demonstrated lower T_{g2} than those obtained by coacervation of block copolymers with poly(Napht) blocks (Table 3.5, **DIG7** and **DIG8-DIG10**).

3.4.2.2 Onset temperature of weight loss

Figure 3.10 illustrates the thermal degradation behavior of DIGs with block copolymers. The onset degradation temperatures can be summarized as follows:

T_{onset} (°C): **DIG9** (200) > **DIG12** (190) > **DIG13** (185) = **DIG7** (185) > **DIG10** (180) > **DIG11** (170) > **DIG8** (160) = **DIG6** (160)

Overall, DIGs with block copolymers demonstrated a thermal stability comparable to that of their parent materials, with T_{onset} values ranging from 160°C to 200°C. This suggests that, even after the formation of DIGs, the thermal stability remains primarily limited to the degradation of the side oxyethylene chains in ionic segments.

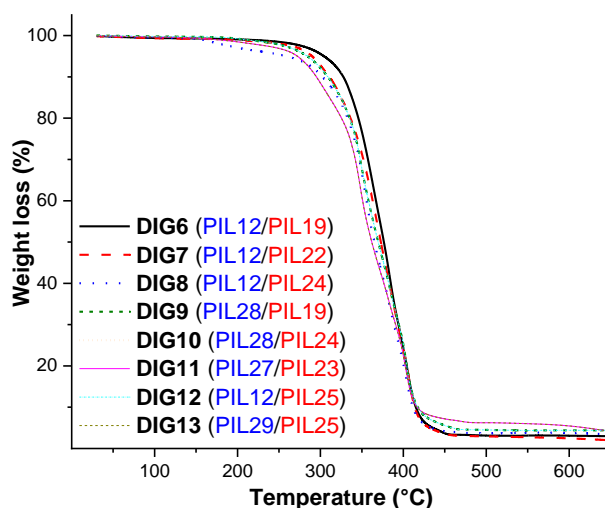


Figure 3.10 TGA traces of **DIG5-DIG13** (5K min⁻¹, under air).

3.4.3 Morphological properties

To visualize DIG morphologies and to support the results observed by DSC, thin films were casted from DMF solutions and examined by AFM. The AFM phase contrast images (Figure 3.11) demonstrated that all DIGs with block copolymers exhibited lamellar or hexagonally packed cylinder (HPC) morphologies, except for **DIG9**, which did not show any phase separation. Specifically, **DIG10-DIG12** presented lamellar morphologies, **DIG7** and **DIG8** exhibited HPC phase separation, and **DIG13** showed regions with both types of morphologies.

The domain lengths for all DIGs exhibiting phase separation were measured and found to range between 68.0 and 33.9 nm (Table 3.5). Analysing the obtained results, it can be concluded that the domain length depends on a number of interrelated parameters, making it impossible to identify a single factor with the most significant contribution.

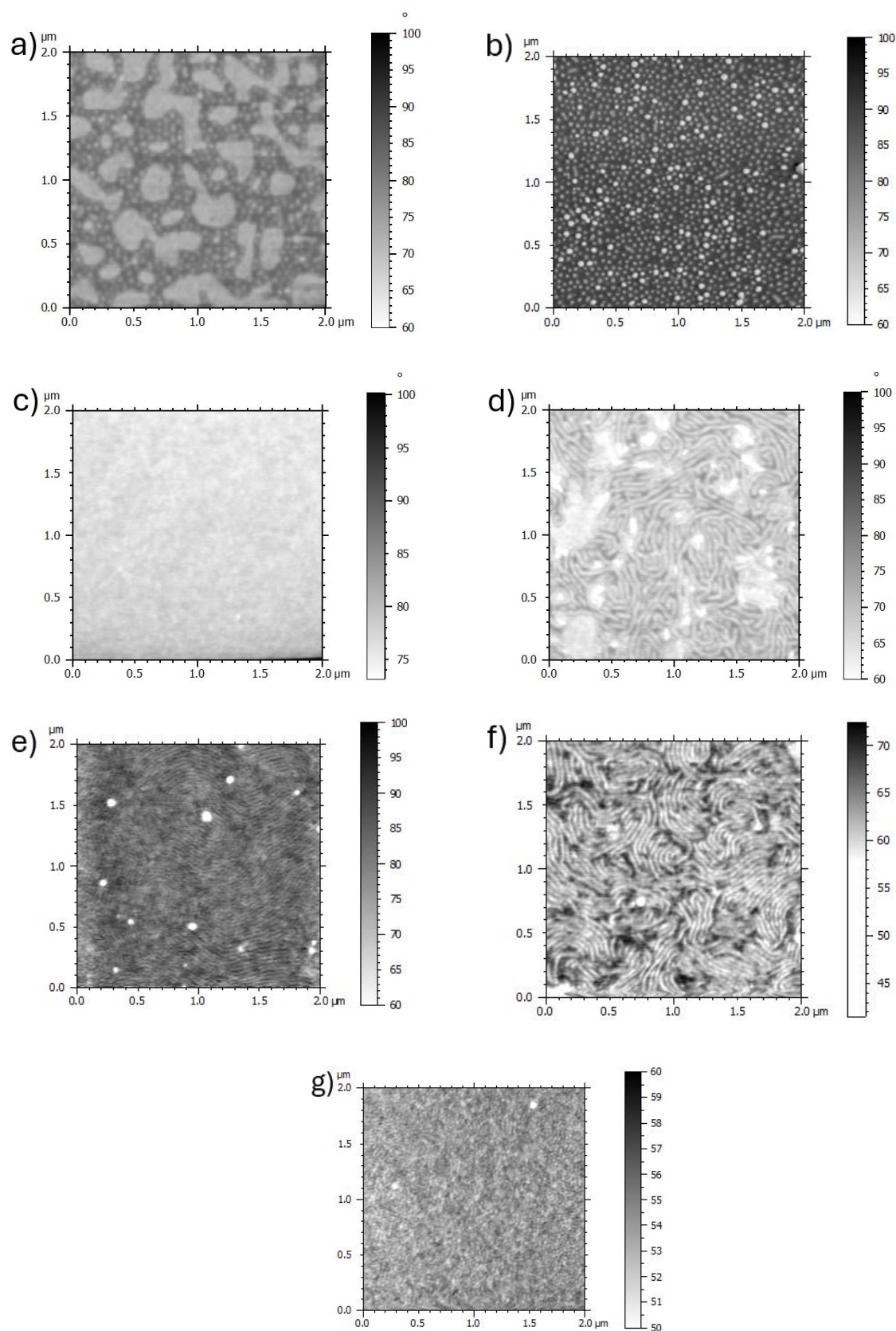


Figure 3.11 AFM images of DIG7 (a), DIG8 (b), DIG9 (c), DIG10 (d), DIG11 (e), DIG12 (f), DIG13 (g) films.

3.4.4 Ionic conductivity

The observed values of DIGs ionic conductivity varied from 1.0×10^{-5} to 2.7×10^{-7} S cm⁻¹ at 25°C (Table 3.5 and Figure 3.12). Analysis of the data suggests that the ionic conductivity is governed by a complex set of interconnected factors, making it challenging to isolate each one individually. However, it is possible to draw several conclusions from the data by comparing DIGs comprising the identical blocks. For example, **DIG6-DIG8**, **DIG12** were prepared from the same anionic building block ((poly(**ILM1**₄₁-*r*-PEGM₄₅)) and different cationic partners. The dependence of ionic conductivity at 25°C on the structure of the cationic block can be summarized as follows:

σ (25°C, S cm⁻¹): **DIG6** (poly(**ILM2**₄₅-*r*-PEGM₄₅), 1.0×10^{-5}) > **DIG12** (poly[(**ILM2**₁₇-*r*-PEGM₇₄)-*b*-Napht₉₉], 2.0×10^{-6}) > **DIG7** (poly[(**ILM2**₄₅-*r*-PEGM₄₅)-*b*-PhEtM₉₉], 5.8×10^{-7}) > **DIG8** (poly[(**ILM2**₄₅-*r*-PEGM₄₅)-*b*-Napht₉₀], 2.7×10^{-7})

These results clearly indicate that the choice of cationic building block significantly impacts the ionic conductivity of DIGs. Notably, the introduction of block copolymers, as compared to random copolymers, leads to a decrease in ionic conductivity from 1.0×10^{-5} to 2.0×10^{-6} S cm⁻¹. The observed trend among block copolymers is likely attributable to the type of morphology exhibited by these samples, rather than solely to the specific structural factors (PEGM:ILM ratio, the nature of neutral high T_g block, overall molecular weight of block copolymer and the molar masses of each segment, etc.). The influence of morphology on ionic conductivity of DIG will depend on several factors: 1) Which phase is continuous (ionic or neutral); 2) Whether the morphology has long-range order or possesses morphological defects and so-called "dead-ends"; 3) What is the direction of the ionic phase (parallel or perpendicular to the plane of conductivity measurement). For example, **DIG12** with lamellar morphology was showing higher ionic conductivity than **DIG7** and **DIG8** with cylindrical phase separation. Thus, it can be speculated that the formation of the long-range-ordered lamellae separation is more beneficial for reaching high ionic conductivity, due to the creation of continuous ion-conducting pathways with high concentration of ions and ethylene oxide solvating groups, that in its turn facilitates the ion transport. In contrast, in HPC morphology there can be a lower degree of long-range order and the decrease in in-plane ionic conductivity likely results by numerous morphological defects and large numbers of grain boundaries that serve as "dead ends" for conductive channels. Lastly, it is worth mentioning that **DIG7-DIG13** exhibited conductivity values in between those of their parent copolymers, while **DIG6** showed conductivity values higher than those of both parent polymers (Table 3.6).

The ionic conductivity of DIGs was measured across a temperature range of 0 to 110°C (Figure 3.12). The observed values for all studied DIGs increased with rising temperature and followed the Vogel-Fulcher-Tammann dependence.

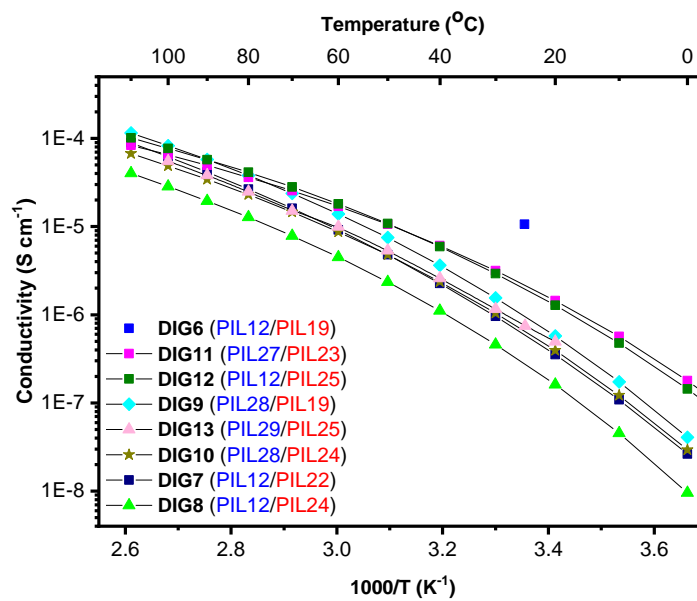


Figure 3.12 Ionic conductivity measured by BDS as a function of reciprocal temperature for **DIG6-DIG13**.

Table 3.6 Comparison of ionic conductivity for DIGs and parent PILs at 25°C

σ at 25°C (S cm ⁻¹)		poly(ILM2 _{45-<i>r</i>} - PEGM ₄₅)	poly[(ILM2 _{17-<i>r</i>} - PEGM ₇₄)- <i>b</i> -PhEtM ₉₉]	poly[(ILM2 _{17-<i>r</i>} - PEGM ₇₄)- <i>b</i> -Napht ₉₉]	poly[(ILM2 _{45-<i>r</i>} - PEGM ₄₅)- <i>b</i> -PhEtM ₉₉]	poly[(ILM2 _{45-<i>r</i>} - PEGM ₄₅)- <i>b</i> -Napht ₉₀]
		5.7×10 ⁻⁶	2.2×10 ⁻⁶	1.2×10 ⁻⁶	5.6×10 ⁻⁷	1.9×10 ⁻⁷
poly(ILM1 _{41-<i>r</i>} - PEGM ₄₅)	5.2×10 ⁻⁶	1.0×10 ⁻⁵ DIG6	-	2.0×10 ⁻⁶ DIG12	5.8×10 ⁻⁷ DIG7	2.7×10 ⁻⁷ DIG8
poly[(ILM1 _{41-<i>r</i>} - PEGM ₄₅)- <i>b</i> -PhEtM ₉₄]	2.0×10 ⁻⁶	-	-	-	-	-
poly[(ILM1 _{12-<i>r</i>} - PEGM ₆₁)- <i>b</i> -PhEtM ₇₄]	1.6×10 ⁻⁶	-	2.1×10 ⁻⁶ DIG11	-	-	-
poly[(ILM1 _{41-<i>r</i>} - PEGM ₄₅)- <i>b</i> -Napht ₇₇]	1.1×10 ⁻⁶	1.1×10 ⁻⁶ DIG9	-	-	-	6.5×10 ⁻⁷ DIG10
poly[(ILM1 _{14-<i>r</i>} - PEGM ₇₃)- <i>b</i> -Napht ₈₆]	4.4×10 ⁻⁷	-	-	7.5×10 ⁻⁷ DIG13	-	-

Table 3.7 Comparison of storage moduli (G') for DIGs and parent PILs at 25°C, 1 rad s⁻¹

G' at 25°C, 1 rad s ⁻¹ (kPa)		poly(ILM2 _{45-<i>r</i>} - PEGM ₄₅)	poly[(ILM2 _{17-<i>r</i>} - PEGM ₇₄)- <i>b</i> -PhEtM ₉₉]	poly[(ILM2 _{17-<i>r</i>} - PEGM ₇₄)- <i>b</i> -Napht ₉₉]	poly[(ILM2 _{45-<i>r</i>} - PEGM ₄₅)- <i>b</i> -PhEtM ₉₉]	poly[(ILM2 _{45-<i>r</i>} - PEGM ₄₅)- <i>b</i> -Napht ₉₀]
		0.1	1615.8	1679.9	512.2	492.8
poly(ILM1 _{41-<i>r</i>} - PEGM ₄₅)	0.1	0.9 DIG6	-	49.9 DIG12	5.4 DIG7	18.5 DIG8
poly[(ILM1 _{41-<i>r</i>} - PEGM ₄₅)- <i>b</i> -PhEtM ₉₄]	-	-	-	-	-	-
poly[(ILM1 _{12-<i>r</i>} - PEGM ₆₁)- <i>b</i> -PhEtM ₇₄]	82.1	-	90.6 DIG11	-	-	-
poly[(ILM1 _{41-<i>r</i>} - PEGM ₄₅)- <i>b</i> -Napht ₇₇]	517.9	18.4 DIG9	-	-	-	160.3 DIG10
poly[(ILM1 _{14-<i>r</i>} - PEGM ₇₃)- <i>b</i> -Napht ₈₆]	170.8	-	-	1826.8 DIG13	-	-

3.4.5 Rheological properties

The rheological behaviour of **DIG6-DIG13** was investigated between -20°C and 120°C and analysed through TTS master curves referenced at $T_0 = 25\text{ °C}$ (Figure 3.13, a and b). Inspecting the TTS plots of DIGs, several conclusions can be made:

1. No terminal regime was observed for all analysed DIGs except for **DIG6**, thus confirming rubbery solid appearance of DIGs in all range of temperatures. Contrary, **DIG6**, similarly to **DIG1**, followed the typical disentanglement behavior at lower frequencies $10^{-3} < \omega.a_T < 10^1$.

2. **DIG9-DIG12** exhibited a plateau in the higher temperature region, which can be associated with DIG's microphase separation.

3. The shift factors (a_T) used in the TTS plots for all DIGs obeyed the WLF law (Figure 3.13, c).

A simplified investigation of the storage modulus at 25°C and 1 rad s⁻¹ revealed that most DIGs with block copolymers exhibited higher stiffness than the model **DIG1**. The observed G' values ranged between 7.9 and 1826.8 kPa. This dependence can be summarized as follows:

G' (kPa, 25°C, 1 rad s⁻¹): **DIG13** (2 block copolymers, 1826.8) > **DIG10** (2 block copolymers, 160.3) > **DIG11** (2 block copolymers, 90.6) > **DIG12** (1 block, 1 random copolymer, 49.9) > **DIG8** (1 block, 1 random copolymers, 21.5) > **DIG9** (1 block, 1 random copolymers, 18.4) > **DIG7** (1 block, 1 random copolymers, 7.9) > **DIG6** (2 random copolymers, 0.9)

All DIGs synthesized from two block copolymers exhibited a storage modulus above 90.6 kPa, with **DIG13** reaching an impressive 1827 kPa. DIGs composed of one block copolymer and one random copolymer demonstrate lower G' values ranging from 49.9 to 7.9 kPa. **DIG6** obtained from two random copolymers showed the lowest G' of only 0.9 kPa. Thus, it can be concluded that the storage modulus strongly depends on the number of block copolymers involved in the formation of DIG.

A comparison of the storage modulus values for DIGs and their corresponding parent PILs showed that majority of DIGs demonstrates storage moduli between those of their parent polymers (Table 3.7). Notably, **DIG6** and **DIG13** exhibited higher storage moduli than both of their parent PILs. For example, **DIG6** demonstrated both enhanced ionic conductivity and improved mechanical properties compared to their parent PILs (Table 3.6, Table 3.7).

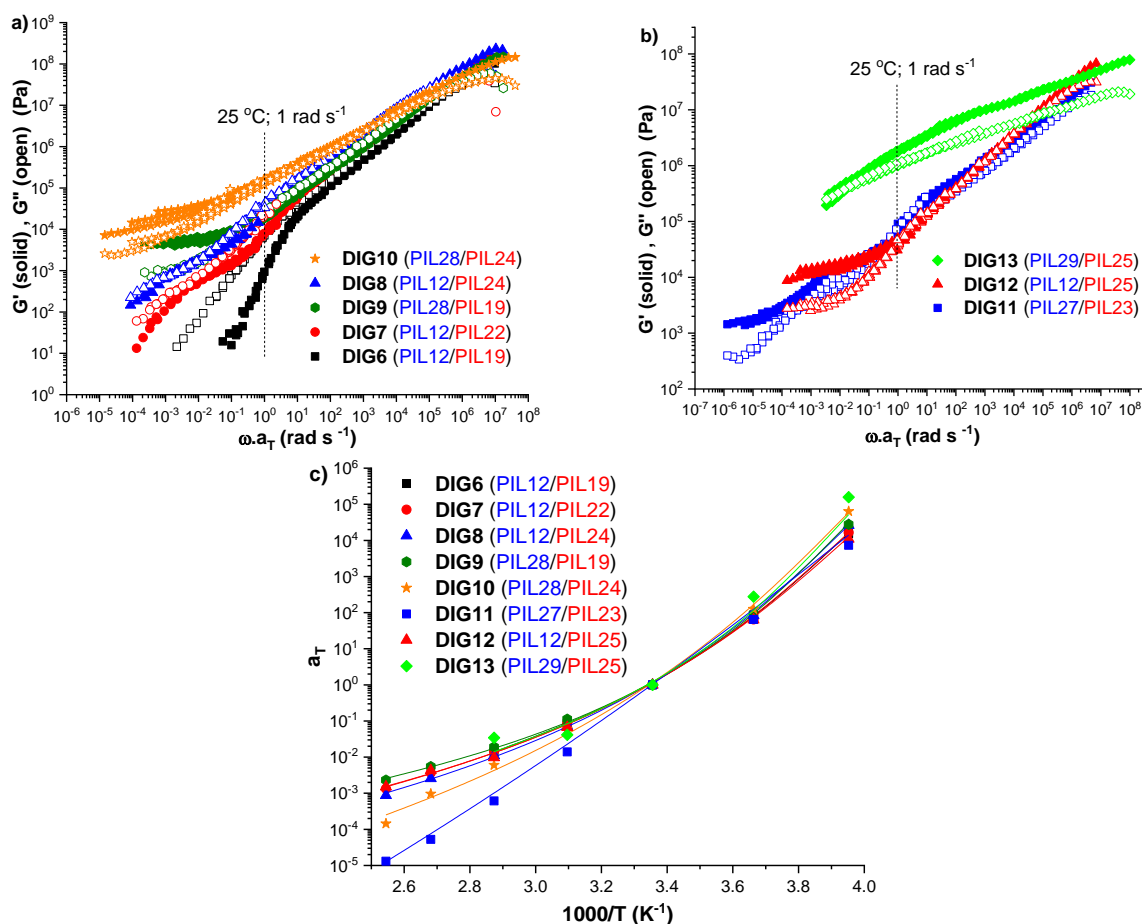
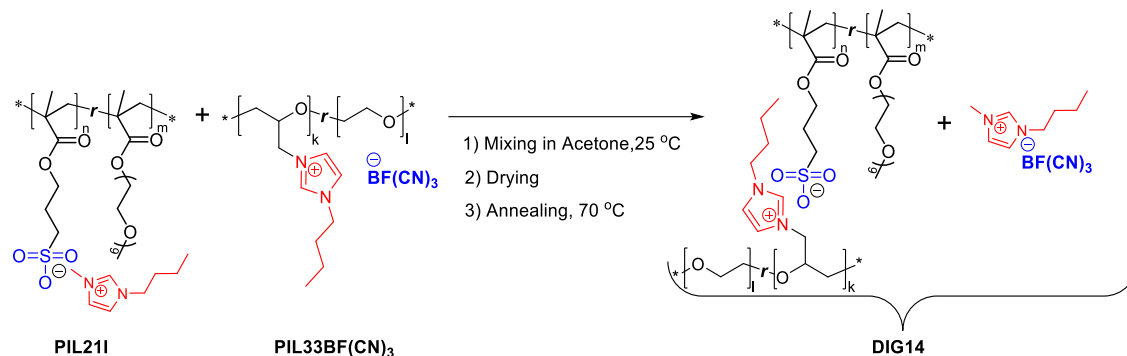


Figure 3.13 TTS master curves of **DIG6-DIG13** obtained by frequency sweep experiments performed from -20 to 120 °C and referenced at $T_0 = 25$ °C (a, b), corresponding a_T shift factors and WLF best fits at $T_0 = 25$ °C for DIGs (c).

3.5 Optimization of DIG structure

The application of the two synthetic strategies in this work led to the synthesis of 13 DIGs. In both cases, improvements in either mechanical properties or ionic conductivity were achieved compared to the parent PILs and model **DIG1**. At the same time, the certain combinations of building blocks resulted in materials that surpassed their individual components in both parameters (**DIG2** and **DIG6**). Figure 3.14 was suggested to illustrate the relationship between ionic conductivity and storage modulus at 25 °C for all synthesized DIGs. The highest conductivity was observed for **DIG1_{IL}**, where an additional percentage of ionic liquid was incorporated into the sample. **DIG6**, composed of two random methacrylate copolymers, exhibited the second-highest conductivity of 1.0×10^{-5} S cm $^{-1}$ at 25 °C. Storage modulus values across all synthesized DIGs ranged from 0.9 to impressive 1827 kPa, with **DIG13**, consisting of two block copolymers, having the highest stiffness. After **DIG1_{IL}** and **DIG6**, the sulfonate-based **DIG2** demonstrated both promising mechanical stability (61.9 kPa at 29 °C, 1 rad s $^{-1}$) and notable ionic conductivity (5.7×10^{-6} S cm $^{-1}$ at 25 °C). This combination of properties made it an excellent candidate for the final iteration of DIG structure optimization. As discussed in Section 3.3.3,

the ionic conductivity of sulfonate-based DIGs is primarily determined by the nature of the generated ionic liquid. Therefore, to enhance the ionic conductivity of sulfonate-based DIGs, the choice of building blocks was focused on the *in situ* formation of the IL with the highest ionic conductivity. Consequently, **PIL33BF(CN)₃** was selected as the cationic building block, while **PIL21I** served as the anionic building block, leading to the formation of **DIG14** with BuMeImBF(CN)₃ ionic liquid (Scheme 3.4, Table 3.8).



Scheme 3.4 Synthetic route for the preparation of **DIG14**.

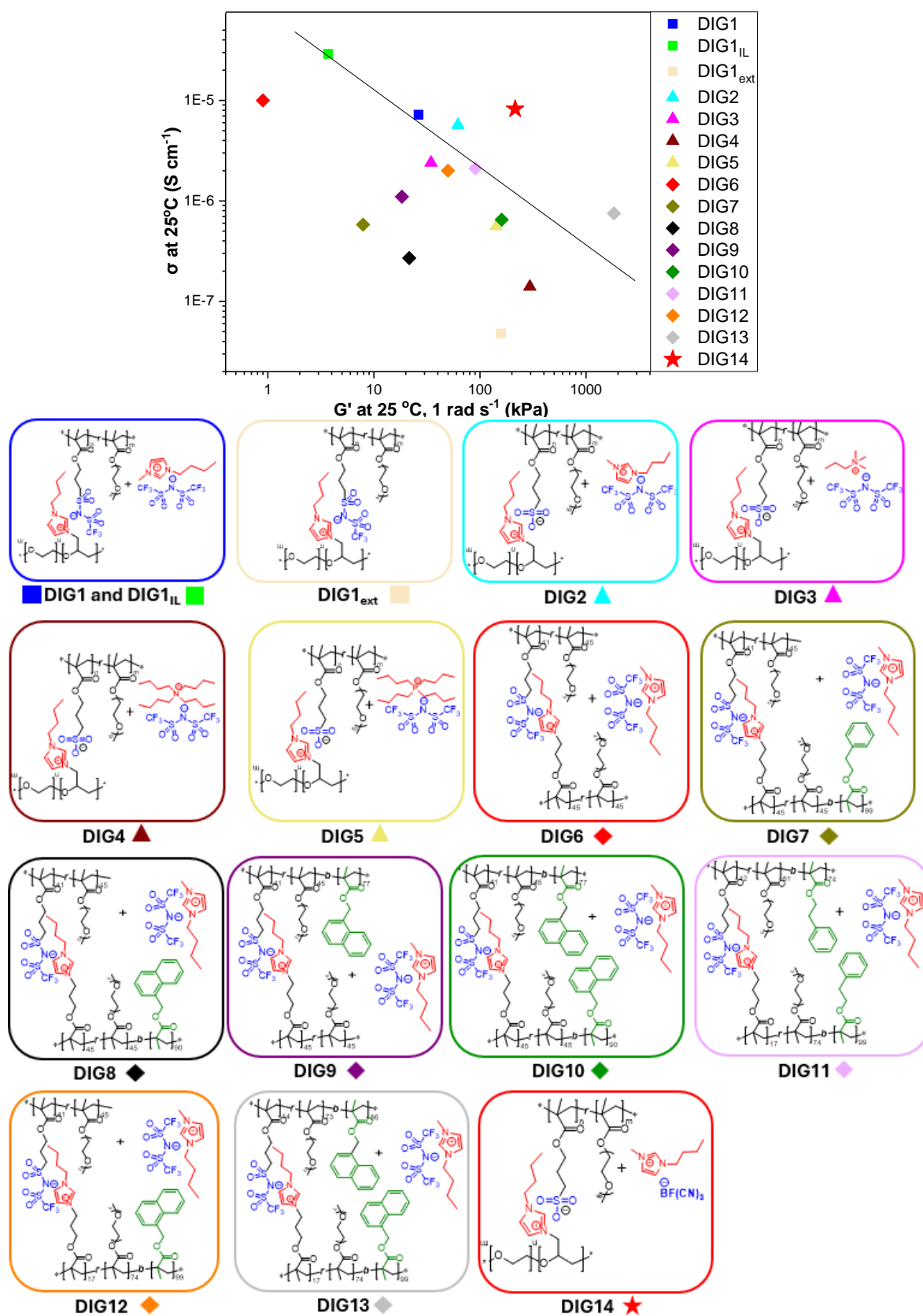


Figure 3.14 Ionic conductivity at 25 °C as a function of the storage modulus (G') obtained at 25 °C and 1 rad s⁻¹ for all synthesized DIGs (for **DIG2-DIG5**, G' was obtained at 29 °C and 1 rad s⁻¹).

3.5.1 Thermal properties of DIG14

DSC analysis of **DIG14** revealed a single transition, corresponding to the glass transition temperature, which was observed at -45°C . This T_g was slightly lower compared to that of **DIG2**. The onset mass loss temperature was found to reach 200°C , consistent with the values recorded for all sulfonate-based DIGs.

Table 3.8 Selected properties of **DIG2** and **DIG14**.

DIG		DIG properties			
Sample	IL generated in situ	G' at 25°C , 1 rad s^{-1} (kPa)	σ at 25°C (S cm^{-1})	T_g , ($^{\circ}\text{C}$) ¹	T_{onset} ($^{\circ}\text{C}$) ²
DIG2		61.9 ³	5.7×10^{-6}	-43	205
DIG14		214.5	8.2×10^{-6}	-45	200

¹Determined by DSC (5 K min^{-1}). ² T_{onset} determined by TGA (5 K min^{-1}). ³At 29°C , 1 rad s^{-1}

3.5.2 Ionic conductivity of DIG14

Transition from **DIG2** with 1-butyl-3-methylimidazolium bis(trifluoromethylsulfonyl)imide to **DIG14** with 1-butyl-3-methylimidazolium tricyanofluoroborate resulted in the increase in ionic conductivity from 5.7×10^{-6} to $8.2 \times 10^{-6} \text{ S cm}^{-1}$ at 25°C (Table 3.8 and Figure 3.15). In the whole temperature range the observed values increased with temperature, following the Vogel-Fulcher-Tammann dependence (Figure 3.15).

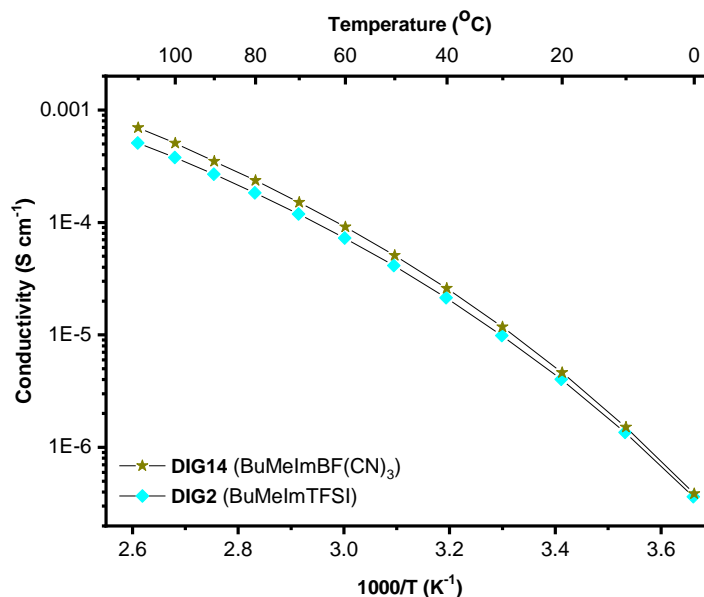


Figure 3.15 Ionic conductivity measured by BDS as a function of reciprocal temperature for DIGs.

3.5.3 Rheological properties of DIG14

The rheological behavior of **DIG14** across the temperature range of -20°C to 100°C is presented in Figure 3.16 (a). Similar to **DIG2**, **DIG14** exhibits a $\omega^{0.5}$ dependence in the frequency range from $10^{-2} < \omega.a_T < 10^3$, with a typical disentanglement behavior at lower frequencies. Due to the broader temperature range analyzed for **DIG14**, the presence of a glassy region can also be observed at higher frequencies, where the material exhibits predominantly elastic behavior. Furthermore, the shift factors obtained from the analysis obey the WLF equation, as shown in Figure 3.16 (b). This indicates a consistent relationship between temperature and viscoelastic behavior, further supporting the material's stability over the studied temperature range.

A comparative investigation of the mechanical properties highlights a significant improvement in **DIG14** compared to **DIG2**. The transition from **DIG2**, which contains BuMeImTFSI, to **DIG14**, containing BuMeImBF(CN)₃, results in a remarkable increase in the storage modulus from 61.9 kPa to 214.5 kPa (at 25°C and 1 rad s⁻¹).

As it can be seen from Figure 3.14, the final step of DIGs structure optimization led to an outstanding enhancement in both the ionic conductivity, reaching 8.2×10^{-6} S cm⁻¹ at 25°C, and the mechanical stability, with a storage modulus of 214.5 kPa (at 25°C and 1 rad s⁻¹). These advancements make **DIG14** the most promising candidate for future applications in supercapacitors.

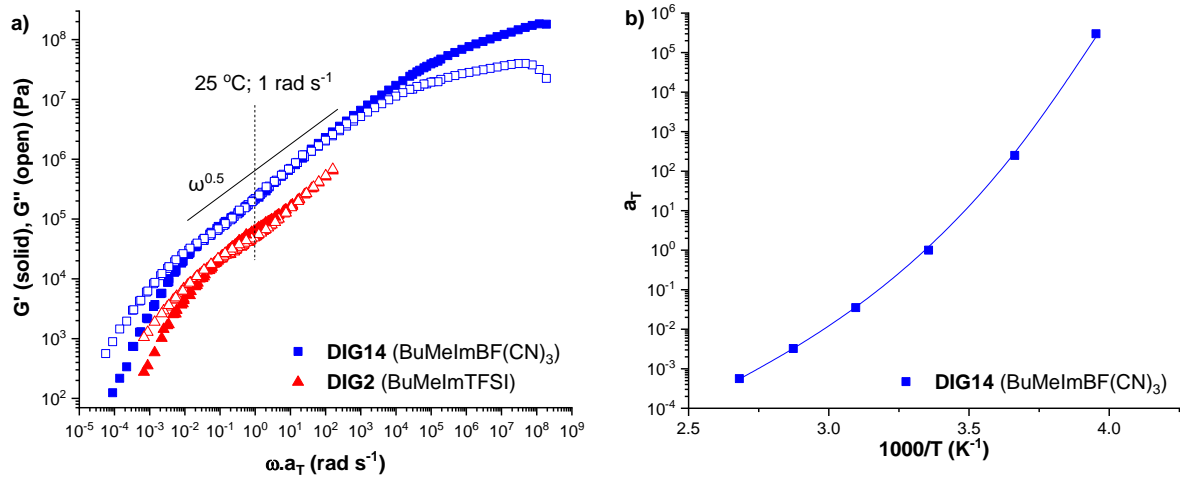


Figure 3.16 TTS master curves of **DIG14** and **DIG2** obtained by frequency sweep experiments performed from -20 to 100 °C and referenced at $T_0 = 25$ °C (a), corresponding a_T shift factors and WLF best fits at $T_0 = 25$ °C for **DIG14** (b).

4. Application of PILs and DIGs in all-solid-state supercapacitors

To fulfil the final objective of this thesis, **DIG14** was used as the electrolyte for an all-solid-state supercapacitor. This choice is justified by the promising combination of properties observed in **DIG14**. It demonstrated a high ionic conductivity of $8.2 \times 10^{-6} \text{ S cm}^{-1}$ at 25°C , along with a rubbery solid consistency, exhibiting a storage modulus of 214.5 kPa at room temperature. Additionally, **DIG14** maintained its solid-like behavior up to 75°C , allowing the investigation of the supercapacitor's performance not only at room temperature but also at elevated temperatures without the risk of leakage or shortcut.

For the supercapacitor assembly named **SC1**, the stainless steel (SST) was chosen as the current collector. This decision was based on SST's widespread use in electrochemistry and its suitability for creating flexible or bendable devices^{148,149}. Furthermore, to evaluate and compare the performance of supercapacitors based on **DIG14**, the two additional supercapacitors **SC2** and **SC3** with parent PILs (**PIL21I** and **PIL33BF(CN)₃**, respectively) were assembled and tested (Table 4.1).

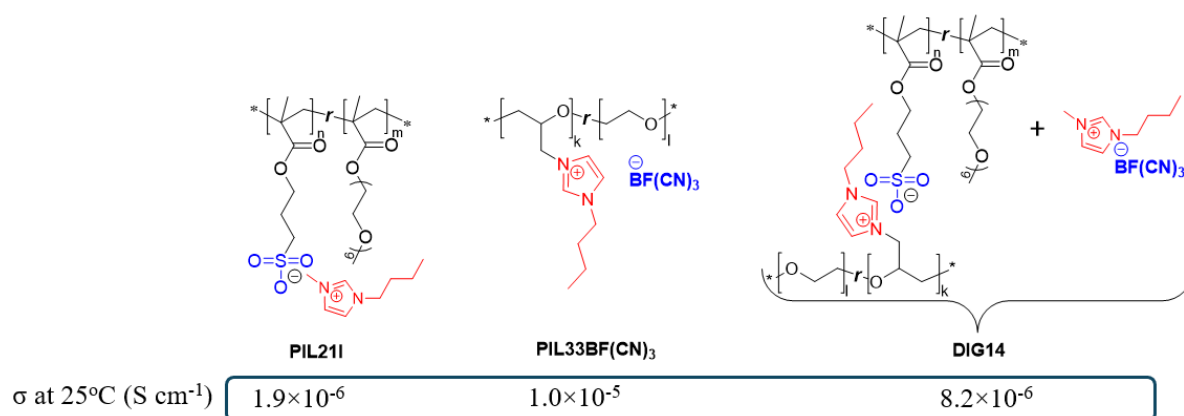


Figure 4.1 Polyelectrolytes used in supercapacitors.

4.1 Preparation of electrodes and supercapacitor assembly

For the preparation of the electrodes, a combination of reduced graphene oxide (rGO), carbon nanotubes (CNTs), and polymer electrolyte (either DIG or PIL) was utilized. The CNTs and rGO served as the active material, while polyelectrolyte is functioned both as a binder and as a source of mobile ions. The coatings were casted from DMF suspensions on a hot SST surface. This allowed for the formation of thin, homogeneous layers of active materials on SST current collector (Figure 4.2).

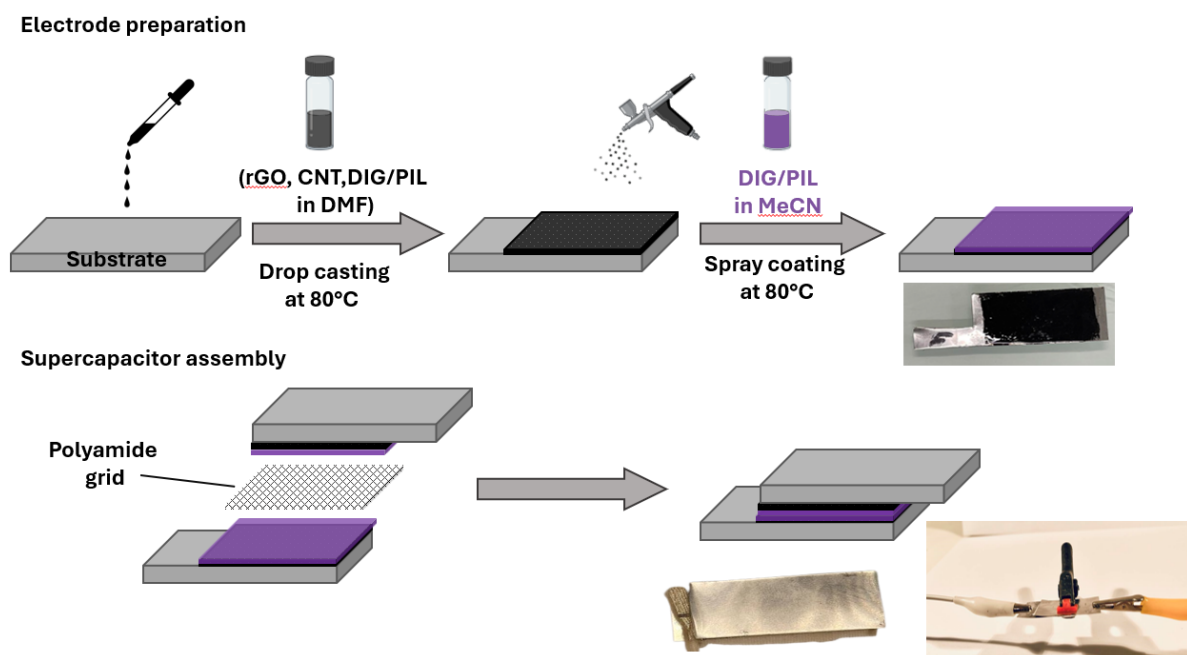


Figure 4.2 Schematic illustration of electrode preparation and supercapacitors assembly.

Subsequently, a solution of polyelectrolyte (either DIG or PIL) in acetonitrile was spray-coated onto the electrode surfaces. This enabled the creation of a thin polyelectrolyte layers on both electrodes without disturbing the active material layer. To prevent short circuits, a flexible polyamide grid was placed on one of the electrodes, and both electrodes were thoroughly dried. Finally, the two prepared electrodes were sandwiched together to form the following symmetrical capacitors:

SC1: SST/rGO+**CNT**+**DIG14**/**DIG14**/rGO+**CNT**+**DIG14**/SST

SC2: SST/rGO+**CNT**+**PIL21I**/ **PIL21I** /rGO+**CNT**+**PIL21I** /SST

SC3: SST/rGO+**CNT**+**PIL33BF(CN)₃**/**PIL33BF(CN)₃**/rGO+**CNT**+ **PIL33BF(CN)₃** /SST

4.2 Supercapacitors testing

The performance of the supercapacitors was evaluated using a two-electrode system configuration, with the results reported as electrodes characteristics relative to the mass of active materials (Table 4.1).

Table 4.1 Selected properties of supercapacitor at a scan rate of 5mV s^{-1} and a potential window of 2V.

SC	Electrolyte	25°C			80°C		
		$C_{SP},$ (F g^{-1}) ¹	$E,$ (Wh kg^{-1}) ²	$P,$ (W kg^{-1}) ³	$C_{SP},$ (F g^{-1}) ¹	$E,$ (Wh kg^{-1}) ²	$P,$ (W kg^{-1}) ³
1	DIG14	19.6	10.9	97.7	43.9	24.4	218.9
2	PIL21I	- ⁴	- ⁴	- ⁴	- ⁴	- ⁴	- ⁴
3	PIL33BF(CN) ₃	8.1	4.5	40.5	16.9	9.4	85.7

¹Specific capacitance. ²Energy density. ³Power density. ⁴Resistive CV curves.

Initially, **SC1** with **DIG14** was tested using cyclic voltammetry at 25°C, with a voltage range from 1.0 to 2.0V (Figure 4.3, a). The cyclic voltammograms exhibited nearly rectangular shapes across all tested voltages, indicating good capacitive behavior with no evidence of any degradation. Increasing the voltage from 1.0 to 2.0V resulted in a significant rise in capacitance, from 7.5 to 19.6 F g⁻¹. Based on these observations, it was decided to conduct further experiments with a potential window set at 2.0V. Figure 4.3 (b) displays the CV curves of **SC1** at various temperatures. The cyclic voltammograms maintained nearly rectangular shapes, suggesting consistent capacitive performance with some internal resistance. The capacitance was increasing from 19.6 to 43.9 F g⁻¹ with increase in temperature from 25 to 80°C. Figure 4.3 (c) illustrates the capacitance evolution of **SC1** as a function of scan rate during CV measurements. At a scan rate of 1 mV s⁻¹, **SC1** exhibited a capacitance of 30.1 F g⁻¹. However, as the scan rate increased, the capacitance gradually declined. At 25°C and a scan rate of 5 mV s⁻¹, the cell experienced a 35% reduction in capacitance, eventually decreasing to 19.6 F g⁻¹. Finally, Figure 4.3 (d) presents the Ragone plot for **SC1**. The energy and power densities at various scan rates (from 10 to 1 mV s⁻¹) were calculated using equations 1.38 and 1.39 applying the voltage of 2V. At 25°C and 5 mV s⁻¹, the energy density and power density were found to be 10.9 Wh kg⁻¹ and 97.7 W kg⁻¹, respectively.

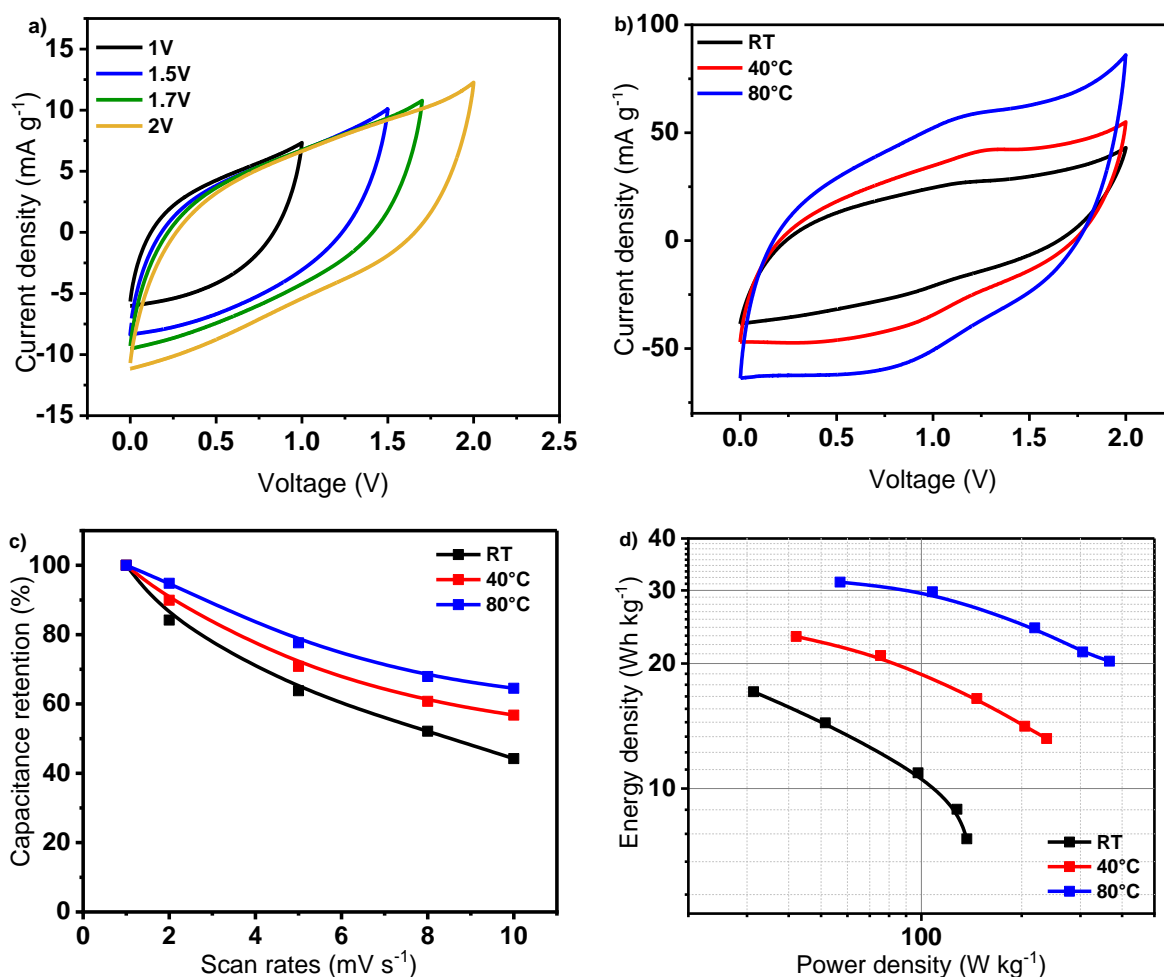


Figure 4.3 CV curves of **SC1** with **DIG14** obtained at 5 mV s^{-1} at 25°C at different potential windows (a), 5 mV s^{-1} from 0 V to 2 V , at different temperatures (b). Capacitance retention as a function of the scan rates at a potential window from 0 to 2 V (c). Ragone plot (d).

Similar tests were performed on **SC2** and **SC3** comprising PIL-based electrolytes under identical conditions. **SC2** with **PIL21I**, exhibited purely resistive behavior, preventing the calculation of its capacitance (Figure 4.4, a). This behavior was attributed to the low ionic conductivity of **PIL21I**. In contrast, **SC3**, displayed nearly rectangular CV profiles typical of electric double-layer capacitors, maintaining this characteristic up to 2 V (Figure 4.4, b). Additionally, **SC3**'s performance was assessed at varying temperatures. As shown in Figure 4.4 (c), an increase in temperature from 25°C to 80°C resulted in a capacitance rise from 8.1 to 16.9 F g^{-1} . Moreover, a comparison of capacitance at different scan rates at 25°C revealed that increasing the scan rate from 1 mV s^{-1} to 5 mV s^{-1} led to a reduction in capacitance by more than 50% .

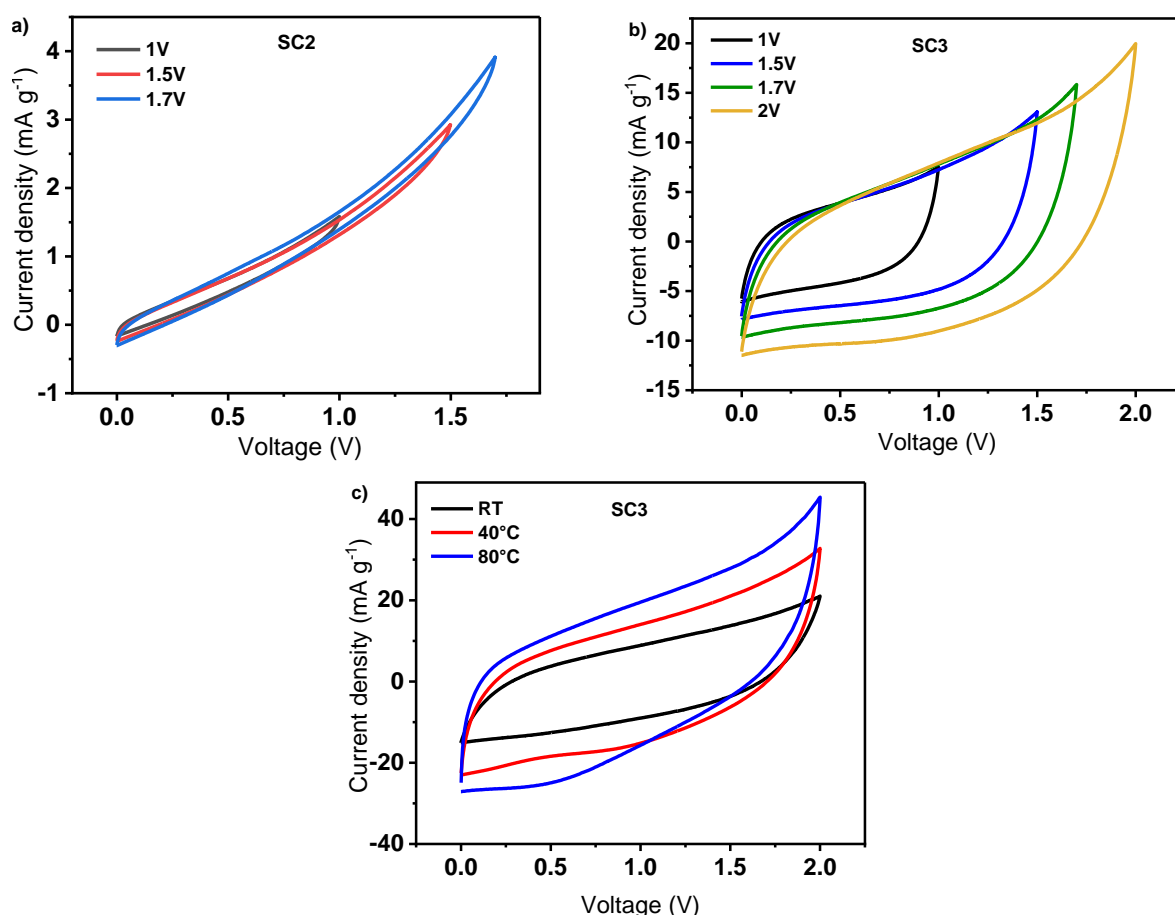


Figure 4.4 CV curves obtained at 5 mV s^{-1} at 25°C at different potential windows for **SC2** (a) and **SC3** (b). CV curves of **SC3** obtained at 5 mV s^{-1} from 0 V to 2 V , at different temperatures (c).

To sum up, **SC1** demonstrated the following characteristics at room temperature: $C_{\text{SP}} 19.6 \text{ F g}^{-1}$, $E 10.9 \text{ Wh kg}^{-1}$, $P 97.7 \text{ W kg}^{-1}$. These findings indicate that, under similar conditions, the system

with **DIG14** outperformed those with PIL-based electrolytes. The capacitance of **SC1** at 25°C was higher than that of **SC3** even at 80°C, and **SC1** exhibited 1.5 times better capacitance retention compared to **SC3**.

While **SC1**'s performance does not yet match that of modern industrial devices^{150,151}, it offers several compelling features that position it as a promising candidate for advanced energy storage applications. These advantages stem primarily from the viscoelastic properties of DIGs and their ability to maintain mechanical stability at elevated temperatures. Notably, this leads to several potential benefits: no need for supercapacitor sealing, no loss of electrolyte, supercapacitor flexibility, and reliable operation over a wide temperature range. As a result, DIGs represent a promising material for the future development of safe and flexible electrochemical devices.



IV. Experimental part

1. Methods

1.1 NMR spectroscopy

NMR spectra were recorded on AMX-600 and Bruker Avance 500 spectrometers (Bruker, Germany) at 25 °C in the indicated deuterated solvents and are listed in part per million (δ , ppm).

The structure of synthesized ILM, PILs and DIGs were verified on AMX-600 spectrometer at 25 °C in DMSO- d_6 . The signals corresponding to the residual protons (^1H : $\delta = 2.50$ ppm) and carbons (^{13}C : $\delta = 39.52$ ppm) of the DMSO- d_6 were used as internal standards for ^1H and ^{13}C NMR, respectively. The C_6F_6 (^{19}F : $\delta = -164.9$ ppm) and $\text{F}_3\text{B}\cdot\text{OEt}_2$ were used as an external standard for ^{19}F and ^{11}B NMR, respectively.

The characterization of DIGs and IL release was done by recording of ^1H and ^{19}F NMR spectra on a Bruker Avance 500 spectrometer in acetone- d_6 at 25 °C using a Bruker BBFO $^1\text{H} / ^{109}\text{Ag}$ - ^{19}F 5mm gradient Z probe. Chemical shifts are reported relative to the acetone- d_6 residual proton peaks (^1H : $\delta = 2.05$ ppm) for ^1H NMR or relative to an external reference for ^{19}F NMR (^{19}F : $\delta = 0.00$ ppm, CFCl_3). Abbreviations for peak multiplicity are given as follows: s for singlet, d for doublet, t for triplet, q for quartet, p for pentet, dt for doublet of triplets, sext for sextet, m for multiplet and br.s for broad.

1.2 IR spectroscopy

IR spectra were acquired on a Magna-750 (Nicolet Instrument Corporation, USA) or on INVENIO R (Bruker, Germany) Fourier IR-spectrometer using KBr pellets or ATR technology (128 scans, resolution is 4 cm^{-1})

1.3 Kinematic and dynamic viscosities

Kinematic viscosities (ν) of ILMs were measured using a calibrated CUSMC-300 Cannon Ubbelohde semi-microcapillary viscometer at 25 °C. The dynamic viscosity (η) was calculated using the equation:

$$\eta = \nu * d \quad (\text{eq 1.1})$$

where d is the density of ILMs determined at 25 °C using a calibrated pycnometer.

1.4 Differential scanning calorimetry (DSC)

Differential scanning calorimetry of PILs was performed on a DSC 300 Caliris® Select (Netzsch, Germany) differential calorimeter in the range of -80 to 150 °C at a heating rate of 5 °C min^{-1}

under an nitrogen atmosphere. When studying the ILMs, a special low heating rate of $2\text{ }^{\circ}\text{C min}^{-1}$ was applied as recommended for the investigation of viscous ionic liquids¹⁵². Two heating–cooling cycles were carried out for each sample. Glass transition temperatures (T_g) were calculated from the second heating curve.

Differential scanning calorimetry measurements for DIGs were done using a DSC Q200 (TA Instrument) calibrated with an indium standard. The samples were prepared in aluminium hermetic pans and the experiments were conducted under a nitrogen purge of 25 mL min^{-1} on ca. 5-10 mg samples. The sample was first heated to $100\text{ }^{\circ}\text{C}$ at a rate of $10\text{ }^{\circ}\text{C min}^{-1}$ and isothermally annealed for 1 min. Then, the temperature was decreased to $-70\text{ }^{\circ}\text{C}$ at a rate of $10\text{ }^{\circ}\text{C min}^{-1}$ followed by a second heating to $100\text{ }^{\circ}\text{C}$ at a rate of $10\text{ }^{\circ}\text{C min}^{-1}$. The glass transition temperatures were measured at the mid-point of the transition (on the second heating cycle) using the TA Thermal Analysis software.

1.5 Thermal mechanical analysis (TMA)

Thermal mechanical analysis (TMA) of PILs was performed under inert atmosphere (N_2) using a DIL 402 select Expedit dilatometer (NETZSCH, Germany) with a constant load of 0.3 N at a heating rate of $5\text{ }^{\circ}\text{C min}^{-1}$ in the range of -100 to $150\text{ }^{\circ}\text{C}$. The heat distortion temperature (T_{HDT}) was determined as a temperature at which a noticeable deformation under applied load and scanning/ heating rate was observed.

1.6 Thermogravimetric analysis (TGA)

Thermal gravimetric analysis (TGA) for ILMs and PILs was carried out in air on a TGA2 STARe System (Mettler Toledo, Switzerland) applying a heating rate of $5\text{ }^{\circ}\text{C min}^{-1}$. The onset weight loss temperature (T_{onset}) was determined as the point in the TGA curve at which a significant deviation from the horizontal was observed. The resulting temperature was then rounded to the nearest 5°C .

Thermogravimetric analysis for DIGs was performed using a TGA Q500 (TA Instruments). A heating ramp from 30 to $700\text{ }^{\circ}\text{C}$ was applied at $10\text{ }^{\circ}\text{C min}^{-1}$ under a helium purge of 60 mL min^{-1} to ca. 5-15 mg samples. T_{onset} was determined as the point in the TGA curve at which a significant deviation from the horizontal was observed. The resulting temperature was then rounded to the nearest 5°C .

1.7 Electrochemical impedance spectroscopy (EIS)

Ionic conductivity of ILMs and PILs was measured by electrochemical impedance spectroscopy (EIS) with a VSP potentiostat/galvanostat (Bio-Logic Science Instruments, France). To avoid any influence of moisture/ humidity on the conductivity of electrolytes, the latter were preliminary dried at $80\text{ }^{\circ}\text{C}/0.1\text{ mbar}$ for 12 h in the B-585 oven (Buchi Glass Drying Oven, Switzerland) filled with P_2O_5 and were transferred under vacuum inside an argon-filled glovebox (MBRAUN MB-Labstar, H_2O and O_2 content $<0.5\text{ ppm}$). ILM samples were placed in TSC 70 closed cell (RHD

instruments, Germany, cell constant was calculated using the solution of conductivity standard) and afterwards was taken out from the glovebox. PIL samples were sandwiched between two stainless steel electrodes. The distance between the electrodes was kept equal to 250 μm using a Teflon spacer ring with an inner area of 0.50 cm^2 . Symmetrical stainless steel/**PIL**/stainless steel assembly was clamped into the 2032-coin cell and afterwards was taken out from the glovebox. EIS experiments were carried by applying a 10 mV perturbation in the frequency range from 10^{-2} to 2×10^5 Hz and in a temperature range from 20 to 100 $^\circ\text{C}$. Temperature was controlled using the programmed M-53 oven (Binder, Germany), where cells were allowed to reach thermal equilibrium for at least 45 min before each test.

1.8 Broadband dielectric spectroscopy (BDS)

Broadband dielectric spectroscopy (BDS) was employed to measure the effect of temperature on the ionic conductivity for DIGs and PILs. The measurements were carried out using a high resolution Alpha–Analyzer (Novocontrol GmbH). The sample temperature was controlled under a flow of pure nitrogen gas (Quatro temperature controller) so that any presence of oxygen and moisture in the measuring chamber can be excluded. The thermal stability was better than 0.1 K, with relative variations less than 0.2 K min^{-1} . For PILs, a solution of 100 mg in acetone (1.5 mL) was deposited drop wise onto a platinum electrode (2 cm in diameter) and the solvent was slowly evaporated under ambient conditions. For DIGs, ca. 100 mg of previously dried samples at 70 $^\circ\text{C}$ under vacuum for at least 24 h were directly placed in the platinum electrode with a stainless steel spatula. In order to remove any traces of solvent or water in the samples, a thermal annealing at 70 $^\circ\text{C}$ under vacuum for 18 h was carried-out. After the thermal treatment, a second platinum electrode (3 cm in diameter) was placed on top of the sample to build up a measurement cell as a parallel plate capacitor. The sample thickness was controlled by employing 100 μm thick Teflon spacers. A further annealing was performed inside the cryostat of the dielectric spectrometer under a flow of pure nitrogen during 3 h at 110 $^\circ\text{C}$. The electrical and dielectric properties were continuously monitored until the equilibrium was reached. Once this equilibration procedure was done, the ionic conductivity measurements were started by measuring the complex conductivity function which is defined by equation 1.2:

$$\sigma^*(\omega, T) = \sigma'(\omega, T) + i\sigma''(\omega, T) \quad (\text{eq 1.2})$$

The conductivity measurements were carried-out from 10 MHz to 0.1 Hz under isothermal frequency sweeps from 110 to -50 $^\circ\text{C}$ in temperature steps of 10 $^\circ\text{C}$. The applied voltage was 0.1 V to exclude any possible non–linear effects. Once the measurements were finished the samples were re-measured at a reference temperature chosen as 30 $^\circ\text{C}$ to validate that the experimental results were reproducible and stable. The DC-conductivity values (σ_{DC}) of the anhydrous PILs and DIGs were obtained by the value of the plateau observed in the frequency dependence of σ' . Above T_g , the

dependence of σ_{DC} on the inverse temperature follows a typical Vogel–Fulcher–Tammann (VFT) behavior for all studied samples. The experimental results were thus fitted with the VFT equation 1.3:

$$\sigma_{DC} = \sigma_{\infty} \times \exp\left(-\frac{B}{(T-T_{VFT})}\right) \quad (\text{eq 1.3})$$

with σ_{DC} the ionic conductivity in the high temperature limit, B a fitting parameter related to the activation energy of the ionic conduction, and T_{VFT} the Vogel temperature.

1.9 Cyclic voltammetry (CV)

Cyclic voltammetry (CV) was used to determine the electrochemical stability window (ESW) of PILs at 25°C. The ESW was studied under an argon atmosphere in a glovebox (MBRAUN MB-Labstar, H₂O and O₂ content <0.5 ppm) at room temperature using a VSP potentiostat/galvanostat (Bio-Logic Science Instruments, France). The three-electrode cells were assembled by sandwiching the polymer sample between two Pt flat electrodes (used as working and counter electrodes) and silver mesh (used as pseudo-reference electrode) to form the following architecture: Pt/PIL/Ag mesh/PIL/Pt. The ESW test was performed by scanning at 5 mV s⁻¹ rate from the open circuit potential (OCV) toward positive or negative potentials.

CV was also used to test supercapacitors. Cyclic voltammetry experiments were performed at different scan rates of 1, 2, 5, 8, 10 mV s⁻¹ in a voltage range of 0 – 2.0 V and at 25, 40 and 80 °C.

1.10 Size exclusion chromatography (SEC).

A 1200 Infinity gel permeation – size exclusion chromatograph (SEC, Agilent Technologies) was used to determine number average molar masses (M_n), weight average molar masses (M_w) and chain dispersities ($\mathcal{D} = M_w/M_n$) of PILs. The chromatograph was equipped with an integrated IR detector, 0.1 M solution of Li(CF₃SO₂)₂N in DMF was used as an eluent at 50 °C and the flow rate was set as 1.0 mL min⁻¹. A set of PL PolarGel-M column and a PL PolarGel-M guard column (Agilent Technologies) was applied for analysis of anionic PILs, while another set of TSKgel G5000-HHR column and TSKgel HHR-H guard column (Tosoh Bioscience) was used to study cationic PILs. Polymer solutions (4 mg mL⁻¹) in 0.1 M solution of Li(CF₃SO₂)₂N in DMF were filtered through 0.20 µm pore size polytetrafluoroethylene (PTFE) filters prior to the measurements. Polymethylmethacrylate standards (EasiVial PMMA, Agilent Technologies, $M_p = 550\text{--}1568000$ g mol⁻¹) were used to perform calibration.

1.11 Rheological measurements

Rheological measurements were performed using a strain-controlled ARES-G2 rheometer (TA Instruments) equipped with an ACS-3 chiller (TA Instruments). Plate-plate disposable aluminum geometries with a diameter of 25 mm were adopted for neat and previously dried PILs. In the case of the dried DIGs, smaller disposable aluminum plates with a diameter of 8 mm were used. Aiming to

eliminate the effect of moisture on the viscoelastic properties of the ionic samples, both PILs and DIGs were dried inside a vacuum oven for at least 24 h at 70 °C before the measurements. To guarantee a maximum contact between the sample and the geometry, a sufficiently thick layer of 0.4–1.5 mm and an initial positive axial force was applied. Frequency sweep tests were conducted at temperatures ranging from -20 °C to 120 °C from 628 rad s⁻¹ to 0.1 rad s⁻¹. To determine the linear viscoelastic region of each sample preliminary strain sweep tests were carried out at a fixed frequency of 1 rad s⁻¹ in a range of deformation between 0.01 and 100%. The master curves were built through time-temperature superposition and were referenced at T₀ = 25 or 29 °C. The corresponding shift factors *a_T* were determined and it was verified that they present a temperature dependence that follows the WLF (Williams-Landel-Ferry) equation 1.4.

$$\log(a_T) = -\frac{C_1(T-T_0)}{C_2+(T-T_0)} \quad (\text{eq 1.4})$$

1.12 Atomic force microscopy (AFM)

Atomic force microscopy (AFM) images were recorded with an MFP-3D Infinity microscope (Asylum Instruments/Oxford Instruments, United Kingdom) in tapping mode (30–35 °C, in air). AC160TS-R3 (Olympus, Japan) cantilevers were applied with a stiffness of 26 N m⁻¹ and resonance frequency of 300 KHz. The images were recorded in the so-called "soft tapping mode," to avoid deformation and indentation of the polymer surface by the tip. The domain periodicity was evaluated on an averaged power density spectrum (PSD) generated from a phase shift channel on three different 2 × 2 μm² images. All of the images were collected with the maximum available number of pixels (512) in each direction. On each image, two profiles were taken, and for each, the distance over ten consecutive periods was recorded. The general procedure for the preparation of the samples for AFM was as follows: borosilicate glass coverslips (22 × 22 mm², thickness no. 1 (0.13–0.16 mm), free from streaks, bubbles, and striations (Epredia, Netherlands)) from hydrolytic class I were rinsed with acetone, then with dichloromethane, and dried with air flow. The solution of PILs or DIGs in anhydrous DMF with a concentration of 100 mg/mL was prepared at RT under an inert atmosphere. The solution was filtered through a 0.22 μm syringe filter and cast at 22 °C onto a glass coverslip placed on a levelled hotplate, whereupon the surface of the hotplate was heated to 80 °C. An inverted glass funnel with the neck filled with cotton was then placed over the top of the glass slide to ensure gradual evaporation (over the course of hours), thus enabling reorganization of the films to achieve (near-)equilibrium morphologies. Finally, the obtained films on the glass coverslips were transferred into the vacuum bell

and dried at 80 °C/1 mbar for 24 h. Prior to AFM analysis, the sample surface was quickly rinsed with anhydrous ethanol for a few seconds and was then dried under a nitrogen flux.

2. Synthesis

2.1 Ionic liquid like monomers (ILMs)

2.1.1 Methacrylic ionic monomers

1-Butyl-3-methylimidazolium 1-[3-(methacryloyloxy)propylsulfonyl]-1-(trifluoromethanesulfonyl)imide (ILM1).

ILM1 was synthesized from lithium 1-[3-(methacryloyloxy)propylsulfonyl]-1-(trifluoromethanesulfonyl)imide^{12,100} via ion metathesis reaction with an excess of 1-methyl-3-butylimidazolium bromide in the aqueous medium.

The solution of lithium 1-[3-(methacryloyloxy)propylsulfonyl]-1-(trifluoromethanesulfonyl)imide (32.50 g, 94.0 mmol) in 150 ml of deionized water was added dropwise to the aqueous solution (60 mL) of 1-methyl-3-butylimidazolium bromide (21.10 g, 96.2 mmol) at room temperature. The formation of an emulsion was observed immediately and the stirring was continued for 2 h at RT. The organic oil was extracted from reaction mixture with DCM. The DCM layer was washed with water (4 × 30 mL), dried over anhydrous magnesium sulfate. MgSO₄ was filtered off, a catalytic amount of 4-methoxyphenol (as an inhibitor) was added and dichloromethane was removed under reduced pressure at RT. Resultant light yellow transparent oil was dried at 25 °C/0.1 mbar for 8 h. Yield: 27.40 g (77 %). $T_g = -63$ °C (DSC); $T_{onset} = 225$ °C (TGA); ¹H NMR (600.2 MHz, DMSO-*d*₆): $\delta = 9.09$ (s, 1H), 7.76 (s, 1H), 7.69 (s, 1H), 6.03 (s, 1H), 5.67 (s, 1H), 4.17 (dt, $J = 13.4, 6.8$ Hz, 4H), 3.85 (s, 3H), 3.10 – 3.04 (m, 2H), 2.06–1.97 (m, 2H), 1.88 (s, 3H), 1.79–1.74 (m, 2H), 1.29–1.23 (m, 2H), 0.90 (t, $J = 7.4$ Hz, 3H); ¹³C NMR (150.9 MHz, DMSO-*d*₆): $\delta = 166.4, 136.5, 135.8, 125.6, 123.6, 122.2, 120.1$ (q, $J_{CF} = 324.5$ Hz), 62.8, 51.3, 48.5, 35.7, 31.3, 23.5, 18.7, 17.9, 13.1; ¹⁹F NMR (564.7 MHz, DMSO-*d*₆): $\delta = -79.8$ (s); IR (ATR-mode): 3151 (m), 3114 (m), 2963 (m, ν_{CH}), 2938 (m, ν_{CH}), 2877 (w, ν_{CH}), 1716 (s, $\nu_{C=O}$), 1637 (m, $\nu_{C=C}$), 1572 (m), 1466 (m, ν_{CH}), 1410 (w), 1321 (vs, ν_{asSO_2}), 1298 (s), 1222 (m, ν_{CF}), 1178 (vs, ν_{sSO_2}), 1123 (s), 1052 (s, ν_{CF}), 1023 (m), 945 (w), 817 (m), 754 (m), 712 (w), 649 (m), 622 (s) cm⁻¹; Calc. for C₁₆H₂₆F₃N₃O₆S₂ (477.5): C, 40.25%; H, 5.49%; N, 8.80%; Found: C, 40.11%; H, 5.40%; N, 8.92%.

3-butyl-1-(3-(methacryloyloxy)propyl) imidazolium bis((trifluoromethyl)sulfonyl)amide (ILM2)

Monomer **ILM2** was prepared via a three steps reaction: 1) synthesis of 3-butyl-1-(3-hydroxypropyl)imidazolium bromide, 2) ion exchange reaction with an excess of LiTFSI and acylation reaction with methacryloyl chloride.

1-Butylimidazole (15.96 g, 128.7 mmol), 3-bromo-1-propanol (21.50 g, 154.0 mmol) and 70 mL of anhydrous toluene were added to a single-neck flask equipped with a magnetic stirrer and a condenser. The resulting mixture was stirred at 50 °C for 72 hours. During the reaction, the mixture separated into two layers. The toluene layer was decanted and the transparent viscous residue was washed with toluene (3 × 50 mL) and dried at 50 °C/0.1 mbar for 3 hours. Yield: 33.10 g (98%).

The solution of lithium bis((trifluoromethyl)sulfonyl)imide (40.70 g, 141.9 mmol) in 30 mL of deionized water was added dropwise to the aqueous solution (70 mL) of 3-butyl-1-(3-hydroxypropyl)imidazolium bromide (31.10 g, 118.2 mmol) at room temperature. The formation of an emulsion was observed immediately and the stirring was continued for 2 h at RT. The organic oil was extracted from reaction mixture with DCM. The DCM layer was washed with water (4 × 30 mL), dried over anhydrous magnesium sulfate and decolorizing charcoal (C_{act}). $MgSO_4$ with C_{act} was filtered off and dichloromethane was removed under reduced pressure at 50 °C. Resultant colorless transparent oil was dried at 50 °C/0.1 mbar for 8 h. Yield: 47.50 g (87 %). 1H NMR (600.2 MHz, DMSO- d_6): δ = 9.17 (s, 1H), 7.76 (d, J = 1.7 Hz, 2H), 4.60 (s, 1H), 4.24 (t, J = 7.1 Hz, 2H), 4.16 (t, J = 7.2 Hz, 2H), 3.42 (t, J = 5.9 Hz, 2H), 1.99 – 1.92 (m, 2H), 1.78 (p, J = 7.5 Hz, 2H), 1.31 – 1.22 (m, 2H), 0.90 (t, J = 7.4 Hz, 3H).

Freshly distilled methacryloyl chloride (13.65 g, 130.6 mmol) was dissolved in 7 mL of dichloromethane and cooled to -10 °C under an inert atmosphere in a three-neck flask equipped with a dropping funnel. In a separate flask, a solution of 3-butyl-1-(3-hydroxypropyl)imidazolium bis((trifluoromethyl)sulfonyl)imide (43.20 g, 93.0 mmol) and triethylamine (15.02 g, 148.8 mmol) in 7 mL of dichloromethane was prepared and transferred to the dropping funnel. This alcohol amine solution was added dropwise to the methacryloyl chloride, maintaining the temperature at -10 °C. A white precipitate formed after the first drops were added, and the solution turned red. After the complete addition, the reaction mixture was stirred at 25 °C for 12 hours. The white precipitate was filtered off, and dichloromethane was removed under reduced pressure at 25 °C. The reddish residue was dissolved in 20 mL of anhydrous THF, resulting in more white precipitate formation. This precipitate was filtered off, and the THF solution was added dropwise to an excess of diethyl ether. The resulting red oil was washed with diethyl ether (2 × 100 mL), dissolved in dichloromethane (300 mL), and passed through a 10 mL silica gel pad. The obtained solution was washed with water (5 × 100 mL), and the dichloromethane layer was dried over anhydrous magnesium sulfate. The magnesium sulfate was filtered off, and dichloromethane was removed under reduced pressure at 25 °C, yielding a red viscous oil. This oil was dissolved in 200 mL of methanol, 200 mg of decolorizing charcoal was added, and the resulting suspension was stirred for 12 hours at 25 °C. Decolorizing charcoal was filtered off, and methanol was removed under reduced pressure at 25 °C. The resulting yellowish oil was dried at 25 °C/0.1 mbar for 1 hour. Yield: 34.00 g (77 %). T_g = -70 °C (DSC); T_{onset} = 245 °C (TGA); 1H NMR

(600.2 MHz, DMSO- d_6): δ = 9.21 (s, 1H), 7.81 (s, 1H), 7.79 (s, 1H), 5.99 (d, 1H), 5.68 (s, 1H), 4.29 (t, J = 7.0 Hz, 2H), 4.15 (q, J = 6.5 Hz, 4H), 2.21 (p, J = 6.6 Hz, 2H), 1.87 (s, 3H), 1.81 – 1.73 (m, 2H), 1.27 (h, J = 7.4 Hz, 2H), 0.90 (t, J = 7.4 Hz, 3H); ^{13}C NMR (150.9 MHz, DMSO- d_6): δ = 166.3, 136.1, 135.6, 125.8, 122.5, 122.5, 119.5 (q, J_{CF} = 321.9 Hz), 61.3, 48.6, 46.4, 31.2, 28.4, 18.7, 17.8, 13.1; ^{19}F NMR (564.7 MHz, DMSO- d_6): δ = -80.8 (s); IR (ATR-mode): 3151 (m), 3114 (m), 2963 (m, ν_{CH}), 2938 (m, ν_{CH}), 2877 (w, ν_{CH}), 1716 (s, $\nu_{\text{C=O}}$), 1637 (m, $\nu_{\text{C=C}}$), 1572 (m), 1466 (m, ν_{CH}), 1410 (w), 1321 (vs, ν_{asSO_2}), 1298 (s), 1222 (m, ν_{CF}), 1178 (vs, ν_{sSO_2}), 1123 (s), 1052 (s, ν_{CF}), 1023 (m), 945 (w), 817 (m), 754 (m), 712 (w), 649 (m), 622 (s) cm^{-1} ; Calc. for $\text{C}_{16}\text{H}_{23}\text{F}_6\text{N}_3\text{O}_6\text{S}_2$ (531.5): C, 36.16%; H, 4.36%; N, 7.91%; Found: C, 36.12%; H, 4.51%; N, 7.84%

2.1.2 Dipropargyl ionic monomers

N,N-Dimethyl-N,N-dipropargylammonium Bis(trifluoromethylsulfonyl)imide (ILM3)
and **N,N-Dibutyl-N,N-dipropargylammonium Bis(trifluoromethylsulfonyl)imide (ILM4)**

Ionic liquid monomers (ILM3) and (ILM4) were synthesized as described previously¹⁰⁴.

N,N,N',N'-tetramethyl-N,N'-dipropargyl-hexane-1,6-diammonium bis(trifluoromethylsulfonyl)imide (ILM5)

Monomer ILM5 was synthesized in two steps: 1) *N*-alkylation of *N,N,N',N'*-tetramethyl-1,6-hexanediamine by propargyl bromide and 2) ion exchange reaction with an excess of LiTFSI.

A solution of propargyl bromide (9.13 g, 76.8 mmol) in anhydrous MeCN (10 mL) was added dropwise to a solution of *N,N,N',N'*-tetramethyl-1,6-hexanediamine (3.78 g, 21.9 mmol) in anhydrous MeCN (20 mL) maintained at 0-5 °C under inert atmosphere. After stirring for 5 minutes the start of the precipitation of a beige powder was observed. Stirring was continued for 1 h at 0-5 °C, then for 1h at 25 °C and finally for 10 h at 55 °C. The reaction mixture was centrifugated for 5 min at 5000 rpm, the mother liquor was decanted and a fresh portion of MeCN was added to the precipitate. After intense shaking the suspension was again centrifugated and this procedure was repeated three times. *N,N,N',N'*-Tetramethyl-*N,N'*-dipropargyl-hexane-1,6-diammonium bromide was isolated by filtration as white-beige powder and dried for 8 h at 70 °C/0.1 mbar (hereinafter with a special flask filled with P_2O_5 and introduced into the vacuum line). Yield: 8.64 g (96%); T_m = 205 °C (DSC).

Lithium bis(trifluoromethylsulfonyl)imide (3.53 g, 12.2 mmol) was dissolved in H_2O (8 mL) and added dropwise to a solution of *N,N,N',N'*-tetramethyl-*N,N'*-dipropargyl-hexane-1,6-diammonium bromide (2.10 g, 5.12 mmol) in H_2O (20 mL) at room temperature. The mixture was stirred 2 h at 25 °C and the precipitation of a yellow powder was observed. The temperature was raised to 70 °C and stirring was continued for 1 h. After cooling down to room temperature the upper aqueous layer was decanted and the residual powder was redissolved in 80 mL of dichloromethane. The DCM solution

was washed with water (3 × 30 mL) and dried over anhydrous MgSO₄. The magnesium sulfate was filtered off, the decolorizing charcoal was added to the solution and the suspension was stirred at room temperature for another 2 h. The charcoal was filtered off and DCM was stripped off under reduced pressure. Bispropargyl monomer **ILM5** was obtained as a white crystalline powder, which was dried at 50 °C/0.1 mbar for 4 h. Yield: 3.45 g (83%); T_m = 68 °C (DSC); T_c = 14 °C (DSC); T_g = -45 °C (DSC); ¹H NMR (300.0 MHz, DMSO-*d*₆): δ = 4.35 (d, J = 3.0 Hz, 4H), 4.02 (t, J = 3.0 Hz, 2H), 3.33 (br.s, 4H), 3.07 (s, 12H), 1.75 - 1.65 (m, 4H), 1.38 – 1.30 (m, 4H); ¹³C NMR (75.5 MHz, DMSO-*d*₆): δ = 119.5 (q, J_{CF} = 322.0 Hz), 82.8, 72.2, 62.9, 53.2, 49.8, 25.1, 21.6; ¹⁹F NMR (282 MHz, DMSO-*d*₆): δ = -78.7 (s); IR (KBr pellet): 3305 (m, ν_{C=H}), 3251 (m, ν_{C=H}), 3049 (w, ν_{CH}), 2996 (w, ν_{CH}), 2966 (m, ν_{CH}), 2626 (w, ν_{CH}), 2867 (w, ν_{CH}), 2135 (w, ν_{C≡H}), 1484 (m), 1423 (w), 1348 (vs, ν_{asS=O}), 1196 (vs, ν_{CF}), 1141 (s, ν_{sS=O}), 1054 (vs, ν_{CF}), 969 (w), 890 (m), 796 (m), 766 (w), 741 (m), 688 (w), 654 (w), 615 (vs, δ_{C=H}), 570 (s), 514 (s) cm⁻¹; Calc. for C₂₀H₃₀F₁₂N₄O₈S₄ (810.7): C, 29.63%; H, 3.73%; N, 6.91%; Found: C, 29.48%; H, 3.66%; N, 6.90%.

1,1'-(hexane-1,6-diyl)bis(3-propargyl-imidazolium) bis(trifluoromethylsulfonyl)imide (ILM6)

Monomer **ILM6** was prepared via a three steps reaction: 1) synthesis of *N*-propargyl imidazole, 2) *N*-alkylation of *N*-propargyl imidazole by 1,6-dibromohexane and ion exchange reaction with an excess of LiTFSI.

A solution of propargyl tosylate (48.08 g, 228.7 mmol) in anhydrous MeCN (100 mL) was added dropwise to a solution of imidazole (34.2 g, 503 mmol) in anhydrous MeCN (140 mL) at 0-5 °C under inert atmosphere. Stirring was continued for 1 h at 0-5 °C and then for 2 h at 40 °C. MeCN was evaporated under reduced pressure at room temperature and the residual oil was distilled under vacuum (bp = 62 °C/0.08 mm Hg). The obtained colorless oil was still containing 10 mol% of imidazole (¹H NMR). To remove impurity 1.5 mL of 37 wt% HCl was added to the oil with vigorous stirring at room temperature. Stirring was continued for 15 minutes and DCM (100 mL) was added to the solution. The organic layer was separated, washed with H₂O (3 × 5 mL) and dried over anhydrous MgSO₄. The magnesium sulfate was filtered off and DCM was evaporated under reduced pressure. *N*-propargyl imidazole was obtained as a yellow oil, which was dried at 25 °C/0.1 mbar for 4 h. Yield: 9.78 g (40%); ¹H NMR (400.0 MHz, DMSO-*d*₆): δ = 7.70 (s, 1H), 7.22 (s, 1H), 6.95 (s, 1H), 4.93 (br.s, 2H), 3.52 (br.s, 2H); ¹³C NMR (100.0 MHz, DMSO-*d*₆): δ = 137.1, 128.9, 119.5, 78.7, 76.2, 35.6; IR (KBr pellet): 3290 (vs, ν_{C≡H}), 3191 (s, ν_{CH imidazole}), 3112 (vs, ν_{CH νCH imidazole}), 2961 (m, ν_{CH}), 2927 (m, ν_{CH}), 2121 (s, ν_{C≡H}), 1670 (w), 1637 (w), 1594 (m), 1505 (vs), 1435 (s), 1392 (s), 1348 (s), 1282 (vs), 1231 (vs), 1107 (s), 1075 (vs), 1029 (s), 944 (m), 907 (s), 820 (vs), 736 (vs, δ_{CH imidazole}), 660 (vs), 616 (vs, δ_{C=H}), 458 (w) cm⁻¹.

A solution of 1,6-dibromohexane (4.50 g, 18.5 mmol) in anhydrous MeCN (25 mL) was added dropwise to a solution of *N*-propargyl imidazole (4.29 g, 40.6 mmol) in anhydrous MeCN (25 mL) maintained at 0-5 °C under inert atmosphere. The stirring was continued for 1 h at 0-5 °C, 2 h at 25 °C, 66 h at 45 °C and 23 h at 60 °C. The precipitation of the light-brown oil was observed and the emulsion was placed in the fridge (5 °C) for 48 h, whereupon the crystallization happened. The light-brown crystals were filtered, washed with Et₂O, then thrice with DCM, filtered again and smashed into powder with a mortar. 1,1'-(Hexane-1,6-diyl)bis(3-propargyl-imidazolium) bromide was crystallized from MeCN/H₂O mixture (150/11 mL) as light-yellow crystals that were dried at 60 °C/0.1 mbar for 12 h. Yield: 6.20 g (73%); $T_m = 139$ °C (DSC).

Lithium bis(trifluoromethylsulfonyl)imide (11.30 g, 39.3 mmol) was dissolved in H₂O (25 mL) and added dropwise to a solution of 1,1'-(hexane-1,6-diyl)bis(3-propargyl-imidazolium) bromide (5.98 g, 13.1 mmol) in H₂O (30 mL) at room temperature. The mixture was stirred for 2 h at 25 °C and the precipitation of a yellow powder was observed. The yellow powder was filtered and dissolved in acetone (60 mL). A solution of lithium bis(trifluoromethylsulfonyl)imide (6.50 g, 22.6 mmol) in acetone (15 mL) was added dropwise under stirring to the obtained solution. The reaction continued overnight at room temperature, whereupon the solvent was evaporated and the residual orange oil was extensively washed with H₂O (5 × 20 mL). The oil was dissolved in MeCN and dried over anhydrous MgSO₄. The magnesium sulfate was filtered off, the decolorizing charcoal was added to the solution and the suspension was stirred at room temperature for another 2 h. The charcoal was filtered off and MeCN was evaporated under reduced pressure. Monomer **ILM6** was obtained as a slightly viscous yellow oil, which was dried at 55 °C/0.1 mbar for 12 h. Yield: 7.09 g (63%); $T_g = -56$ °C (DSC); ¹H NMR (600.0 MHz, DMSO-*d*₆): $\delta = 9.26$ (s, 2H), 7.81 (s, 4H), 5.18 (br.s, 4H), 4.19 (t, $J = 7.2$ Hz, 4H), 3.81 (br.s, 2H), 1.80 (t, $J = 7.2$ Hz, 4H), 1.28 (br.s, 4H); ¹³C NMR (151.0 MHz, DMSO-*d*₆): $\delta = 136.1$, 122.8, 122.4, 119.5 (q, $J_{CF} = 322.0$ Hz), 78.9, 75.9, 48.9, 38.6, 29.1, 24.9; ¹⁹F NMR (565.0 MHz, DMSO-*d*₆): $\delta = -78.8$ (s); IR (KBr pellet): 3277 (m, $\nu_{C=H}$), 3151 (s, ν_{CH} imidazolium), 2949 (m, ν_{CH}), 2868 (w, ν_{CH}), 2138 (w, $\nu_{C=H}$), 1564 (s), 1475 (w), 1444 (w), 1350 (vs, $\nu_{asS=O}$), 1330 (vs), 1193 (vs, ν_{CF}), 1137 (vs, $\nu_{sS=O}$), 1055 (vs, ν_{CF}), 955 (w), 842 (m), 790 (s), 740 (s, δ_{CH} imidazolium), 654 (m), 614 (vs, $\delta_{C=H}$), 570 (vs), 513 (s), 406 (m) cm⁻¹; Calc. for C₂₂H₂₄F₁₂N₆O₈S₄ (856.7): C, 30.84%; H, 2.82%; F, 26.61%; Found: C, 31.18%; H, 2.80%; F, 26.69%.

2.2 Poly(ionic liquid)s (PIL)s

2.2.1 Triazole/triazolium PILs (PIL1-PIL9)

Synthesis of poly(1,2,3-triazole)s PIL1-PIL4.

PIL1-PIL4 were synthesized via AA + BB CuAAC polyaddition and a typical procedure is detailed below by the example of poly(1,2,3-triazole) **PIL4** preparation.

Dipropargyl **ILM6** (1.01 g, 1.18 mmol), 1,11-diazido-3,6,9-trioxaundecane (0.29 g, 1.18 mmol) and *N,N*-diisopropylethylamine (0.31 g, 2.36 mmol) were dissolved in anhydrous DMF (6 mL) under inert atmosphere at room temperature. Afterwards the CuIP(OEt)₃ (42.2 mg, 0.118 mmol) was added in one portion to the transparent yellow solution and stirring was continued in the dark for 68 h at 80 °C. The resulting brown solution was precipitated into the excess of diethyl ether and the brown oil was centrifugated (10000 RPM, 5 min). The oil was dissolved in MeCN (5 mL) and precipitated twice into an excess of H₂O containing 2-3 drops of PMEDTA and then thrice in H₂O. Poly(1,2,3-triazole) **PIL4** was recovered as a dark brown gummy material and was dried at 80 °C/0.1 mbar for 12 h. Yield: 0.82 g (63%); *T_g* = -12 °C (DSC); ¹H NMR (600.0 MHz, DMSO-*d*₆): δ = 9.26 (s, 2H), 8.22 (s, 2H), 7.78 (s, 2H), 7.76 (s, 2H), 5.53 (s, 4H), 4.55 (t, *J* = 4.8 Hz, 4H), 4.17 (t, *J* = 7.8 Hz, 4H), 3.82 (t, *J* = 5.4 Hz, 4H), 3.58 – 3.49 (m, 4H), 3.50 – 3.42 (m, 4H), 1.84 – 1.75 (m, 4H), 1.32 – 1.24 (m, 4H); ¹³C NMR (151 MHz, DMSO-*d*₆): δ = 140.2, 136.1, 124.9, 122.6, 120.0 (q, *J*_{CF} = 322.0 Hz), 69.6, 69.5, 68.6, 49.6, 48.9, 43.8, 29.1, 24.9; ¹⁹F NMR (565.0 MHz, DMSO-*d*₆): δ = -78.8 (s); IR (ATR mode): 3152 (m, ν_{CH} imidazolium), 3113 (w, ν_{CH} triazole), 3096 (w, ν_{CH} triazole), 2934 (w, ν_{CH}), 2916 (w, ν_{CH}), 2868 (m, ν_{CH}), 1697 (w), 1598 (w), 1563 (m), 1515 (w), 1449 (m), 1348 (s, ν_{asS=O}), 1329 (s), 1180 (vs, ν_{CF}), 1132 (vs, ν_{sS=O}), 1051 (vs, ν_{CF}), 833 (m), 740 (s, δ_{CH} imidazolium), 652 (m), 613 (vs, δ_{C≡H}), 599 (s), 570 (vs), 531 (w), 512 (vs) cm⁻¹; Calc. for C₃₁H₄₄F₁₂N₁₂O₁₁S₄ (1117.0): C, 33.33%; H, 3.97%; N, 15.05%; Found: C, 33.19%; H, 3.96%; N, 14.94%.

Synthesis of poly(1,2,3-triazolium)s **PIL5-PIL9**

Polymers **PIL5-PIL9** were synthesized in two steps: *N*-alkylation of the 1,2,3-triazole groups of polymers **PIL2-PIL4** by an excess of CH₃I and subsequent ion exchange reaction with LiTFSI. A typical procedure is given below by the example of **PIL8** preparation.

Iodomethane (0.93 g, 6.54 mmol) was added to a solution of poly(1,2,3-triazole) **PIL4** (0.72 g, 0.654 mmol) in anhydrous DMF (10 mL) at room temperature under inert atmosphere. Stirring was continued at 60 °C for 90 h, whereupon additional CH₃I (0.50 g, 3.52 mmol) was added and the solution was further stirred at 80 °C for 72 h. The crude reaction mixture was diluted with DMF and precipitated two times in acetone to yield a dark brown viscous oil which was separated by centrifugation (10000 RPM, 10 min).

The obtained oil was redissolved in H₂O (20 mL) and an aqueous solution of LiTFSI (0.69 g, 2.4 mmol in 5 mL of H₂O) was added dropwise under vigorous stirring at room temperature. The mixture was stirred for 12 h at 40 °C and the precipitation of a viscous brown oil was observed. The aqueous layer was decanted and the oil was washed with H₂O (3 × 20 mL), dissolved in acetone (6 mL) and precipitated again into an excess of H₂O. Polymer **PIL8** was recovered as a brown gummy solid after centrifugation (10000 RPM, 10 min) and drying at 80 °C/0.1 mbar for 12 h. Yield: 0.67 g (69%);

$T_g = -1\text{ }^{\circ}\text{C}$ (DSC); ^1H NMR (600 MHz, DMSO- d_6): $\delta = 9.30$ (s, 2H), 8.97 (s, 2H), 7.85 (br.s, 4H), 5.84 (s, 4H), 4.83 (t, $J = 4.8$ Hz, 4H), 4.34 (s, 6H), 4.18 (t, $J = 7.8$ Hz, 4H), 3.92 (t, $J = 5.4$ Hz, 4H), 3.58 (br.s, 4H), 3.51 (br.s, 4H), 1.82 (br.s, 4H), 1.35 (br.s, 4H); ^{13}C NMR (151 MHz, DMSO- d_6): $\delta = 137.2$, 131.4, 122.9, 122.7, 120.0 (q, $J_{\text{CF}} = 322.0$ Hz), 69.5, 67.4, 53.4, 49.1, 40.3, 38.4, 29.2, 25.1; ^{19}F NMR (565 MHz, DMSO- d_6): $\delta = -78.8$ (s); IR (ATR mode): 3151 (w, ν_{CH} imidazolium), 3119 (w, ν_{CH} triazolium), 3089 (w, ν_{CH} triazolium), 2929 (w, ν_{CH}), 2875 (m, ν_{CH}), 1561 (m), 1457 (m), 1346 (s, $\nu_{\text{asS=O}}$), 1328 (s), 1175 (vs, ν_{CF}), 1131 (vs, $\nu_{\text{S=O}}$), 1050 (vs, ν_{CF}), 935 (w), 843 (m), 791 (s), 741 (s, δ_{CH} imidazolium), 692 (m, δ_{CH} triazolium), 652 (s), 611 (vs, $\delta_{\text{C=H}}$), 598 (s), 569 (vs), 505 (vs) cm^{-1} ; Calc. for $\text{C}_{37}\text{H}_{50}\text{F}_{24}\text{N}_{14}\text{O}_{19}\text{S}_8$ (1707.4): C, 26.03%; H, 2.95%; N, 11.49%; Found: C, 26.07%; H, 2.91%; N, 11.51%.

2.2.2 Methacrylate based polyelectrolytes (PIL10-PIL29)

RAFT polymerization of ILM1, ILM2 and ILM7

Random copolymers **poly(ILM1_n-*r*-PEGM_m)**, **poly(ILM2_n-*r*-PEGM_m)** and **poly(ILM7₁₂₈-*r*-PEGM₁₂₈)** were prepared via RAFT copolymerization. While the detailed loadings and reaction times for the synthesis of **PIL10** - **PIL12**, **PIL14** – **PIL21** are presented in Table IV.1, the typical polymerization procedure is given bellow by the example of **poly(ILM1₉₄-*r*-PEGM₁₀₃) (PIL13)** synthesis.

A solution of **ILM1** (3.00 g, 6.28 mmol), PEGM (3.14 g, 6.29 mmol), CPCP (17.1 mg, 0.061 mmol) and AIBN (2.01 mg, 0.012 mmol, [AIBN]:[CPCP]=1:5 by mol) in anhydrous DMF (19.5 mL, 18.4 g, [DMF]:[ILM1+PEGM]=3:1 by weight) was transferred to a Schlenk flask equipped with magnetic stirring bar. The solution was de-gassed via three freeze-pump-thaw cycles and flashed with argon, whereupon the flask was placed into a bath preheated at 60 $^{\circ}\text{C}$. Polymerization was further carried out under at 60 $^{\circ}\text{C}$ for 72 h. The resultant viscous pink polymer solution was diluted with DMF and precipitated into an excess of diethyl ether. The precipitated residue was then dissolved in a small amount of deionized water and dialyzed until the conductivity of the used dialysate reached 5 mS cm^{-1} . The obtained neat aqueous solution of **PIL13** was then concentrated using a freeze dryer. Isolated copolymer represented pink sticky mass that was dried at 60 $^{\circ}\text{C}$ /0.1 mbar for 24 h in B-585 oven (Buchi Glass Drying Oven, Switzerland) filled with P_2O_5 . Yield: 5.00 g (82%); $T_g = -46\text{ }^{\circ}\text{C}$ (by DSC); $T_{\text{onset}} = 165^{\circ}\text{C}$ (TGA); ^1H NMR (600.2 MHz, DMSO- d_6): $\delta = 9.07$ (s, 1H), 7.74 (s, 1H), 7.68 (s, 1H), 4.16 (t, $J = 7.2$ Hz, 2H), 4.01 (br.s., 4H), 3.85 (s, 3H), 3.80 – 3.42 (m, 39H), 3.24 (s, 3H), 3.00 (s, 2H), 2.19 – 1.31 (m, 6H), 1.77 (p, $J = 7.4$ Hz, 2H), 1.27 (sext, $J = 7.4$ Hz, 2H), 1.25 – 0.45 (m, 6H), 0.90 (t, $J = 7.4$ Hz, 3H); ^{13}C NMR (150.9 MHz, DMSO- d_6): $\delta = 176.7$, 136.5, 123.6, 122.2, 120.1 (q, $J_{\text{CF}} = 324.3$ Hz), 71.3, 69.8, 69.56, 67.8, 63.8, 58.0, 51.1, 48.5, 35.7, 31.3, 23.01, 18.7, 16.6, 13.2; ^{19}F NMR (564.7 MHz, DMSO- d_6): $\delta = -79.8$ (s); IR (ATR-mode): 3151 (w), 3111 (w), 2871 (s, ν_{CH}), 1727 (s, $\nu_{\text{C=O}}$), 1572 (w), 1454 (m, ν_{CH}), 1387 (w), 1351 (w), 1322 (s, ν_{asSO_2}), 1298 (m), 1248 (m, $\nu_{\text{as-C-O-C-}}$), 1224 (m, ν_{CF}), 1177

(vs, ν_{SO_2}), 1120 (vs, $\nu_{\text{C-O}}$), 1054 (s, ν_{CF}), 949 (m), 852 (m), 621 (s) cm^{-1} ; Calc. for $\text{C}_{41}\text{H}_{74}\text{N}_3\text{F}_3\text{O}_{18}\text{S}_2$ (1018.2): C, 48.37%; H, 7.33%; N, 4.13%; Found: C, 48.04%; H, 6.99%; N, 4.29%.

Poly[(1-butyl-3-methylimidazolium 1-[3-(methacryloyloxy)propylsulfonyl]-1-(trifluoromethanesulfonyl)imide)] (poly(ILM1₇₄) (PIL10)

Yield: 1.50 g (88 %); $T_g = -13^\circ\text{C}$ (DSC); $T_{\text{onset}} = 275^\circ\text{C}$ (TGA); ^1H NMR (600.2 MHz, DMSO-d_6): $\delta = 9.04$ (s, 1H), 7.72 (s, 1H), 7.65 (s, 1H), 4.15 (t, $J = 7.2$ Hz, 2H), 3.98 (br.s, 2H), 3.85 (s, 3H), 3.01 (br.s, 2H), 1.95 (br.s, 2H), 1.77 (p, $J = 7.3$ Hz, 2H), 1.67 (br.s, 2H), 1.25 (sext, $J = 7.4$ Hz, 2H), 0.89 (t, $J = 7.4$ Hz, 3H), 0.74 (br.s, 3H); ^{13}C NMR (150.9 MHz, DMSO-d_6): $\delta = 176.7$, 136.4, 123.5, 122.1, 120.1 (q, $J_{\text{CF}} = 324.0$ Hz), 63.1, 51.1, 48.5, 44.1, 35.6, 31.3, 22.3, 18.7, 16.6, 13.1; ^{19}F NMR (564.7 MHz, DMSO-d_6): $\delta = -79.8$ (s)

Poly[(1-butyl-3-methylimidazolium 1-[3-(methacryloyloxy)propylsulfonyl]-1-(trifluoromethanesulfonyl)imide)-*r*-(poly(ethyleneglycol) methyl ether methacrylate)] poly(ILM1_{31-r}-PEGM₃₄) (PIL11)

Yield: 4.79 g (78 %); $T_g = -40^\circ\text{C}$ (DSC); $T_{\text{onset}} = 165^\circ\text{C}$ (TGA); ^1H NMR (600.2 MHz, DMSO-d_6): $\delta = 9.07$ (s, 1H), 7.74 (s, 1H), 7.68 (s, 1H), 4.16 (t, $J = 7.2$ Hz, 2H), 4.01 (br.s, 4H), 3.85 (s, 3H), 3.75 - 3.34 (m, 35H), 3.24 (s, 3H), 3.01 (br.s, 2H), 1.96 (br.s, 2H), 1.77 (p, $J = 7.3$ Hz, 3H), 1.71 (br.s, 4H), 1.27 (sext, $J = 7.4$ Hz, 2H), 0.90 (t, $J = 7.4$ Hz, 3H), 0.78 (br.s, 6H); ^{13}C NMR (150.9 MHz, DMSO-d_6): $\delta = 176.7$, 136.5, 123.6, 122.2 120.1 (q, $J_{\text{CF}} = 324.3$ Hz), 71.3, 69.8, 69.56, 67.8, 63.8, 58.0, 51.1, 48.5, 35.7, 31.3, 23.01, 18.7, 16.6, 13.2; ^{19}F NMR (564.7 MHz, DMSO-d_6): $\delta = -79.8$ (s).

Poly[(1-butyl-3-methylimidazolium 1-[3-(methacryloyloxy)propylsulfonyl]-1-(trifluoromethanesulfonyl)imide)-*r*-(poly(ethyleneglycol) methyl ether methacrylate)] poly(ILM1_{41-r}-PEGM₄₅) (PIL12)

Yield: 6.55 g (80 %); $T_g = -41^\circ\text{C}$ (DSC); $T_{\text{onset}} = 165^\circ\text{C}$ (TGA); ^1H NMR (600.2 MHz, DMSO-d_6): $\delta = 9.07$ (s, 1H), 7.74 (s, 1H), 7.68 (s, 1H), 4.16 (t, $J = 7.2$ Hz, 2H), 4.01 (br.s, 4H), 3.85 (s, 3H), 3.75 - 3.34 (m, 35H), 3.24 (s, 3H), 3.01 (br.s, 2H), 1.96 (br.s, 2H), 1.77 (p, $J = 7.3$ Hz, 3H), 1.71 (br.s, 4H), 1.27 (sext, $J = 7.4$ Hz, 2H), 0.90 (t, $J = 7.4$ Hz, 3H), 0.78 (br.s, 6H); ^{13}C NMR (150.9 MHz, DMSO-d_6): $\delta = 176.7$, 136.5, 123.6, 122.2 120.1 (q, $J_{\text{CF}} = 324.3$ Hz), 71.3, 69.8, 69.56, 67.8, 63.8, 58.0, 51.1, 48.5, 35.7, 31.3, 23.01, 18.7, 16.6, 13.2; ^{19}F NMR (564.7 MHz, DMSO-d_6): $\delta = -79.8$ (s).

Poly[(1-butyl-3-methylimidazolium 1-[3-(methacryloyloxy)propylsulfonyl]-1-(trifluoromethanesulfonyl)imide)-*r*-(poly(ethyleneglycol) methyl ether methacrylate)] poly(ILM1_{14-r}-PEGM₄₉) (PIL14)

Yield: 2.52 g (81 %); $T_g = -54^\circ\text{C}$ (DSC); $T_{\text{onset}} = 160^\circ\text{C}$ (TGA); ^1H NMR (600.2 MHz, DMSO-d_6): $\delta = 9.07$ (s, 1H), 7.74 (s, 1H), 7.68 (s, 1H), 4.16 (t, $J = 7.2$ Hz, 2H), 4.01 (br.s, 9H), 3.85 (s, 3H),

3.75 - 3.34 (m, 112H), 3.24 (s, 10H), 3.01 (br.s, 2H), 1.96 (br.s, 2H), 1.77 (p, $J = 7.3$ Hz, 3H), 1.71 (br.s, 9H), 1.27 (sext, $J = 7.4$ Hz, 2H), 0.90 (t, $J = 7.4$ Hz, 3H), 0.78 (br.s, 13H); ^{13}C NMR (150.9 MHz, DMSO- d_6): $\delta = 176.7, 136.5, 123.6, 122.2, 120.1$ (q, $J_{\text{CF}} = 324.3$ Hz), 71.3, 69.8, 69.56, 67.8, 63.8, 58.0, 51.1, 48.5, 35.7, 31.3, 23.01, 18.7, 16.6, 13.2; ^{19}F NMR (564.7 MHz, DMSO- d_6): $\delta = -79.8$ (s).

Poly[(1-butyl-3-methylimidazolium 1-[3-(methacryloyloxy)propylsulfonyl]-1-(trifluoromethanesulfonyl)imide)-*r*-(poly(ethyleneglycol) methyl ether methacrylate)] poly(ILM1₁₀-*r*-PEGM₅₄) (PIL15)

Yield: 2.34 g (75 %); $T_g = -57^\circ\text{C}$ (DSC); $T_{\text{onset}} = 160^\circ\text{C}$ (TGA); ^1H NMR (600.2 MHz, DMSO- d_6): $\delta = 9.07$ (s, 1H), 7.74 (s, 1H), 7.68 (s, 1H), 4.16 (t, $J = 7.2$ Hz, 2H), 4.01 (br.s, 13H), 3.85 (s, 3H), 3.75 - 3.34 (m, 176H), 3.24 (s, 16H), 3.01 (br.s, 2H), 1.96 (br.s, 2H), 1.77 (p, $J = 7.3$ Hz, 3H), 1.71 (br.s, 13H), 1.27 (sext, $J = 7.4$ Hz, 2H), 0.90 (t, $J = 7.4$ Hz, 3H), 0.78 (br.s, 19H); ^{13}C NMR (150.9 MHz, DMSO- d_6): $\delta = 176.7, 136.5, 123.6, 122.2, 120.1$ (q, $J_{\text{CF}} = 324.3$ Hz), 71.3, 69.8, 69.56, 67.8, 63.8, 58.0, 51.1, 48.5, 35.7, 31.3, 23.01, 18.7, 16.6, 13.2; ^{19}F NMR (564.7 MHz, DMSO- d_6): $\delta = -79.8$ (s).

Poly[(1-butyl-3-methylimidazolium 1-[3-(methacryloyloxy)propylsulfonyl]-1-(trifluoromethanesulfonyl)imide)-*r*-(poly(ethyleneglycol) methyl ether methacrylate)] poly(ILM1₈-*r*-PEGM₅₆) (PIL16)

Yield: 2.43 g (73 %); $T_g = -58^\circ\text{C}$ (DSC); $T_{\text{onset}} = 160^\circ\text{C}$ (TGA); ^1H NMR (600.2 MHz, DMSO- d_6): $\delta = 9.07$ (s, 1H), 7.74 (s, 1H), 7.68 (s, 1H), 4.16 (t, $J = 7.2$ Hz, 2H), 4.01 (br.s, 16H), 3.85 (s, 3H), 3.75 - 3.34 (m, 237H), 3.24 (s, 21H), 3.01 (br.s, 2H), 1.96 (br.s, 2H), 1.77 (p, $J = 7.3$ Hz, 3H), 1.71 (br.s, 16H), 1.27 (sext, $J = 7.4$ Hz, 2H), 0.90 (t, $J = 7.4$ Hz, 3H), 0.78 (br.s, 24H); ^{13}C NMR (150.9 MHz, DMSO- d_6): $\delta = 176.7, 136.5, 123.6, 122.2, 120.1$ (q, $J_{\text{CF}} = 324.3$ Hz), 71.3, 69.8, 69.56, 67.8, 63.8, 58.0, 51.1, 48.5, 35.7, 31.3, 23.01, 18.7, 16.6, 13.2; ^{19}F NMR (564.7 MHz, DMSO- d_6): $\delta = -79.8$ (s).

Poly[(1-butyl-3-methylimidazolium 1-[3-(methacryloyloxy)propylsulfonyl]-1-(trifluoromethanesulfonyl)imide)-*r*-(poly(ethyleneglycol) methyl ether methacrylate)] poly(ILM1₆-*r*-PEGM₅₈) (PIL17)

Yield: 2.52 g (81 %); $T_g = -62^\circ\text{C}$ (DSC); $T_{\text{onset}} = 160^\circ\text{C}$ (TGA); ^1H NMR (600.2 MHz, DMSO- d_6): $\delta = 9.07$ (s, 1H), 7.74 (s, 1H), 7.68 (s, 1H), 4.16 (t, $J = 7.2$ Hz, 2H), 4.01 (br.s, 22H), 3.85 (s, 3H), 3.75 - 3.34 (m, 339H), 3.24 (s, 30H), 3.01 (br.s, 2H), 1.96 (br.s, 2H), 1.77 (p, $J = 7.3$ Hz, 3H), 1.71 (br.s, 22H), 1.27 (sext, $J = 7.4$ Hz, 2H), 0.90 (t, $J = 7.4$ Hz, 3H), 0.78 (br.s, 33H); ^{13}C NMR (150.9 MHz, DMSO- d_6): $\delta = 176.7, 136.5, 123.6, 122.2, 120.1$ (q, $J_{\text{CF}} = 324.3$ Hz), 71.3, 69.8, 69.56, 67.8, 63.8, 58.0, 51.1, 48.5, 35.7, 31.3, 23.01, 18.7, 16.6, 13.2; ^{19}F NMR (564.7 MHz, DMSO- d_6): $\delta = -79.8$ (s).

Poly[(3-butyl-1-(3-(methacryloyloxy)propyl)imidazolium bis((trifluoromethyl)sulfonyl)imide)] poly(ILM2₅₁) (PIL18)

For the synthesis of **PIL18** polymers the same procedure was used as for **PIL13** with the exceptions that CPDB was used as CTA and acetone/H₂O mixture (5:1 by vol) was used as dialysate.

Yield: 2.80 g (70 %); $T_g = -6^\circ\text{C}$ (DSC); $T_{onset} = 290^\circ\text{C}$ (TGA); ¹H NMR (600.2 MHz, DMSO-d₆): $\delta = 9.11$ (s, 1H), 7.78 (s, 1H), 7.68 (s, 1H), 4.40 – 4.10 (m, 4H), 4.09 – 3.78 (m, 2H), 2.11 (br.s, 2H), 1.78 (br.s, 2H), 1.69 (br.s, 2H), 1.27 (br.s, 2zH), 0.92 (s, 3H), 0.76 (br.s, 3H); ¹³C NMR (150.9 MHz, DMSO-d₆): $\delta = 176.7, 135.9, 122.6, 122.2, 119.5$ (q, $J_{CF} = 321.9$ Hz), 61.6, 48.7, 46.1, 44.4, 31.2, 28.1, 18.7, 16.6, 13.1; ¹⁹F NMR (564.7 MHz, DMSO-d₆): $\delta = -81.0$ (s).

Poly[(3-butyl-1-(3-(methacryloyloxy)propyl)imidazolium bis((trifluoromethyl)sulfonyl)imide)-*r*-(poly(ethyleneglycol) methyl ether methacrylate)] poly(ILM2_{45-r}-PEGM₄₅) (PIL19)

For the synthesis of **PIL19** polymers the same procedure was used as for **PIL13** with the exceptions that CPDB was used CTA and acetone/H₂O mixture (5:1 by vol) was used as dialysate.

Yield: 5.81 g (83 %); $T_g = -38^\circ\text{C}$ (DSC); $T_{onset} = 160^\circ\text{C}$ (TGA); ¹H NMR (600.2 MHz, DMSO-d₆): $\delta = 9.14$ (s, 1H), 7.80 (s, 1H), 7.74 (s, 1H), 4.26 – 4.11 (m, 4H), 4.10 – 3.85 (m, 4H), 3.68 – 3.36 (m, 33H), 3.23 (s, 3H), 2.14 (br.s, 2H), 1.78 (br.s, 2H), 1.70 (br.s, 4H), 1.27 (br.s, 2H), 0.90 (br.s, 3H), 0.78 (br.s, 6H); ¹³C NMR (150.9 MHz, DMSO-d₆): $\delta = 176.7, 176.1, 136.1, 122.6, 122.4, 119.5$ (q, $J_{CF} = 321.9$ Hz), 71.3, 69.8, 69.6, 67.8, 63.9, 54.9, 48.6, 46.1, 44.5, 44.2, 31.3, 28.1, 18.8, 17.9, 16.4, 13.2; ¹⁹F NMR (564.7 MHz, DMSO-d₆): $\delta = -81.0$ (s); IR (ATR-mode): 3151 (w), 3111 (w), 2871 (s, ν_{CH}), 1727 (s, $\nu_{C=O}$), 1572 (w), 1454 (m, ν_{CH}), 1387 (w), 1351 (w), 1322 (s, ν_{asSO_2}), 1298 (m), 1248 (m, $\nu_{as-C-O-C}$), 1224 (m, ν_{CF}), 1177 (vs, ν_{sSO_2}), 1120 (vs, ν_{C-O-C}), 1054 (s, ν_{CF}), 949 (m), 852 (m), 621 (s) cm⁻¹; Calc. for C₃₉H₇₀N₃F₆O₁₇S₂ (1031.1): C, 45.43%; H, 6.84%; N, 4.08%; Found: C, 45.31%; H, 6.84%; N, 4.55%.

Poly[(3-butyl-1-(3-(methacryloyloxy)propyl)imidazolium bis((trifluoromethyl)sulfonyl)imide)-*r*-(poly(ethyleneglycol) methyl ether methacrylate)] poly(ILM2_{18-r}-PEGM₇₈) (PIL20)

For the synthesis of **PIL20** polymers the same procedure was used as for **PIL13** with the exceptions that CPDB was used CTA and acetone/H₂O mixture (5:1 by vol) was used as dialysate.

Yield: 10.78 g (77 %); $T_g = -57^\circ\text{C}$ (DSC); $T_{onset} = 160^\circ\text{C}$ (TGA); ¹H NMR (600.2 MHz, DMSO-d₆): $\delta = 9.14$ (s, 1H), 7.80 (s, 1H), 7.74 (s, 1H), 4.26 – 4.11 (m, 4H), 4.10 – 3.85 (m, 11H), 3.68 – 3.36 (m, 142H), 3.23 (s, 3H), 2.14 (br.s, 2H), 1.78 (br.s, 2H), 1.70 (br.s, 11H), 1.27 (br.s, 2H), 0.90 (br.s, 3H), 0.78 (br.s, 16H); ¹³C NMR (150.9 MHz, DMSO-d₆): $\delta = 176.7, 176.1, 136.1, 122.6, 122.4, 119.5$

(q, $J_{CF} = 321.9$ Hz), 71.3, 69.8, 69.6, 67.8, 63.9, 54.9, 48.6, 46.1, 44.5, 44.2, 31.3, 28.1, 18.8, 17.9, 16.4, 13.2; ^{19}F NMR (564.7 MHz, DMSO- d_6): $\delta = -81.0$ (s).

Poly[(potassium 3-(methacryloyloxy)propane-1-sulfonate)-*r*-(poly(ethyleneglycol) methyl ether methacrylate)] poly(ILM7₁₂₈-*r*-PEGM₁₂₈) (PIL21)

The same procedure as for **PIL13** was followed, except that a DMF/H₂O mixture (3:2 by vol) was used as the solvent for the RAFT polymerization.

Yield: 34.57 g (95 %); ^1H NMR (600.2 MHz, DMSO- d_6): $\delta = 4.03$ (br.s, 4H), 3.82 – 3.35 (m, 32H), 3.25 (s, 3H), 2.53 (br.s, 2H), 1.89 (br.s, 2H), 1.73 (br.s, 4H), 1.20 – 0.56 (m, 6H); ^{13}C NMR (150.9 MHz, DMSO- d_6): $\delta = 176.7, 176.1, 71.2, 69.6, 67.8, 63.9, 58.0, 47.8, 44.5, 44.1, 24.3, 18.0, 16.3$.

Ion metathesis

Polyelectrolytes **PIL21I**, **PIL21A**, **PIL21S** and **PIL21P** were synthesized via ion metathesis between **PIL21** and the corresponding bromide salts following the general procedure given for **poly[(1-butyl-3-methylimidazolium 3-(methacryloyloxy)propane-1-sulfonate)-*r*-(poly(ethyleneglycol) methyl ether methacrylate)] poly(ILM7BuMeIm₁₂₈-*r*-PEGM₁₂₈) (PIL21I)** below.

PIL21 (1.50 g, 2.01 mmol) was dissolved in 10 mL of deionized water and placed into a dialysis bag. The solution was dialyzed twice under vigorous stirring using a 0.5M solution of 1-butyl-3-methylimidazolium bromide (33.00 g, 150.58 mmol in 300 mL) as the dialysate. Following this, the sample was dialyzed with deionized water to remove excess salt. The resulting aqueous solution of **PIL21I** was concentrated using a freeze dryer. Isolated copolymer represented pink sticky mass that was dried at 60 °C/0.1 mbar for 24 h in B-585 oven (Buchi Glass Drying Oven, Switzerland) filled with P₂O₅. Yield: 1.3 g (76 %); $T_g = -40^\circ\text{C}$ (DSC); $T_{onset} = 205^\circ\text{C}$ (TGA); ^1H NMR (600.2 MHz, DMSO- d_6): $\delta = 9.24$ (s, 1H), 7.81 (s, 1H), 7.74 (s, 1H), 4.19 (t, $J = 7.1$ Hz, 2H), 4.01 (br.s, 4H), 3.87 (s, 3H), 3.82 – 3.35 (m, 34H), 3.24 (s, 3H), 2.46 (br.s, 2H), 1.87 (br.s, 2H), 1.82 – 1.74 (m, 2H), 1.69 (br.s, 4H), 1.33 – 1.24 (m, 2H), 0.90 (t, $J = 7.4$, 3H), 0.76 (br.s, 6H); ^{13}C NMR (150.9 MHz, DMSO- d_6): $\delta = 176.1, 136.6, 123.5, 122.2, 71.2, 69.7, 69.5, 67.7, 64.2, 57.9, 53.4, 48.4, 47.8, 44.1, 35.6, 31.3, 24.3, 18.7, 16.4, 13.1$; IR (ATR-mode): 3100 (w, ν_{CH}), 2930 (m, ν_{CH}), 2871 (m, ν_{CH}), 1727 (s, $\nu_{\text{C=O}}$), 1572 (w), 1454 (m, ν_{CH}), 1351 (w), 1235 (m, $\nu_{\text{as-C-O-C-}}$), 1140 (vs, ν_{SO_2}), 1100 (vs, $\nu_{\text{C-O-}}$), 1035 (s), 947 (m), 852 (m), 747 (s) cm^{-1} ; Calc. for C₃₈H₇₀N₂O₁₆S (843.0): C, 54.14%; H, 8.37%; N, 3.32

Poly[(tetrabutylammonium 3-(methacryloyloxy)propane-1-sulfonate)-*r*-(poly(ethyleneglycol) methyl ether methacrylate)] poly(ILM7Bu₄N₁₂₈-*r*-PEGM₁₂₈) (PIL21S)

The same procedure was used as for **PIL21I** with the exception that aqueous solution of tetrabutylammonium bromide (49.13 g, 150.58 mmol) in 300 mL was used as an initial dialysate.

Yield: 1.44 g (75 %); $T_g = -36^\circ\text{C}$ (DSC); $T_{onset} = 190^\circ\text{C}$ (TGA); ^1H NMR (600.2 MHz, DMSO- d_6): $\delta = 4.02$ (br.s, 4H), 3.82 – 3.35 (m, 35H), 3.29 – 3.14 (m, 11H), 2.41 (br.s, 2H), 1.84 (br.s, 2H), 1.76 (br.s, 4H), 1.59 (br.s, 8H), 1.36 – 1.27 (m, 8H), 0.98 – 0.90 (m, 12H), 0.78 (br.s, 6H); ^{13}C NMR (150.9 MHz, DMSO- d_6): $\delta = 176.8, 71.2, 69.7, 69.5, 67.8, 64.3, 57.9, 57.5, 47.8, 44.2, 24.4, 23.1, 19.1, 16.4, 13.4$; Calc. for $\text{C}_{46}\text{H}_{91}\text{NO}_{16}\text{S}$ (946.3): C, 58.39%; H, 9.69%; N, 3.39%.

Poly[(tetrabutylphosphonium 3-(methacryloyloxy)propane-1-sulfonate)-*r*-(poly(ethyleneglycol) methyl ether methacrylate)] poly(ILM7Bu₄P₁₂₈-*r*-PEGM₁₂₈) (PIL21P)

The same procedure was used as for **PIL21I** with the exception that aqueous solution of tetrabutylphosphonium bromide (51.04 g, 150.58 mmol) in 300 mL was used as an initial dialysate.

Yield: 1.56 g (80 %); $T_g = -52^\circ\text{C}$ (DSC); $T_{onset} = 250^\circ\text{C}$ (TGA); ^1H NMR (600.2 MHz, DMSO- d_6): $\delta = 4.01$ (br.s, 4H), 3.82 – 3.35 (m, 34H), 3.24 (s, 3H), 2.42 (br.s, 2H), 2.27 – 2.15 (m, 8H), 1.85 (br.s, 2H), 1.75 (br.s, 4H), 1.54 – 1.32 (m, 16H), 0.97 – 0.87 (m, 12H), 0.78 (br.s, 6H); ^{13}C NMR (150.9 MHz, DMSO- d_6): $\delta = 176.5, 71.2, 69.7, 69.5, 67.7, 63.7, 58.0, 47.9, 44.1, 24.3, 23.4, 23.2, 22.6, 17.4, 17.1, 13.2$; Calc. for $\text{C}_{46}\text{H}_{91}\text{PO}_{16}\text{S}$ (963.3): C, 57.36%; H, 9.52%.

Poly[(trimethylpropylammonium 3-(methacryloyloxy)propane-1-sulfonate)-*r*-(poly(ethyleneglycol) methyl ether methacrylate)] poly(ILM7PrMe₃N₁₂₈-*r*-PEGM₁₂₈) (PIL21A)

The same procedure was used as for **PIL21I** with the exception that aqueous solution of trimethylpropylammonium bromide (27.30 g, 150.58 mmol) in 300 mL was used as an initial dialysate.

Yield: 1.49 g (92 %); $T_g = -29^\circ\text{C}$ (DSC); $T_{onset} = 205^\circ\text{C}$ (TGA); ^1H NMR (600.2 MHz, DMSO- d_6): $\delta = 4.01$ (br.s, 4H), 3.82 – 3.35 (m, 34H), 3.32 – 3.26 (m, 2H), 3.24 (s, 3H), 3.08 (s, 9H), 2.45 (br.s, 2H), 1.87 (br.s, 2H), 1.76 – 1.66 (m, 2H), 1.63 (br.s, 4H), 0.91 (t, $J = 7.3$ Hz, 3H), 0.77 (br.s, 6H); ^{13}C NMR (150.9 MHz, DMSO- d_6): $\delta = 176.1, 71.3, 69.8, 69.6, 67.8, 66.5, 63.9, 58.0, 52.0, 47.9, 44.1, 24.4, 15.7, 10.4$; Calc. for $\text{C}_{36}\text{H}_{71}\text{NO}_{16}\text{S}$ (806.01): C, 53.65%; H, 8.88%; N, 3.98%.

Synthesis of [(ILM_{*n*}-*r*-PEGM_{*m*})-*b*-Arm_{*k*}] block copolymers

Poly[(ILM_{*n*}-*r*-PEGM_{*m*})-*b*-Arm_{*k*}] block copolymers were synthesized via RAFT polymerization of 2-phenylethyl methacrylate or (1-naphthyl)methyl methacrylate in the presence of the respective **poly(ILM_{*n*}-*r*-PEGM_{*m*})** macro-CTA. The typical polymerization procedure is given below by the example of **poly[(ILM2₄₅-*r*-PEGM₄₅)-*b*-PhEtM₉₉] (PIL22)** synthesis, while the detailed loadings for the preparation of **PIL23 – PIL29** are presented in Table IV.2.

The solution of poly(ILM2₄₅-*r*-PEGM₄₅) macro-CTA (2.69 g, 58.37 μmol), PhEtM (1.87 g, 9.83 mmol) and AIBN (1.90 mg, 11.67 μmol) in 14.50 mL of anhydrous DMF (13.70 g) with initial reagents ratio of $[\text{PhEtM}]_0:[\text{macro-CTA}]_0:[\text{AIBN}]_0=168:1:0.2$ was quantitatively transferred to the

Schlenk flask equipped with magnetic stirring bar, degassed by three freeze-evacuate-thaw cycles, flashed with argon and placed in the bath preheated to 60°C. Polymerization proceeded at 60°C for 48 h, whereupon the reaction was stopped by rapid cooling with liquid nitrogen. The obtained viscous polymer solution was diluted with dichloromethane and precipitated twice in a large excess of diethyl ether. The obtained block copolymer was dried at 25°C/0.1 mbar for 24 h and then at 60°C/0.1 mbar for 24 h in B-585 oven filled with P₂O₅ to give a slightly pink solid wax material. Yield: 3.15 g (69 %); $T_{g1} = -33^{\circ}\text{C}$ (TMA); $T_{g2} = 46^{\circ}\text{C}$ (TMA); $T_{onset} = 170^{\circ}\text{C}$ (TGA); ¹H NMR (600.2 MHz, DMSO-d₆): $\delta = 9.15$ (s, 1H), 7.81 (s, 1H), 7.75 (s, 1H), 7.18 (d, $J = 32.2$ Hz, 12H), 4.40 – 4.16 (m, 4H), 4.15 – 3.76 (m, 9H), 3.75 – 3.36 (m, 34H), 3.24 (s, 3H), 2.81 (br.s, 4H), 2.15 (br.s, 2H), 1.79 (br.s, 2H), 1.55 (s, 8H), 1.27 (br.s, 2H), 0.91 (br.s, 3H), 0.82 – 0.37 (m, 13H); ¹³C NMR (150.9 MHz, DMSO-d₆): $\delta = 177.2$, 176.9, 176.0, 138.2, 136.5, 129.1, 128.7, 126.8, 123.0, 122.8, 119.9 (q, $J_{CF} = 322.3$ Hz), 71.7, 70.2, 70.0, 68.2, 65.4, 64.3, 62.0, 58.4, 53.9, 49.2, 46.5, 44.6, 34.4, 31.7, 28.6, 19.2, 18.4, 17.0, 13.6; ¹⁹F NMR (564.7 MHz, DMSO-d₆): $\delta = -81.0$ (s); IR (ATR-mode): 3033 (w, ν_{CH} , Ar), 2875 (vs, ν_{CH} , Al), 1729 (vs, $\nu_{C=O}$), 1455 (m, $\nu_{C=C}$, Ar), 1353 (m, ν_{asSO_2}), 1246 (m), 1190 (s, ν_{CF}), 1138 (vs, $\nu_{O=C-O-}$), 1111 (vs, ν_{C-O-C-}), 953 (w), 851 (w), 748 (w, δ_{CH} , Ar), 701 (w, δ_{CH} , Ar) cm⁻¹; Calc. for C₆₉H₁₀₅N₃F₆O₂₂S₂ (1506.7): C, 55.00%; H, 7.02%; N, 2.79%; Found: C, 54.87%; H, 6.83%; N, 2.90%.

Poly[(ILM2_{17-r}-PEGM₇₄)-*b*-PhEtM₉₉] (PIL23)

Yield: 3.62 g (54 %); $T_{g1} = -52^{\circ}\text{C}$ (TMA); $T_{g2} = 44^{\circ}\text{C}$ (TMA); $T_{onset} = 165^{\circ}\text{C}$ (TGA); ¹H NMR (600.2 MHz, DMSO-d₆): $\delta = 9.15$ (s, 1H), 7.81 (s, 1H), 7.75 (s, 1H), 7.18 (d, $J = 32.2$ Hz, 32H), 4.40 – 4.16 (m, 4H), 4.15 – 3.76 (m, 23H), 3.75 – 3.36 (m, 146H), 3.24 (s, 14H), 2.81 (br.s, 12H), 2.15 (br.s, 2H), 1.79 (br.s, 2H), 1.55 (s, 22H), 1.27 (br.s, 2H), 0.91 (br.s, 3H), 0.82 – 0.37 (m, 34H); ¹³C NMR (150.9 MHz, DMSO-d₆): $\delta = 177.2$, 176.9, 176.0, 138.2, 136.5, 129.1, 128.7, 126.8, 123.0, 122.8, 119.9 (q, $J_{CF} = 322.3$ Hz), 71.7, 70.2, 70.0, 68.2, 65.4, 64.3, 62.0, 58.4, 53.9, 49.2, 46.5, 44.6, 34.4, 31.7, 28.6, 19.2, 18.4, 17.0, 13.6; ¹⁹F NMR (564.7 MHz, DMSO-d₆): $\delta = -81.0$ (s).

Poly[(ILM2_{45-r}-PEGM₄₅)-*b*-Napht₉₀] (PIL24)

Yield: 3.61 g (73 %); $T_{g1} = -37^{\circ}\text{C}$ (TMA); $T_{g2} = 105^{\circ}\text{C}$ (TMA); $T_{onset} = 190^{\circ}\text{C}$ (TGA); ¹H NMR (600.2 MHz, DMSO-d₆): $\delta = 9.16$ (s, 1H), 8.16 – 6.86 (m, 18H), 5.23 (br.s, 4H), 4.21 (d, $J = 35.4$ Hz, 4H), 4.15 – 3.76 (m, 4H), 3.75 – 3.36 (m, 33H), 3.24 (s, 3H), 2.15 (br.s, 2H), 1.80 (br.s, 2H), 1.68 (s, 8H), 1.28 (br.s, 2H), 0.92 (br.s, 3H), 0.82 – 0.37 (m, 12H); ¹³C NMR (150.9 MHz, DMSO-d₆): $\delta = 176.8$, 176.1, 136.5, 133.5, 131.5, 131.0, 129.3, 128.8, 127.8, 126.8, 126.3, 125.6, 123.7, 123.08, 122.86, 119.9 (q, $J_{CF} = 322.0$ Hz), 71.7, 70.2, 70.0, 68.2, 64.9, 64.3, 62.1, 58.4, 53.9, 49.2, 46.5, 44.7, 31.7, 28.6, 19.2, 18.2, 16.6, 13.6; ¹⁹F NMR (564.7 MHz, DMSO-d₆): $\delta = -81.0$ (s); Calc. for C₇₃₅H₉₉₂N₃₀F₆₀O₂₁₆S₂₀ (15485.0): C, 57.01%; H, 6.46%; N, 2.71%; Found: C, 56.59%; H, 6.65%; N, 2.86%.

Poly[(ILM2₁₇-*r*-PEGM₇₄)-*b*-Napht₉₉] (PIL25)

Yield: 4.92 g (75 %); $T_{g1} = -48^{\circ}\text{C}$ (TMA); $T_{g2} = 85^{\circ}\text{C}$ (TMA); $T_{onset} = 180^{\circ}\text{C}$ (TGA); ^1H NMR (600.2 MHz, DMSO- d_6): $\delta = 9.16$ (s, 1H), 8.16 – 6.86 (m, 48H), 5.23 (br.s, 12H), 4.21 (d, $J = 35.4$ Hz, 4H), 4.15 – 3.76 (m, 11H), 3.75 – 3.36 (m, 146H), 3.24 (s, 14H), 2.15 (br.s, 2H), 1.80 (br.s, 2H), 1.68 (s, 23H), 1.28 (br.s, 2H), 0.92 (br.s, 3H), 0.82 – 0.37 (m, 34H); ^{13}C NMR (150.9 MHz, DMSO- d_6): $\delta = 176.8, 176.1, 136.5, 133.5, 131.5, 131.0, 129.3, 128.8, 127.8, 126.8, 126.3, 125.6, 123.7, 123.08, 122.86, 119.9$ (q, $J_{CF} = 322.0$ Hz), 71.7, 70.2, 70.0, 68.2, 64.9, 64.3, 62.1, 58.4, 53.9, 49.2, 46.5, 44.7, 31.7, 28.6, 19.2, 18.2, 16.6, 13.6; ^{19}F NMR (564.7 MHz, DMSO- d_6): $\delta = -81.0$ (s).

Poly[(ILM1₄₁-*r*-PEGM₄₅)-*b*-PhEtM₉₄] (PIL26)

Yield: 5.10 g (75 %); $T_{g1} = -37^{\circ}\text{C}$ (TMA); $T_{g2} = 45^{\circ}\text{C}$ (TMA); $T_{onset} = 185^{\circ}\text{C}$ (TGA); ^1H NMR (600.2 MHz, DMSO- d_6): $\delta = 9.07$ (s, 1H), 7.75 (s, 1H), 7.68 (s, 1H), 7.29 – 7.06 (m, 12H), 4.16 (t, $J = 7.2$ Hz, 2H), 4.12 – 3.89 (m, 9H), 3.86 (s, 3H), 3.75 – 3.36 (m, 38H), 3.24 (s, 3H), 3.01 (br.s, 2H), 2.82 (br.s, 5H), 1.98 (br.s, 2H), 1.77 (p, $J = 7.2$ Hz, 2H), 1.63 (s, 9H), 1.27 (sext, $J = 7.4$ Hz, 2H), 0.90 (t, $J = 7.4$ Hz, 3H), 0.87 – 0.47 (m, 13H); ^{13}C NMR (150.9 MHz, DMSO- d_6): $\delta = 176.9, 138.2, 136.9, 129.1, 128.7, 126.8, 124.0, 122.7, 120.1$ (q, $J_{CF} = 324.3$ Hz), 71.7, 70.2, 70.0, 68.3, 65.4, 64.3, 58.4, 54.0, 51.5, 48.9, 44.6, 36.1, 34.4, 31.8, 23.5, 19.2, 17.0, 13.7; ^{19}F NMR (564.7 MHz, DMSO- d_6): $\delta = -79.8$ (s); Calc. for $\text{C}_{69}\text{H}_{87}\text{N}_3\text{F}_3\text{O}_{17}\text{S}_2$ (1506.7): C, 61.32%; H, 6.49%; N, 3.11%; Found: C, 56.42%; H, 6.89%; N, 2.81%.

Poly[(ILM1₁₂-*r*-PEGM₆₁)-*b*-PhEtM₇₄] (PIL27)

Yield: 8.77 g (76%); $T_{g1} = -46^{\circ}\text{C}$ (TMA); $T_{g2} = 67^{\circ}\text{C}$ (TMA); $T_{onset} = 160^{\circ}\text{C}$ (TGA); ^1H NMR (600.2 MHz, DMSO- d_6): $\delta = 9.07$ (s, 1H), 7.75 (s, 1H), 7.68 (s, 1H), 7.29 – 7.06 (m, 33H), 4.16 (t, $J = 7.2$ Hz, 2H), 4.12 – 3.89 (m, 25H), 3.86 (s, 3H), 3.75 – 3.36 (m, 172H), 3.24 (s, 16H), 3.01 (br.s, 2H), 2.82 (br.s, 12H), 1.98 (br.s, 2H), 1.77 (p, $J = 7.2$ Hz, 2H), 1.63 (s, 25H), 1.27 (sext, $J = 7.4$ Hz, 2H), 0.90 (t, $J = 7.4$ Hz, 3H), 0.87 – 0.47 (m, 37H); ^{13}C NMR (150.9 MHz, DMSO- d_6): $\delta = 176.9, 138.2, 136.9, 129.1, 128.7, 126.8, 124.0, 122.7, 120.1$ (q, $J_{CF} = 324.3$ Hz), 71.7, 70.2, 70.0, 68.3, 65.4, 64.3, 58.4, 54.0, 51.5, 48.9, 44.6, 36.1, 34.4, 31.8, 23.5, 19.2, 17.0, 13.7; ^{19}F NMR (564.7 MHz, DMSO- d_6): $\delta = -79.8$ (s).

Poly[(ILM1₄₁-*r*-PEGM₄₅)-*b*-Napht₇₇] (PIL28)

Yield: 4.85 g (77 %); $T_{g1} = -35^{\circ}\text{C}$ (TMA); $T_{g2} = 81^{\circ}\text{C}$ (TMA); $T_{onset} = 180^{\circ}\text{C}$ (TGA); ^1H NMR (600.2 MHz, DMSO- d_6): $\delta = 9.08$ (s, 1H), 7.92 – 7.02 (m, 17H), 5.29 (br.s, 4H), 4.17 (t, $J = 7.2$ Hz, 2H), 4.02 (br.s, 4H), 3.86 (s, 2H), 3.75 – 3.36 (s, 35H), 3.25 (s, 3H), 3.02 (s, 2H), 1.97 (s, 2H), 1.77 (p, $J = 7.3$ Hz, 2H), 1.65 (s, 8H), 1.27 (sext, $J = 7.4$ Hz, 2H), 0.91 (t, $J = 7.4$ Hz, 3H), 0.86 – 0.45 (m, 12H); ^{13}C NMR (150.9 MHz, DMSO- d_6): $\delta = 176.8, 136.9, 133.5, 131.5, 131.0, 129.3, 128.8, 127.8, 126.8,$

125.5, 124.0, 122.7, 120.1 (q, $J_{\text{CF}} = 324.3$ Hz), 71.7, 70.7, 70.0, 68.2, 64.9, 64.3, 63.7, 58.5, 53.8, 51.6, 44.6, 36.1, 31.8, 23.5, 19.2, 18.4, 16.6, 13.7; ^{19}F NMR (564.7 MHz, DMSO- d_6): $\delta = -79.9$ (s); Calc. for $\text{C}_{70}\text{H}_{101}\text{N}_3\text{F}_3\text{O}_{22}\text{S}_2$ (1457.7): C, 57.68%; H, 6.98%; N, 2.88%; Found: C, 57.82%; H, 7.14%; N, 2.99%.

Poly[(ILM1₁₄-*r*-PEGM₇₃)-*b*-Napht₈₆] (PIL29)

Yield: 3.00 g (65%); $T_{g1} = -42^\circ\text{C}$ (TMA); $T_{g2} = 46^\circ\text{C}$ (TMA); $T_{\text{onset}} = 180^\circ\text{C}$ (TGA); ^1H NMR (600.2 MHz, DMSO- d_6): $\delta = 9.08$ (s, 1H), 7.92 – 7.02 (m, 50H), 5.29 (br.s, 13H), 4.17 (t, $J = 7.2$ Hz, 2H), 4.02 (br.s, 13H), 3.86 (s, 2H), 3.75 – 3.36 (s, 178H), 3.25 (s, 16H), 3.02 (s, 2H), 1.97 (s, 2H), 1.77 (p, $J = 7.3$ Hz, 2H), 1.65 (s, 25H), 1.27 (sext, $J = 7.4$ Hz, 2H), 0.91 (t, $J = 7.4$ Hz, 3H), 0.86 – 0.45 (m, 37H); ^{13}C NMR (150.9 MHz, DMSO- d_6): $\delta = 176.8, 136.9, 133.5, 131.5, 131.0, 129.3, 128.8, 127.8, 126.8, 125.5, 124.0, 122.7, 120.1$ (q, $J_{\text{CF}} = 324.3$ Hz), 71.7, 70.7, 70.0, 68.2, 64.9, 64.3, 63.7, 58.5, 53.8, 51.6, 44.6, 36.1, 31.8, 23.5, 19.2, 18.4, 16.6, 13.7; ^{19}F NMR (564.7 MHz, DMSO- d_6): $\delta = -79.9$ (s); Calc. for $\text{C}_{229}\text{H}_{340}\text{N}_3\text{F}_6\text{O}_{76}\text{S}_2$ (4472.2): C, 61.50%; H, 7.66%; N, 0.94%; Found: C, 61.82%; H, 7.68%; N, 0.94%.

Table IV.1 Loadings for the synthesis of random **poly(ILM_n-*r*-PEGM_m)** copolymers.

	Reaction time	[PEGM]		[ILM]		[CTA]		[AIBN]		[DMF]		([PEGM] _o + [ILM] _o): [CTA] _o : [AIBN] _o
	(h)	(g)	(mmol)	(g)	(mmol)	(mg)	(μmol)	(mg)	(μmol)	(g)	(mL)	
poly(ILM1 ₇₄)	72	0	0	1.70	3.56	4.75	17.00	0.56	3.4	5.10	5.40	209:1:0.2
poly(ILM1 _{31-<i>r</i>} -PEGM ₃₄)	12	3.14	6.28	3.00	6.28	49.02	175.50	5.76	35.09	18.42	19.51	72:1:0.2
poly(ILM1 _{41-<i>r</i>} -PEGM ₄₅)	48	4.19	8.38	4.00	8.38	50.84	182.00	6.00	36.00	24.56	26.02	92:1:0.2
poly(ILM1 _{94-<i>r</i>} -PEGM ₁₀₃)	72	3.14	6.28	3.00	6.28	17.16	61.41	2.01	12.28	18.42	19.52	205:1:0.2
poly(ILM1 _{14-<i>r</i>} -PEGM ₄₉)	12	2.36	4.71	0.75	1.57	24.79	88.74	2.91	17.75	9.31	9.87	71:1:0.2
poly(ILM1 _{10-<i>r</i>} -PEGM ₅₄)	12	2.62	5.24	0.50	1.05	24.89	89.08	2.92	17.82	9.35	9.90	71:1:0.2
poly(ILM1 _{8-<i>r</i>} -PEGM ₅₆)	12	2.93	5.86	0.40	0.84	26.59	95.19	3.12	19.04	9.99	10.58	70:1:0.2
poly(ILM1 _{6-<i>r</i>} -PEGM ₅₈)	12	2.82	5.65	0.30	0.63	24.96	89.35	2.93	17.87	9.38	9.94	70:1:0.2
poly(ILM2 ₅₁)	72	0	0	4.00	7.53	31.01	140.35	3.40	20.00	30.30	32.53	54:1:0.2
poly(ILM2 _{45-<i>r</i>} -PEGM ₄₅)	72	3.01	6.00	4.00	7.53	31.03	140.21	4.60	28.00	21.03	22.28	97:1:0.2
poly(ILM2 _{18-<i>r</i>} -PEGM ₇₈)	72	11.00	22.00	3.00	5.64	61.99	280.13	9.20	56.00	42.02	44.51	99:1:0.2
poly(ILM7 _{128-<i>r</i>} -PEGM ₁₂₈)	72	24.39	48.80	12.00	48.78	101.60	363.90	11.90	73.00	109.17	115.65	268:1:0.2

Table IV.2 Loadings for the synthesis of **poly[(ILM_n-*r*-PEGM_m)-*b*-Ar_k]** block copolymers.

	[Ar]		[macro-CTA]		[AIBN]		[DMF]		[Ar] _o : [macro-CTA] _o : [AIBN] _o
	(g)	(mmol)	(g)	(μmol)	(mg)	(μmol)	(g)	(mL)	
poly[(ILM2 _{45-<i>r</i>} -PEGM ₄₅)- <i>b</i> -PhEtM ₉₉]	1.87	9.83	2.69	58.37	1.90	11.67	13.70	14.50	168:1:0.2
poly[(ILM2 _{17-<i>r</i>} -PEGM ₇₄)- <i>b</i> -PhEtM ₉₉]	2.69	14.18	4.00	84.21	2.80	16.84	20.10	21.30	168:1:0.2
poly[(ILM2 _{45-<i>r</i>} -PEGM ₄₅)- <i>b</i> -Napht ₉₀]	1.96	8.66	3.00	65.22	2.10	13.04	14.90	15.80	133:1:0.2
poly[(ILM2 _{17-<i>r</i>} -PEGM ₇₄)- <i>b</i> -Napht ₉₉]	2.53	11.18	4.00	84.21	2.80	16.84	19.60	20.70	133:1:0.2
poly[(ILM1 _{41-<i>r</i>} -PEGM ₄₅)- <i>b</i> -PhEtM ₉₄]	2.58	13.56	4.40	103.04	3.40	20.61	20.90	22.20	132:1:0.2
poly[(ILM1 _{12-<i>r</i>} -PEGM ₆₁)- <i>b</i> -PhEtM ₇₄]	4.14	21.78	7.30	188.14	6.17	37.62	34.32	36.35	116:1:0.2
poly[(ILM1 _{41-<i>r</i>} -PEGM ₄₅)- <i>b</i> -NaphtM ₇₇]	2.29	10.15	4.00	95.58	3.10	19.11	18.90	20.00	106:1:0.2
poly[(ILM1 _{14-<i>r</i>} -PEGM ₇₃)- <i>b</i> -Napht ₈₆]	1.65	7.31	3.00	68.81	2.26	13.76	13.95	14.78	106:1:0.2

Determination of monomer units numbers and $M_{n(NMR)}$ in poly(ILM-r-PEGM) and poly[(ILM_n-r-PEGM_m)-b-Ark] copolymers

Determination of monomers conversion (q) in the synthesis of poly(ILM-r-PEGM) copolymers

For the calculation of total monomer conversion (q) the ^1H NMR spectra of the reaction mixture were recorded before and after polymerization. The solvent (DMF) was used as an internal standard as it was not evaporated in course of reaction due to its high boiling point. In ^1H NMR spectra of the reaction mixture before polymerization each of the integrals of $\text{C}=\text{CH}_2$ signals (a_1 , a'_1 on Figure IV.1) from both monomers at 6.03-6.04 and 5.69-5.68 ppm were assigned as “1”. At the same time the signal of DMF ($\text{H}-\text{CO}-\text{N}(\text{CH}_3)_2$, b) at 7.58 ppm was integrated. Then, in the ^1H NMR spectra of the reaction mixture after polymerization the signal of DMF was integrated and set as the standard with the same value as before. The $\text{C}=\text{CH}_2$ (a_2 , a'_2 on Figure IV.1) signals of the residual monomers were integrated and the conversion (q) was calculated in accordance with the equation 1.5:

$$q = \frac{(a+a')_1 - (a+a')_2}{2} \quad (\text{eq 1.5})$$

Figure IV.1 provides an example for the anionic **PIL11**, and the conversion for the polymerization of **ILM2** and **ILM7** was calculated using the same approach.

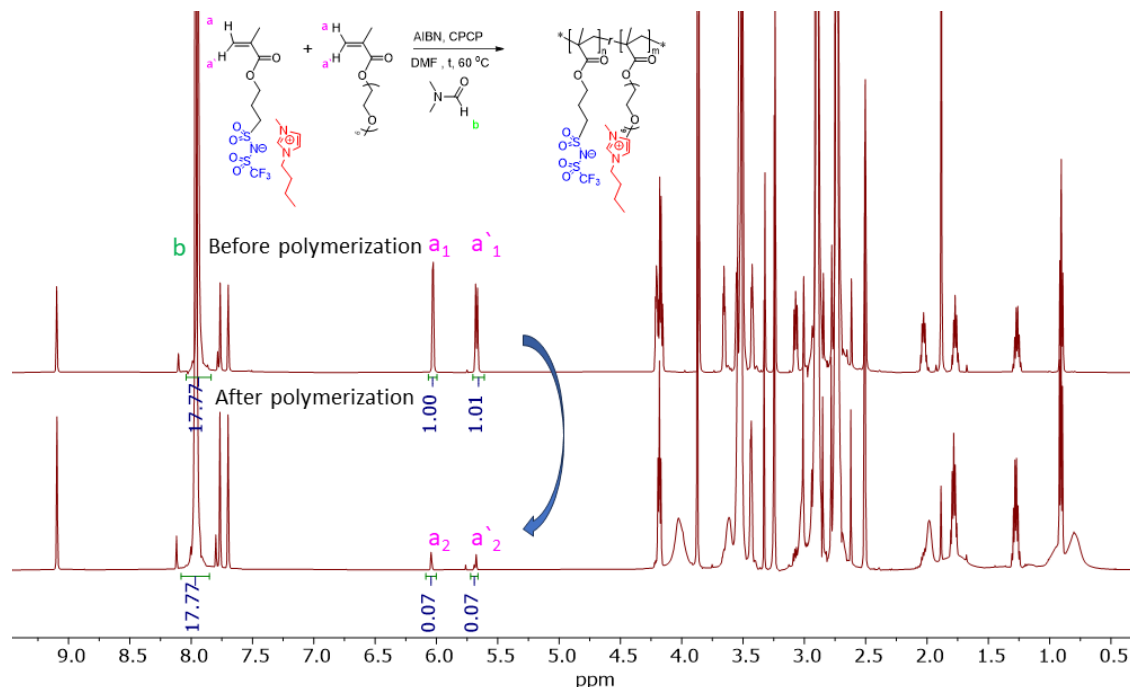


Figure IV.1 ^1H NMR spectra of reaction mixture before and after the RAFT copolymerization of ILM11 (25 °C, $\text{DMSO}-d_6$).

Determination of PEGM:ILM ratios in poly(ILM-r-PEGM) copolymers

The proportion of **ILM1** (X_{ILM1}) and **PEGM** (X_{PEGM}) units was determined by ^1H NMR in isolated copolymer sample using integrals of the signals at 3.24 ppm (-O-CH₃ from **PEGM**, see 7 on Figure IV.2, a) and at 3.00 ppm (-CH₂-SO₂-N-SO₂CF₃ from **ILM1**, see 6 on Figure IV.2, a) and the following equations:

$$X_{ILM1} = \frac{I_{ILM1}^n}{I_{ILM1}^n + I_{PEGM}^n} \quad (\text{eq 1.6})$$

$$X_{PEGM} = \frac{I_{PEGM}^n}{I_{ILM1}^n + I_{PEGM}^n} \quad (\text{eq 1.7})$$

$$I_{ILM1}^n = \frac{(6)}{n(H)} \quad (\text{eq 1.8})$$

$$I_{PEGM}^n = \frac{(7)}{n(H)} \quad (\text{eq 1.9})$$

$$PEGM:ILM1 = X_{PEGM}/X_{ILM1} \quad (\text{eq 1.10})$$

, where I_{ILM1}^n is the normalized integral for signal 6, I_{PEGM}^n is the normalized integral for signal 7, $n(H)$ is the number of hydrogens in the group.

The proportion of **ILM2** (X_{ILM2}) and **PEGM** (X_{PEGM}) units was determined by ^1H NMR in isolated copolymer sample using the integrals of the signals at 3.24 ppm (-O-CH₃ from **PEGM**, see 6 on Figure IV.2, b) and at 7.80, 7.74 ppm (-N-CH=CH-N- from **ILM2**, see 17,18 on Figure IV.2, b) and the following equations:

$$X_{ILM2} = \frac{I_{ILM2}^n}{I_{ILM2}^n + I_{PEGM}^n} \quad (\text{eq 1.11})$$

$$X_{PEGM} = \frac{I_{PEGM}^n}{I_{ILM2}^n + I_{PEGM}^n} \quad (\text{eq 1.12})$$

$$I_{ILM2}^n = \frac{(17,18)}{n(H)} \quad (\text{eq 1.13})$$

$$I_{PEGM}^n = \frac{(6)}{n(H)} \quad (\text{eq 1.14})$$

$$PEGM:ILM2 = X_{PEGM}/X_{ILM2} \quad (\text{eq 1.15})$$

, where I_{ILM2}^n is the normalized integral for signals 17, 18, I_{PEGM}^n is the normalized integral for signal 6, $n(H)$ is the number of hydrogens in the group.

The proportion of **ILM7** (X_{ILM7}) and **PEGM** (X_{PEGM}) units was determined by ^1H NMR in isolated copolymer sample using the integrals of the signal at 3.25 ppm (-O-CH₃ from **PEGM**, see 8 on

Figure IV.2, c) and the broad signal at 4.05 ppm (-O-CH₂-CH₂-CH₂-S- from **ILM7**, see **3** and -C(=O)-O-CH₂-CH₂-O- from **PEGM** see **4** on Figure IV.2, c) and the following equations:

$$X_{ILM7} = \frac{I_{ILM7}^n}{I_{ILM7}^n + I_{PEGM}^n} \quad (\text{eq 1.16})$$

$$X_{PEGM} = \frac{I_{PEGM}^n}{I_{ILM7}^n + I_{PEGM}^n} \quad (\text{eq 1.17})$$

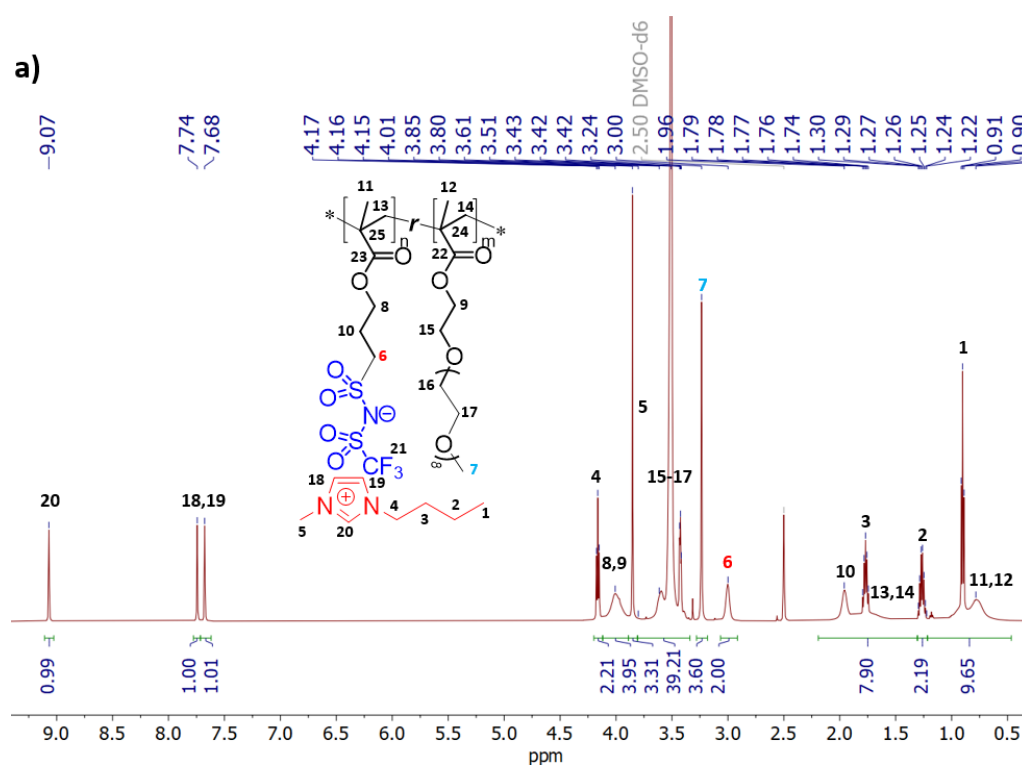
$$I_{PEGM}^n = \frac{(8)}{n(H)} \quad (\text{eq 1.18})$$

$$4 = n(H) * I_{PEGM}^n \quad (\text{eq 1.19})$$

$$I_{ILM7}^n = \frac{(3,4)-4}{n(H)} \quad (\text{eq 1.20})$$

$$PEGM:ILM7 = X_{PEGM}/X_{ILM7} \quad (\text{eq 1.21})$$

, where I_{ILM7}^n is the normalized integral for signals **3**, I_{PEGM}^n is the normalized integral for signal **8**, $n(H)$ is the number of hydrogens in the group.



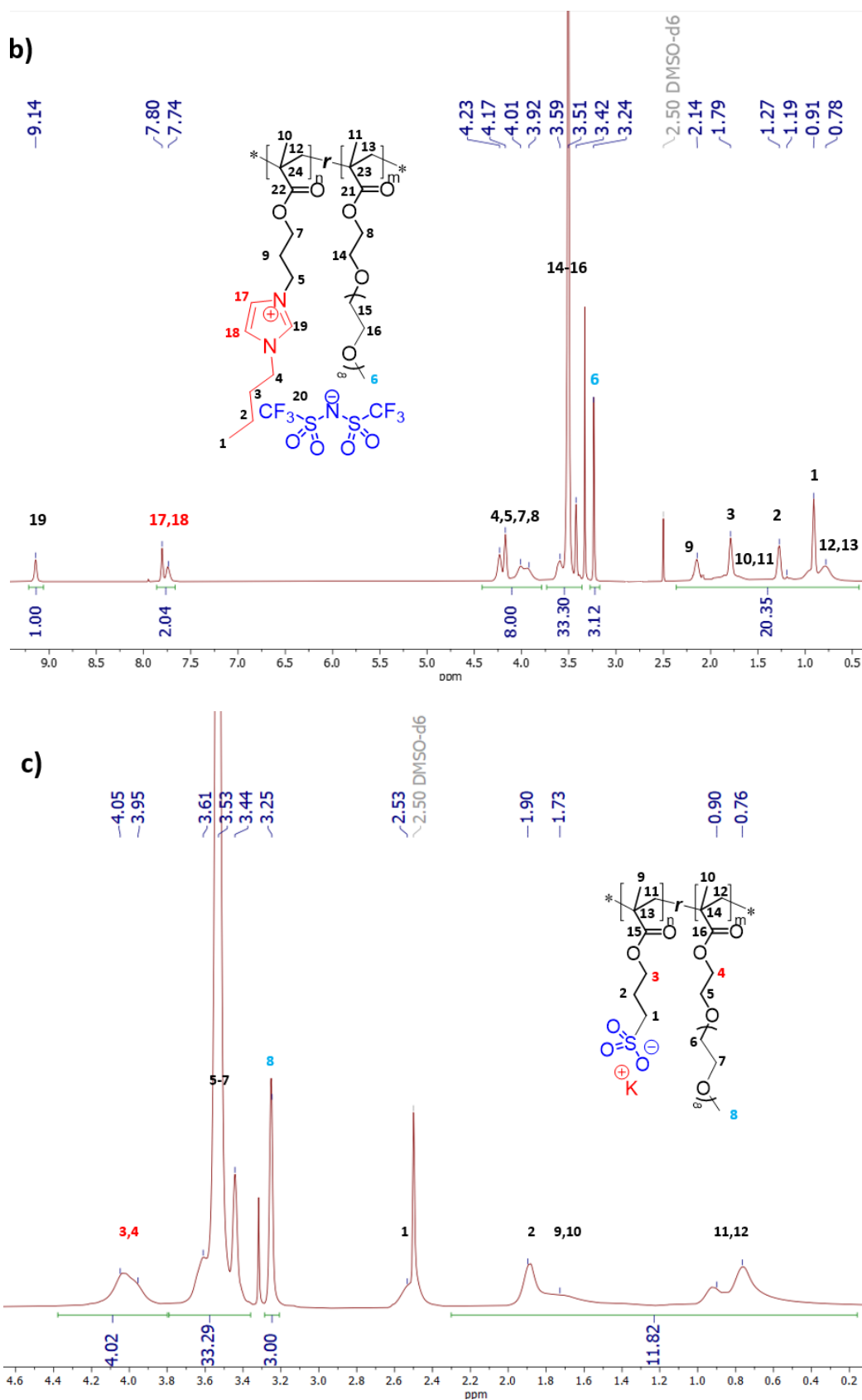


Figure IV.2 ^1H NMR of PIL13 (a), PIL19 (b), PIL21 (c) (25 °C, DMSO- d_6).

Determination of monomer units numbers and $M_{n(NMR)}$ in poly(ILM-r-PEGM) copolymers

The number of monomer units (**n** and **m**) and the $M_{n(NMR)}$ for poly(ILM_n-r-PEGM_m) copolymers were defined by the equations 1.22-1.24:

$$\mathbf{n} = X_{ILM} \times q \times \frac{[ILM]_0 + [PEGM]_0}{[CTA]_0} \quad (\text{eq 1.22})$$

$$\mathbf{m} = X_{PEGM} \times q \times \frac{[ILM]_0 + [PEGM]_0}{[CTA]_0} \quad (\text{eq 1.23})$$

$$M_{n(NMR)} = \mathbf{n} \times M_{ILM} + \mathbf{m} \times M_{PEGM} + M_{CTA} \quad (\text{eq 1.24})$$

where X_{ILM} and X_{PEGM} – the proportions of ILM and PEGM units in the copolymer determined by equations 1.6 – 1.21, q – the total conversion of the monomers, $[ILM]_0$, $[PEGM]_0$ and $[CTA]_0$ are the initial concentrations of ILM, PEGM monomers and chain transfer agent; M_{ILM} , M_{PEGM} and M_{CTA} – the molecular weights of monomers and CTA.

Determination of monomers conversion (q) in the synthesis of poly[(ILM_n-r-PEGM_m)-b-Ar_k] block copolymers

For the calculation of total monomers conversion (q) the ^1H NMR spectra of the reaction mixture were recorded before and after polymerization. The solvent (DMF) was used as an internal standard. In ^1H NMR spectra of the reaction mixture before polymerization each of the integrals of $\text{C}=\text{CH}_2$ signals (**b**₁ and **b'**₁ on Figure IV.3) from PhEtM monomer at 5.64 and 5.14 ppm were assigned as “1”. At the same time the signal of DMF ($\text{H}-\text{CO}-\text{N}(\text{CH}_3)_2$, **c**) at 7.58 ppm was integrated. Then, in the ^1H NMR spectra of the reaction mixture after polymerization the signal of DMF (**c** on Figure IV.3) was integrated and set as the standard with the same value as before. The $\text{C}=\text{CH}_2$ signals of the residual monomer (**b**₂ and **b'**₂ on Figure IV.3) were integrated and the conversion (q) was calculated in accordance with the equation 1.25:

$$q = \frac{(b+b')_1 - (b+b')_2}{2} \quad (\text{eq 1.25})$$

Figure IV.3 provides an example for the cationic **PIL22** having PhEtM block, and the conversion for the copolymerization of cationic random copolymers with Napht and anionic random copolymers with PhEtM and Napht was calculated using the same approach.

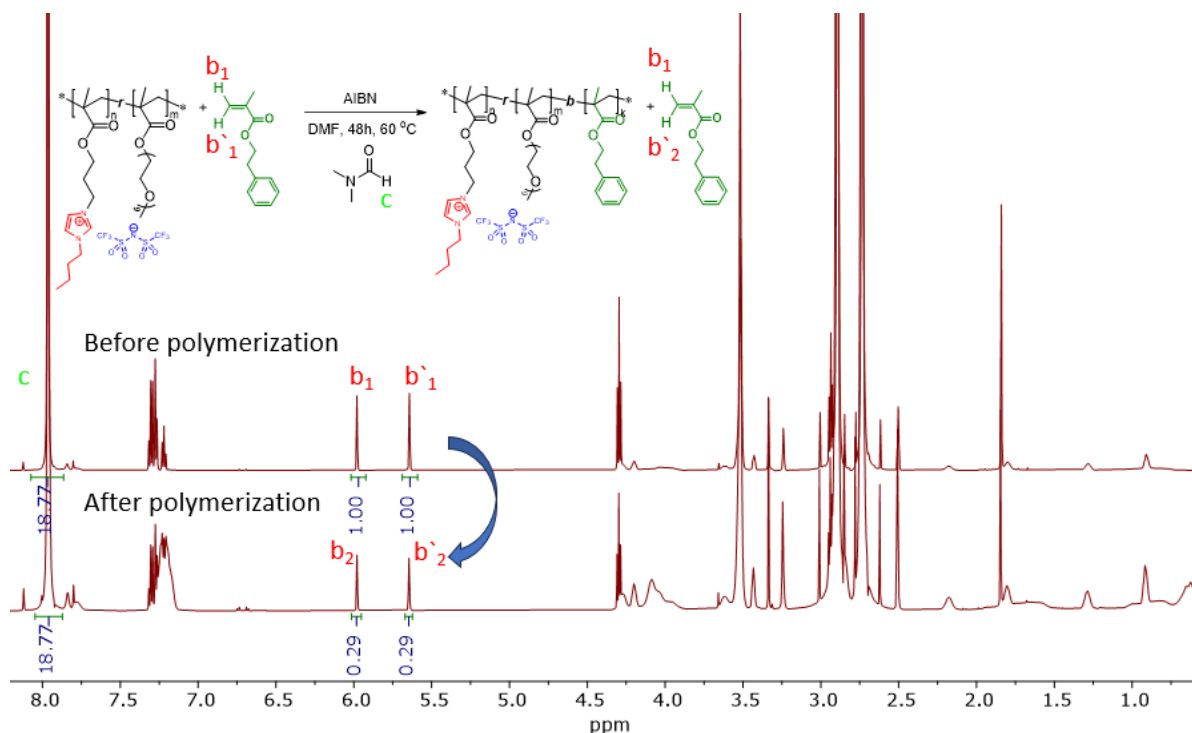


Figure IV.3 ^1H NMR of reaction mixture before and after the RAFT copolymerization of **PIL22** (25 °C, DMSO-d_6).

Determination of Ar (PhEtM or Napht) units number and $M_{n(\text{NMR})}$ in poly[(ILM $_n$ -r-PEGM $_m$)-b-Ar $_k$] block copolymers.

The number of monomer units k in poly[(**ILM2** $_n$ -r-PEGM $_m$)-b-PhEtM $_k$] was calculated using the following equation 1.26:

$$k = n \times \frac{14/2}{30/1} \quad (\text{eq 1.26})$$

where k and n are the number of the PhEtM and **ILM2** units, respectively; 14 is the integral of -O-CH $_2$ -CH $_2$ -Ph signal from PhEtM monomer at 2.81 ppm (14 on Figure IV.4, a); 30 is the integral of -NCHN- signal from **ILM2** units at 9.15 ppm (30 on Figure IV.4, a).

To check the correctness of the k determination, the following equation (eq. 1.27) can be used as well:

$$k = q \times \frac{[\text{PhEtM}]_0}{[\text{macro-CTA}]_0} \quad (\text{eq 1.27})$$

where q is the PhEtM monomer conversion (defined by eq. 1.25), $[\text{PhEtM}]_0$ and $[\text{macro-CTA}]_0$ are the initial concentrations of PhEtM and poly(**ILM2** $_n$ -r-PEGM $_m$) macro-CTA, respectively.

For anionic block copolymers copolymers **PIL26** and **PIL27** the number of monomer units k in poly[(**ILM1** _{n} - r -PEGM _{m})- b -PhEtM _{k}] was calculated in a similar manner using equation 1.26, where k and n are the number of the PhEtM and **ILM1** units, respectively; **14** is the integral of -O-CH₂-CH₂-Ph signal from PhEtM monomer at 2.82 ppm; **30** is the integral of -NCHN- signal from **ILM1** units at 9.07 ppm.

The $M_{n(NMR)}$ of poly[(ILM _{n} - r -PEGM _{m})- b -PhEtM _{k}] block copolymers was defined by the simplified equation 1.28:

$$M_{n(NMR)} = k \times M_{PhEtM} + M_{macro-CTA} \quad (\text{eq 1.28})$$

where k is the number of PhEtM units; M_{PhEtM} and $M_{macro-CTA}$ are the molecular weights of PhEtM monomer and poly(ILM- r -PEGM) macro-CTA, respectively.

The number of monomer units k in poly[(**ILM2** _{n} - r -PEGM _{m})- b -Napht _{k}] was calculated using the following equation 1.29:

$$k = n \times \frac{\mathbf{13}/_2}{\mathbf{29}/_1} \quad (\text{eq 1.29})$$

where k and n are the number of the Napht and **ILM2** units, respectively; **13** is the integral of -O-CH₂-Napht signal from Napht monomer at 5.23 ppm (**13** on Figure IV.4, b); **29** is the integral of -NCHN- signal from **ILM2** units at 9.16 ppm (**29** on Figure IV.4, b).

To check the correctness of the k determination, the following equation (eq. 1.30) can be used as well:

$$k = q \times \frac{[Napht]_0}{[macro-CTA]_0} \quad (\text{eq 1.30})$$

where q is the Napht monomer conversion (defined by eq. 1.25), $[Napht]_0$ and $[macro-CTA]_0$ are the initial concentrations of Napht and poly(**ILM2**- r -PEGM) macro-CTA, respectively.

For anionic block copolymers **PIL28** and **PIL29** the number of monomer units k in poly[(**ILM1** _{n} - r -PEGM _{m})- b -Napht _{k}] was calculated in a similar manner using equation 1.29, where k and n are the number of the Napht and **ILM1** units, respectively, **13** is the integral of -O-CH₂-Napht signal from Napht monomer at 5.23 ppm, **29** is the integral of -NCHN- signal from **ILM1** units at 9.16 ppm.

The $M_{n(NMR)}$ of poly[(ILM _{n} - r -PEGM _{m})- b -Napht _{k}] block copolymers was defined by the simplified equation 1.31:

$$M_{n(NMR)} = k \times M_{Napht} + M_{macro-CTA} \quad (\text{eq 1.31})$$

where k is the number of Napht units; M_{Napht} and $M_{\text{macro-CTA}}$ are the molecular weights of Napht monomer and poly(ILM-*r*-PEGM) macro-CTA, respectively.

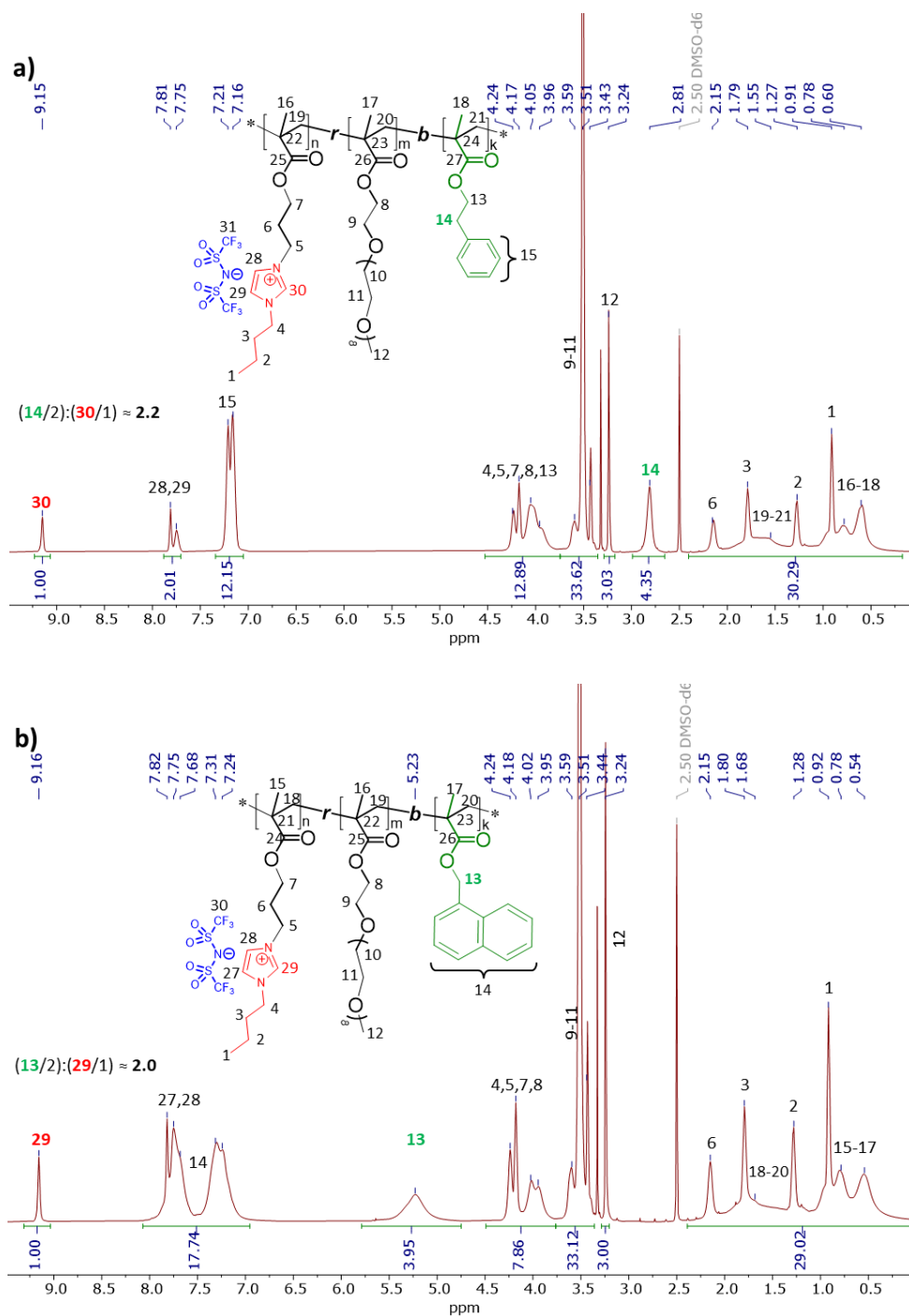


Figure IV.4 ^1H NMR of PIL22 (a), PIL24 (b) (25 °C, DMSO- d_6).

2.2.3 Epichlorohydrin-derived PILs (PIL30-PIL37)

Synthesis of mono N-substituted imidazoles

N-(2-methyl-3-(trimethylsilyl)propyl) imidazole

The sodium hydride (8.01 g, 60wt% dispersion in mineral oil) was loaded to the Schlenk flask equipped with magnetic stirrer and fritted glass filter (Schlaker reaction tube). The flask was accurately evacuated and then filled with an inert atmosphere. The NaH was washed with freshly distilled n-hexane (3×50 mL) and dried at RT/0.1 mbar for 1 h to produce neat sodium hydride (4.81 g, 200.0 mmol). Further on 120 ml of anhydrous DMF were injected into the flask via syringe under vigorous stirring. After the formation of NaH dispersion, the argon flow was increased, the septum was removed and the imidazole (13.63 g, 200.0 mmol) was added in several portions under the inert flow (CAUTION: the addition of imidazole is accompanied by exothermic reaction and by a vigorous evolution of hydrogen gas!). After stirring at RT for 30 minutes the formation of light brown solution was observed, the septum was placed back to close the Schlenk flask and the argon flow was decreased. The (3-chloro-2-methylpropyl)-trimethylsilane (6.60 g, 40.0 mol) was added to the reaction solution dropwise via syringe. The reaction was continued for 10 h at RT and then for 30 h at 50°C. The resultant inorganic precipitate was filtered off and the filtrate was diluted with 450 mL of benzene. The solution was slowly poured into the ultra-pure water (1250 mL) under stirring and the organic layer was separated. The aqueous layer was washed with benzene (5×50 ml), the organic layers were combined and dried over anhydrous MgSO_4 . Magnesium sulfate was filtered off and benzene was evaporated under reduced pressure. The resultant yellowish liquid was dried at 50 °C/0.1 mbar for 3 hours. Yield: 7.36 g (94%); ^1H NMR (400.0 MHz, CDCl_3): δ = 7.34 (s, 1H), 6.95 (s, 1H), 6.79 (s, 1H), 3.72-3.56 (m, 2H), 1.97-1.89 (m, 1H), 0.83 (d, J = 6.6 Hz, 3H), 0.52-0.28 (m, 2H), -0.05 (s, 9H); ^{13}C NMR (100.6 MHz, CDCl_3): δ = 137.2, 129.0, 118.9, 55.9, 31.6, 21.6, 19.8, -0.8; IR (KBr pellet): 3110 (m, ν_{CH}), 2955 (vs, ν_{CH}), 2897 (s, ν_{CH}), 1507 (s), 1460 (m), 1284 (m), 1248 (vs, $\nu_{\text{Si-CH}_3}$), 1110 (m), 1077 (m), 1032 (m), 910 (w), 840 (vs, $\nu_{\text{Si-CH}_3}$), 741 (m), 692 (m), 665 (w) cm^{-1} ; Calc. for $\text{C}_{10}\text{H}_{20}\text{N}_2\text{Si}$ (196.37): C, 61.17%; H, 10.27%; Si, 14.30%; Found: C, 60.52%; H, 10.50%; Si, 13.82%.

N-((1,1,3,3,3-pentamethyldisiloxaneyl)methyl) imidazole

Imidazole (15.97 g, 235.0 mmol), 1-(chloromethyl)-1,1,3,3,3-pentamethyldisiloxane (9.35 g, 47.0 mmol), KI (0.15 g, 0.9 mmol) and K_2CO_3 (6.49 g, 47.0 mmol) were loaded into the high-pressure vessel. The 150 mL of anhydrous acetonitrile were added into the vessel via syringe, the vessel was flushed with argon, closed and the stirring was continued at RT until the formation of fine dispersion. Then the temperature was increased to 80°C and the reaction was carried out additionally for 2 days. Afterwards the reaction mass was cooled down to RT and the inorganic precipitate was filtered off. Acetonitrile was evaporated under reduced pressure to give yellowish solid residue, which was further dissolved in 100 mL of H_2O . The aqueous solution was extracted with n-hexane (5×50 ml) and the organic layer was dried over anhydrous MgSO_4 . Magnesium sulfate was filtered off and hexane was evaporated under reduced pressure. The product representing a colorless liquid was dried at 50 °C/0.1 mbar for 5 h. Yield: 4.23 g (39%); ^1H NMR (400.0 MHz, CDCl_3): δ = 7.35 (s, 1H), 7.01 (s, 1H), 6.81

(s, 1H), 3.45 (s, 2H), 0.12 (s, 6H), 0.06 (s, 9H); ^{13}C NMR (100.6 MHz, CDCl_3): δ = 137.5, 128.9, 119.9, 39.2, 1.7, -0.9; IR (ATR-mode): 3110 (w, ν_{CH}), 2955 (m, ν_{CH}), 2900 (m, ν_{CH}), 1507(s), 1250 (s, $\nu_{\text{Si-CH}_3}$), 1080 (s), 840 (s, $\nu_{\text{Si-CH}_3}$), 740 (m), 660 (w), 530 (w), cm^{-1} . Calc. for $\text{C}_9\text{H}_{20}\text{N}_2\text{OSi}_2$ (228.11): C, 47.32%; H, 8.82%; N, 12.26%; Si, 24.59%; Found: C, 47.28%; H, 8.98%; N, 12.31%; Si, 24.44%.

N-(3,3,4,4,5,5,6,6,6-nonafluorohexyl) imidazole

The solution of 3,3,4,4,5,5,6,6,6-nonafluorohexan-1-ol (10.00 g, 37.9 mmol) in 15 ml of pyridine was added dropwise to the solution of 4-toluenesulfonyl chloride (7.58 g, 39.7 mmol) in 30 ml of pyridine at 0°C under inert atmosphere. The reaction mixture was stirred for 3 hours at 0 °C, then gradually heated to room temperature, filtered off from the precipitated pyridine chloride, and poured into an ice-cold 2M HCl aqueous solution. The precipitated waxy residue was washed with ultra-pure water, then with saturated NaHCO_3 aqueous solution and finally several times with ultra-pure water. Afterwards the precipitate was dissolved in 100 mL of dichloromethane and washed thoroughly with water (4 x 25mL). The organic layer was separated, dried over anhydrous MgSO_4 , filtered and the dichloromethane was evaporated under reduced pressure. The resultant product representing white waxy solid was dried at 25°C/0.1 mbar for 2 h. Yield: 11.36 g (72%); ^1H NMR (400.0 MHz, DMSO-d_6): δ = 7.81 (d, J = 8.2 Hz, 2H), 7.49 (d, J = 8.2 Hz, 2H), 4.29 (t, J = 6.7 Hz, 2H), 2.73-2.64 (m, 2H), 2.41 (s, 3H); ^{13}C NMR (100.6 MHz, DMSO-d_6): δ = 145.2, 131.7, 130.1, 127.6, 62.4, 29.5, 20.9; ^{19}F NMR (376.5 MHz, DMSO-d_6): δ = -22.6 (s), -54.8 (s), -66.0 (s), -67.6 (s).

The solution of 3,3,4,4,5,5,6,6,6-nonafluorohexyl-4-methylbenzenesulfonate (10.30 g, 24.6 mmol) in 50 ml of anhydrous DMF was added to the solution of imidazole (4.20 g, 61.7 mmol) in 10 ml of anhydrous DMF at 50°C under inert atmosphere. The reaction was further heated to 85 °C and carried out at this temperature for 72 h. DMF was evaporated at 80°C/15 mbar and the residue was extracted with 100 ml of anhydrous diethyl ether. Et_2O solution was filtered from imidazolium tosylate and the solvent was evaporated at 25°C/15 mbar, providing slightly yellow transparent oil. To remove the imidazole residue, the oil was extracted with anhydrous *n*-hexane (4 × 25 mL) and then dried at 25°C/15 mbar. Finally, the oil was dissolved in 80 mL of dichloromethane, washed with water (3 × 10 mL) and the organic layer was dried over anhydrous MgSO_4 . Magnesium sulfate was filtered off and dichloromethane was evaporated under reduced pressure. The product, representing colorless oil, was dried at 50 °C/0.1 mbar for 5 h. Yield: 4.21 g (54%); ^1H NMR (400.0 MHz, CDCl_3): δ = 7.51 (s, 1H), 7.09 (s, 1H), 6.93 (s, 1H), 4.42-4.41 (m, 2H), 2.95-2.64 (m, 2H); ^{13}C NMR (100.6 MHz, CDCl_3): δ = 137.1, 130.4, 129.7, 118.6, 69.1, 53.4, 38.8, 32.9, 31.2; ^{19}F NMR (376.5 MHz, CDCl_3): δ = -81.0 (s), -114.5 (s), -124.4 (s), -126.0 (s); IR (KBr pellet): 3112 (m, ν_{CH}), 2932 (m, ν_{CH}), 2859 (m, ν_{CH}), 1678 (m), 1510 (s), 1439 (s), 1389 (s ν_{CF}), 1354 (s, ν_{CF}), 1231 (vs, ν_{CF}), 1134 (s), 1100 (m, ν_{CF}), 1010 (m), 878 (m), 828 (m), 750 (m), 623 (m) cm^{-1} ; Calc. for $\text{C}_9\text{H}_7\text{F}_9\text{N}_2$ (314.15): C, 34.41%; H, 2.25%; F, 54.43%; Found: C, 36.37%; H, 3.09%; F, 46.47%.

Synthesis of poly(epiiodohydrin-co-ethylene oxide)

Poly(epichlorohydrin-co-ethylene oxide) (3.58 g, 26.2 mmol) was dissolved in 70 mL of anhydrous acetone under inert atmosphere at 40°C. The freshly dried NaI (9.8 g, 65.5 mmol) was added in one portion to the flask under inert flow. The mixture was stirred for 3 days at 50°C, the resultant slurry was cooled down to RT and centrifuged. The yellow sticky precipitate was collected, dissolved in DMF (50 ml) and precipitated into the excess of H₂O. The precipitation from DMF solution into water was repeated and the yellowish rubber-like polymer was collected, washed with water and dried at 60°C /0.1 mbar for 1 day. Yield: 5.3 g (90 %); ¹H NMR (400.0 MHz, DMSO-d₆): δ = 3.77-3.58 (m, 3H), 3.53 (br. s., 4H), 3.46-3.26 (m, 2H); ¹³C NMR (100.6 MHz, DMSO-d₆): δ = 77.7, 76.7, 70.0, 68.5, 44.3.

Synthesis of halide PILs

Quaternization of mono N-substituted imidazoles with poly(epichlorohydrin-co-ethylene oxide)

The majority of the chloride PILs was synthesized via quaternization reaction of respective mono N-substituted imidazoles by poly(epichlorohydrin-co-ethylene oxide) following the general procedure provided for the preparation of poly(1-methyl-3-[oxiran-2-ylmethyl]-1-imidazole-3-ium-co-ethylene oxide) chloride below.

Poly(epichlorohydrin-co-ethylene oxide) (3.58 g, 26.2 mmol) was dissolved in 40 ml of anhydrous DMF under inert atmosphere on stirring at 70 °C in a high-pressure vessel (CAUTION: the dissolution can take up to 12 h). N-methylimidazole (21.48 g, 262.0 mmol) was added in one portion to the polymer solution under inert flow. The temperature was then raised to 90 °C and the stirring was continued for 3 days. The viscous solution was cooled down and ~1/2 of the solvent was removed under reduced pressure at 65 °C. Afterwards polymer was precipitated into the excess of acetone. The resultant poly(1-methyl-3-[oxiran-2-ylmethyl]-1-imidazole-3-ium-co-ethylene oxide) chloride was obtained as sticky light brown solid. It was thoroughly washed with acetone and dried at 70 °C/0.1 mbar for 1 day. Yield: 5.33 g (93%); ¹H NMR (400.0 MHz, D₂O): δ = 8.77 (s, 1H), 7.53-7.51 (m, 2H), 4.48-4.33 (m, 2H), 3.92 (s, 3H), 3.70-3.61 (m, 7H); ¹³C NMR (100.6 MHz, D₂O): δ = 136.7, 123.5, 123.2, 76.5, 70.4, 69.6, 50.0, 35.9, 30.3; IR (KBr pellet): 3151 (m), 3102 (m, ν_{CH}), 2913 (w), 2877 (s, ν_{CH}), 1647 (w), 1570 (m, ν_{CN}), 1456 (w), 1347 (w), 1172 (s, ν_{CN}), 1102 (s), 952 (w), 843 (w), 751 (w), 624 (m) cm⁻¹.

Quaternization of N-((1,1,3,3,3-pentamethyldisiloxaneyl)methyl) imidazole with poly(epiiodohydrin-co-ethylene oxide)

Poly(epiiodohydrin-co-ethylene oxide) (2.93 g, 13.0 mmol) was dissolved in 50 ml of anhydrous DMF under inert atmosphere at 70°C in a high-pressure vessel. After the formation of clear

solution, the 1-((1,1,3,3,3-pentamethyldisiloxaneyl)methyl) imidazole (3.86 g, 16.9 mmol) was added in one portion to the reaction vessel. The temperature was raised to 80 °C (CAUTION: the increase in reaction temperature above 80 °C leads to crosslinking reactions) and the stirring was continued for 3 days. The viscous solution was cooled down to RT and precipitated into the excess of anhydrous Et₂O. The resultant poly(1-methyl-3-[oxiran-2-ylmethyl]-1-imidazole-3-ium-co-ethylene oxide) iodide in a form of white sticky solid was dried at RT/0.1 mbar for 2 h. Yield: 3.97 g (67%); ¹H NMR (400.0 MHz, DMSO-d₆): δ = 8.74 (br. s., 1H), 7.73-7.79 (s, 2H), 4.54-4.12 (m, 3H), 4.12-3.47 (m, 22H), 0.16 (s, 6H), 0.05 (s, 9H).

Quaternization degree (q) determination

The quaternization degree **q** was determined by ¹H NMR using integral in the region of 4.10-3.40 ppm and the following equations:

$$Q = \frac{I_{PIL33Cl}^n}{I_{PIL33Cl}^n + I_{Hydrin}^n} \times 100\% \quad (\text{eq 1.32})$$

$$I_{PIL33Cl}^n = \frac{I_{PIL33Cl}^{theor}}{n_{PIL33Cl}} = \frac{7}{7} = 1 \quad (\text{eq 1.33})$$

$$I_{Hydrin}^n = \frac{I_{Hydrin}}{n_{Hydrin}} = \frac{I_{PIL33Cl}^{exp} - I_{PIL33Cl}^{theor}}{n_{Hydrin}} = \frac{7.46 - 7.0}{9} = 0.051 \quad (\text{eq 1.34})$$

$$Q = \frac{1}{1 + 0.051} \times 100\% = 95\% \quad (\text{eq 1.35})$$

, where $I_{PIL33Cl}^n$ is the normalized integral for quaternized polymer **PIL33Cl** in the region of 4.10-3.40 ppm, I_{Hydrin}^n is the normalized integral for unmodified Hydrin polymer in the region of 4.10-3.40 ppm, $I_{PIL33Cl}^{theor}$ is the theoretical integral for fully quaternized polymer **PIL33Cl** in the region of 4.10-3.40 ppm, $n_{PIL33Cl}$ is the theoretical number of protons corresponding to fully quaternized polymer **PIL33Cl** in region of 4.10-3.40 ppm (Figure IV.5, b, signals 1-4), I_{Hydrin} is the integral for unmodified Hydrin in the region of 4.10-3.40 ppm, n_{Hydrin} is the theoretical number of protons corresponding to unmodified Hydrin in region of 4.10-3.40 ppm (Figure IV.5, a, signals 1'-5'), $I_{PIL33Cl}^{exp}$ is the experimentally determined integral for fully quaternized polymer **PIL33Cl** in the region of 4.10-3.40 ppm.

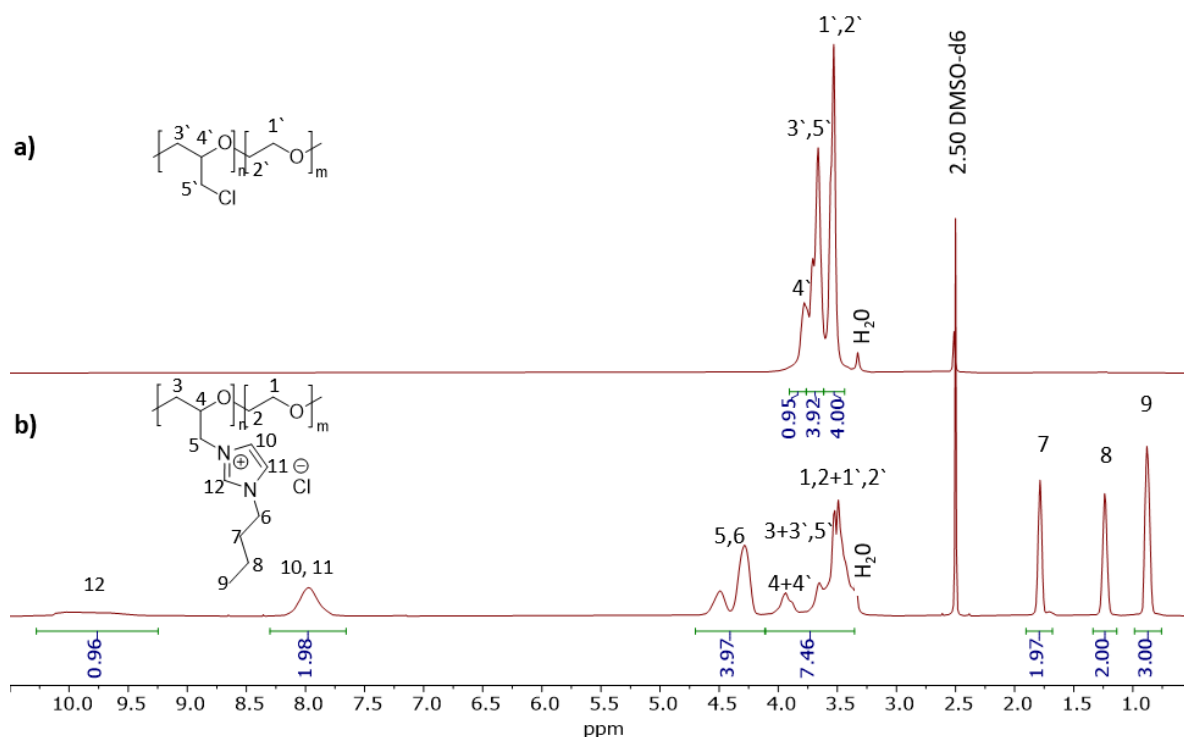


Figure IV.5 Comparison of ^1H NMR of poly(epichlorohydrin-co-ethylene oxide) (a) and poly(1-butyl-3-[oxiran-2-ylmethyl]-1-imidazole-3-ium-co-ethylene oxide) chloride (b).

Ion metathesis

Polyelectrolytes **PIL30TFSI-PIL36TFSI**, **PIL33BF₄**, **PIL33TFSAM**, **PIL33BF(CN)₃** and **PIL33BF₃CF₃** were synthesized via ion metathesis between corresponding chloride PILs and metal salts following general procedure given for poly(1-methyl-3-[oxiran-2-ylmethyl]-1-imidazole-3-ium-co-ethylene oxide) bis(trifluoromethylsulfonyl) imide (**PIL30TFSI**) below.

The solution of lithium bis(trifluoromethylsulfonyl)imide (13.43 g, 45.0 mmol) in 30 ml of ultra-pure water was added dropwise to the aqueous solution (100 ml) of poly(1-methyl-3-[oxiran-2-ylmethyl]-1-imidazole-3-ium-co-ethylene oxide) chloride (5.12 g, 23.4 mmol) at room temperature. The formation of a precipitate was observed immediately and the stirring was continued for 2 h at RT. The precipitated sticky product was collected, thoroughly washed with water, redissolved in acetone and reprecipitated in H₂O again. Polymer representing slightly yellow sticky solid was dried at 70 °C /0.1 mbar for 2 days in B-585 oven (Buchi Glass Drying Oven, Switzerland) filled with P₂O₅. Afterwards it was transferred under vacuum into the argon filled glove box (MBRAUN MB-Labstar, H₂O and O₂ content < 0.5 ppm) and was stored for 5 days prior to further investigation. Yield: 9.25 g (85 %); $T_g = -10^\circ\text{C}$ (DSC); $T_{onset} = 290^\circ\text{C}$ (TGA); ^1H NMR (400.0 MHz, acetone-d₆): $\delta = 8.92$ (s, 1H), 7.67 (s, 2H), 4.60-4.46 (m, 2H), 4.04 (s, 3H), 3.78-3.64 (m, 6H), 2.91 (s, 1H); ^{13}C NMR (100.6 MHz, acetone-d₆): $\delta = 138.0, 125.6-116.0$ (q, $J_{\text{CF}} = 321$ Hz), 124.3, 77.3, 71.4, 70.9, 69.9, 51.1, 36.6; ^{19}F NMR (376.5 MHz, acetone-d₆): $\delta = -80.9$ (s); IR (ATR-mode): 3159 (m, ν_{CH}), 3121 (m, ν_{CH}), 2881 (m, ν_{CH}),

1572 (m), 1456 (m), 1354 (vs, ν_{asSO_2}), 1195 (vs, ν_{CF}), 1138 (s, ν_{SO_2}), 1058 (vs, ν_{CF}), 741 (m), 618 (s), 571 (s), 512 (m) cm^{-1} ; Calc. for $\text{C}_{11}\text{H}_{15}\text{F}_6\text{N}_3\text{O}_6\text{S}_2$ (463.03): C, 28.51%; H, 3.26%; F, 24.60%; Found: C, 28.18%; H, 3.34%; F, 24.20%.

Poly(1-ethyl-3-[oxiran-2-ylmethyl]-1-imidazole-3-ium-co-ethylene oxide) bis(trifluoromethylsulfonyl) imide (PIL31TFSI)

Yield: 7.14 g (92 %); $T_g = -16^\circ\text{C}$ (DSC); $T_{\text{onset}} = 290^\circ\text{C}$ (TGA); ^1H NMR (400.0 MHz, DMSO-d_6): $\delta = 9.05\text{--}9.03$ (m, 1H), 7.80 (s, 1H), 7.65 (s, 1H), 4.38–4.22 (m, 4H), 3.83–3.65 (m, 2H), 3.52–3.33 (m, 5H), 1.43 (s, 3H); ^{13}C NMR (100.6 MHz, DMSO-d_6): $\delta = 136.3, 123.3, 122.7\text{--}116.3$ (q, $J_{\text{CF}} = 320$ Hz), 121.3, 76.0, 70.0, 69.6, 59.8, 44.3, 15.1; ^{19}F NMR (376.5 MHz, DMSO-d_6): $\delta = -80.8$ (s).

Poly(1-propyl-3-[oxiran-2-ylmethyl]-1-imidazole-3-ium-co-ethylene oxide) bis(trifluoromethylsulfonyl) imide (PIL32TFSI)

Yield: 5.65 g (90 %); $T_g = -20^\circ\text{C}$ (DSC); $T_{\text{onset}} = 290^\circ\text{C}$ (TGA); ^1H NMR (400.0 MHz, DMSO-d_6): $\delta = 9.09$ (s, 1H), 7.85 (s, 1H), 7.69 (s, 1H), 4.45–4.19 (m, 4H), 3.88–3.39 (m, 7H), 1.87 (s, 2H), 1.43 (s, 3H); ^{13}C NMR (100.6 MHz, DMSO-d_6): $\delta = 137.0, 123.8\text{--}116.7$ (q, $J_{\text{CF}} = 320$ Hz), 122.3, 76.4, 70.5, 69.7, 50.8, 50.3, 23.3, 10.7; ^{19}F NMR (376.5 MHz, DMSO-d_6): $\delta = -80.9$ (s).

Poly(1-butyl-3-[oxiran-2-ylmethyl]-1-imidazole-3-ium-co-ethylene oxide) bis(trifluoromethylsulfonyl) imide (PIL33TFSI)

Yield: 5.65 g (80 %); $T_g = -25^\circ\text{C}$ (DSC); $T_{\text{onset}} = 310^\circ\text{C}$ (TGA); ^1H NMR (400.0 MHz, DMSO-d_6): $\delta = 9.06$ (s, 1H), 7.80 (s, 1H), 7.68 (s, 1H), 4.40–4.18 (m, 4H), 4.18–3.81 (m, 2H), 3.81–3.43 (m, 5H), 1.79 (s, 2H), 1.25 (s, 2H), 0.90 (s, 3H); ^{13}C NMR (100.6 MHz, DMSO-d_6): $\delta = 136.7, 123.4, 122.7\text{--}116.3$ (q, $J_{\text{CF}} = 320$ Hz), 78.0, 70.1, 69.7, 48.8, 48.6, 44.1, 31.4, 18.7, 13.2; ^{19}F NMR (376.5 MHz, DMSO-d_6): $\delta = -80.9$ (s); Calc. for $\text{C}_{14}\text{H}_{21}\text{F}_6\text{N}_3\text{O}_6\text{S}_2$ (505.07): C, 33.27%; H, 4.19%; Found: C, 33.06%; H, 4.11%.

Poly(1-hexyl-3-[oxiran-2-ylmethyl]-1-imidazole-3-ium-co-ethylene oxide) bis(trifluoromethylsulfonyl) imide (PIL34TFSI)

Yield: 8.01 g (85 %); $T_g = -21^\circ\text{C}$ (DSC); $T_{\text{onset}} = 320^\circ\text{C}$ (TGA); ^1H NMR (400.0 MHz, DMSO-d_6): $\delta = 9.07$ (s, 1H), 7.80 (s, 1H), 7.66 (s, 1H), 4.40–4.18 (m, 4H), 3.85–3.65 (m, 2H), 3.52–3.31 (m, 5H), 1.80 (s, 2H), 1.27 (s, 6H), 0.86 (s, 3H); ^{13}C NMR (100.6 MHz, DMSO-d_6): $\delta = 137.0, 123.1\text{--}116.7$ (q, $J_{\text{CF}} = 320$ Hz), 122.6, 76.4, 70.5, 69.7, 50.3, 49.4, 30.9, 29.9, 25.6, 22.3, 14.1; ^{19}F NMR (376.5 MHz, DMSO-d_6): $\delta = -80.9$ (s).

Poly(1-(2-methyl-3-(trimethylsilyl)propyl)-3-[oxiran-2-ylmethyl]-1-imidazole-3-ium-co-ethylene oxide) bis(trifluoromethylsulfonyl) imide (PIL35TFSI)

Yield: 6.79 g (89 %); $T_g = -6^\circ\text{C}$ (DSC); $T_{onset} = 285^\circ\text{C}$ (TGA); ^1H NMR (400.0 MHz, acetone- d_6): $\delta = 8.95$ (br. s., 1H), 7.75 (br. s., 2H), 4.62-3.43 (m, 11H), 2.25 (s, 1H), 0.96 (s, 3H), 0.71-0.44 (m, 2H), 0.02 (s, 9H); ^{13}C NMR (100.6 MHz, acetone- d_6): $\delta = 139.4$, 126.2, 124.5-118.1 (q, $J_{\text{CF}} = 320$ Hz), 120.2, 70.2, 60.4, 55.6, 32.2, 32.0, 22.9, 20.4, 0.2; ^{19}F NMR (376.5 MHz, acetone- d_6): $\delta = -80.8$ (s); IR (KBr pellet): 3155 (m, ν_{CH}), 3119 (m, ν_{CH}), 2968 (m, ν_{CH}), 2893 (m, ν_{CH}), 1568 (s), 1468 (m), 1352 (vs, ν_{asSO_2}), 1190 (vs, ν_{CF}), 1138 (s, ν_{sSO_2}), 1055 (vs, ν_{CF}), 845 (m, $\nu_{\text{Si-CH}_3}$), 791 (m), 743 (w), 648 (s), 615 (m) cm^{-1} .

Poly(1-(3,3,4,4,5,5,6,6,6-nonafluorohexyl)-3-[oxiran-2-ylmethyl]-1-imidazole-3-ium-co-ethylene oxide) bis(trifluoromethylsulfonyl) imide (PIL36TFSI)

Yield: 4.32 g (87 %); $T_g = 6^\circ\text{C}$ (DSC); $T_{onset} = 280^\circ\text{C}$ (TGA); ^1H NMR (400.0 MHz, DMSO- d_6): $\delta = 9.16$ (s, 1H), 7.92 (s, 1H), 7.67 (br. s., 1H), 4.60 (s, 2H), 4.41-4.21 (m, 2H), 3.84-3.48 (m, 7H), 3.00 (s, 2H); ^{13}C NMR (100.6 MHz, DMSO- d_6): $\delta = 137.3$, 124.2-114.6 (q, $J_{\text{CF}} = 320$ Hz), 123.6, 122.3, 115.4, 76.1, 75.7, 69.6, 68.5, 49.8, 41.3, 29.9; ^{19}F NMR (376.5 MHz, DMSO- d_6): $\delta = -79.1$ (s), -81.0 (s), -113.9 (s), -124.4 (s), -126.1 (s); IR (KBr pellet): 3153 (m, ν_{CH}), 3120 (m, ν_{CH}), 3096 (m, ν_{CH}), 2920 (m), 2882 (m, ν_{CH}), 1568 (m), 1457 (w), 1352 (vs, ν_{asSO_2}), 1233 (vs, ν_{CF}), 1197 (vs, ν_{CF}), 1134 (vs, ν_{sSO_2}), 1058 (vs, ν_{CF}), 881 (m), 791 (m), 740 (w), 710 (w), 617 (m), 601 (m), cm^{-1} ; Calc. for $\text{C}_{16}\text{H}_{16}\text{F}_{15}\text{N}_3\text{O}_6\text{S}_2$ (695.39): C, 27.63%; H, 2.32%; S, 9.22%; Found: C, 27.07%; H, 2.27%; S, 9.02%.

Poly(1-butyl-3-[oxiran-2-ylmethyl]-1-imidazole-3-ium-co-ethylene oxide) tetrafluoroborate (PIL33BF₄)

The same procedure was used as for **PIL30TFSI** with the exception that aqueous solution of NaBF_4 (1.05 g, 9.6 mmol) in 10 mL was added dropwise to a solution of poly(1-butyl-3-[oxiran-2-ylmethyl]-1-imidazole-3-ium-co-ethylene oxide) chloride (1.25 g, 4.8 mmol) in 10 mL of ultra-pure water. Yield: 0.9 g (60 %); $T_g = 11^\circ\text{C}$ (DSC); $T_{onset} = 270^\circ\text{C}$ (TGA); ^1H NMR (400.0 MHz, DMSO- d_6): $\delta = 9.03$ (br. s., 1H), 7.80 (s, 1H), 7.65 (br. s., 1H), 4.37-4.19 (m, 4H), 4.00-3.37 (m, 7H), 1.77 (s, 2H), 1.24 (s, 2H), 0.89 (s, 3H); ^{13}C NMR (100.6 MHz, DMSO- d_6): $\delta = 136.6$, 123.4, 122.2, 75.9, 70.1, 69.7, 49.6, 48.7, 44.1, 31.4, 18.7, 13.2; ^{19}F NMR (376.5 MHz, DMSO- d_6): $\delta = -150.5$ (s); ^{11}B NMR (192.5 MHz, DMSO- d_6): $\delta = -1.3$ (s); IR (ATR-mode): 3153 (w, ν_{CH}), 3116 (w, ν_{CH}), 2963 (w, ν_{CH}), 2934 (w, ν_{CH}), 2875 (w, ν_{CH}), 1564 (m), 1465 (m), 1344 (w), 1167 (m, ν_{CO}), 1046 (vs), 1033 (vs, ν_{BF}), 848 (m), 749 (w), 642 (m) cm^{-1} ; Calc. for $\text{C}_{14}\text{H}_{21}\text{F}_3\text{N}_4\text{O}_4\text{S}$ (312.12): C, 46.18%; H, 6.78%; Found: C, 45.69%; H, 6.93%.

Poly(1-butyl-3-[oxiran-2-ylmethyl]-1-imidazole-3-ium-co-ethylene oxide) 2,2,2-trifluoromethylsulfonyl-N-cyanoamide (PIL33TFSAM)

The same procedure was used as for **PIL30TFSI** with the exception that the aqueous solution of KTFSAM (1.1 g, 5.2 mmol) in 10 mL was added dropwise to a solution of poly(1-butyl-3-[oxiran-

2-ylmethyl]-1-imidazole-3-ium-co-ethylene oxide) chloride (0.68 g, 2.6 mmol) in 10 mL of water. Yield: 0.9 g (86 %); $T_g = -27^\circ\text{C}$ (DSC); $T_{onset} = 260^\circ\text{C}$ (TGA); ^1H NMR (400.0 MHz, DMSO- d_6): $\delta = 9.06$ (br. s., 1H), 7.80 (s, 1H), 7.65 (br. s., 1H), 4.38-4.19 (m, 4H), 4.00-3.37 (m, 7H), 1.78 (s, 2H), 1.26 (s, 2H), 0.90 (s, 3H); ^{13}C NMR (100.6 MHz, DMSO- d_6): $\delta = 136.6, 123.4, 122.2, 123.5 - 117.1$ (q, $J_{CF} = 325$ Hz), 114.3, 75.8, 70.1, 69.7, 68.5, 49.6, 48.7, 44.1, 31.4, 18.7, 13.2; ^{19}F NMR (376.5 MHz, DMSO- d_6): $\delta = -79.9$ (s); IR (ATR-mode): 3147 (w, ν_{CH}), 3110 (w, ν_{CH}), 2963 (w, ν_{CH}), 2935 (w, ν_{CH}), 2876 (w, ν_{CH}), 2359 (w), 2342 (w), 2187 (s, ν_{CN}), 1563 (m), 1464 (m), 1328 (s, ν_{asSO_2}), 1212 (vs, ν_{CF}), 1165 (s, ν_{sSO_2}), 1114 (vs, ν_{CF}), 829 (s), 751 (w), 635 (s) cm^{-1} ; Calc. for $\text{C}_{14}\text{H}_{21}\text{F}_3\text{N}_4\text{O}_4\text{S}$ (398.40): C, 42.21%; H, 5.31%; F, 14.31%; Found: C, 41.47%; H, 5.33%; F, 13.9%.

Poly(1-butyl-3-[oxiran-2-ylmethyl]-1-imidazole-3-ium-co-ethylene oxide) tricyanofluoroborate (PIL33BF(CN)₃)

The same procedure was used as for **PIL30TFSI** with the exception that aqueous solution of KBF(CN)_3 (1.30 g, 8.8 mmol) in 10 mL was added dropwise to a solution of poly(1-butyl-3-[oxiran-2-ylmethyl]-1-imidazole-3-ium-co-ethylene oxide) chloride (1.15 g, 4.4 mmol) in 10 mL of water. Yield: 1.3 g (92 %); $T_g = -31^\circ\text{C}$ (DSC); $T_{onset} = 250^\circ\text{C}$ (TGA); ^1H NMR (400.0 MHz, DMSO- d_6): $\delta = 9.06$ (br. s., 1H), 7.80 (s, 1H), 7.65 (br. s., 1H), 4.38-4.19 (m, 4H), 4.00-3.37 (m, 7H), 1.78 (s, 2H), 1.26 (s, 2H), 0.90 (s, 3H); ^{13}C NMR (100.6 MHz, DMSO- d_6): $\delta = 136.7, 126.5$ (m), 123.4, 122.2, 75.9, 70.1, 69.7, 49.6, 48.7, 44.1, 31.4, 18.7, 13.2; ^{19}F NMR (376.5 MHz, DMSO- d_6): $\delta = -213.3 - -213.0$ (m); ^{11}B NMR (192.5 MHz, DMSO- d_6): $\delta = -17.9$ (d, $J = 44.7$ Hz); IR (ATR-mode): 3149 (m, ν_{CH}), 3113 (w, ν_{CH}), 2962 (w, ν_{CH}), 2934 (w, ν_{CH}), 2877 (w, ν_{CH}), 2214 (w, ν_{CN}), 1562 (m), 1463 (m), 1344 (w), 1164 (m, ν_{CO}), 1097 (vs), 1051 (vs, ν_F), 939 (m), 902 (vs), 748 (w), 630 (s) cm^{-1} ; Calc. for $\text{C}_{15}\text{H}_{21}\text{BFN}_5\text{O}_2$ (333.17): C, 54.08%; H, 6.35%; B, 3.24%; Found: C, 52.30%; H, 6.19%; B, 3.03%.

Poly(1-butyl-3-[oxiran-2-ylmethyl]-1-imidazole-3-ium-co-ethylene oxide) trifluoro(trifluoromethyl)borate (PIL33BF₃CF₃)

The same procedure was used as for **PIL30TFSI** with the exception that aqueous solution of KBF_3CF_3 (1.56 g, 8.8 mmol) in 10 mL was added dropwise to a solution of poly(1-butyl-3-[oxiran-2-ylmethyl]-1-imidazole-3-ium-co-ethylene oxide) chloride (1.15 g, 4.4 mmol) in 10 mL of water. Yield: 1.4 g (89 %); $T_g = -9^\circ\text{C}$ (DSC); $T_{onset} = 185^\circ\text{C}$ (TGA); ^1H NMR (400.0 MHz, DMSO- d_6): $\delta = 9.05$ (br. s., 1H), 7.80 (s, 1H), 7.65 (br. s., 1H), 4.38-4.19 (m, 4H), 4.00-3.37 (m, 7H), 1.77 (s, 2H), 1.25 (s, 2H), 0.89 (s, 3H); ^{13}C NMR (100.6 MHz, DMSO- d_6): $\delta = 136.5, 123.3, 122.1, 76.1, 70.1, 68.5, 49.8, 48.6, 44.1, 31.4, 18.7, 13.2$; ^{19}F NMR (376.5 MHz, DMSO- d_6): $\delta = -76.5$ (dd, $J = 64.5, 31.7$ Hz, CF_3), -156.4 (dd, $J = 79.3, 39.2$ Hz, F); ^{11}B NMR (192.5 MHz, DMSO- d_6): $\delta = -1.5$ (m); IR (ATR-mode): 3156 (m, ν_{CH}), 3116 (w, ν_{CH}), 2963 (w, ν_{CH}), 2936 (w, ν_{CH}), 2877 (w, ν_{CH}), 1564 (m), 1465 (m), 1344 (w), 1252

(w), 1166 (m, ν_{CO}), 1045 (vs, ν_{BF}), 975 (s), 949 (vs, ν_{CF}) 843 (m), 747 (w), 633 (s) cm^{-1} ; Calc. for $\text{C}_{13}\text{H}_{21}\text{BF}_6\text{N}_2\text{O}_2$ (362.12): C, 43.12%; H, 5.85%; B, 2.99%; Found: C, 42.65%; H, 5.90%; B, 2.73%.

Poly(1-((1,1,3,3,3-pentamethyldisiloxaneyl)methyl)-3-[oxiran-2-ylmethyl]-1-imidazole-3-ium-co-ethylene oxide) bis(trifluoromethylsulfonyl) imide (PIL37TFSI)

The solution of LiTFSI (5.01 g, 17.4 mmol) in 10 mL of anhydrous acetone was added dropwise to the solution of poly(1-methyl-3-[oxiran-2-ylmethyl]-1-imidazole-3-ium-co-ethylene oxide) iodide (3.97 g, 8.7 mmol) in 20 mL of anhydrous acetone. The solution was further stirred for 1 h at RT, whereupon the product was precipitated into the excess of anhydrous Et_2O . The yellowish sticky polymer was collected, washed with Et_2O and dried at 60°C /0.1 mbar for 1 d. Yield: 3.95 g (50 %); $T_g = -2^\circ\text{C}$ (DSC); $T_{\text{onset}} = 185^\circ\text{C}$ (TGA); ^1H NMR (400.0 MHz, DMSO-d_6): $\delta = 8.96$ (br. s., 1H), 7.73 (s, 1H), 7.59 (br. s., 1H), 4.61-4.01 (m, 3H), 4.00-3.40 (m, 22H), 0.16 (s, 6H), 0.05 (s, 9H); ^{13}C NMR (100.6 MHz, DMSO-d_6): $\delta = 135.8, 123.3, 122.9, 122.6-116.2$ (q, $J_{\text{CF}} = 320$ Hz), 77.6, 75.9, 69.7, 68.7, 41.2, 29.6, 1.7, -1.1; ^{19}F NMR (376.5 MHz, DMSO-d_6): $\delta = -79.4$ (s); IR (KBr pellet): 3153 (m, ν_{CH}), 3120 (m, ν_{CH}), 3096 (m, ν_{CH}), 2920 (m), 2882 (m, ν_{CH}), 1568, 1457, 1352 (vs, ν_{asSO_2}), 1197 (vs, ν_{CF}), 1134 (vs, ν_{sSO_2}), 1058 (vs, ν_{CF}), 861 (m, $\nu_{\text{Si-CH}_3}$), 791 (m), 740 (w), 710 (w), 617 (m), 601 (m), cm^{-1} ; Calc. for $\text{C}_{16}\text{H}_{29}\text{F}_6\text{N}_3\text{O}_7\text{S}_2\text{Si}_2$ (609.66): C, 31.52%; H, 4.79%; Found: C, 31.43%; H, 5.12%.

2.3 Dynamic ion gels (DIG)s

General procedure for the preparation of DIGs

Dynamic ion gels **DIG1-DIG14** were synthesized via complex coacervation between corresponding anionic and anionic PILs following general procedure given for **DIG1** below.

A solution of poly(1-butyl-3-[oxiran-2-ylmethyl]-1-imidazole-3-ium-co-ethylene oxide) bis(trifluoromethylsulfonyl) imide (**PIL33TFSI**) (0.125 g, 0.241 mmol of ion pairs, 33 wt%) in 1.0 mL of acetone was added drop-wise into a solution of poly[(1-butyl-3-methylimidazolium 1-[3-(methacryloyloxy)propylsulfonyl]-1-(trifluoromethanesulfonyl)imide)-*r*-(poly(ethyleneglycol) methyl ether methacrylate)] (**PIL13**) (260 mg, 0.241 mmol of ion pairs, 67 wt%) in 1.0 mL of acetone under constant stirring. The formation of a turbid suspension was observed immediately. The resulting suspension, having a total polymer concentration of ~ 20 wt%, was vortex mixed for 1 min to improve mixing quality. Acetone was evaporated under reduced pressure and the resulting DIG was annealed at 70°C /0.1 mbar for 12 hours.

3. Supercapacitors assembly and testing

Supercapacitors were fabricated using a suspension of rGO-CNTs-DIG (or rGO-CNTs-PIL) at a concentration of 5 mg/mL, as depicted in Figure 4.2. The process began by creating a stable dispersion of rGO-CNTs (15 wt%) through ultrasonic treatment in a DMF solvent for 2 hours. Subsequently, 30

wt% of DIG or PIL (relative to the weight of rGO) was added to the suspension under continuous stirring. This dispersion was then deposited onto stainless steel substrates (304L type, 0.1 mm thick, 1.5 x 3 cm², Thermo Scientific Chemicals) using a drop-casting technique, ensuring the entire substrate area was covered (2.5 mg/cm² per electrode). The substrates were heated consistently at 85°C to evaporate the solvent. The electrodes were then dried in a vacuum oven at 85°C and 1 mbar for 12 hours. Following this, a DIG (or PIL) solution in acetonitrile (50 mg/mL) was spray-casted onto the electrodes, forming a solid polymeric film layer after solvent evaporation. A polyamide spacer was then placed on one of the electrodes, and additional layers of the electrolyte solution were deposited onto the spacer. This allowed the pores in the spacer to be filled, creating solid polymeric film layer on top of the spacer after evaporation. The electrodes were further dried in air at 85°C for 3 hours. Finally, the electrodes, were assembled in a sandwich configuration to form the supercapacitor. Electrochemical measurements were performed under various conditions, starting at ambient temperature and later at an elevated temperature of 80°C.

Supercapacitors were studied via cyclic voltammetry, with all characterizations conducted using two-electrode cell configurations in varying voltage ranges with different scan rates. Before recording the data, the device was pre-cycled 20 times at 10 mV s⁻¹ to ensure that the system reached a steady state. The specific capacitance of the devices was determined using the following equation:

$$C_{cell} = \left(\frac{\int \frac{i}{m} dv}{\Delta V * v} \right) / 2 \quad (\text{eq 1.36})$$

$$C_{SP} = C_{cell} * 4 \quad (\text{eq 1.37})$$

where i is the discharge current, m is the total mass of active materials, v is the scan rate, ΔV is the potential window.

The energy density and power density were calculated following the equation (1.38) and (1.39) respectively:

$$E = \frac{C_{SP}}{2} * V^2 \quad (\text{eq 1.38})$$

$$P = \frac{E}{t_{dis}} \quad (\text{eq 1.39})$$

Where V is the voltage, t_{dis} is the discharge time.



V. Conclusions

1. The novel class of polymer materials, termed **dynamic ion gels (DIGs)**, was developed through the solution mixing and complex coacervation of oppositely charged poly(ionic liquid)s (PILs) and for the first time was evaluated as electrolyte materials in all-solid-state safe supercapacitors.

2. A series of six ionic liquid monomers (ILMs) comprising two methacrylic and four dipropargyl ILMs was prepared, with four of them being synthesized and characterized for the first time. The developed synthetic procedures enabled the synthesis of these monomers with high purity ($\geq 98\%$) and in good yields ($>85\%$). The resulting ILMs exhibited ionic conductivities in the order of $\sim 10^{-4}$ S cm $^{-1}$ (at 25°C), closely approaching the conductivity levels of commonly used ionic liquids ($3 \times 10^{-3} \div 8 \times 10^{-3}$ S cm $^{-1}$ at 25°C). Specifically, the anionic **ILM1** demonstrated an ionic conductivity of 2.4×10^{-4} S cm $^{-1}$ (25°C), while the cationic **ILM2** exhibited an even higher conductivity of 4.1×10^{-4} S cm $^{-1}$ (25°C).

3. The new ionic dipropargyl ILMs (**ILM3-ILM6**) were used for the synthesis of first family of PILs via sequential AA + BB polyaddition Cu(I)-catalyzed azide–alkyne cycloaddition and subsequent N-alkylation reaction of poly(1,2,3-triazole) intermediates. This yielded nine PILs that contain one to four ion pairs per repeat unit and one or two types of ammonium, imidazolium or 1,2,3-triazolium counter-cations. Their physical, ion conducting and electrochemical properties were investigated. Within the studied PILs the T_g and ionic conductivity were all found to be significantly affected by the repeat unit charge density. Generally, the higher was the repeat unit charge density of PIL the higher were the observed T_g values (ranging from -35 to 15°C) and the lower were their ionic conductivity (varying in the range from 4.9×10^{-10} to 1.8×10^{-5} S cm $^{-1}$ at 25°C). These dependences passed through a maximum when PILs had two cations per monomer unit that were separated by alkyl or oxyethylene chains. For almost all combinations, 1,2,3-triazolium-containing PILs showed the highest ionic conductivity. Notably, among those polyelectrolytes **PIL9** exhibited the highest ionic conductivity of 1.8×10^{-5} S cm $^{-1}$ at 25°C, placing it among the top 20 PILs with the highest conductivity published to date (Table I.1). The rheological study of **PIL9** viscoelastic properties showed the storage modulus of 0.1 kPa (at 25°C and 1 rad $^{-1}$), which was below average among all PILs under current investigation.

4. The methacrylic ILMs (**ILM1**, **ILM7** and **ILM2**) were used in RAFT (co)polymerization to prepare three other families of PILs. First, random copolymerization of ionic methacrylic ILMs with poly(ethylene glycol)methyl ether methacrylate (PEGM). Varying the nature of the ionic monomer and the PEGM:ILM ratio the 16 random ionic copolymers poly(**ILM_n-*r*-PEGM_m**) have been synthesized.

Investigating the electrochemical properties of methacrylate PILs it was found that polyelectrolytes based on the cationic **ILM2** generally exhibited higher conductivity in comparison with anionic random copolymers derived from **ILM1**. Analysing **ILM1** copolymers having the same molecular weight, but differ in PEGM:**ILM1** ratio, it was discovered that ionic conductivity strongly depends on PEGM content, varying from 1.2×10^{-5} to 3.6×10^{-7} S cm⁻¹ at 25°C. At this, it was established that the PEGM content vs. conductivity dependence was passing through the maximum at PEGM:**ILM1** ratio equal to 3.4 for **PIL14**. The random copolymers (AB) with optimal structures were further used as macro-chain transfer agents to prepare third family of PILs, composed of eight ionic **AB-b-C** type block copolymers, where the C-block was obtained by post polymerization of 2-phenylethyl methacrylate or (1-naphthyl)methyl methacrylate. The partial incompatibility between ionic and neutral blocks in the ionic AB-C type block copolymers resulted in a microphase-separated lamellar morphology, where the neutral high T_g domains were responsible for the mechanical properties, while the soft ionic domains with low T_g were possessing elevated concentration of mobile ions and enhancing the overall ionic conductivity. Consequently, these **AB-b-C** type block copolymers, while exhibiting higher mechanical properties (the storage moduli ranged from 82.1 to 1680 kPa at 25°C and 1 rad s⁻¹) compared to parent random copolymers were able to maintain comparable level of ionic conductivity (up to 2.2×10^{-6} S cm⁻¹ at 25°C).

5. The fifth family of PILs was synthesized via chemical modification of poly(epichlorohydrin-co-ethylene oxide) with monosubstituted imidazoles. These PILs differ by imidazolium side chains length (alkyl ($-C_nH_{2n+1}$, $n = 1 - 6$)) and the presence of heteroatoms (silyl, siloxane and perfluoroalkyl) as well as by the type of anion (bis(trifluoromethylsulfonyl)imide (TFSI), 2,2,2-trifluoromethylsulfonyl-N-cyanoamide (TFSAM), trifluoro(trifluoromethyl)borate (BF₃CF₃) or tricyanofluoroborate (BF(CN)₃)). The study of their thermal and electrochemical properties revealed that all TFSI-based PILs with alkyl side chains possess lower glass transition temperatures and higher ionic conductivities than those bearing heteroatomic substituents. Among them the highest conductivity (4.7×10^{-6} S cm⁻¹ at 25°C) was shown by the **PIL33TFSI** with an *n*-butyl side chain. Further expansion of the *n*-butyl substituted PILs family by ion exchange allowed for additional increase in ionic conductivity of the resultant polyelectrolytes, reaching as high value as 1.0×10^{-5} S cm⁻¹ (at 25 °C) for **PIL33BF(CN)₃**. The study of **PIL33BF(CN)₃** rheological properties revealed sufficient storage modulus of 22 kPa (at 25°C and 1 rad s⁻¹).

6. PILs synthesized in this work were further used as building blocks to create **DIGs**. The work started from the anionic **PIL13** and cationic **PIL33TFSI** coacervation study to synthesize model **DIG1**, that served as a proof-of-concept. It was demonstrated that although the coacervation process was sensitive to experimental parameters (such as solvent type, order of mixing, and temperature), the subsequent solvent evaporation and the annealing steps consistently produced equivalent DIGs. The

successful dynamic gelation process, resulting in the formation of dynamic ionic cross-links and *in situ* formation of an ionic liquid, was fully confirmed by quantitative ^{19}F NMR, gravimetric methods and rheological experiments. The beneficial impact of the released IL was demonstrated by DSC and BDS. It was demonstrated that the formation of DIG improves the ionic conductivity in comparison with parent PILs ($7.2 \times 10^{-6} \text{ S cm}^{-1}$ at 25°C). At the same time, the viscoelastic properties were found to be strongly affected by the presence of released IL resulting in the decrease of G' from 158 to 26.4 kPa (at 25°C and 1 rad s^{-1}) for the extracted **DIG1_{ext}** and **DIG1** annealed after coacervation (IL content increases from 0 to $\sim 24 \text{ wt } \%$), that was explained by plasticization and dilution of the entanglements.

7. To enhance the viscoelastic properties of DIGs, two approaches were suggested and employed. The first approach involves the introduction of the PIL building blocks with sulfonate (SO_3^-) anions, that differ from TFSI analogues by smaller size of the ion, higher charge localization and significantly stronger ion interaction with counter cations. This strategy led to the development of four DIGs (**DIG2-DIG5**) based on **PIL33TFSI** and sulfonate PILs having the same structure of the main chain, identical molecular weight, but differ in the nature of the counter cation (ammonium, imidazolium or phosphonium). By example of **DIG2**, it was again demonstrated that DIGs exhibited both superior mechanical properties and higher ionic conductivity compared to parent PILs. Moreover, due to the presence of SO_3^- anions the formation of much stronger dynamic ionic crosslinks in **DIG2** (compared to **DIG1**) was leading to the enhancement of the viscoelastic properties without compromise in ionic conductivity: $\sigma = 7.2 \times 10^{-6}$ and $5.7 \times 10^{-6} \text{ S cm}^{-1}$ (25°C), $G' = 26.4$ and 61.9 kPa (25°C and 1 rad s^{-1}) for **DIG1** and **DIG2**, respectively. The second approach was focused on the utilization of ionic **AB-b-C** type block copolymers as building blocks in the preparation of seven new DIGs (**DIG7-DIG13**). The resulting DIGs were found to self-assemble into a lamellar or hexagonally packed cylinder morphologies, exhibiting a significant improvement in viscoelastic (mechanical) performance compared to **DIG1-DIG5** (with G' values ranging from 7.9 to 1827 kPa at 25°C and 1 rad s^{-1}) with preservation of a comparable level of ionic conductivity (10^{-6} to $10^{-7} \text{ S cm}^{-1}$ at 25°C).

7. The final iteration of DIG optimization resulted in **DIG14**, based on sulfonate **PIL21I** and **PIL33BF(CN)₃** with the BF(CN)_3 counter anion. **DIG14** exhibited the most attractive performance profile, significantly outperforming other DIGs and PILs in terms of ionic conductivity ($\sigma = 8.2 \times 10^{-6} \text{ S cm}^{-1}$ (25°C)) and mechanical stiffness, ($G' = 214.5 \text{ kPa}$ (25°C and 1 rad s^{-1})). This best-performing DIG was then used in the assembly and testing of all-solid-state supercapacitors with reduced graphene oxide (rGO) and carbon nanotubes (CNTs) electrode materials and having symmetrical trilayer configuration: **DIG14**+rGO+CNTs / **DIG14** / **DIG14**+rGO+CNTs. This supercapacitor demonstrated the following characteristics: specific capacitance $C_{\text{SP}} = 19.6 \text{ F g}^{-1}$, energy $E = 10.9 \text{ Wh kg}^{-1}$ and power $P = 97.7 \text{ W kg}^{-1}$ (at 25°C , 5 mV s^{-1} scan rate, potential window of 2V), markedly outperforming supercapacitors based on the parent **PIL21I** and **PIL33BF(CN)₃** under similar conditions. Due to the

excellent viscoelastic properties of **DIG14** the supercapacitor was capable to be cycled at higher temperatures (80 °C) without shortcutting and demonstrated $C_{SP} = 43.9 \text{ F g}^{-1}$, $E = 24.4 \text{ Wh kg}^{-1}$ and power $P = 218.9 \text{ W kg}^{-1}$. These results represent a significant input in the field as the suggested DIG approach creates a new pathway to highly efficient, flexible, lightweight and safe supercapacitors requiring no sealing and tolerant of a much broader range of application conditions (reduced pressures, high voltages and temperatures, etc.).

8. In conclusion, the concept of DIGs has proven to be effective in developing of materials with high ionic conductivity and appealing viscoelastic properties, often surpassing the performance of the parent polymeric building blocks. DIG properties could be tailored and improved by further structural design of the building blocks (e.g., chemical nature and polymerization degree of the PILs, content and chemical nature of the ion pairs, etc.). Such flexibility in the design of DIGs allows for fine-tuning material properties to meet specific application requirements, thus making DIGs excellent potential candidates for the next generation of safe and flexible polymer-based electrochemical devices requiring high conductivity in the solid state, for example thin-film transistors, solar cells, smart windows, actuators, etc.



VI. Acknowledgements

I would first like to thank the Luxembourg National Research Fund (FNR) and the Agency Nationale de la Recherche (ANR) for funding the DISAFECAP project (INTER/ANR/19/13358226), which made this work possible. My gratitude also extends to the University of Luxembourg (UL) for hosting me as a Ph.D. student and for providing excellent administrative support, high-quality transferable skills training, the Learning Centre, and the Food Lab.

I am deeply grateful to the Luxembourg Institute of Science and Technology (LIST) for fostering an exceptional working environment, with its unique range of equipment and facilities, a wealth of specialists always ready to assist, and the "tastiest" coffee to fuel our efforts. Special thanks to Prof. Alexander Shaplov for his endless passion for science and his invaluable scientific expertise, support, and mentorship throughout this research. Your guidance has greatly enhanced my research skills, advanced my career, and empowered me to pursue groundbreaking research endeavours.

I also extend my appreciation to the members of the jury for accepting to review my work.

My sincere gratitude goes to all the trainees, former and current Ph.D. students, and postdocs for the wonderful moments we've shared over the past few years. Special thanks to Vladislav Shevtsov, Dr. Sergey Zubkevich, Celia Ziane, and Dr. Arpan Datta Sarma for being the best labmates and for their unwavering motivation, which has constantly inspired me to keep moving forward. I am also grateful to BaschaRhymes (Oussema Kachouri, Andrea Iannotta, and Margo Bonmatin) for the SkyJo obsession and the countless laughs we've shared. To the French-speaking team: Antoine, for being a great neighbour and a role model; Dr. Dhahabia Abdallah Boina, for her warm smile and openness; Aymane El Bouhali, for being so enigmatic; Charles Jehl and Vincent Boulic, for their great sense of humor; and Tinatin Kouprava, for her delicious cookies. Thank you all for making this journey so memorable.

My sincere acknowledgment goes to the researchers at LIST (Prof. Daniel Schmidt, Dr. Reiner Dieden, and our great boss ever, Dr. Stephan Westermann) and INEOS RAS (Dr. Elena Lozinskaya) for the fruitful scientific discussions. I am also grateful to the team at Cergy Paris University (Dr. Cedric Plesse, Prof. Pierre Henri Aubert and Hazar Guemiza) for their assistance in electrode preparation, supercapacitor assembly, and testing as well as electrochemistry teaching. Furthermore, I appreciate the great support from Université Claude Bernard Lyon 1 (Prof. Eric Drockenmuller, Prof. Damien Montarnal, and Dr. Malak Alaa Eddine) in the rheological and conductivity investigations of DIGs and PILs as well as extra useful advices in chemistry from Prof. Eric Drockenmuller. I would also like to mention the technical support provided by my supervisor, Dr. Reiner Dieden, along with Benoît

Marcolini, Régis Vaudemont, and Patrick Grysan. Your invaluable help has significantly shaped my Ph.D. experience.

Finally, a heartfelt thank you to my incredible parents, Roman and Tatiana, for their unwavering support throughout this journey. You have always believed in me and my decisions, offering guidance and a listening ear whenever I needed it. I am deeply indebted to you for giving me the strength and dedication to become the person I am today. A special thanks also goes to both my grandmothers, who taught me the values of hard work and patience.

And saving the best for last, Melissa. You are my complete opposite, and because of that, you offer me a completely different perspective on the world, opening my eyes to new opportunities I might have otherwise missed. Thank you for teaching me to value and stand up for myself, and for always motivating me to aim higher and pursue greater goals. Your inspiration has been my driving force, and without you, I would stop moving way back there.



VII. Dissemination

Published articles

1. Cotessat, M.; Flachard, D.; **Nosov, D.R.**; Lozinskaya, E. I.; Ponkratov, D. O.; Schmidt, D. F.; Drockenmuller, E.; Shaplov, A. S. Effects of Repeat Unit Charge Density on the Physical and Electrochemical Properties of Novel Heterocationic Poly(Ionic Liquid)s. *New Journal of Chemistry* **2021**, 45 (1), 53–65. <https://doi.org/10.1039/D0NJ04143B>.
2. Soares, B. F.; **Nosov, D. R.**; Pires, J. M.; Tyutyunov, A. A.; Lozinskaya, E. I.; Antonov, D. Y.; Shaplov, A. S.; Marrucho, I. M. Tuning CO₂ Separation Performance of Ionic Liquids through Asymmetric Anions. *Molecules* **2022**, 27 (2), 1–23. <https://doi.org/10.3390/molecules27020413>.
3. **Nosov, D. R.**; Ronnasi, B.; Lozinskaya, E. I.; Ponkratov, D. O.; Puchot, L.; Grysan, P.; Schmidt, D. F.; Lessard, B. H.; Shaplov, A. S. Mechanically Robust Poly(Ionic Liquid) Block Copolymers as Self-Assembling Gating Materials for Single-Walled Carbon-Nanotube-Based Thin-Film Transistors. *ACS Appl Polym Mater* **2023**, 5 (4), 2639–2653. <https://doi.org/10.1021/acsapm.2c02223>.
4. Tomšík, E.; **Nosov, D. R.**; Ivanko, I.; Pokorný, V.; Konefał, M.; Černochová, Z.; Tadzyszak, K.; Schmidt, D. F.; Shaplov, A. S. A New Method to Prepare Stable Polyaniline Dispersions for Highly Loaded Cathodes of All-Polymer Li-Ion Batteries. *Polymers (Basel)* **2023**, 15 (11), 2508. <https://doi.org/10.3390/polym15112508>.
5. Alaa Eddine, M.; **Nosov, D. R.**; Lepre, L. F.; Serghei, A.; Schmidt, D. F.; Montarnal, D.; Shaplov, A. S.; Drockenmuller, E. Dynamic Ion Gels from the Complex Coacervation of Oppositely Charged Poly(Ionic Liquid)s. *ACS Macro Lett* **2024**, 921–927. <https://doi.org/10.1021/ACSMACROLETT.4C00253>.
6. Karatrantos, A. V.; Middendorf, M.; **Nosov, D. R.**; Cai, Q.; Westermann, S.; Hoffmann, K.; Nürnberg, P.; Shaplov, A. S.; Schönhoff, M. Diffusion and Structure of Propylene Carbonate-Metal Salt Electrolyte Solutions for Post-Lithium-Ion Batteries: From Experiment to Simulation. *J Chem Phys* **2024**, 161 (5), 54502. <https://doi.org/10.1063/5.0216222/3305717>.
7. **Nosov, D. R.**; Lozinskaya, E. I.; Antonov, D.Y.; Ponkratov, D.O.; Tyutyunov, A.A.; Alaa Eddine, M.; Plesse, C.; Schmidt, D.F.; Shaplov, A.S. Design of highly conductive PILs by simple

modification of poly(epichlorohydrin-co-ethylene oxide) with monosubstituted imidazoles. *ACS Polymers Au*, **2024**, xx, xxx. <https://doi.org/>.

Conferences

1. **Nosov, D. R.**; Lepre, L.F.; Shaplov, A.S.; Drockenmuller, E. “New trends in development of highly conductive poly(ionic liquid)s”, International Composites Conference "IMAGINENANO 2021", Bilbao, Spain, November 23-24, 2021. (**Oral talk**)

2. **Nosov, D. R.**; Lepre, L.F.; Shaplov, A.S.; Drockenmuller, E.; Plesse, C. “Dynamic ion gels (DIGs) from complex coacervation of oppositely charged poly(ionic liquid)s.”, International Symposium on Polymer Electrolytes 2022 (ISPE17), Niagara-on-the-lake, Canada, October 2-7, 2022.

3. **Nosov, D. R.**; Lepre, L.F.; Shaplov, A.S.; Drockenmuller, E. “Novel polymer electrolytes derived from coacervation of oppositely charged poly(ionic liquids) and/or silica nanoparticles”. PhD Days 2022, Université du Luxembourg, Luxembourg, October 1, 2022. (**Oral talk**)

4. **Nosov, D. R.**; Lepre, L.F.; Shaplov, A.S.; Schmidt, D.F.; Drockenmuller, E.; Plesse, C. "Dynamic ion gels (DIGs) from complex coacervation of oppositely charged poly(ionic liquid)s as a novel approach for highly conductive materials”, 7th International Symposium "Frontiers in Polymer Science" Gothenburg, Sweden, 29 May- 1 June, 2023. (**Oral talk**)

5. **Nosov, D. R.**; Lepre, L.F.; Shaplov, A.S.; Drockenmuller, E.; Plesse, C. “Dynamic Ion Gels (DIGs) as next opportunity for electrochemical devicesDynamic Ion Gels (DIGs) as next opportunity for electrochemical devices”, European Winter School & Workshop on solid-state energy conversion & storage, Sestriere, Italy, March 19-24, 2023.

6. **Nosov, D. R.**; Lepre, L.F.; Shaplov, A.S.; Schmidt, D.F.; Drockenmuller, E.; Plesse, C. “Dynamic Ion Gels (DIGs) – the ionic materials of the future”, 11th EPF Summer School, "Polymers and Ionic Liquids”, Bertinoro, Italy, May 2-5, 2023.

7. **Nosov, D. R.**; Ronnasi, B.; Lingua, G.; Guemiza, H.; Lozinskaya, E. I.; Ponkratov, D. O.; Grysan, P.; Lessard, B.H.; Gerbaldi, C.; Shaplov, A.S. “Single-ion-conducting block copolymers with improved conductivity and mechanical performance for all-solid-state Li batteries and thin film transistors”, Lithium Battery Discussions "LIBD10 2023", Arcachon, France, June 18-23, 2023.



VIII. References

- (1) Scrosati, B.; Garche, J. Lithium Batteries: Status, Prospects and Future. *J Power Sources* **2010**, *195* (9), 2419–2430. <https://doi.org/10.1016/J.JPOWSOUR.2009.11.048>.
- (2) Armand, M.; Tarascon, J.-M. Building Better Batteries. *Nature* **2008**, *451* (7179), 652–657. <https://doi.org/10.1038/451652a>.
- (3) Goodenough, J. B.; Park, K.-S. The Li-Ion Rechargeable Battery: A Perspective. *J Am Chem Soc* **2013**, *135* (4), 1167–1176. <https://doi.org/10.1021/ja3091438>.
- (4) Xu, K. Nonaqueous Liquid Electrolytes for Lithium-Based Rechargeable Batteries. *Chem Rev* **2004**, *104* (10), 4303–4417. <https://doi.org/10.1021/cr030203g>.
- (5) Manthiram, A.; Fu, Y.; Su, Y.-S. Challenges and Prospects of Lithium–Sulfur Batteries. *Acc Chem Res* **2013**, *46* (5), 1125–1134. <https://doi.org/10.1021/ar300179v>.
- (6) Ohno, H.; Ito, K. Room-Temperature Molten Salt Polymers as a Matrix for Fast Ion Conduction. *Chem Lett* **1998**, *27* (8), 751–752. <https://doi.org/10.1246/cl.1998.751>.
- (7) Yuan, J.; Mecerreyes, D.; Antonietti, M. Poly(Ionic Liquid)s: An Update. *Prog Polym Sci* **2013**, *38* (7), 1009–1036. <https://doi.org/10.1016/J.PROGPOLYMSCI.2013.04.002>.
- (8) Mecerreyes, D. Polymeric Ionic Liquids: Broadening the Properties and Applications of Polyelectrolytes. *Progress in Polymer Science (Oxford)* **2011**, *36* (12), 1629–1648. <https://doi.org/10.1016/J.PROGPOLYMSCI.2011.05.007>.
- (9) Zhou, D.; Shanmukaraj, D.; Tkacheva, A.; Armand, M.; Wang, G. Polymer Electrolytes for Lithium-Based Batteries: Advances and Prospects. *Chem* **2019**, *5* (9), 2326–2352. <https://doi.org/10.1016/J.CHEMPR.2019.05.009>.
- (10) Shaplov, A. S.; Ponkratov, D. O.; Vygodskii, Y. S. Poly(Ionic Liquid)s: Synthesis, Properties, and Application. *Polymer Science Series B* **2016**, *58* (2), 73–142. <https://doi.org/10.1134/S156009041602007X>.
- (11) Ponkratov, D. O.; Lozinskaya, E. I.; Vlasov, P. S.; Aubert, P.-H.; Plesse, C.; Vidal, F.; Vygodskii, Y. S.; Shaplov, A. S. Synthesis of Novel Families of Conductive Cationic Poly(Ionic Liquid)s and Their Application in All-Polymer Flexible Pseudo-Supercapacitors. *Electrochim Acta* **2018**, *281*, 777–788. <https://doi.org/10.1016/j.electacta.2018.05.191>.

- (12) Porcarelli, L.; Shaplov, A. S.; Salsamendi, M.; Nair, J. R.; Vygodskii, Y. S.; Mecerreyes, D.; Gerbaldi, C. Single-Ion Block Copoly(Ionic Liquid)s as Electrolytes for All-Solid State Lithium Batteries. *ACS Appl Mater Interfaces* **2016**, *8* (16), 10350–10359. <https://doi.org/10.1021/acsami.6b01973>.
- (13) Bocharova, V.; Sokolov, A. P. Perspectives for Polymer Electrolytes: A View from Fundamentals of Ionic Conductivity. *Macromolecules*. **2020**, pp 4141–4157. <https://doi.org/10.1021/acs.macromol.9b02742>.
- (14) Shaplov, A. S.; Marcilla, R.; Mecerreyes, D. Recent Advances in Innovative Polymer Electrolytes Based on Poly(Ionic Liquid)s. *Electrochim Acta* **2015**, *175*, 18–34. <https://doi.org/10.1016/J.ELECTACTA.2015.03.038>.
- (15) Zhu, J.; Zhang, Z.; Zhao, S.; Westover, A. S.; Belharouak, I.; Cao, P. F. Single-Ion Conducting Polymer Electrolytes for Solid-State Lithium–Metal Batteries: Design, Performance, and Challenges. *Adv Energy Mater* **2021**, *11* (14), 1–18. <https://doi.org/10.1002/aenm.202003836>.
- (16) Feng, H.; Lu, X.; Wang, W.; Kang, N. G.; Mays, J. W. Block Copolymers: Synthesis, Self-Assembly, and Applications. *Polymers (Basel)* **2017**, *9* (10). <https://doi.org/10.3390/polym9100494>.
- (17) Kim, Y. M.; Choi, W. Y.; Kwon, J. H.; Lee, J. K.; Moon, H. C. Functional Ion Gels: Versatile Electrolyte Platforms for Electrochemical Applications †. *Chemistry of Materials* **2021**, *33* (8), 2683–2705. <https://doi.org/10.1021/acs.chemmater.1c00330>.
- (18) Jamil, R.; Silvester, D. S. Ionic Liquid Gel Polymer Electrolytes for Flexible Supercapacitors: Challenges and Prospects. *Curr Opin Electrochem* **2022**, *35*, 101046. <https://doi.org/10.1016/j.coelec.2022.101046>.
- (19) Zhang, S. Y.; Zhuang, Q.; Zhang, M.; Wang, H.; Gao, Z.; Sun, J. K.; Yuan, J. Poly(Ionic Liquid) Composites. *Chem Soc Rev* **2020**, *49* (6), 1726–1755. <https://doi.org/10.1039/c8cs00938d>.
- (20) Hallinan, D. T.; Villaluenga, I.; Balsara, N. P. Polymer and Composite Electrolytes. *MRS Bull* **2018**, *43* (10), 775–781. <https://doi.org/10.1557/mrs.2018.212>.
- (21) Puguan, J. M. C.; Botton, L. B.; Kim, H. Triazole-Based Ionene Exhibiting Tunable Structure and Ionic Conductivity Obtained via Cycloaddition Reaction: A New Polyelectrolyte for Electrochromic Devices. *Solar Energy Materials and Solar Cells* **2018**, *188* (June), 210–218. <https://doi.org/10.1016/j.solmat.2018.09.009>.

- (22) Hu, H.; Yuan, W.; Jia, Z.; Baker, G. L. Ionic Liquid-Based Random Copolymers: A New Type of Polymer Electrolyte with Low Glass Transition Temperature. *RSC Adv* **2015**, 5 (5), 3135–3140. <https://doi.org/10.1039/c4ra13432j>.
- (23) Jourdain, A.; Serghei, A.; Drockenmuller, E. Enhanced Ionic Conductivity of a 1,2,3-Triazolium-Based Poly(Siloxane Ionic Liquid) Homopolymer. *ACS Macro Lett* **2016**, 5 (11), 1283–1286. <https://doi.org/10.1021/ACSMACROLETT.6B00761>.
- (24) Shaplov, A. S.; Lozinskaya, E. I.; Losada, R.; Wandrey, C.; Zdvizhkov, A. T.; Korlyukov, A. A.; Lyssenko, K. A.; Malyshkina, I. A.; Vygodskii, Y. S. Polymerization of the New Double-Charged Monomer Bis-1,3(N,N,N-Trimethylammonium Dicyanamide)-2-Propylmethacrylate and Ionic Conductivity of the Novel Polyelectrolytes. *Polym Adv Technol* **2011**, 22 (4), 448–457. <https://doi.org/10.1002/PAT.1569>.
- (25) Wojnarowska, Z.; Feng, H.; Fu, Y.; Cheng, S.; Carroll, B.; Kumar, R.; Novikov, V. N.; Kisliuk, A. M.; Saito, T.; Kang, N. G.; Mays, J. W.; Sokolov, A. P.; Bocharova, V. Effect of Chain Rigidity on the Decoupling of Ion Motion from Segmental Relaxation in Polymerized Ionic Liquids: Ambient and Elevated Pressure Studies. *Macromolecules* **2017**, 50 (17), 6710–6721. <https://doi.org/10.1021/acs.macromol.7b01217>.
- (26) Ikeda, T. Poly(Ionic Liquid)s with Branched Side Chains: Polymer Design for Breaking the Conventional Record of Ionic Conductivity. *Polym Chem* **2021**, 12 (5), 711–718. <https://doi.org/10.1039/d0py01333a>.
- (27) Lee, M.; Choi, U. H.; Salas-De La Cruz, D.; Mittal, A.; Winey, K. I.; Colby, R. H.; Gibson, H. W. Imidazolium Polyesters: Structure-Property Relationships in Thermal Behavior, Ionic Conductivity, and Morphology. *Adv Funct Mater* **2011**, 21 (4), 708–717. <https://doi.org/10.1002/ADFM.201001878>.
- (28) Lee, M.; Choi, U. H.; Colby, R. H.; Gibson, H. W. Ion Conduction in Imidazolium Acrylate Ionic Liquids and Their Polymers. *Chemistry of Materials* **2010**, 22 (21), 5814–5822. <https://doi.org/10.1021/CM101407D>.
- (29) Li, H.; Zhang, H.; Liao, X.; Sun, R.; Xie, M. Incorporating Trifunctional 1,6-Heptadiyne Moiety into Polyacetylene Ionomer for Improving Its Physical and Conductive Properties. *Polym Chem* **2020**, 11 (19), 3322–3331. <https://doi.org/10.1039/d0py00109k>.
- (30) Chen, M.; Dugger, J. W.; Li, X.; Wang, Y.; Kumar, R.; Meek, K. M.; Uhrig, D. W.; Browning, J. F.; Madsen, L. A.; Long, T. E.; Lokitz, B. S. Polymerized Ionic Liquids: Effects of Counter-Anions on Ion Conduction and Polymerization Kinetics. *J Polym Sci A Polym Chem* **2018**, 56 (13), 1346–1357. <https://doi.org/10.1002/pola.29015>.

- (31) Price, T. L.; Choi, U. H.; Schoonover, D. V.; Wang, D.; Heflin, J. R.; Xie, R.; Colby, R. H.; Gibson, H. W. Studies of Ion Conductance in Polymers Derived from Norbornene Imidazolium Salts Containing Ethyleneoxy Moieties. *Macromolecules* **2019**, *52* (4), 1389–1399. <https://doi.org/10.1021/acs.macromol.8b02303>.
- (32) Cotessat, M.; Flachard, D.; Nosov, D.; Lozinskaya, E. I.; Ponkratov, D. O.; Schmidt, D. F.; Drockenmuller, E.; Shaplov, A. S. Effects of Repeat Unit Charge Density on the Physical and Electrochemical Properties of Novel Heterocationic Poly(Ionic Liquid)s. *New Journal of Chemistry* **2021**, *45* (1), 53–65. <https://doi.org/10.1039/D0NJ04143B>.
- (33) Anaya, O.; Kallel Elloumi, A.; Thankappan, H.; Abdelhedi Miladi, I.; Serghei, A.; Ben Romdhane, H.; Drockenmuller, E. Synthesis and Structure/Properties Correlations of Fluorinated Poly(1,2,3-Triazolium)s. *Chemistry Africa* **2020**, *3* (3), 759–768. <https://doi.org/10.1007/s42250-020-00164-1>.
- (34) Sood, R.; Zhang, B.; Serghei, A.; Bernard, J.; Drockenmuller, E. Triethylene Glycol-Based Poly(1,2,3-Triazolium Acrylate)s with Enhanced Ionic Conductivity. *Polym Chem* **2015**, *6* (18), 3521–3528. <https://doi.org/10.1039/C5PY00273G>.
- (35) Colliat-Dangus, G.; Obadia, M. M.; Vygodskii, Y. S.; Serghei, A.; Shaplov, A. S.; Drockenmuller, E. Unconventional Poly(Ionic Liquid)s Combining Motionless Main Chain 1,2,3-Triazolium Cations and High Ionic Conductivity. *Polym Chem* **2015**, *6* (23), 4299–4308. <https://doi.org/10.1039/C5PY00526D>.
- (36) Wu, J.; Chen, J.; Wang, J.; Liao, X.; Xie, M.; Sun, R. Synthesis and Conductivity of Hyperbranched Poly(Triazolium)s with Various End-Capping Groups. *Polym Chem* **2016**, *7* (3), 633–642. <https://doi.org/10.1039/C5PY01735A>.
- (37) Shaplov, A. S.; Ponkratov, D. O.; Aubert, P. H.; Lozinskaya, E. I.; Plesse, C.; Maziz, A.; Vlasov, P. S.; Vidal, F.; Vygodskii, Y. S. Truly Solid State Electrochromic Devices Constructed from Polymeric Ionic Liquids as Solid Electrolytes and Electrodes Formulated by Vapor Phase Polymerization of 3,4-Ethylenedioxythiophene. *Polymer (Guildf)* **2014**, *55* (16), 3385–3396. <https://doi.org/10.1016/J.POLYMER.2014.04.013>.
- (38) Frenzel, F.; Guterman, R.; Anton, A. M.; Yuan, J.; Kremer, F. Molecular Dynamics and Charge Transport in Highly Conductive Polymeric Ionic Liquids. *Macromolecules* **2017**, *50* (10), 4022–4029. <https://doi.org/10.1021/acs.macromol.7b00554>.
- (39) Qian, W.; Texter, J.; Yan, F. Frontiers in Poly(Ionic Liquid)s: Syntheses and Applications. *Chem Soc Rev* **2017**, *46* (4), 1124–1159. <https://doi.org/10.1039/c6cs00620e>.

- (40) Ogihara, W.; Washiro, S.; Nakajima, H.; Ohno, H. Effect of Cation Structure on the Electrochemical and Thermal Properties of Ion Conductive Polymers Obtained from Polymerizable Ionic Liquids. *Electrochim Acta* **2006**, *51* (13), 2614–2619. <https://doi.org/10.1016/j.electacta.2005.07.043>.
- (41) Shaplov, A. S.; Lozinskaya, E. I.; Ponkratov, D. O.; Malyskhina, I. A.; Vidal, F.; Aubert, P. H.; Okatova, O. V.; Pavlov, G. M.; Komarova, L. I.; Wandrey, C.; Vygodskii, Y. S. Bis(Trifluoromethylsulfonyl)Amide Based “Polymeric Ionic Liquids”: Synthesis, Purification and Peculiarities of Structure-Properties Relationships. *Electrochim Acta* **2011**, *57* (1), 74–90. <https://doi.org/10.1016/j.electacta.2011.06.041>.
- (42) Ye, Y.; Elabd, Y. A. Anion Exchanged Polymerized Ionic Liquids: High Free Volume Single Ion Conductors. *Polymer (Guildf)* **2011**, *52* (5), 1309–1317. <https://doi.org/10.1016/j.polymer.2011.01.031>.
- (43) Ikeda, T.; Moriyama, S.; Kim, J. Imidazolium-Based Poly(Ionic Liquid)s with Poly(Ethylene Oxide) Main Chains: Effects of Spacer and Tail Structures on Ionic Conductivity. *J Polym Sci A Polym Chem* **2016**, *54* (18), 2896–2906. <https://doi.org/10.1002/pola.28175>.
- (44) Partl, G. J.; Naier, B. F. E.; Bakry, R.; Schlapp-Hackl, I.; Kopacka, H.; Wurst, K.; Gelbrich, T.; Fliri, L.; Schottenberger, H. Can’t Touch This: Highly Omniphobic Coatings Based on Self-Textured C6-Fluoroponytailed Polyvinylimidazolium Monoliths. *J Fluor Chem* **2021**, *249* (May), 109839. <https://doi.org/10.1016/j.jfluchem.2021.109839>.
- (45) Chen, S.; Funtan, A.; Gao, F.; Cui, B.; Meister, A.; Parkin, S. S. P.; Binder, W. H. Synthesis and Morphology of Semifluorinated Polymeric Ionic Liquids. *Macromolecules* **2018**, *51* (21), 8620–8628. <https://doi.org/10.1021/acs.macromol.8b01624>.
- (46) Kaestner, P.; Strehmel, V. Synthesis of Ionic Polymers by Free Radical Polymerization Using Aprotic Trimethylsilylmethyl-Substituted Monomers. *Journal of Polymer Science* **2020**, *58* (7), 977–987. <https://doi.org/10.1002/pol.20190310>.
- (47) Cordella, D.; Ouhib, F.; Aqil, A.; Defize, T.; Jérôme, C.; Serghei, A.; Drockenmuller, E.; Aissou, K.; Taton, D.; Detrembleur, C. Fluorinated Poly(Ionic Liquid) Diblock Copolymers Obtained by Cobalt-Mediated Radical Polymerization-Induced Self-Assembly. *ACS Macro Lett* **2017**, *6* (2), 121–126. <https://doi.org/10.1021/acsmacrolett.6b00899>.
- (48) Shaplov, A. S.; Marcilla, R.; Mecerreyes, D. Recent Advances in Innovative Polymer Electrolytes Based on Poly(Ionic Liquid)s. *Electrochim Acta* **2015**, *175*, 18–34. <https://doi.org/10.1016/j.electacta.2015.03.038>.

- (49) Sinha, K.; Wang, W.; Winey, K. I.; Maranas, J. K. Dynamic Patterning in PEO-Based Single Ion Conductors for Li Ion Batteries. *Macromolecules* **2012**, *45* (10), 4354–4362. <https://doi.org/10.1021/ma300051y>.
- (50) Green, M. D.; Long, T. E. Polymer Reviews Designing Imidazole-Based Ionic Liquids and Ionic Liquid Monomers for Emerging Technologies REVIEWS Designing Imidazole-Based Ionic Liquids and Ionic Liquid Monomers for Emerging Technologies. **2009**. <https://doi.org/10.1080/15583720903288914>.
- (51) Jaeger, W.; Bohrisch, J.; Laschewsky, A. Synthetic Polymers with Quaternary Nitrogen Atoms-Synthesis and Structure of the Most Used Type of Cationic Polyelectrolytes. *Progress in Polymer Science (Oxford)* **2010**, *35* (5), 511–577. <https://doi.org/10.1016/j.progpolymsci.2010.01.002>.
- (52) Yuan, J.; Mecerreyes, D.; Antonietti, M. Progress in Polymer Science Poly (Ionic Liquid) S: An Update. *Prog Polym Sci* **2013**, *38* (7), 1009–1036. <https://doi.org/10.1016/j.progpolymsci.2013.04.002>.
- (53) Meek, K. M.; Elabd, Y. A. Polymerized Ionic Liquid Block Copolymers for Electrochemical Energy. *J Mater Chem A Mater* **2015**, *3* (48), 24187–24194. <https://doi.org/10.1039/c5ta07170d>.
- (54) Obadia, M. M.; Drockenmuller, E. Poly(1,2,3-Triazolium)s: A New Class of Functional Polymer Electrolytes. *Chemical Communications* **2016**, *52* (12), 2433–2450. <https://doi.org/10.1039/C5CC09861K>.
- (55) Ohno, H. Design of Ion Conductive Polymers Based on Ionic Liquids. <https://doi.org/10.1002/masy.200750435>.
- (56) Bocharova, V.; Sokolov, A. P. Perspectives for Polymer Electrolytes: A View from Fundamentals of Ionic Conductivity. *Macromolecules*. 2020, pp 4141–4157. <https://doi.org/10.1021/acs.macromol.9b02742>.
- (57) Dou, S.; Zhang, S.; Klein, R. J.; Runt, J.; Colby, R. H. Synthesis and Characterization of Poly(Ethylene Glycol)-Based Single-Ion Conductors. *Chemistry of Materials* **2006**, *18* (18), 4288–4295. <https://doi.org/10.1021/cm0603699>.
- (58) Xue, Z.; He, D.; Xie, X. Poly(Ethylene Oxide)-Based Electrolytes for Lithium-Ion Batteries. *J Mater Chem A Mater* **2015**, *3* (38), 19218–19253. <https://doi.org/10.1039/c5ta03471j>.

- (59) Hu, H.; Yuan, W.; Lu, L.; Zhao, H.; Jia, Z.; Baker, G. L. Low Glass Transition Temperature Polymer Electrolyte Prepared from Ionic Liquid Grafted Polyethylene Oxide. *J Polym Sci A Polym Chem* **2014**, *52* (15), 2104–2110. <https://doi.org/10.1002/pola.27217>.
- (60) Ponkratov, D. O.; Lozinskaya, E. I.; Vlasov, P. S.; Aubert, P.-H.; Plesse, C.; Vidal, F.; Vygodskii, Y. S.; Shaplov, A. S. Synthesis of Novel Families of Conductive Cationic Poly(Ionic Liquid)s and Their Application in All-Polymer Flexible Pseudo-Supercapacitors. *Electrochim Acta* **2018**, *281*, 777–788. <https://doi.org/10.1016/j.electacta.2018.05.191>.
- (61) Hu, H.; Yuan, W.; Jia, Z.; Baker, G. L. Ionic Liquid-Based Random Copolymers: A New Type of Polymer Electrolyte with Low Glass Transition Temperature. *RSC Adv* **2015**, *5* (5), 3135–3140. <https://doi.org/10.1039/c4ra13432j>.
- (62) Matsumoto, K.; Chijiwa, T.; Endo, T. Cationic Polymerization of a Novel Oxetane-Bearing Ionic Liquid Structure and Properties of the Obtained Poly(Ionic Liquid). *J Polym Sci A Polym Chem* **2014**, *52* (20), 2986–2990. <https://doi.org/10.1002/pola.27342>.
- (63) Matsumoto, K.; Yano, T.; Date, S.; Odahara, Y.; Narimura, S. Synthesis of Imidazolium-Based Poly(Ionic Liquid)s and Their Application to Ion-Exchange Materials. *Polymer Bulletin* **2021**, *78* (9), 5165–5180. <https://doi.org/10.1007/s00289-020-03364-4>.
- (64) Ratner, M. A.; Shriver, D. F. Ion Transport in Solvent-Free Polymers. *Chem Rev* **1988**, *88* (1), 109–124. <https://doi.org/10.1021/cr00083a006>.
- (65) Di Noto, V.; Lavina, S.; Giffin, G. A.; Negro, E.; Scrosati, B. Polymer Electrolytes: Present, Past and Future. *Electrochim Acta* **2011**, *57* (1), 4–13. <https://doi.org/10.1016/j.electacta.2011.08.048>.
- (66) Obadia, M. M.; Ebastien Fagour, S.; Vygodskii, Y. S.; Ed Eric Vidal, F.; Serghei, A.; Shaplov, A. S.; Drockenmuller, E. Probing the Effect of Anion Structure on the Physical Properties of Cationic 1,2,3-Triazolium-Based Poly(Ionic Liquid)s. *J. Polym. Sci., Part A: Polym. Chem* **2016**, *54*, 2191–2199. <https://doi.org/10.1002/pola.28092>.
- (67) Mudraboyina, B. P.; Obadia, M. M.; Ne Allaoua, I.; Sood, R.; Serghei, A.; Drockenmuller, E. ,2,3-Triazolium-Based Poly(Ionic Liquid)s with Enhanced Ion Conducting Properties Obtained through a Click Chemistry Polyaddition Strategy. **2014**. <https://doi.org/10.1021/cm500021z>.
- (68) Marcilla, R.; Alcaide, F.; Sardon, H.; Pomposo, J. A.; Pozo-Gonzalo, C.; Mecerreyes, D. Tailor-Made Polymer Electrolytes Based upon Ionic Liquids and Their

Application in All-Plastic Electrochromic Devices. *Electrochem commun* **2006**, 8 (3), 482–488. <https://doi.org/10.1016/j.elecom.2006.01.013>.

(69) Vygodskii, Y. S.; Mel'nik, O. A.; Lozinskaya, E. I.; Shaplov, A. S.; Malyshkina, I. A.; Gavrilova, N. D.; Lyssenko, K. A.; Antipin, M. Y.; Golovanov, D. G.; Korlyukov, A. A.; Ignat'ev, N.; Welz-Biermann, U. The Influence of Ionic Liquid's Nature on Free Radical Polymerization of Vinyl Monomers and Ionic Conductivity of the Obtained Polymeric Materials. <https://doi.org/10.1002/pat.795>.

(70) Shaplov, A. S.; Ponkratov, D. O.; Aubert, P. H.; Lozinskaya, E. I.; Plesse, C.; Maziz, A.; Vlasov, P. S.; Vidal, F.; Vygodskii, Y. S. Truly Solid State Electrochromic Devices Constructed from Polymeric Ionic Liquids as Solid Electrolytes and Electrodes Formulated by Vapor Phase Polymerization of 3,4-Ethylenedioxythiophene. *Polymer (Guildf)* **2014**, 55 (16), 3385–3396. <https://doi.org/10.1016/j.polymer.2014.04.013>.

(71) Vygodskii, Y. S.; Shaplov, A. S.; Lozinskaya, E. I.; Lyssenko, K. A.; Golovanov, D. G.; Malyshkina, I. A.; Gavrilova, N. D.; Buchmeiser, M. R. Conductive Polymer Electrolytes Derived from Poly(Norbornene)s with Pendant Ionic Imidazolium Moieties. <https://doi.org/10.1002/macp.200700378>.

(72) Sood, R.; Zhang, B.; Serghei, A.; Bernard, J.; Drockenmuller, E. Triethylene Glycol-Based Poly(1,2,3-Triazolium Acrylate)s with Enhanced Ionic Conductivity. *Polym Chem* **2015**, 6 (18), 3521–3528. <https://doi.org/10.1039/c5py00273g>.

(73) Matsumoto, H.; Sakaebe, H.; Tatsumi, K. Preparation of Room Temperature Ionic Liquids Based on Aliphatic Onium Cations and Asymmetric Amide Anions and Their Electrochemical Properties as a Lithium Battery Electrolyte. *J Power Sources* **2005**, 146 (1–2), 45–50. <https://doi.org/10.1016/j.jpowsour.2005.03.103>.

(74) Shaplov, A. S.; Lozinskaya, E. I.; Vlasov, P. S.; Morozova, S. M.; Antonov, D. Y.; Aubert, P. H.; Armand, M.; Vygodskii, Y. S. New Family of Highly Conductive and Low Viscous Ionic Liquids with Asymmetric 2,2,2-Trifluoromethylsulfonyl-N-Cyanoamide Anion. *Electrochim Acta* **2015**, 175, 254–260. <https://doi.org/10.1016/j.electacta.2015.02.228>.

(75) Meek, K. M.; Elabd, Y. A. Polymerized Ionic Liquid Block Copolymers for Electrochemical Energy. *J Mater Chem A Mater* **2015**, 3 (48), 24187–24194. <https://doi.org/10.1039/C5TA07170D>.

(76) Mai, Y.; Eisenberg, A. Self-Assembly of Block Copolymers. *Chem Soc Rev* **2012**, 41 (18), 5969–5985. <https://doi.org/10.1039/c2cs35115c>.

- (77) Hashimoto, T.; Shibayama, M.; Fujimura, M.; Kawai, H. Microphase Separation (of Block Copolymers). *Memoirs of the Faculty of Engineering, Kyoto University* **2014**, 43 (pt 2), 1–6. https://doi.org/10.1007/978-3-642-36199-9_149-1.
- (78) Ruzette, A. V.; Leibler, L. Block Copolymers in Tomorrow's Plastics. *Nature Materials* **2005**, 4 (1), 19–31. <https://doi.org/10.1038/NMAT1295>.
- (79) Choi, J. H.; Ye, Y.; Elabd, Y. A.; Winey, K. I. Network Structure and Strong Microphase Separation for High Ion Conductivity in Polymerized Ionic Liquid Block Copolymers. *Macromolecules* **2013**, 46 (13), 5290–5300. <https://doi.org/10.1021/ma400562a>.
- (80) Ye, Y.; Choi, J. H.; Winey, K. I.; Elabd, Y. A. Polymerized Ionic Liquid Block and Random Copolymers: Effect of Weak Microphase Separation on Ion Transport. *Macromolecules* **2012**, 45 (17), 7027–7035. <https://doi.org/10.1021/ma301036b>.
- (81) Bouchet, R.; Maria, S.; Meziane, R.; Aboulaich, A.; Lienafa, L.; Bonnet, J. P.; Phan, T. N. T.; Bertin, D.; Gigmes, D.; Devaux, D.; Denoyel, R.; Armand, M. Single-Ion BAB Triblock Copolymers as Highly Efficient Electrolytes for Lithium-Metal Batteries. *Nat Mater* **2013**, 12 (5), 452–457. <https://doi.org/10.1038/nmat3602>.
- (82) Jangu, C.; Savage, A. M.; Zhang, Z.; Schultz, A. R.; Madsen, L. A.; Beyer, F. L.; Long, T. E. Sulfonimide-Containing Triblock Copolymers for Improved Conductivity and Mechanical Performance. *Macromolecules* **2015**, 48 (13), 4520–4528. <https://doi.org/10.1021/acs.macromol.5b01009>.
- (83) Rojas, A. A.; Inceoglu, S.; Mackay, N. G.; Thelen, J. L.; Devaux, D.; Stone, G. M.; Balsara, N. P. Effect of Lithium-Ion Concentration on Morphology and Ion Transport in Single-Ion-Conducting Block Copolymer Electrolytes. *Macromolecules* **2015**, 48 (18), 6589–6595. <https://doi.org/10.1021/acs.macromol.5b01193>.
- (84) Inceoglu, S.; Rojas, A. A.; Devaux, D.; Chen, X. C.; Stone, G. M.; Balsara, N. P. Morphology-Conductivity Relationship of Single-Ion-Conducting Block Copolymer Electrolytes for Lithium Batteries. *ACS Macro Lett* **2014**, 3 (6), 510–514. <https://doi.org/10.1021/mz5001948>.
- (85) Lozinskaya, E. I.; Ponkratov, D. O.; Malyshkina, I. A.; Grysan, P.; Lingua, G.; Gerbaldi, C.; Shaplov, A. S.; Vygodskii, Y. S. Self-Assembly of Li Single-Ion-Conducting Block Copolymers for Improved Conductivity and Viscoelastic Properties. *Electrochim Acta* **2022**, 413 (March), 140126. <https://doi.org/10.1016/j.electacta.2022.140126>.

- (86) Bungenberg de Jong, H. G., and H. R. K. Coacervation (Partial Miscibility in Colloid Systems). *Proc. K. Ned. Akad. Wet* **1929**, 32, 849–856.
- (87) Huang, H.; Trentle, M.; Liu, Z.; Xiang, K.; Higgins, W.; Wang, Y.; Xue, B.; Yang, S. Polymer Complex Fiber: Property, Functionality, and Applications. *ACS Appl Mater Interfaces* **2023**, 15 (6), 7639–7662. https://doi.org/10.1021/ACSAMI.2C19583/SUPPL_FILE/AM2C19583_SI_001.PDF.
- (88) Yamamoto, H.; Senoo, Y. Polyion Complex Fiber and Capsule Formed by Self-Assembly of Chitosan and Gellan at Solution Interfaces. [https://doi.org/10.1002/\(SICI\)1521-3935\(20000101\)201:1](https://doi.org/10.1002/(SICI)1521-3935(20000101)201:1).
- (89) Lang, W.; Huang, H.; Yang, L.; Luo, R.; Wang, Y.; Xue, B.; Yang, S. Polymer Complex Multilayers for Drug Delivery and Medical Devices. *ACS Appl Bio Mater* **2023**, 6 (9), 3555–3565. https://doi.org/10.1021/ACSABM.3C00404/ASSET/IMAGES/MEDIUM/MT3C00404_0007.GIF.
- (90) Engelhardt, J.; Zuilhof, H.; van der Gucht, J.; de Smet, L. C. P. M.; Maaskant, E. Polyester-Based Polyelectrolyte Complexes: Combining Thermo- and Saloplastic Properties. *ACS Appl Polym Mater* **2024**, 6 (8), 4409–4418. <https://doi.org/10.1021/acsapm.3c02566>.
- (91) van Lange, S. G. M.; te Brake, D. W.; Portale, G.; Palanisamy, A.; Sprakel, J.; van der Gucht, J. Moderated Ionic Bonding for Water-Free Recyclable Polyelectrolyte Complex Materials. *Sci Adv* **2024**, 10 (2), 3606. <https://doi.org/10.1126/sciadv.adi3606>.
- (92) Tseghai, G. B.; Mengistie, D. A.; Malengier, B.; Fante, K. A.; Van Langenhove, L. PEDOT:PSS-Based Conductive Textiles and Their Applications. *Sensors (Switzerland)* **2020**, 20 (7), 1–18. <https://doi.org/10.3390/s20071881>.
- (93) Louwet, F.; Groenendaal, L.; Dhaen, J.; Manca, J.; Van Luppen, J.; Verdonck, E.; Leenders, L. PEDOT/PSS: Synthesis, Characterization, Properties and Applications. *Synth Met* **2003**, 135–136, 115–117. [https://doi.org/10.1016/S0379-6779\(02\)00518-0](https://doi.org/10.1016/S0379-6779(02)00518-0).
- (94) Porcarelli, L.; Vlasov, P. S.; Ponkratov, D. O.; Lozinskaya, E. I.; Antonov, D. Y.; Nair, J. R.; Gerbaldi, C.; Mecerreyes, D.; Shaplov, A. S. Design of Ionic Liquid like Monomers towards Easy-Accessible Single-Ion Conducting Polymer Electrolytes. *Eur Polym J* **2018**, 107 (June), 218–228. <https://doi.org/10.1016/j.eurpolymj.2018.08.014>.

- (95) Zhang, H.; Li, C.; Piszcz, M.; Coya, E.; Rojo, T.; Rodriguez-Martinez, L. M.; Armand, M.; Zhou, Z. Single Lithium-Ion Conducting Solid Polymer Electrolytes: Advances and Perspectives. *Chem Soc Rev* **2017**, *46* (3), 797–815. <https://doi.org/10.1039/c6cs00491a>.
- (96) Vygodskii, Y. S.; Shaplov, A. S.; Lozinskaya, E. I.; Lyssenko, K. A.; Golovanov, D. G.; Malyshkina, I. A.; Gavrilova, N. D.; Buchmeiser, M. R. Conductive Polymer Electrolytes Derived from Poly(Norbornene)s with Pendant Ionic Imidazolium Moieties. *Macromol Chem Phys* **2008**, *209* (1), 40–51. <https://doi.org/10.1002/macp.200700378>.
- (97) Ogihara, W.; Washiro, S.; Nakajima, H.; Ohno, H. Effect of Cation Structure on the Electrochemical and Thermal Properties of Ion Conductive Polymers Obtained from Polymerizable Ionic Liquids. *Electrochim Acta* **2006**, *51* (13), 2614–2619. <https://doi.org/10.1016/j.electacta.2005.07.043>.
- (98) Shaplov, A. S.; Lozinskaya, E. I.; Ponkratov, D. O.; Malyshkina, I. A.; Vidal, F.; Aubert, P. H.; Okatova, O. V.; Pavlov, G. M.; Komarova, L. I.; Wandrey, C.; Vygodskii, Y. S. Bis(Trifluoromethylsulfonyl)Amide Based “Polymeric Ionic Liquids”: Synthesis, Purification and Peculiarities of Structure-Properties Relationships. *Electrochim Acta* **2011**, *57* (1), 74–90. <https://doi.org/10.1016/J.ELECTACTA.2011.06.041>.
- (99) Ye, Y.; Elabd, Y. A. Anion Exchanged Polymerized Ionic Liquids: High Free Volume Single Ion Conductors. *Polymer (Guildf)* **2011**, *52* (5), 1309–1317. <https://doi.org/10.1016/j.polymer.2011.01.031>.
- (100) Shaplov, A. S.; Vlasov, P. S.; Armand, M.; Lozinskaya, E. I.; Ponkratov, D. O.; Malyshkina, I. A.; Vidal, F.; Okatova, O. V.; Pavlov, G. M.; Wandrey, C.; Godovikov, I. A.; Vygodskii, Y. S. Design and Synthesis of New Anionic “Polymeric Ionic Liquids” with High Charge Delocalization. *Polym Chem* **2011**, *2* (11), 2609–2618. <https://doi.org/10.1039/c1py00282a>.
- (101) Shaplov, A. S.; Goujon, L.; Vidal, F.; Lozinskaya, E. I.; Meyer, F.; Malyshkina, I. A.; Chevrot, C.; Teyssié, D.; Odinet, I. L.; Vygodskii, Y. S. Ionic IPNs as Novel Candidates for Highly Conductive Solid Polymer Electrolytes. *J Polym Sci A Polym Chem* **2009**, *47* (17), 4245–4266. <https://doi.org/10.1002/pola.23478>.
- (102) Washiro, S.; Yoshizawa, M.; Nakajima, H.; Ohno, H. Highly Ion Conductive Flexible Films Composed of Network Polymers Based on Polymerizable Ionic Liquids. *Polymer (Guildf)* **2004**, *45* (5), 1577–1582. <https://doi.org/10.1016/j.polymer.2004.01.003>.

- (103) Yoshizawa, M.; Ohno, H. Synthesis of Molten Salt-Type Polymer Brush and Effect of Brush Structure on the Ionic Conductivity. *Electrochim Acta* **2001**, *46* (10–11), 1723–1728. [https://doi.org/10.1016/S0013-4686\(00\)00777-5](https://doi.org/10.1016/S0013-4686(00)00777-5).
- (104) Vygodskii, Y. S.; Shaplov, A. S.; Lozinskaya, E. I.; Vlasov, P. S.; Malyshkina, I. A.; Gavrilova, N. D.; Santhosh Kumar, P.; Buchmeiser, M. R. Cyclopolymerization of *N*, *N*-Dipropargylamines and *N*, *N*-Dipropargyl Ammonium Salts. *Macromolecules* **2008**, *41* (6), 1919–1928. <https://doi.org/10.1021/ma7022777>.
- (105) Dimitrov-Raytchev, P.; Beghdadi, S.; Serghei, A.; Drockenmuller, E. Main-Chain 1,2,3-Triazolium-Based Poly(Ionic Liquid)s Issued from AB + AB Click Chemistry Polyaddition. *J Polym Sci A Polym Chem* **2013**, *51* (1), 34–38. <https://doi.org/10.1002/POLA.26326>.
- (106) Binauld, S.; Fleury, E.; Drockenmuller, E. Solving the Loss of Orthogonality during the Polyaddition of α -Azide- ω -Alkyne Monomers Catalyzed by Cu(PPh₃)₃Br: Application to the Synthesis of High-Molar Mass Polytriazoles. *J Polym Sci A Polym Chem* **2010**, *48* (11), 2470–2476. <https://doi.org/10.1002/POLA.24018>.
- (107) Zhang, S.; Sun, N.; He, X.; Lu, X.; Zhang, X. Physical Properties of Ionic Liquids: Database and Evaluation. *J Phys Chem Ref Data* **2006**, *35* (4), 1475–1517. <https://doi.org/10.1063/1.2204959>.
- (108) Ogihara, W.; Washiro, S.; Nakajima, H.; Ohno, H. Effect of Cation Structure on the Electrochemical and Thermal Properties of Ion Conductive Polymers Obtained from Polymerizable Ionic Liquids. *Electrochim Acta* **2006**, *51* (13), 2614–2619. <https://doi.org/10.1016/J.ELECTACTA.2005.07.043>.
- (109) Obadia, M. M.; Jourdain, A.; Cassagnau, P.; Montarnal, D.; Drockenmuller, E. Tuning the Viscosity Profile of Ionic Vitrimers Incorporating 1,2,3-Triazolium Cross-Links. *Adv Funct Mater* **2017**, *27* (45). <https://doi.org/10.1002/ADFM.201703258>.
- (110) Matsumoto, H.; Sakaebe, H.; Tatsumi, K. Preparation of Room Temperature Ionic Liquids Based on Aliphatic Onium Cations and Asymmetric Amide Anions and Their Electrochemical Properties as a Lithium Battery Electrolyte. *J Power Sources* **2005**, *146* (1–2), 45–50. <https://doi.org/10.1016/J.JPOWSOUR.2005.03.103>.
- (111) Watanabe, M.; Thomas, M. L.; Zhang, S.; Ueno, K.; Yasuda, T.; Dokko, K. Application of Ionic Liquids to Energy Storage and Conversion Materials and Devices. *Chem Rev* **2017**, *117* (10), 7190–7239. <https://doi.org/10.1021/ACS.CHEMREV.6B00504>.

- (112) Flachard, D.; Rolland, J.; Obadia, M. M.; Serghei, A.; Bouchet, R.; Drockenmuller, E. A 1,2,3-Triazolate Lithium Salt with Ionic Liquid Properties at Room Temperature. *Chemical Communications* **2018**, 54 (65), 9035–9038. <https://doi.org/10.1039/C8CC04463E>.
- (113) Williams, M. L.; Landel, R. F.; Ferry, J. D. The Temperature Dependence of Relaxation Mechanisms in Amorphous Polymers and Other Glass-Forming Liquids. *J Am Chem Soc* **1955**, 77 (14), 3701–3707. <https://doi.org/10.1021/ja01619a008>.
- (114) Vinogradov, G. V.; Malkin, A. Ya. *Rheology of Polymers*; Springer Berlin Heidelberg: Berlin, Heidelberg, 1980. <https://doi.org/10.1007/978-3-642-52204-8>.
- (115) Perrier, S. 50th Anniversary Perspective: RAFT Polymerization - A User Guide. *Macromolecules*. American Chemical Society October 10, **2017**, pp 7433–7447. <https://doi.org/10.1021/acs.macromol.7b00767>.
- (116) Nosov, D. R.; Ronnasi, B.; Lozinskaya, E. I.; Ponkratov, D. O.; Puchot, L.; Grysan, P.; Schmidt, D. F.; Lessard, B. H.; Shaplov, A. S. Mechanically Robust Poly(Ionic Liquid) Block Copolymers as Self-Assembling Gating Materials for Single-Walled Carbon-Nanotube-Based Thin-Film Transistors. *ACS Appl Polym Mater* **2023**, 5 (4), 2639–2653. <https://doi.org/10.1021/acsapm.2c02223>.
- (117) Braunecker, W. A.; Matyjaszewski, K. Controlled/Living Radical Polymerization: Features, Developments, and Perspectives. *Progress in Polymer Science (Oxford)*. January 2007, pp 93–146. <https://doi.org/10.1016/j.progpolymsci.2006.11.002>.
- (118) Meek, K. M.; Elabd, Y. A. Sulfonated Polymerized Ionic Liquid Block Copolymers. *Macromol Rapid Commun* **2016**, 37 (14), 1200–1206. <https://doi.org/10.1002/marc.201600089>.
- (119) Hu, Y.-F.; Xu, C.-M. Effect of the Structures of Ionic Liquids on Their Physical-Chemical Properties and the Phase Behavior of Mixtures Involving Ionic Liquids. *Chem Rev* **2006**, 0 (0), 0–0. <https://doi.org/10.1021/CR0502044>.
- (120) Babanejad, N.; Kandalam, U.; Omid, Y.; Omidian, H. Functional Properties of Thermally Tampered Poly(Ethylene Oxide). *Bioimpacts* **2022**, 12 (5), 471. <https://doi.org/10.34172/BI.2022.24077>.
- (121) Tsunashima, K.; Sugiya, M. Physical and Electrochemical Properties of Low-Viscosity Phosphonium Ionic Liquids as Potential Electrolytes. *Electrochem commun* **2007**, 9 (9), 2353–2358. <https://doi.org/10.1016/J.ELECOM.2007.07.003>.

- (122) Hemp, S. T.; Zhang, M.; Allen, M. H.; Cheng, S.; Moore, R. B.; Long, T. E. Comparing Ammonium and Phosphonium Polymerized Ionic Liquids: Thermal Analysis, Conductivity, and Morphology. *Macromol Chem Phys* **2013**, *214* (18), 2099–2107. <https://doi.org/10.1002/MACP.201300322>.
- (123) Borah, P.; Dutta, A. A Conductivity Study of Polyelectrolytes Based on 4-Vinyl Pyridine and Butylmethacrylate. *Ionics (Kiel)* **2008**, *14* (4), 313–321. <https://doi.org/10.1007/S11581-008-0203-6/FIGURES/8>.
- (124) Gouveia, A. S. L.; Bernardes, C. E. S.; Tomé, L. C.; Lozinskaya, E. I.; Vygodskii, Y. S.; Shaplov, A. S.; Lopes, J. N. C.; Marrucho, I. M. Ionic Liquids with Anions Based on Fluorosulfonyl Derivatives: From Asymmetrical Substitutions to a Consistent Force Field Model. *Physical Chemistry Chemical Physics* **2017**, *19* (43), 29617–29624. <https://doi.org/10.1039/C7CP06081E>.
- (125) Sprenger, J. A. P.; Landmann, J.; Drisch, M.; Ignatev, N.; Finze, M. Syntheses of Tricyanofluoroborates $M[BF(CN)_3]$ ($M = Na, K$): $(CH_3)_3SiCl$ Catalysis, Countercation Effect, and Reaction Intermediates. *Inorg Chem* **2015**, *54* (7), 3403–3412. <https://doi.org/10.1021/ic503077c>.
- (126) Soares, B. F.; Nosov, D. R.; Pires, J. M.; Tyutyunov, A. A.; Lozinskaya, E. I.; Antonov, D. Y.; Shaplov, A. S.; Marrucho, I. M. Tuning CO₂ Separation Performance of Ionic Liquids through Asymmetric Anions. *Molecules* **2022**, *27* (413), 1–23. <https://doi.org/10.3390/molecules27020413>.
- (127) Paschoal, V. H.; Faria, L. F. O.; Ribeiro, M. C. C. Vibrational Spectroscopy of Ionic Liquids. *Chem Rev* **2017**, *117* (10), 7053–7112. <https://doi.org/10.1021/acs.chemrev.6b00461>.
- (128) Heimer, N. E.; Del Sesto, R. E.; Meng, Z.; Wilkes, J. S.; Carper, W. R. Vibrational Spectra of Imidazolium Tetrafluoroborate Ionic Liquids. *J Mol Liq* **2006**, *124* (1–3), 84–95. <https://doi.org/10.1016/j.molliq.2005.08.004>.
- (129) López-Martin, I.; Burello, E.; Davey, P. N.; Seddon, K. R.; Rothenberg, G. Anion and Cation Effects on Imidazolium Salt Melting Points: A Descriptor Modelling Study. *ChemPhysChem* **2007**, *8* (5), 690–695. <https://doi.org/10.1002/cphc.200600637>.
- (130) Zhou, W.; Yang, H.; Guo, X.; Lu, J. Thermal Degradation Behaviors of Some Branched and Linear Polysiloxanes. *Polym Degrad Stab* **2006**, *91* (7), 1471–1475. <https://doi.org/10.1016/j.polymdegradstab.2005.10.005>.

- (131) Zhou, Z. Bin; Matsumoto, H.; Tatsumi, K. Low-Melting, Low-Viscous, Hydrophobic Ionic Liquids: 1-Alkyl(Alkyl Ether)-3-Methylimidazolium Perfluoroalkyltrifluoroborate. *Chemistry - A European Journal* **2004**, *10* (24), 6581–6591. <https://doi.org/10.1002/chem.200400533>.
- (132) Wang, H.; Wang, J.; Zhang, S.; Pei, Y.; Zhuo, K. Ionic Association of the Ionic Liquids [C4mim][BF4], [C4mim][PF6], and [Cnmim]Br in Molecular Solvents. *ChemPhysChem* **2009**, *10* (14), 2516–2523. <https://doi.org/10.1002/cphc.200900438>.
- (133) Krogstad, D. V.; Lynd, N. A.; Choi, S. H.; Spruell, J. M.; Hawker, C. J.; Kramer, E. J.; Tirrell, M. V. Effects of Polymer and Salt Concentration on the Structure and Properties of Triblock Copolymer Coacervate Hydrogels. *Macromolecules* **2013**, *46* (4), 1512–1518. <https://doi.org/10.1021/ma302299r>.
- (134) Timilsena, Y. P.; Akanbi, T. O.; Khalid, N.; Adhikari, B.; Barrow, C. J. Complex Coacervation: Principles, Mechanisms and Applications in Microencapsulation. *Int J Biol Macromol* **2019**, *121*, 1276–1286. <https://doi.org/10.1016/j.ijbiomac.2018.10.144>.
- (135) Srivastava, S.; Levi, A. E.; Goldfeld, D. J.; Tirrell, M. V. Structure, Morphology, and Rheology of Polyelectrolyte Complex Hydrogels Formed by Self-Assembly of Oppositely Charged Triblock Polyelectrolytes. *Macromolecules* **2020**, *53* (14), 5763–5774. <https://doi.org/10.1021/acs.macromol.0c00847>.
- (136) Blocher McTigue, W. C.; Voke, E.; Chang, L. W.; Perry, S. L. The Benefit of Poor Mixing: Kinetics of Coacervation. *Physical Chemistry Chemical Physics* **2020**, *22* (36), 20643–20657. <https://doi.org/10.1039/d0cp03224g>.
- (137) MacFarlane, D. R.; Meakin, P.; Amini, N.; Forsyth, M. Structural Studies of Ambient Temperature Plastic Crystal Ion Conductors. *Journal of Physics Condensed Matter* **2001**, *13* (36), 8257–8267. <https://doi.org/10.1088/0953-8984/13/36/303>.
- (138) Jing, B.; Xu, D.; Wang, X.; Zhu, Y. Multiresponsive, Critical Gel Behaviors of Polyzwitterion-Polyoxometalate Coacervate Complexes. *Macromolecules* **2018**, *51* (22), 9405–9411. <https://doi.org/10.1021/acs.macromol.8b01759>.
- (139) Winter, H. H.; Mours, M. Rheology of Polymers Near Liquid-Solid Transitions. *Advances in Polymer Science* **1997**, *134*, 164–234. https://doi.org/10.1007/3-540-68449-2_3.

- (140) Ferreira, M.; Jing, B.; Lorenzana, A.; Zhu, Y. Effect of Polyampholyte Net Charge on Complex Coacervation between Polyampholytes and Inorganic Polyoxometalate Giant Anions. *Soft Matter* **2020**, *16* (45), 10280–10289. <https://doi.org/10.1039/d0sm01565b>.
- (141) Jing, B.; Ferreira, M.; Lin, K.; Li, R.; Yavitt, B. M.; Qiu, J.; Fukuto, M.; Zhu, Y. Ultrastructure of Critical-Gel-like Polyzwitterion-Polyoxometalate Complex Coacervates: Effects of Temperature, Salt Concentration, and Shear. *Macromolecules* **2020**, *53* (24), 10972–10980. <https://doi.org/10.1021/acs.macromol.0c01618>.
- (142) Naert, P.; Rabaey, K.; Stevens, C. V. Ionic Liquid Ion Exchange: Exclusion from Strong Interactions Condemns Cations to the Most Weakly Interacting Anions and Dictates Reaction Equilibrium. *Green Chemistry* **2018**, *20* (18), 4277–4286. <https://doi.org/10.1039/C8GC01869C>.
- (143) Maeda, Y.; Paul, D. R. Effect of Antiplasticization on Gas Sorption and Transport. III. Free Volume Interpretation. *J Polym Sci B Polym Phys* **1987**, *25* (5), 1005–1016. <https://doi.org/10.1002/POLB.1987.090250503>.
- (144) White, R. P.; Lipson, J. E. G. Polymer Free Volume and Its Connection to the Glass Transition. *Macromolecules* **2016**, *49* (11), 3987–4007. <https://doi.org/10.1021/acs.macromol.6b00215>.
- (145) Fagnant, D. P.; Desilva, M. A.; Brennecke, J. F. Solid–Liquid Equilibria Measurements of Mixtures of Lithium Bis(Trifluoromethanesulfonyl)Imide with Varying Alkyl Chain Length Ammonium Bis(Trifluoromethanesulfonyl)Imide Ionic Liquids. *J Chem Eng Data* **2016**, *61* (2), 958–967. <https://doi.org/10.1021/acs.jced.5b00807>.
- (146) Del Sesto, R. E.; Corley, C.; Robertson, A.; Wilkes, J. S. Tetraalkylphosphonium-Based Ionic Liquids. *J Organomet Chem* **2005**, *690* (10), 2536–2542. <https://doi.org/10.1016/J.JORGANCHEM.2004.09.060>.
- (147) Yoshizawa-Fujita, M.; Kousa, Y.; Kidena, K.; Ohira, A.; Takeoka, Y.; Rikukawa, M. Proton Transport Properties in an Ionic Liquid Having a Hydroxyl Group. *Physical Chemistry Chemical Physics* **2011**, *13* (29), 13427–13432. <https://doi.org/10.1039/C1CP21387C>.
- (148) He, Y.; Chen, W.; Li, X.; Zhang, Z.; Fu, J.; Zhao, C.; Xie, E. Freestanding Three-Dimensional Graphene/MnO₂ Composite Networks as Ultralight and Flexible Supercapacitor Electrodes. *ACS Nano* **2013**, *7* (1), 174–182. <https://doi.org/10.1021/nn304833s>.

- (149) Abdisattar, A.; Yeleuov, M.; Daulbayev, C.; Askaruly, K.; Tolynbekov, A.; Taurbekov, A.; Prikhodko, N. Recent Advances and Challenges of Current Collectors for Supercapacitors. *Electrochem commun* **2022**, *142*, 107373. <https://doi.org/10.1016/J.ELECOM.2022.107373>.
- (150) Alexandre, S. A.; Silva, G. G.; Trigueiro, J. P. C.; Lavall, R. L. Tuning the Electrochemical Properties of Carbon-Based Supercapacitors by Composite Preparation and Cell Asymmetries. *Electrochim Acta* **2023**, *465*, 143004. <https://doi.org/10.1016/J.ELECTACTA.2023.143004>.
- (151) Alexandre, S. A.; Silva, G. G.; Santamaría, R.; Trigueiro, J. P. C.; Lavall, R. L. A Highly Adhesive PIL/IL Gel Polymer Electrolyte for Use in Flexible Solid State Supercapacitors. *Electrochim Acta* **2019**, *299*, 789–799. <https://doi.org/10.1016/J.ELECTACTA.2019.01.029>.
- (152) Gómez, E.; Calvar, N.; Domínguez, Á. Thermal Behaviour of Pure Ionic Liquids. In *Ionic Liquids - Current State of the Art*; InTech, **2015**. <https://doi.org/10.5772/59271>.